

**Reionization from Z to A:  
Lessons from  $z \sim 6 - 7$  Lyman- $\alpha$  emitters  
and local analogs of high-redshift galaxies**

**A DISSERTATION  
SUBMITTED TO THE FACULTY OF THE GRADUATE SCHOOL  
OF THE UNIVERSITY OF MINNESOTA  
BY**

Micaela Bresette Bagley

**IN PARTIAL FULFILLMENT OF THE REQUIREMENTS  
FOR THE DEGREE OF  
Doctor of Philosophy**

M. Claudia Scarlata

August, 2018

© Micaela Bresette Bagley 2018  
ALL RIGHTS RESERVED

# Acknowledgements

Graduate school has been quite a journey, one that I would never have completed alone. I would not be here without the help and support of so many people. I'll never be able to thank you all for everything you've done for me.

First, to my advisor, Claudia Scarlata: I have learned so much from working with you these last six years. Thank you for all you have taught me, both by word and by example. Thank you for helping me through my frustration, for allowing me time to learn from my failures, and for inspiring me to always question. You have introduced me to incredible people, sent me to amazing places, and helped me find my confidence. I admire you as a researcher, mentor, colleague, and friend.

To the members of MifA: thank you to everyone for creating the collaborative and supportive environment that makes MifA special. I would like to specifically thank Hugh Dickinson, John Phillips, Michael Rutkowski, and Sourabh Chauhan for all the discussions and help throughout the years. Thank you, Terry Jones, for sharing dust and polarization with me. Thank you to my additional committee members, Lucy Fortson and Larry Rudnick, for your time and feedback. And thank you, Terry Thibeault, for your help navigating all the hurdles of grad school life. The department won't be the same without you.

To all members of the WISP team: I am grateful for all I have learned through telecons and meetings with you all. I would like to thank Alaina Henry and Marc Rafelski for the many interesting discussions and helpful comments. Thank you Matt Malkan and Harry Teplitz for your support and advice. And thank you to Ivano Baronchelli, Yu Sophia Dai, and James Colbert for all your help with data reduction and for answering my never-ending stream of questions. Additionally, the emission line catalog presented in Chapter 2 would not exist without the monumental effort of first Alaina Henry improving the line detection process and then all the heroic line finders: Claudia Scarlata, Karlen Shahinyan, Ivano Baronchelli, Ben Sunnquist, Vihang Mehta, Marc Rafelski, Michael Rutkowski, Melanie Beck, and Yu Sophia Dai.

To my collaborators in the Euclid Consortium: thank you to Jason Rhodes and Alina

Kiessling for all the advice, support, and encouragement; Yun Wang and Peter Capak for all your help during my time at IPAC; and Andreas Faisst, Dan Masters, and Alex Merson for hanging out at IPAC and at conferences, with bagels and beers.

To all MifA grad students: thank you collectively for putting up with me for the past six years. Thank you for listening to my rants and sharing your own. Thank you for the group study sessions, roof beers, camping trips, game and movie nights, and coffee and Bun Mi runs that made grad school survivable. Thank you to all my office mates throughout the years for tolerating all the distractions and for answering all my annoying questions. Thank you, Melanie Beck, for always being willing to shoot the ... breeze with me. And Zahra Forootaninia and Mehdi Lame'e for your warmth and for cheering me up any time of day. To Karl Young and Erin Stuhlsatz: thank you for all the frisbee and donuts. To Melanie Galloway: thank you for teaching me all the swords. And thanks to all my Gumbros for the good times.

To Michael Gordon, Karlen Shahinyan, and Vihang Mehta: your friendship has carried me through grad school and has been my single biggest motivation to come in each day. I really wouldn't be here without you.

To my parents: you have all been incredible sources of love and support. Thank you to Mom and Pete, Dad and Abby for believing in me and encouraging me every step of the way. Thank you for the packages, calls, texts, and emails, for supporting me in all my moves further and further from home. Thank you to Mark and Linda for welcoming me into your family as your own. Thank you for the love you have extended to me, for providing the bubble and, of course, for all the doggy day care.

To Meg's friends (initially) for so quickly and completely welcoming me into your friend circles: Caitlyn, Emily, Anna, Andy, Julie, Damian, LOLA(!), Willy, Cyri, Allie, Mark, Kristen, and Eileen. To Deb and Sarah: thank you for pulling me back every time I fall off the edge of the Earth. And finally, to Veronica: thank you for all the pictures of cute animals and the offers to have so many people sit on your head.

Last but certainly not least, to my wife, Meg: you are my rock, my strength, my courage, my light, and my humor. Thank you for putting up with the stress and the crazy, for laughing with me, for upside-down cow-skulling our problems together, and for always showing me what actually matters. I am so lucky to have you as a partner, and I can't wait for our next joys and challenges.

Much of the research presented in this thesis uses observations and analysis from the WISP Survey. Support for the WISP HST Programs GO-11696, 12283, 12568, 12902, 13517, 13352, and 14178 was provided by NASA through grants from the Space Telescope Science Institute, which is operated by the Association of Universities for Research in Astronomy, Inc., under NASA contract NAS5-26555.

Chapter 4 is largely taken from a paper published in ApJ, and the acknowledgements for that paper are as follows:

We thank the anonymous referee for a careful review and suggestions that improved the manuscript. This research was partially supported by NASA ROSES grant 12-EUCLID12-0004. Support for HST Programs GO-11696, 12283, 12568, 12902, 13517, 13352, and 14178 was provided by NASA through grants from the Space Telescope Science Institute, which is operated by the Association of Universities for Research in Astronomy, Inc., under NASA contract NAS5-26555. T. Garel is grateful to the LABEX Lyon Institute of Origins (ANR-10-LABX-0066) of the Université de Lyon for its financial support within the programme ‘Investissements d’Avenir’ (ANR-11-IDEX-0007) of the French government operated by the National Research Agency (ANR). This research has made use of NASA’s Astrophysics Data System Bibliographic Services.

The work presented in Chapter 6 was supported by NASA ROSES grant 12-EUCLID12-0004.

# Dedication

do grá mo chroí

## Abstract

The dark ages that followed recombination ended with the appearance of metal-free stars and the subsequent formation of numerous low-mass, metal-poor galaxies. The collective ionizing background from these newly-forming galaxies is thought to be responsible for the reionization of the diffuse hydrogen in the intergalactic medium (IGM) between redshifts 10 and 6.5. The progression of the reionization history of the universe depends on the nature of these first sources — their number densities, luminosities, clustering, and production rates of ionizing photons — which is currently the subject of considerable observational and theoretical efforts. In this thesis, we combine both local and distant observations in a two-part approach to studying the Epoch of Reionization: exploring the progression of the transition and investigating the sources responsible for initiating and maintaining it.

In the first part, we present the results of a systematic search for Lyman- $\alpha$  emitting galaxies (LAEs) at redshifts greater than 6. Ly $\alpha$  photons are produced by a resonant transition and so are sensitive to the presence of even a small fraction of neutral hydrogen. The evolving neutral hydrogen fraction in the IGM can therefore be constrained using observations of the Ly $\alpha$  output from galaxies around the end of reionization. We select high-redshift LAE candidates using imaging and spectroscopic data from the the *HST* WFC3 Infrared Spectroscopic Parallel (WISP) Survey. The sample selection combines an emission line search with a cut on galaxy colors chosen to identify a Lyman break. This approach, when combined with the broad spectral coverage of the WISP Survey, eliminates almost all lower-redshift contaminants. We find two LAEs at  $z = 6.38$  and  $6.44$  with line luminosities of  $L_{\text{Ly}\alpha} \sim 4.7 \times 10^{43} \text{ erg s}^{-1}$ , putting them among the brightest LAEs discovered at these redshifts. The WISP LAEs have a high number density of  $7.7 \times 10^{-6} \text{ Mpc}^{-3}$ . We argue that the LAEs reside in megaparsec-scale ionized bubbles that allow the Ly $\alpha$  photons to redshift out of resonance before encountering the neutral IGM. In the context of recent detections of similarly bright, high-redshift LAEs, we discuss the implications of the high number densities for a non-homogeneous or “patchy” reionization process. After considering possible ionizing sources for the WISP bubbles, we conclude that the observed LAEs alone are not sufficient.

In the second part of this thesis, we present an analysis of a sample of local galaxies that are potential analogs to those responsible for the reionization of the IGM. Observational studies at  $z > 7$  are limited to the brightest sources, and the more common, fainter, lower-mass galaxies that are expected to be responsible for reionization remain largely inaccessible.

Additionally, emission at  $\lambda < 1216\text{\AA}$  from galaxies at these redshifts is absorbed by the neutral hydrogen in the IGM. Analogs of these high-redshift galaxies are therefore required in order to study the properties of the galaxies that contributed to reionization. Selected from the Sloan Digital Sky Survey for their large  $[\text{O III}]/[\text{O II}]$  ratios and high  $\text{H}\alpha$  equivalent widths, the local galaxies have very low masses and high-ionization lines present in their spectra. We perform a careful two-dimensional reduction and calibration that preserves the spatial information in both the continuum and emission lines. We present preliminary results and describe the next steps of this project, including fitting the spectrum of each galaxy with ionization models to estimate galactic properties such as gas temperature, elemental abundance, and the production rate of ionizing radiation. Both the emission lines and continua of the spectra are spatially extended, allowing for the spatial mapping of these properties. We compare these measurements with those of similar local analogs in the literature to show that these galaxies are candidate Lyman continuum leakers, a necessity for ionizing the hydrogen in the IGM at high redshift.

Finally, in anticipation of future slitless cosmological surveys, we use the WISP and 3D-HST *HST* grism surveys to provide constraints on the observed distributions and properties of emission line galaxies at redshifts  $z \sim 1 - 2$ . We calculate the number densities of  $\text{H}\alpha + [\text{N II}]$  and  $[\text{O III}]\lambda 5007$ -emitters, and the equivalent width and emission size distributions that ESA's Euclid mission can expect to detect. Such observations are crucial for calibrating the simulations and mock catalogs used to test the survey design and expected results.

# Contents

<b>Acknowledgements</b>	<b>i</b>
<b>Dedication</b>	<b>iv</b>
<b>Abstract</b>	<b>v</b>
<b>List of Tables</b>	<b>x</b>
<b>List of Figures</b>	<b>xi</b>
<b>1 Introduction</b>	<b>1</b>
1.1 The Current Cosmological Model . . . . .	1
1.2 The early history of the universe . . . . .	2
1.2.1 The (Re)ionization of intergalactic hydrogen . . . . .	3
1.3 Constraining the reionization history . . . . .	7
1.4 Observational probes of the epoch of reionization . . . . .	10
1.4.1 The Ly $\alpha$ Forest and Gunn-Peterson trough . . . . .	10
1.4.2 Thomson scattering optical depth . . . . .	12
1.4.3 Lyman- $\alpha$ emitting galaxies . . . . .	13
1.4.4 LAE Clustering . . . . .	18
1.4.5 Local analogs . . . . .	20
1.5 This Thesis . . . . .	21
<b>2 Observations: The WISP Survey</b>	<b>22</b>
2.1 WISP Survey Overview . . . . .	22
2.1.1 Slitless Grism Data . . . . .	23
2.2 WISP Data Reduction . . . . .	26
2.2.1 Grism Depths . . . . .	29

2.3	Photometric catalog . . . . .	31
2.3.1	PSF-Matched Photometry . . . . .	32
2.4	Emission line catalog . . . . .	33
2.4.1	Emission Line Candidate Identification . . . . .	35
2.4.2	Emission Line Candidate Inspection . . . . .	39
2.4.3	Emission Line Measurements . . . . .	42
2.4.4	Catalog Completeness . . . . .	47
<b>3</b>	<b>Simulated Data</b>	<b>52</b>
3.1	Completeness of the WISP Survey . . . . .	52
3.2	Simulated template library . . . . .	58
<b>4</b>	<b>A High Space Density of Luminous Ly<math>\alpha</math> Emitters at <math>z \sim 6.5</math></b>	<b>62</b>
4.1	Introduction . . . . .	62
4.2	Observations - The WISP Survey . . . . .	64
4.3	Sample Selection . . . . .	67
4.3.1	Choosing the selection criteria . . . . .	67
4.3.2	Selection criteria . . . . .	69
4.4	Contamination . . . . .	69
4.4.1	Emission line misidentification . . . . .	72
4.5	Results . . . . .	75
4.5.1	$z > 6$ LAEs . . . . .	75
4.5.2	What are the redder UVIS dropouts? . . . . .	77
4.5.3	Calculation of the number density . . . . .	78
4.5.4	Extended Ly $\alpha$ emission . . . . .	81
4.6	Discussion . . . . .	84
4.6.1	The number density of $z \sim 6.5$ LAEs . . . . .	84
4.6.2	Evolution to $z \gtrsim 7$ . . . . .	88
4.6.3	Extent of Ly $\alpha$ halos . . . . .	90
4.6.4	Ionized bubbles . . . . .	91
4.7	Summary . . . . .	95
<b>5</b>	<b>Local Analogs</b>	<b>97</b>
5.1	Introduction . . . . .	97
5.1.1	Sample Selection . . . . .	98
5.2	Observations . . . . .	101

5.2.1	Spectral Reduction and Calibration . . . . .	102
5.3	Early Results . . . . .	105
5.3.1	Spatial extent of emission lines . . . . .	106
5.4	Discussion and Future Work . . . . .	107
5.4.1	High [O III]/[O II] and the Escape of Lyman Continuum Photons . . . . .	109
<b>6</b>	<b>Forecasts for ESA’s Euclid Dark Energy Mission</b>	<b>110</b>
6.1	Introduction . . . . .	110
6.2	Euclid Sample . . . . .	111
6.2.1	The 3D-HST+AGHAST Survey . . . . .	113
6.2.2	Sample Selection . . . . .	114
6.3	Results . . . . .	117
6.3.1	Emission Line Number Counts . . . . .	117
6.3.2	Emission and continuum sizes . . . . .	120
6.3.3	Equivalent Width of $H\alpha + [N II]$ . . . . .	126
6.4	Discussion . . . . .	128
6.4.1	[O III] Line Profile . . . . .	128
6.4.2	Redshift Accuracy . . . . .	129
6.4.3	Contaminating Redshifts . . . . .	132
<b>7</b>	<b>Summary</b>	<b>137</b>
	<b>References</b>	<b>139</b>

# List of Tables

2.1	The WISP Survey: WISP Fields . . . . .	30
2.2	The WISP Survey: Emission Line Detection Parameters . . . . .	38
2.3	The WISP Survey: Model Spectrum Parameters . . . . .	43
3.1	Simulated Data: Input parameters for simulated sources . . . . .	53
3.2	Simulated Data: Luminosity Functions used in synthetic catalog . . . . .	59
4.1	LAEs at $z \sim 6.5$ : WISP Fields used in this work, exposure times and depths	65
4.1	LAEs at $z \sim 6.5$ : WISP Fields used in this work, exposure times and depths	66
4.2	LAEs at $z \sim 6.5$ : WISP LAEs . . . . .	76
5.1	Local Analogs: Summary of Observations . . . . .	102
6.1	Euclid Forecasts: Euclid Sample Selection Criteria . . . . .	116
6.2	Euclid Forecasts: WS Number counts for lines with $\lambda_{\text{obs}} \geq 12500 \text{ \AA}$ . . . . .	119

# List of Figures

1.1	Introduction: The history of the universe . . . . .	4
1.2	Introduction: Emission and absorption line wavelengths . . . . .	6
1.3	Introduction: The Ly $\alpha$ forest . . . . .	10
1.4	Introduction: Lyman break and LAE narrowband detection techniques . . .	15
1.5	Introduction: LAE and LBG clustering . . . . .	19
2.1	The WISP Survey: Filter set . . . . .	23
2.2	The WISP Survey: Field locations . . . . .	24
2.3	The WISP Survey: Spectral features in grism data . . . . .	25
2.4	The WISP Survey: The multi-component sky background . . . . .	27
2.5	The WISP Survey: Field emission line sensitivity limits . . . . .	29
2.6	The WISP Survey: Photometric aperture types . . . . .	31
2.7	The WISP Survey: Isophotal photometry comparison . . . . .	34
2.8	The WISP Survey: Ricker wavelet . . . . .	36
2.9	The WISP Survey: Example of a continuous wavelet transform . . . . .	37
2.10	The WISP Survey: Display from interactive line finding procedure . . . . .	41
2.11	The WISP Survey: Emission line S/N . . . . .	45
2.12	The WISP Survey: Redshift distribution of emission line catalog . . . . .	46
2.13	The WISP Survey: Flux distribution of emission line catalog . . . . .	47
2.14	The WISP Survey: Imaging completeness . . . . .	49
2.15	The WISP Survey: Completeness of WISP emission line catalog . . . . .	50
3.1	Simulated Data: Input parameter distributions for completeness analysis . .	55
3.2	Simulated Data: Emission line flux comparison . . . . .	56
3.3	Simulated Data: Source size comparison . . . . .	57
3.4	Simulated Data: Example of processing template spectra . . . . .	61
4.1	LAEs at $z \sim 6.5$ : Color-color plot identifying $z > 6$ dropout galaxies . . . .	70
4.2	LAEs at $z \sim 6.5$ : Expected sample contamination . . . . .	71
4.3	LAEs at $z \sim 6.5$ : Low-redshift emission line galaxy contaminants . . . . .	73

4.4	LAEs at $z \sim 6.5$ : Emission line ratios from the WISP catalog . . . . .	74
4.5	LAEs at $z \sim 6.5$ : Direct image postage stamps . . . . .	77
4.6	LAEs at $z \sim 6.5$ : One- and two-dimensional spectra . . . . .	78
4.7	LAEs at $z \sim 6.5$ : Representation of grism volume calculation . . . . .	79
4.8	LAEs at $z \sim 6.5$ : Total effective volume reached in WISP fields . . . . .	80
4.9	LAEs at $z \sim 6.5$ : Cumulative number density . . . . .	82
4.10	LAEs at $z \sim 6.5$ : Spatial emission profiles . . . . .	83
4.11	LAEs at $z \sim 6.5$ : Expected number counts at $z > 7$ . . . . .	84
4.12	LAEs at $z \sim 6.5$ : Cumulative number densities at $z \sim 7$ . . . . .	89
5.1	Local Analogs: Mass distribution of local analogs . . . . .	98
5.2	Local Analogs: BPT emission line diagram . . . . .	100
5.3	Local Analogs: Target postage stamps . . . . .	101
5.4	Local Analogs: Flux conservation through rotation . . . . .	103
5.5	Local Analogs: Example MODS spectrum . . . . .	106
5.6	Local Analogs: Oxygen ratios and $H\beta$ EW . . . . .	107
5.7	Local Analogs: Spatially-extended emission . . . . .	108
6.1	Euclid Forecasts: Wavelength and redshift coverage . . . . .	112
6.2	Euclid Forecasts: Wide Survey sample . . . . .	115
6.3	Euclid Forecasts: Number densities of $H\alpha+[N II]$ and $[O III]\lambda 5007$ -emitters . . . . .	117
6.4	Euclid Forecasts: Number density of all emission line sources . . . . .	118
6.5	Euclid Forecasts: Flux comparison . . . . .	120
6.6	Euclid Forecasts: Empirical PSFs . . . . .	122
6.7	Euclid Forecasts: Modeling emission shape and size . . . . .	124
6.8	Euclid Forecasts: Continuum and emission line sizes . . . . .	125
6.9	Euclid Forecasts: $H\alpha+[N II]$ EW distribution . . . . .	127
6.10	Euclid Forecasts: $[O III]$ line profiles . . . . .	130
6.11	Euclid Forecasts: Redshift accuracy from simulations . . . . .	131
6.12	Euclid Forecasts: Redshift accuracy from observations . . . . .	132
6.13	Euclid Forecasts: Redshift misidentification . . . . .	134
6.14	Euclid Forecasts: Redshift sample purity . . . . .	135

# Chapter 1

## Introduction

The Epoch of Reionization is an exciting frontier in astronomy that is on the verge of experiencing rapid development thanks to upcoming missions such as the James Webb Space Telescope and Euclid. Today, surveys continue to improve our understanding of the reionization history of the universe while planning to make the most of these future observations. Direct studies of Ly $\alpha$ -emitting galaxies (LAEs) at  $z \gtrsim 6.5$  allow us to probe the state of the intergalactic medium (IGM) during reionization. Meanwhile, detailed studies of the small, powerful galaxies in our own backyard help us understand the physical properties of the sources responsible for creating the bulk of the ionizing radiation at high redshift. In this dissertation, we are combining work related to the observed number density of LAEs during reionization with an analysis of local galaxy analogs.

This Introduction describes some of the context and motivation for the work presented in the later chapters. In the following sections, we briefly discuss the early history of the universe, the processes of photoionization and recombination, and the observational probes used to constrain the reionization history.

### 1.1 The Current Cosmological Model

We adopt the  $\Lambda$  cold dark matter ( $\Lambda$ CDM) cosmological framework. Under the  $\Lambda$ CDM model, the universe contains a cosmological constant,  $\Lambda$ , which is associated with the unknown “dark energy” thought to be responsible for the accelerated expansion of the universe. The Hubble parameter,  $H(t)$ , describes the expansion rate and is defined as

$$H(t) = \frac{\dot{a}(t)}{a(t)}, \quad (1.1)$$

where  $a(t)$  is the scale factor of the universe at time  $t$ , and  $a(t_0) = 1$  at the present day ( $t_0$ ). The wavelengths of photons traveling through the universe are redshifted by the expansion. The ratio of the observed to emitted wavelengths, or equivalently the ratio of the scale factors at the time of emission and observation,

$$1 + z \equiv \frac{\lambda_{\text{obs}}}{\lambda_{\text{emit}}} = \frac{a(t_0)}{a(t_{\text{emit}})} \quad (1.2)$$

is a measure of how much the universe has expanded since the time of the emission, where  $z$  is the redshift of the source emitting the light. For reference, under this assumed cosmology, the age of the universe at a redshift of  $z = 6.5$  was  $\sim 0.825$  Gyr. Cosmological redshift is distinct from the Doppler shift imparted by the peculiar (radial) velocity of the emitting source with respect to the observer, which may act to redshift or blueshift the light. The redshifts measured to distant sources include the affect of the cosmic expansion as well as the sources' peculiar velocity. For all but the closest sources, however, cosmological redshift is the dominant term in measurements of  $z$  and the redshift from the peculiar velocity can be neglected.

The Hubble parameter at time  $t$  is given by  $H(z) = H_0 E(z)$ , where  $H_0$  is the Hubble constant or  $H(t = t_0)$ . The term  $E(z)$  is parameterized in terms of the density parameters associated with each of the major components of the universe:

$$E(z) = \sqrt{\Omega_{\Lambda,0} + (1 - \Omega_0)(1 + z)^2 + \Omega_{m,0}(1 + z)^3 + \Omega_{r,0}(1 + z)^4}. \quad (1.3)$$

In this formalism,  $\Omega_{\Lambda}$  is the density parameter for the cosmological constant,  $\Lambda$ ;  $\Omega_m$  is the density parameter for matter, including all baryons and dark matter; and  $\Omega_r$  is for radiation (photons) and relativistic particles. Each density parameter is defined as the ratio at time  $t$  of the density of the given component to a critical density,  $\rho_{\text{crit}}$ :

$$\Omega_* = \frac{\rho_*(t)}{\rho_{\text{crit}}}, \quad \rho_{\text{crit}}(t) = \frac{3H^2(t)}{8\pi G}. \quad (1.4)$$

Here,  $G = 6.67 \times 10^{-8} \text{ cm}^3 \text{ g}^{-1} \text{ s}^{-2}$  is the gravitational constant.  $\Omega_0$ , the total density parameter at  $t_0$ , is the sum of these three components and is very close to 1, indicating that the universe is “flat”.

Throughout this thesis, we assume  $\Omega_M = 0.3$ ,  $\Omega_{\Lambda} = 0.7$ , and  $H_0 = 70 \text{ km s}^{-1} \text{ Mpc}^{-1}$ , with  $h = H_0/(100 \text{ km s}^{-1} \text{ Mpc}^{-1})$  as the reduced Hubble constant.

## 1.2 The early history of the universe

Following the Big Bang, the universe consisted of a hot, dense plasma of protons, electrons, and photons. During this time, the mean free path of photons was very short, meaning a

photon could travel only a short distance before interacting with a proton or an electron (see Section 1.4.2 for a brief discussion on Thomson scattering). As a result of the photon scatterings, the universe was essentially opaque to electromagnetic radiation. After roughly 370,000 years (at  $z_{\text{rec}} \sim 1100$ ), the universe had expanded and cooled to the point where the free electrons and protons could combine to form neutral hydrogen atoms. This transition is called recombination. With the electrons bound in neutral atoms, the photons no longer interacted with matter through scattering and traveled unimpeded through the universe. This event is called photon decoupling or last scattering, and occurred at a temperature of  $T_{\text{rec}} \sim 3000$  K. The decoupled photons are still observable today as background radiation that has been redshifted by the expansion of the universe. The radiation is a blackbody with a temperature  $T_{\text{rec}}/(1 + z_{\text{rec}}) = 2.7$  K, peaking at microwave wavelengths and forming the cosmic microwave background (CMB).

At this time, the only source of light was these photons released during recombination. Known as the Dark Ages, this period in the universe’s history continued for millions of years until the formation of the first generation of stars and galaxies. These “first lights” emitted photons energetic enough to ionize the surrounding hydrogen. The ionized regions around luminous sources expanded until all of the cold, neutral hydrogen in the IGM was eventually returned to its ionized state from before the epoch of recombination. This reionization of the universe is discussed in more detail in the following sections. Today, we see evidence that this process was inhomogeneous in observations of the Ly $\alpha$  emission from galaxies during the epoch of reionization. A schematic illustration of the history of the universe is shown in Figure 1.1.

### 1.2.1 The (Re)ionization of intergalactic hydrogen

Photoionization is the process by which an atom absorbs a photon with enough energy to kick an electron past the ionization threshold so it is no longer bound to the nucleus. In the case of the hydrogen atom, which consists of one electron and one proton, the photoionization process can be written:



where  $\gamma$  is a photon of energy  $h\nu \geq 13.6$  eV. However, photoionization does not occur in isolation. The free electrons and protons produced by ionizing hydrogen will quickly recombine depending on the conditions of the medium. The H II regions that form around massive O/B stars are classic examples of these competing processes. In the idealized spherical and constant density case, the ionized regions extend out to a distance called the

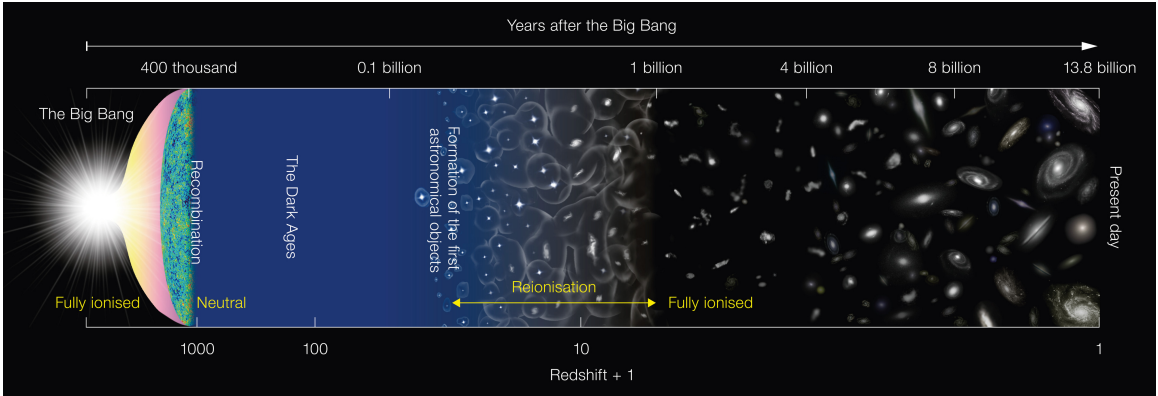


**Figure 1.1** A representation of the history of the universe, leading from the Big Bang at left to the present day. The redshift and time since the Big Bang are shown on the bottom and top  $x$ -axes, respectively. In this thesis we are concerned with the epoch of reionization, when the neutral hydrogen in the IGM became ionized. As illustrated here, we expect that this process began in small bubbles around ionizing sources that expanded outward until the hydrogen in the IGM was fully ionized. This diagram is not to scale. **Credit:** National Astronomical Observatory of Japan (NAOJ)

Strömngren radius, at which the rates of photoionizations and recombinations in the volume are balanced (Strömngren, 1939). As we will see, the situation in the IGM is similar, though complicated by several factors.

Both recombination and photoionization depend on the number density of the relevant particles and an effective cross-section for their interaction. In the case of photoionization, the dependence is on the density of neutral hydrogen atoms,  $n_{\text{H}^0}$ , the production rate of ionizing radiation,  $J_{\nu \geq \nu_0}$ , and the frequency-dependent photoionization cross-section,  $\sigma_{\text{ion}}(\nu)$ . The photoionization rate per unit volume can be written:

$$\Gamma_{\text{ion}} = n_{\text{H}^0} \int_{\nu_0}^{\infty} \frac{4\pi J_{\nu}}{h\nu} \sigma_{\text{ion}}(\nu) d\nu. \quad (1.6)$$

The integration is over all frequencies greater than or equal to the ionization threshold for hydrogen  $\nu_0 = 3.29 \times 10^{15}$  Hz, corresponding to  $\lambda = 912 \text{ \AA}$ . The term  $4\pi J_{\nu}/h\nu$  is the number of photons per unit time, area, and frequency produced by the ionizing source. We discuss the possible sources responsible for creating the ionizing radiation in the following section. While less energy is required to ionize a hydrogen atom in an excited state, we adopt the simplifying assumption that all hydrogen in the IGM is in the ground state<sup>1</sup>. The

<sup>1</sup> This is a reasonable assumption given that electrons in excited states quickly return to the hydrogen ground state through radiative cascades. The lifetime of electrons in excited states is  $\sim 10^{-4} - 10^{-8}$  seconds (the exception is the transition from  $n=2, l=0$  to  $n=1, l=0$ , which results in two-photon emission and has a lifetime of  $\sim 0.12$  seconds; Osterbrock, 1989).

photoionization cross-section can be approximated as (Osterbrock, 1989; Mo et al., 2010):

$$\sigma_{\text{ion}}(\nu) = 6.3 \times 10^{-18} \left( \frac{\nu}{\nu_0} \right)^{-3} \text{ cm}^2. \quad (1.7)$$

and is a measure of the probability that the interaction presented in equation 1.5 will occur.

The volumetric rate of recombinations depends on the number densities of free electrons and hydrogen nuclei,  $n_e$  and  $n_p$ , respectively:

$$\Gamma_{\text{rec}} = n_p n_e \alpha(T). \quad (1.8)$$

The recombination coefficient,  $\alpha(T)$ , is proportional to the cross-section for the interaction and the velocity of the electrons:  $\sigma_{\text{rec}} v$ . As the velocities of the electrons follow a Maxwell-Boltzmann distribution and are therefore dependent on the temperature, the recombination coefficient is a function of the temperature of the electrons. Electrons can recombine to any energy level, though if a captured electron goes directly to the ground state, the emitted photon (with  $E_\gamma \geq 13.6$  eV) will immediately be absorbed by and ionize a nearby neutral hydrogen atom. Recombinations directly to the  $n = 1$  energy level therefore do not contribute to the overall recombination rate. Instead, the relevant recombinations are to the excited energy levels, from which the electrons quickly cascade to lower energy states. Some of the energy levels of the hydrogen atom and the corresponding transitions are shown in Figure 1.2. Once an electron reaches the  $n = 2$  level, there are two ways for it to reach the ground state. The electron can either transition directly to  $n = 1$  emitting a Ly $\alpha$  photon, or it can reach the ground state through a two-photon decay process. Approximately 68% of radiative cascades following a recombination event result in the emission of a Ly $\alpha$  photon (e.g., Dijkstra, 2014). In the second case, the electron transitions to the ground state with no change in angular momentum quantum number,  $l$ , violating the  $\Delta l = \pm 1$  transition rule. Because this transition is forbidden, the electron essentially first jumps to a ‘virtual’ level between  $n = 2$  and  $n = 1$  and then to the ground state, emitting two photons in the process with energies that sum to that of  $\Delta E_{1 \rightarrow 2} = 10.2$  eV (see e.g., Spitzer & Greenstein, 1951; Nussbaumer & Schmutz, 1984). This process results in a continuum of emission, since the two photons can have any combination of energies that sum to  $\Delta E_{1 \rightarrow 2}$ .

There is a specific recombination coefficient associated with each energy level, and the total coefficient  $\alpha_A$  is the sum of all possible recombinations:

$$\alpha_A = \sum_n \sum_{l=0}^{n-1} \alpha_{n,l}(T). \quad (1.9)$$

For conditions with a sufficiently high optical depth to Lyman photons, however, transitions to the  $n = 1$  level can be neglected. Lyman photons are absorbed by neutral hydrogen atoms

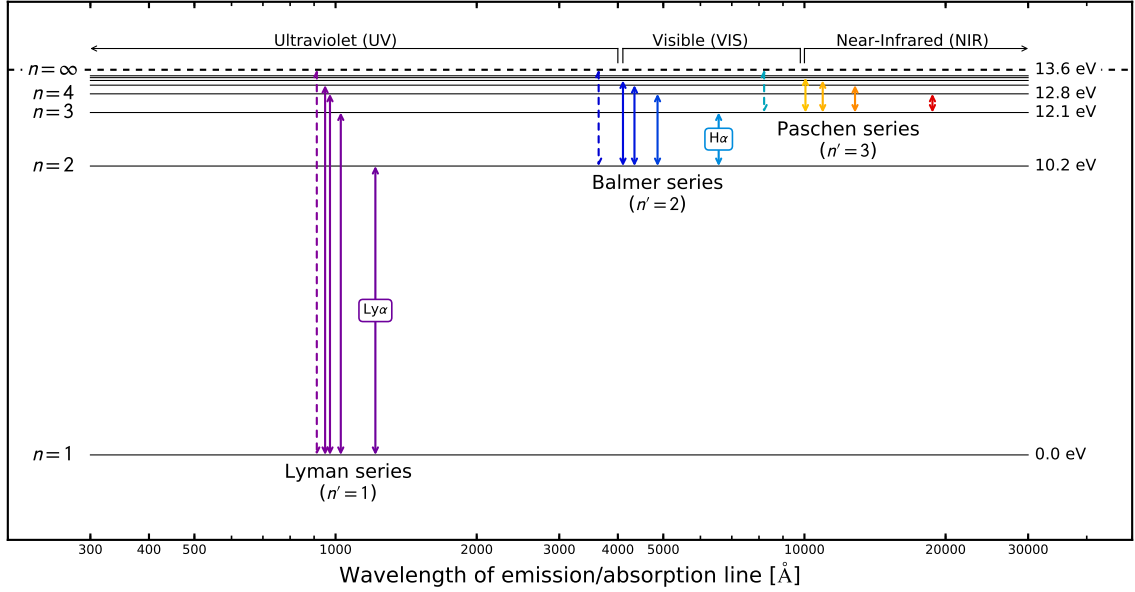


**Figure 1.2** This energy level diagram shows the first several energy levels of the hydrogen atom as well as the ionization energy, 13.6 eV. The transitions between energy levels are shown here color-coded by the wavelength corresponding to the energy of the transition.

and resonantly scattered, or re-emitted at the same wavelength. Yet with each absorption comes the possibility that the electron will de-excite via a different path: the emission of a Balmer series photon, for example, followed by the two-photon continuum emission described above. The result is that the mean number density of  $n > 1$  series photons emitted per unit time, enhanced by the redistributed energy from the Lyman series photons, is higher than predicted in the limit of low optical depth. The optically thin (“Case A” recombination) and optically thick (“Case B”) limits are both extremes that likely bracket real conditions. The recombination coefficient for Case B,  $\alpha_B$ , is calculated by summing over recombinations to all energy levels except those to the  $n = 1$  level. The recombination time is given as

$$t_{\text{rec}} = \frac{1}{n_e \alpha_B(T)}. \quad (1.10)$$

Finally, for a medium of pure hydrogen, there is an equal number of free electrons and free protons:  $n_e \sim n_p$ . The recombination rate  $\Gamma_{\text{rec}}$  in equation 1.8 therefore depends on the square of the density.

The reionization of the IGM began locally in expanding bubbles around the first sources of ionizing photons. Both the expansion of the universe and the ionizing radiation emitted by the central sources contributes to the increasing size of the bubbles. The expansion of the universe decreases the density of free electrons and hydrogen nuclei, thereby increasing

the recombination time and decreasing the recombination rate. Meanwhile, the bubble radii also increase due to the accumulation of ionizing photons within the volume.

These ionized bubbles are similar to the classic Strömgen spheres, with the addition of a few complicating factors beyond the effect of the cosmic expansion. First, the radiation sources, young star-bursting galaxies and active galactic nuclei, are likely not producing ionizing radiation at a constant rate. Second, even for a constant source of ionizing radiation, variations in the density of the IGM will strongly affect the rate of recombinations. Given the density dependence of  $\Gamma_{\text{rec}}$ , if the hydrogen in the IGM is mainly distributed in dense clumps, the overall recombination time will be short. The close proximity of electrons and protons in the clumps will lead to the rapid re-capture of free electrons. Additionally, pockets of neutral hydrogen will be partially shielded from the ionizing photons provided the densities are high enough (e.g. Miralda-Escudé et al., 2000; Rahmati et al., 2013; Chardin et al., 2018). In order to account for this inhomogeneity in the IGM, a clumping factor is defined:

$$C \equiv \langle n_{\text{H}}^2 \rangle / \langle n_{\text{H}} \rangle^2, \quad (1.11)$$

where the angle brackets represent the volume average, and  $C = 1$  corresponds to uniformly distributed hydrogen. Finally, the recombination time in the low-density IGM is longer than the Hubble time, or the age of the universe, during the epoch of reionization. A proper Strömgen sphere does not form because the sources will stop emitting ionizing radiation before the equilibrium radius is reached where  $\Gamma_{\text{ion}} = \Gamma_{\text{rec}}$  (Cen & Haiman, 2000). However, in practice, the ionized region may be limited to  $\sim 20$  comoving Mpc in radius, at which point the ionization of the IGM proceeds through the overlap of multiple bubbles (Furlanetto & Oh, 2005).

### 1.3 Constraining the reionization history

Given the interplay between photoionization and recombination discussed in Section 1.2.1, we can see that the IGM will remain globally ionized as long as there is at least one ionizing photon for every hydrogen atom plus enough ionizing photons to counteract any recombinations that occur. Stiavelli (2009) defines the factor by which the number density of ionizing photons must exceed that of hydrogen:

$$B \equiv \int_{t_1}^{t_2} \dot{n}_{\text{ion}} dt. \quad (1.12)$$

When integrated over the length of cosmic reionization,  $\Delta z = t_2 - t_1$ ,  $B$  is the ratio of the number density of ionizing photons to that of hydrogen atoms. If every hydrogen atom

stayed ionized, i.e., there were no recombinations, then  $B = 1$ . Here we are neglecting the effects of the helium in the IGM, though we note that the presence of helium atoms only increases  $B$  by  $\sim 9\%$  (Stiavelli, 2009). However, the effects of any inhomogeneities in the IGM are much larger and can require  $\geq 6$  times as many ionizing photons as hydrogen atoms to maintain a fully ionized IGM (Stiavelli, 2009). Values of  $B$  calculated from simulations depend on the length of the epoch of reionization and the IGM clumping factor assumed for the given ionization model. Two of the observational probes discussed in the following section — the Gunn-Peterson trough and the Thomson scattering optical depth — help constrain the length of reionization. The IGM clumping factor, however, remains a significant source of uncertainty.

The two most likely sources of the ionizing radiation necessary for reionization are quasars and young, star-forming galaxies. In either case, each population’s contribution to the global ionizing photon budget depends on a few factors: the number of sources producing ionizing radiation, their production rate of ionizing photon, and the fraction of the ionizing radiation that escapes into the IGM. Quasars are the bright central regions of galaxies that contain a supermassive black hole surrounded by an accretion disk. Powerful radiation is emitted from these active galactic nuclei (AGN) as the material in the accretion disks moves towards the central black hole. Close to 100% of the ionizing radiation produced by quasars is expected to escape to the IGM (e.g. Loeb & Barkana, 2001; Cristiani et al., 2016). However, recent studies are finding that AGN were likely not the dominant source of ionizing radiation during reionization (e.g. Laporte et al., 2017). In fact, the AGN contribution to the emissivity of ionizing radiation was as much as an order of magnitude too low to maintain an ionized IGM at  $z \gtrsim 6$  (Onoue et al., 2017; Parsa et al., 2018).

Meanwhile, the necessary ionizing photon budget can be produced by galaxies given some assumptions on the number of sources required and the fraction of ionizing radiation able to escape to the IGM. Emitted by hot, massive stars, ionizing photons are produced in large quantities in star-forming regions of galaxies. The production rate of ionizing photons is therefore related to the total UV luminosity density created through star formation in galaxies (e.g., Robertson et al., 2013, 2015):

$$\dot{n}_{\text{ion}} = f_{\text{esc}} \xi_{\text{ion}} \rho_{\text{UV}}, \quad (1.13)$$

where  $f_{\text{esc}}$  is the fraction of ionizing photons that are able to escape the interstellar medium of galaxies and reach the IGM. The term  $\xi_{\text{ion}}$  is the production rate of ionizing photons that are emitted per unit UV (1200 Å) luminosity density. It is effectively the efficiency with which the stellar populations create ionizing photons. The UV density is found by

integrating the UV luminosity function (LF) down to a limiting luminosity:

$$\rho_{\text{UV}} = \int L \phi(L) dL. \quad (1.14)$$

The LF, which describes the volume number density of galaxies per luminosity bin, is typically parameterized with a Schechter (1976) function:

$$\phi(L) = \frac{\phi_*}{L_*} \left( \frac{L}{L_*} \right)^\alpha e^{-L/L_*}. \quad (1.15)$$

This formalism of the LF has a power law with slope  $\alpha$  at the faint end ( $L < L_*$ ) and drops off exponentially at the bright end ( $L > L_*$ ), reflecting the fact that the brightest galaxies are rare. The parameter  $\phi_*$  is the number density of galaxies at the characteristic luminosity  $L_*$ . The LF is often written in terms of magnitudes rather than luminosity, where the conversion from luminosity to absolute magnitude is  $L/L_* = 10^{-(M-M_*)/2.5}$ .

The value of  $\dot{n}_{\text{ion}}$  depends strongly on the luminosity or magnitude limit to which equation 1.14 is integrated. Extending to fainter luminosities increases the number of galaxies contributing to  $\rho_{\text{UV}}$ . The UV LF is typically integrated down to  $L \sim 0.001L_*$ , which corresponds to an absolute magnitude of  $M_{\text{UV}} \sim -13$  at  $z = 7$  (Robertson et al., 2015). The current general consensus is that in order for galaxies to fully ionize the IGM, the UV LF must extend down to  $M \geq -14$  to  $-13$  with  $f_{\text{esc}} \sim 10 - 20\%$  (e.g. Schmidt et al., 2014; Finkelstein et al., 2015; Rutkowski et al., 2016; Ishigaki et al., 2018). However, as this luminosity is below the detection limit of *HST* observations, the faint end of the UV LF remains somewhat unconstrained. The UV LF may flatten or even turn over at  $M \gtrsim -14$ , reflecting the fact that the ionizing radiation field in the IGM can suppress star formation in low mass galaxies and that there is a minimum halo mass capable of cooling and forming stars (Stiavelli, 2009). Surveys of galaxies magnified by gravitational lensing (Atek et al., 2014, 2015; Ishigaki et al., 2015, 2018) are pushing observations down to  $M_{\text{UV}} = -12.5$  at  $z \sim 6$  and  $-15$  at  $z \sim 8$  with no evidence of a turnover (Livermore et al., 2017), yet uncertainties in the lensing models may complicate the results (Bouwens et al., 2017).

By way of a summary, there are three important topics relevant for characterizing the progression of the reionization of the IGM: the number density and clustering properties of galaxies during the epoch of reionization, the ionizing power of these galaxies (the number of ionizing photons they produce), and the fraction of the ionizing photons that are able to pass through the local interstellar media and escape into the IGM,  $f_{\text{esc}}$ . The research presented in this thesis is related primarily to the first two of these topics by observing galaxies during reionization (Chapter 4) and analyzing the ionizing power of local analogs to reionization-era galaxies (Chapter 5). We also discuss predictions on the number counts of  $z > 6.5$  galaxies that the future Euclid mission will be able to detect.

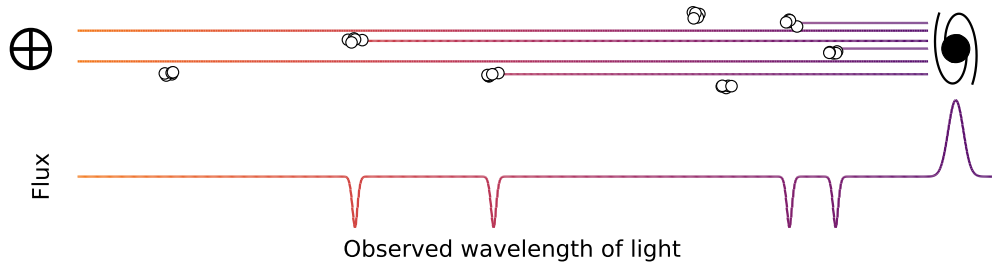


**Figure 1.3** A cartoon representation of the creation of the Ly $\alpha$  forest. Photons emitted from a distant source redshift as they travel through the IGM. If they are at the Ly $\alpha$  resonance ( $\lambda = 1216 \text{ \AA}$ ,  $\nu = 2.47 \times 10^{15} \text{ Hz}$ ) when they encounter neutral hydrogen, they will be absorbed. The wavelengths of the absorption features in the spectrum correspond to the redshift at which the photons encountered the neutral hydrogen.

## 1.4 Observational probes of the epoch of reionization

### 1.4.1 The Ly $\alpha$ Forest and Gunn-Peterson trough

As described in Section 1.1, photons emitted by a distant source are redshifted by an amount  $(1 + z)$  as they travel through the intergalactic medium (IGM). We consider now photons blueward of Ly $\alpha$  at emission wavelengths  $\lambda_{\text{emit}} < \lambda_{\text{Ly}\alpha} = 1216 \text{ \AA}$ . At some point as they propagate, the photons are redshifted through the Ly $\alpha$  resonance of the local hydrogen atoms, meaning the redshifted photons have a wavelength equal to that of Ly $\alpha$  in the rest frame of the hydrogen atoms they encounter. The photons are resonantly scattered by the neutral hydrogen and are therefore removed from the line of sight of an Earth observer. This effect is schematically represented in Figure 1.3. The many absorptions along the line of sight are observed in the spectra of bright, distant quasars. They are collectively referred to as the Ly $\alpha$  forest. However, complete absorption is observed blueward of Ly $\alpha$  in the spectra of quasars at  $z \geq 6$  (Becker et al., 2001; Fan et al., 2006). This absorption or decrement in the UV continuum blueward of Ly $\alpha$  compared to that which is expected is called the Gunn-Peterson trough (Gunn & Peterson, 1965). In what follows, we briefly derive the relationship between the IGM optical depth to Ly $\alpha$  photons and the average fraction of neutral hydrogen in the IGM. Full derivations of this relationship can be found in, for example, Rybicki & Lightman (1986) and Mo et al. (2010).

Ly $\alpha$  photons will travel through the IGM provided the optical depth they experience is  $\tau_{\text{IGM}} < 1$ . Optical depth is a measure of the absorption of light as it passes through a

medium:

$$\tau = \int n \sigma \, dl, \quad (1.16)$$

where the number density of particles in the medium  $n$  and the cross section for absorption  $\sigma$  are integrated along the path length through the medium. The intensity of the light emerging from the medium will be decreased by a factor  $e^{-\tau}$ . Let the photons emitted from a source at redshift  $z_e$  have a frequency  $\nu_e$ . They will be absorbed at a redshift  $z_a$  when they have frequency  $\nu_a = \nu_{\text{Ly}\alpha}$ . The photons that arrive at Earth from the emitting source will have frequency  $\nu_0$ . These frequencies are related by:

$$\nu_e = \frac{1 + z_e}{1 + z_a} \nu_{\text{Ly}\alpha} = (1 + z_e) \nu_0. \quad (1.17)$$

The optical depth due to absorption can be written:

$$\tau = \int n_{\text{HI}}(t_a) \sigma(\nu_e) \, dl = \int_0^{z_e} n_{\text{HI}}[t(z_a)] \sigma((1 + z_e)\nu_0) \frac{dl}{dz} dz, \quad (1.18)$$

where  $n_{\text{HI}}(t(z_a))$  is the number density of neutral hydrogen atoms at the time of absorption. Absorption can occur anywhere along the line of sight between the emitting source and the observer, and so we integrate over redshift, from  $z = 0$  (today) to  $z_e$ . The cross-section for absorption,  $\sigma(\nu)$ , is given by:

$$\sigma(\nu) = \frac{\pi q_e^2}{m_e c} f_{1 \rightarrow 2} \phi(\nu). \quad (1.19)$$

Here,  $q_e$  is the electron charge,  $m_e$  is the mass of the electron,  $f_{1 \rightarrow 2} = 0.416$  is the oscillator strength for the  $n = 1 \rightarrow 2$  transition, and  $\phi(\nu)$  is the line profile shape, which is strongly peaked at  $\nu = \nu_0$  and normalized to 1 over all frequencies. For absorption of Ly $\alpha$  photons, this becomes (Mo et al., 2010):

$$n_{\text{HI}}(t_a) = 2.4 \times 10^{-11} h E(z_a) \tau \text{ [cm}^{-3}\text{]}, \quad (1.20)$$

where the Hubble parameter at redshift  $z_a$  is  $H(z_a) = H_0 E(z_a)$ ,  $H_0$  is the value of the Hubble constant today,  $h = H_0/100 \text{ km s}^{-1} \text{ Mpc}^{-1}$  is the dimensionless Hubble constant, and  $E(z)$  is defined in equation 1.3.

The Gunn-Peterson trough is due to neutral hydrogen absorption along the specific line of sight to a high-redshift source. Variations in the quasar redshifts at which the trough appears may be caused by the patchiness of the reionization process. Given a high enough density of bright, high-redshift quasars, it would in theory be possible to map the bubble morphology of the IGM towards the end of reionization. The Gunn-Peterson optical depth increases rapidly at  $z > 6$  (Fan et al., 2006), yet this increase does not signify an analogously

rapid increase in the density of neutral hydrogen. The large cross-section of the resonance transition means that Ly $\alpha$  photons can be almost completely absorbed in the presence of a small amount of neutral hydrogen. Therefore, observations of the Gunn-Peterson trough constrain the end of reionization, but must be combined with other observational probes to understand the progression of the transition.

### 1.4.2 Thomson scattering optical depth

Thomson scattering refers to the scattering of light by a charged particle such as an electron. The incident electromagnetic wave accelerates the electron through the Lorentz force, passing energy to the electron that is then re-emitted at the same frequency. Following recombination and the formation of neutral hydrogen, the mean free path of photons increased dramatically, becoming effectively infinite. The mean free path,  $l_{\text{mfp}}$ , is the average distance a photon travels before encountering and scattering off of a free electron. It can be written  $l_{\text{mfp}} = \frac{1}{n_e \sigma_{\text{T}}}$ , where  $n_e$  is the volume number density of free electrons and  $\sigma_{\text{T}}$  is the effective cross section area for interaction and Thomson scattering. Optical depth is inversely proportional to the mean free path, and is found by integrating along the path length of the photons. Given the relationship between distance, time, and redshift, we can express the path length in terms of the length of time the photons travel:

$$\tau(z) = \int_{t(z)}^{t_0} n_e \sigma_{\text{T}} c dt'. \quad (1.21)$$

Here, the integration is performed from the time at redshift  $z$ ,  $t(z)$ , to the present,  $t_0$ . The Thomson scattering cross-section is proportional to the square of the classical electron radius,  $r_0$  (Rybicki & Lightman, 1986):

$$\begin{aligned} \sigma_{\text{T}} &= \frac{8\pi}{3} r_0^2, \\ r_0 &= \frac{q_e^2}{m_e c^2}. \end{aligned} \quad (1.22)$$

where  $q_e$  is the electron charge, and  $m_e c^2$  is the electron rest frame energy. This cross section,  $\sigma_{\text{T}} = 0.665 \times 10^{-24} \text{ cm}^2$ , is independent of the frequency of the incident light.

During the epoch of reionization, there were once again free electrons in the IGM, reducing the mean free path of the CMB photons released during recombination. Thomson scattering between the free electrons and CMB photons adds to the polarization of the CMB at large angular scales. The amplitude of this effect depends on the Thomson optical depth, and the angular scale of this additional polarization corresponds to the redshift at which the ionized fraction of the IGM started to increase. In an analysis of the 2015 Planck data release (Planck Collaboration et al., 2016a), Planck Collaboration et al. (2016b) measure an

optical depth to Thomson scattering of  $\tau = 0.058 \pm 0.012$ . They find that the IGM was 50% ionized at  $z \sim 7.2 - 8.8$ , where the exact value depends on the reionization model, assumed priors, and any constraints that are applied to the analysis. However, almost all models show that the ionized fraction was  $\sim 0.1$  at  $z = 10$ . Taken together with the constraint from the observations of the Gunn-Peterson trough, the current picture is of a relatively rapid reionization process occurring between  $z = 10$  and  $z = 6$ , a time period of less than half a billion years.

### 1.4.3 Lyman- $\alpha$ emitting galaxies

The result of a resonant transition, Ly $\alpha$  photons are highly sensitive to even small amounts of neutral hydrogen and are therefore a powerful tool for probing the ionization state of the IGM. Ly $\alpha$  photons are absorbed as they travel through a partially neutral IGM, while the optical depth to lower-energy UV photons (e.g.,  $\lambda \gtrsim 1500 \text{ \AA}$ ) is much lower. Therefore, a drop in the observed number density of Ly $\alpha$  emitters (LAEs) as well as in the observed fraction of LAEs among star-forming galaxies is expected at  $z \gtrsim 6$  due to the increase in neutral hydrogen in the IGM (e.g. Stark et al., 2010; Ota et al., 2017).

However, the evolution in the number density of LAEs and the resulting measurements of the Ly $\alpha$  LF with redshift remain a subject of debate. Specifically, observational studies comparing the  $z \simeq 5.7$ ,  $z \simeq 6.5$ , and  $z \geq 7$  Ly $\alpha$  LFs have reached inconsistent conclusions. Some find a deficit with increasing redshift in the number density of Ly $\alpha$  emitters (LAEs) either at the bright end of the LF (e.g., Kashikawa et al., 2011), the faint end of the LF (e.g., Matthee et al., 2014, 2015), or at all luminosities (Konno et al., 2014). Additionally, recent and ongoing surveys have identified a potential excess in the number density of bright LAEs at  $z \gtrsim 6.5$  (Santos et al., 2016; Bagley et al., 2017; Konno et al., 2018).

Different survey completeness limits, contamination from low-redshift interlopers, and cosmic variance may all contribute to the discrepant results. In what follows, we briefly describe the common techniques used to detect high-redshift galaxies, the contaminants that can enter high-redshift samples, and the effect of cosmic variance on the observed number counts of galaxies.

#### The Lyman Break Technique

The most common method for identifying high-redshift galaxies is the Lyman break technique. Photons with wavelengths blueward of the Lyman limit ( $912 \text{ \AA}$ ) are energetic enough to ionize neutral hydrogen, producing a break in the spectrum of the host galaxy. At  $z \gtrsim 5.5$ , the IGM becomes optically thick to photons blueward of Ly $\alpha$ , shifting the spectral break to

$\sim 1216 \text{ \AA}$ . When the galaxy is observed with two imaging filters, one redward of the break and the other blueward, the galaxy will be much brighter in the redder filter than in the bluer filter. If the absorption is strong enough, the galaxy will not be detected in the filter blueward of the break. The galaxy is said to have “dropped out” of the blue filter, the wavelength of which provides a rough estimate of the redshift of the galaxy. For example, a synthetic spectrum of a  $z = 6.5$  galaxy is shown in Figure 1.4 with the transmission curves for four broadband filters. The flux from the galaxy in the blue filter is much lower than in the orange filter, indicating that a spectral break exists somewhere between the two filters.

Many galaxy surveys have calculated the rest frame UV LF at high redshift (e.g., Stark et al., 2009; Oesch et al., 2010, 2014; Bouwens et al., 2011, 2015; Schmidt et al., 2014; McLure et al., 2010, 2013) and the majority of  $z > 7$  candidates targeted for spectroscopic confirmation (e.g., Vanzella et al., 2011; Pentericci et al., 2011, 2014; Ono et al., 2012; Schenker et al., 2012) are identified from broadband colors indicative of a Lyman break. Since imaging can efficiently cover very large areas, this detection method makes it possible to quickly build large samples of high-redshift candidate galaxies. However, this advantage comes at the expense of sample purity. Both the  $4000 \text{ \AA}$  spectral break in intermediate-redshift galaxies ( $z \sim 1.5$ ) with old stellar populations and cool stars such as L and T dwarfs can mimic the colors of a Lyman break at high redshift. Contamination rates in LBG samples can be as high as  $\sim 50\%$  for the faint galaxies that are crucial for measuring the faint-end of the LF (Dickinson et al., 2004). LBG sample contamination can be mitigated by increasing the number of filters used to constrain the spectral shape at other wavelengths (e.g. Stanway et al., 2008; Finkelstein et al., 2015). An additional complication of the Lyman break technique is that the width of the imaging filters prevents accurate redshift measurements. Follow-up spectroscopy is needed in order to confirm high-redshift candidate, determine more accurate redshifts, and statistically quantify the redshift contamination of the sample. This necessity for spectroscopic follow-up observations reduces the efficiency of the Lyman break technique. Additionally, the faint galaxies that are important for reionizing the IGM may fall below the flux limit of Lyman break surveys (see for example the samples of Dressler et al., 2011, 2015; Henry et al., 2012).

### **Narrowband Detection**

Whereas broadband filters provide measurements of the continuum emission of a galaxy, very narrow filters can be used to detect and measure emission lines (e.g., Cowie & Hu, 1998). A narrowband detection involves imaging in a narrow filter tuned to measure an emission line at a very specific wavelength and therefore redshift. A broadband measurement

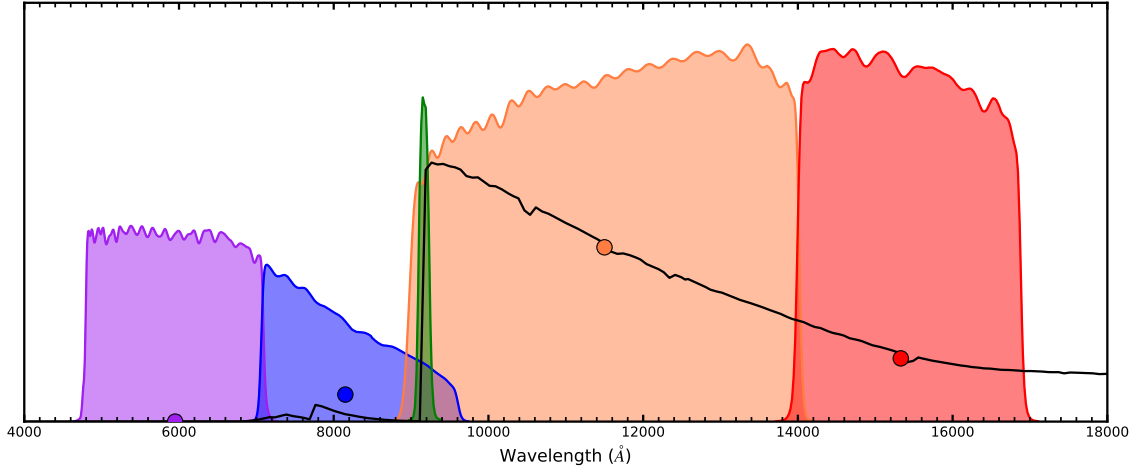


**Figure 1.4** An example of the Lyman break and narrowband detection methods. A template spectrum of a galaxy at  $z = 6.5$  is shown in black. The filter profiles of four broadband filters are shown with the flux density of the spectrum in each filter indicated by circles. *Lyman Break Technique:* By comparing the flux density in the blue filter with that in the orange filter, we can detect the presence of a spectral break. Additional filters on either side of the break help better constrain the shape of the spectrum and reject contaminants. *Narrowband Technique:* We can detect LAEs using narrow filters tuned to detect  $\text{Ly}\alpha$  at specific redshifts. The green narrowband filter will detect  $\text{Ly}\alpha$  at  $z = 6.5$ . (Note that  $\text{Ly}\alpha$  emission is not displayed in this figure.) The flux density in the orange broadband filter is used as a measure of the continuum emission.

at a nearby wavelength is used to determine the level of the continuum. The equivalent width of the line is determined by comparing the strength of the emission in the broad and narrowband filters. Narrow band samples are constructed through a selection on both the flux and equivalent width of emission lines. In Figure 1.4, the green filter is set to detect  $\text{Ly}\alpha$  emission at  $z = 6.5$ .

Narrow band imaging is a valuable technique for emission line galaxy surveys, especially for high-redshift LAE searches (Rhoads et al., 2000; Hu et al., 2010; Ota et al., 2010; Ouchi et al., 2010; Kashikawa et al., 2011; Hibon et al., 2012; Konno et al., 2014; Zheng et al., 2017). Particular progress has been made recently with large area surveys performed with Suprime-Cam (Miyazaki et al., 2002) on the Subaru telescope (e.g., Matthee et al., 2015; Hu et al., 2016; Konno et al., 2018). As an imaging technique, narrowband detection is as efficient as Lyman break searches. The contamination rates from lower-redshift sources are much lower in narrowband-selected samples (e.g., Matthee et al., 2014) and are typically limited to emission line galaxies in narrow redshift ranges, where  $\text{H}\alpha$  or  $[\text{O II}]$  may be detected instead of  $\text{Ly}\alpha$ . (There is also the possibility that transient objects such as variable active galactic

nuclei or supernovae can contaminate the sample, particularly if the narrow and broadband observations are not taken at the same time.) The redshifts of emission lines detected in a narrowband are much more precise than those measured using the Lyman break technique, with  $\Delta z \sim 0.1$ . However, follow-up spectroscopy is still required for redshift confirmation and line flux calibration (Rhoads et al., 2003; Matthee et al., 2014).

### Grism Spectroscopy

Slitless grism instruments obtain spectroscopic measurements of all sources in a field-of-view simultaneously. This technique therefore combines the efficiency of imaging with the wealth of information provided by spectroscopy. Such measurements are unbiased in that they do not require candidate pre-selection. Additionally, depending on the grism resolution, the spectroscopic redshift measurements have accuracies of  $\Delta z \sim 0.02 - 0.15$  (Malhotra et al., 2005, and see Chapter 6), on par with or better than the redshift accuracies achieved with narrowband measurements. Grism observations have been used to detect both the Lyman break as well as the Ly $\alpha$  emission line (e.g. Malhotra et al., 2005; Rhoads et al., 2009, 2013; Oesch et al., 2015; Bagley et al., 2017; Schmidt et al., 2016; Larson et al., 2018). Finally, the wavelength coverage and resolution afforded by spectroscopy helps rule out lower-redshift contamination by the detection (or lack thereof) of additional emission lines (see Section 4.4). However, slitless spectroscopy must also contend with the challenges of crowding and spectral confusion, as the dispersed light from nearby objects can overlap significantly in a grism exposure.

Much of the research presented in this thesis makes use of the *HST*/WFC3 grisms to detect emission line galaxies at both  $z > 6$  (Chapter 4) and  $z \sim 1 - 2$  (Chapter 6). We present the details of these observations in Chapter 2 and specifically describe the grism as a spectroscopic instrument in more detail in Section 2.1.1.

### Cosmic variance

While observational issues do exist, the observed disagreement in the number density of high-redshift LAEs could also be caused by real astrophysical phenomena. Reionization is not expected to proceed at the same rate on all scales (e.g., Mesinger & Furlanetto, 2008; Zheng et al., 2011; Treu et al., 2012), but rather to be a patchy and inhomogeneous process depending on the luminosity of ionizing sources and the galaxy clustering properties. The effect of both luminosity and clustering is to produce large ionized bubbles (on scales of a few megaparsecs, depending on the exact luminosity) that allow Ly $\alpha$  photons to redshift out of resonance before encountering the IGM. Therefore, we may expect the most luminous LAEs

to be visible out to earlier times. Conversely, it will take the fainter galaxies longer to ionize bubbles large enough to allow Ly $\alpha$  photons to escape (e.g., Matthee et al., 2015; Ono et al., 2012; Stark et al., 2016). Additionally, around luminous sources and/or highly clustered regions, we may expect an enhancement in the number density of galaxies showing Ly $\alpha$  in emission (Castellano et al., 2016; Mason et al., 2018). We further discuss reionization-induced clustering and its observational signatures in the next section.

### The “bright bump”

Given the multitude of LAE searches at  $z \gtrsim 6.5$ , we are beginning to close in on a consistent picture of reionization. New wide-area narrowband surveys are compensating for their limited redshift range by covering tens of square degrees (Matthee et al., 2015; Hu et al., 2017; Konno et al., 2018), and the WFC3 Infrared Parallel Spectroscopic (WISP, PI Malkan; Atek et al., 2010) Survey provides imaging and spectroscopy from hundreds of independent fields. These surveys are significantly less susceptible to cosmic variance and reionization-induced clustering than their predecessors and are therefore detecting less biased samples of the rare, bright LAEs at  $z \sim 6 - 7$ .

In Chapter 4, we present the results of a systematic search for  $z > 6$  LAEs in the uncorrelated pointings of the WISP Survey and using the full wavelength coverage of WFC3 spectroscopy:  $0.8 \leq \lambda \leq 1.7 \mu\text{m}$ . Through extensive modeling of synthetic sources, we show that our selection method combining spectral detection of a single emission line with the requirement for colors consistent with a Lyman break rules out almost all contamination from low-redshift interlopers. We find two LAEs at  $z = 6.4$  with line luminosities of  $L_{\text{Ly}\alpha} \sim 4.7 \times 10^{43} \text{ erg s}^{-1}$ , making them among the brightest detected at  $z \sim 6.5$ . The resulting number density of LAEs computed in the WISP volume is larger than expected at the bright end for a Schechter-like function, constituting an excess or “bright bump” in the Ly $\alpha$  LF. One interpretation for this bright bump is that we are observing LAEs embedded in locally ionized bubbles that are large enough to allow Ly $\alpha$  photons to redshift out of resonance before encountering the neutral IGM. In order to create the ionizing bubbles themselves, these bright LAEs must be producing a high density of hydrogen-ionizing photons per unit UV luminosity ( $\xi_{\text{ion}}$ ; see Section 1.3). Indeed, the detection of strong UV emission lines in the spectra of  $z > 7$  LAEs indicates that hard ionizing continua may be common in these high-redshift galaxies, contributing to the ionization of the IGM that makes it possible to observe Ly $\alpha$  radiation from galaxies at  $z > 7$  (Stark et al., 2015; Mainali et al., 2018). However, there is mounting evidence that the brightest LAEs at  $z \gtrsim 6.5$  alone were not capable of ionizing bubbles large enough to allow transmission of Ly $\alpha$  photons (see

Section 4.6.4 as well as Vanzella et al., 2011; Castellano et al., 2016).

While similar high number densities of bright LAEs have been noted by Santos et al. (2016) and Konno et al. (2018), the extent of the excess remains unconstrained. The situation at  $z > 8$  is even more uncertain, with no clear evidence for a non-Schechter LF (e.g. Livermore et al., 2018). Looking to the future, upcoming slitless cosmological surveys such as Euclid will shed more light on the bright end of the Ly $\alpha$  LF by detecting hundreds more high-redshift bright LAEs.

#### 1.4.4 LAE Clustering

The probability of finding a galaxy a distance  $r$  from another galaxy within a volume element  $dV$  is (Peebles, 1993):

$$dP = n[1 + \xi(r)]dV, \quad (1.23)$$

where  $\xi(r)$  is the correlation function and describes the clustering strength of the population. It measures the probability of observing a number of galaxies per unit volume that is in excess of that expected for a population drawn randomly from a Poisson distribution. The correlation function can be calculated by comparing the numbers of observed galaxy pairs as a function of separation distance  $r$  with those of a randomly generated catalog of sources with the same volume coverage. In this way, the clustering strength of a population of galaxies, such as those during the epoch of reionization, can be measured (e.g., Robertson, 2010; Barone-Nugent et al., 2014).

Reionization is expected to be an inhomogeneous process, starting locally around ionizing sources and expanding outwards (e.g., Mesinger & Furlanetto, 2008; Zheng et al., 2011; Treu et al., 2012). The Ly $\alpha$  emission from galaxies in locally ionized bubbles will escape provided that the photons can redshift out of resonance before encountering the neutral hydrogen in the IGM (Miralda-Escudé, 1998). On the other hand, Ly $\alpha$  photons from galaxies in predominantly neutral regions of the IGM will be absorbed. The observed distribution of LAEs will therefore contain an imprint of the patchy reionization process (Furlanetto et al., 2006; McQuinn et al., 2007; Mesinger & Furlanetto, 2008). The distribution of the galaxies detected based on their UV continuum emission ( $\lambda \gtrsim 1500 \text{ \AA}$ ) and spectral break, i.e., using the Lyman break technique described in Section 1.4.3, will not be affected by the neutral IGM. Therefore, the observed LAEs will be more clustered than Lyman break galaxies (LBGs), and so the ratio of their correlation functions will provide a constraint on the neutral hydrogen fraction in the IGM (McQuinn et al., 2007). Finally, as the neutral hydrogen fraction decreases, the observed LAE clustering signal will approach that of the

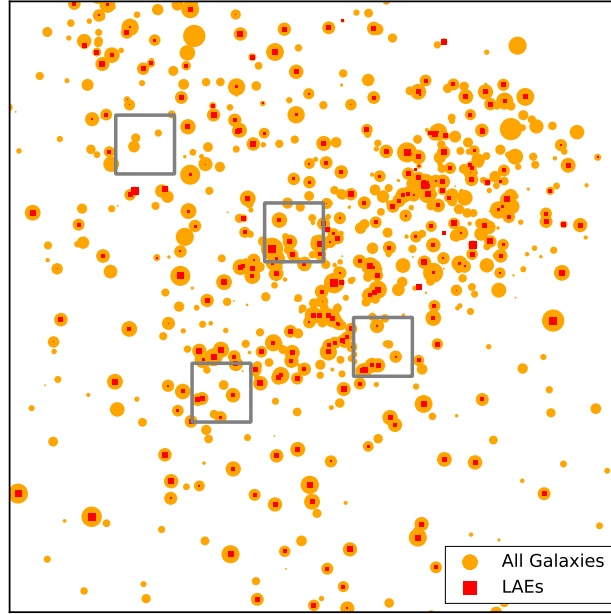


**Figure 1.5** Mock distributions of all galaxies (orange circles) and those observed with  $\text{Ly}\alpha$  in emission (red squares) are shown for a large projected area. The LAEs are more strongly clustered than LBGs, due to the extra clustering signal induced by a patch reionization process. Single-pointing observations like the grey squares will measure inconsistent fractions of galaxies emitting  $\text{Ly}\alpha$ . Surveys covering much larger areas, such as the Euclid Deep Survey, are necessary in order to get a better sense of the full picture. This figure has been adapted from Mason et al. (in preparation) and is intended as an illustrative example only.

underlying galaxy population. The redshift evolution of LAE clustering and, more specifically, of  $\xi_{\text{LAE}}/\xi_{\text{LBG}}$ , will probe the evolution in the neutral hydrogen fraction (Greig & Mesinger, 2017).

Figure 1.5 is an illustrative example of the observed density of LAEs in a partially neutral IGM compared with that of all galaxies. The orange circles represent galaxies detected through the Lyman break technique, not all of which are detected in  $\text{Ly}\alpha$  (red squares). The LAEs are more strongly clustered than the LBGs. The galaxy distribution in Figure 1.5 also demonstrates how single pointings and small fields-of-view such as the grey squares will be more susceptible to the effects of cosmic variance than surveys covering tens of square degrees.

The large areas covered by Euclid and WFIRST, planned galaxy redshift surveys designed to probe dark energy, make them ideal for observations of LAEs during the epoch of reionization. The European Space Agency’s Euclid Mission will include a Deep Survey covering 40 square degrees down to a depth of  $\sim 6 \times 10^{-17} \text{ erg s}^{-1} \text{ cm}^{-2}$ . In addition to

the Red grism ( $1.25 \leq \lambda \leq 1.8 \mu\text{m}$ ) used for the full Wide Survey, the Euclid Deep Survey will use a Blue grism to obtain slitless spectroscopic measurements in the wavelength range  $0.92 \leq \lambda \leq 1.35 \mu\text{m}$ . The Blue grism will therefore be able to detect LAEs at  $z \geq 6.57$  with luminosities down to  $L_{\text{Ly}\alpha} \sim 2.9 \times 10^{43} \text{ erg s}^{-1}$ . The wide area and full wavelength coverage results in a survey volume that is 10 – 50 times larger than the current largest LAE surveys (Matthee et al., 2015; Konno et al., 2018). Euclid will significantly reduce the current uncertainties at the bright end of the Ly $\alpha$  LF discussed in the previous section and in Chapter 4. It will be able to definitively measure the clustering strength of LAEs at  $z \gtrsim 6.5$ . With the addition of the multi-wavelength, ground-based support imaging, Euclid will also measure the clustering of LBGs in the same volume, making a statistically significant measurement of  $\xi_{\text{LAE}}/\xi_{\text{LBG}}$  possible. At the time of this writing, however, Euclid is scheduled to launch in late 2021 to early 2022.

In the meantime, we focus on providing observational constraints on the expected outcome of the Euclid Wide Survey. For survey design and optimization, it is critical to have a reliable and sufficiently precise knowledge of the expected numbers of emission line galaxies in the survey volumes at these redshifts. Additionally, much of the work done in preparation for Euclid and WFIRST involves building mock catalogs to predict the number densities of galaxies they will detect. It is crucial that these simulations correctly assign line fluxes to galaxies as a function of their size, luminosity, and mass in order to properly account for observational selection effects. We therefore turn to the intermediate redshifts where H $\alpha$  and [O III] selected galaxies will be used to trace the large scale structure of the universe. Given the similarities between the *HST*/WFC3 grisms and the Euclid/NISP Red grism, we can observationally replicate both the observational and selection effects that can be expected for the dark energy mission. We use two *HST* grism surveys, WISP and 3D-HST+AGHAST, to measure the observed number counts and sizes of emission line galaxies (ELGs) at  $z \sim 1 - 2$ . In Chapter 6, we present measurements of the cumulative number densities of H $\alpha$  and [O III]-selected galaxies, characterize the distributions of emission line ratios and equivalent widths, and compare the galaxy sizes as measured in both the continuum and the emission lines.

#### 1.4.5 Local analogs

As it is currently prohibitively difficult to comprehensively study galaxies at  $z \gtrsim 6$ , we look to the local universe to study the physical processes in galaxies that are comparable to those responsible for ionizing the IGM. Additionally, while JWST will revolutionize studies of the bright, high-mass galaxies at  $z \gtrsim 6$ , the fainter, low-mass population that contributes the

most to the ionizing photon budget will still only be accessible via imaging. Since galaxies with masses  $M \gtrsim 10^{8-9}M_{\odot}$  are not capable of maintaining reionization alone (Robertson et al., 2015; Rutkowski et al., 2016), proper low-redshift analogs should be faint and low mass ( $M < 10^8M_{\odot}$ ). Analogous to those that formed at early times in the universe, they should be low metallicity and therefore have hard ionizing spectra (Schaerer, 2003). The Green Pea galaxies (Cardamone et al., 2009; Henry et al., 2015) are well-studied local analog candidates, but are at least an order of magnitude more massive than expected drivers of the Epoch of Reionization. We therefore turn to lower-mass local galaxies, and present sample selection, data reduction, and preliminary results in Chapter 5.

## 1.5 This Thesis

The material in this thesis is organized as follows:

- Chapter 2 describes the observational data from the WISP Survey, which is used for many of the projects presented in this thesis.
- The creation of the simulated data, necessary for evaluation of survey completeness, sample selection, and sample contamination, is described in Chapter 3.
- Chapter 4 presents the detection and analysis of LAEs towards the end of the epoch of reionization.
- Chapter 5 presents the reduction and early results of an analysis of a sample of local analogs to high-redshift galaxies.
- Chapter 6 describes observational forecasts for ESA’s upcoming Euclid mission.
- The work is briefly summarized in Chapter 7.

All magnitudes in this thesis are expressed in the AB system, which for a flux  $f_{\nu}$  in units of  $\text{erg s}^{-1} \text{cm}^{-2} \text{Hz}^{-1}$  is given by  $m_{\text{AB}} = -2.5\log_{10}f_{\nu} - 48.6$  (Oke & Gunn, 1983). The zero point 48.6 is calculated using a reference spectrum that is flat in  $f_{\nu}$ . All filters therefore have the same zero point, and a source with a flat spectrum will have zero color,  $m_2 - m_1 = 0$ , in the AB system.

## Chapter 2

# Observations: The WISP Survey

### 2.1 WISP Survey Overview

The WFC3 Infrared Spectroscopic Parallel (WISP) Survey (PI: M. Malkan, Atek et al., 2010) is a near-infrared slitless grism spectroscopic program which efficiently accrues WFC3<sup>1</sup> data while other *HST* instruments are in use. Observations with either the Cosmic Origins Spectrograph (COS, Froning & Green, 2009) or the Space Telescope Imager and Spectrograph (STIS, Kimble et al., 1998) typically require long integrations of a single pointing. During such integrations, WFC3 (Kimble et al., 2008) can be used to observe fields offset by  $5'.5$  and  $4'.75$  from the COS and STIS primary targets, respectively. WFC3 has a field of view of  $123'' \times 134''$  and  $162'' \times 162''$  for the IR ( $0'.13/\text{pixel}$ ) and UVIS ( $0'.04/\text{pixel}$ ) cameras, respectively. To date the WISP survey has observed 483 fields collectively covering more than  $2000 \text{ arcmin}^2$ .

We use both of WFC3's IR grisms: G102 ( $0.8 - 1.1 \mu\text{m}$ ,  $R \sim 210$ ,  $\Delta\lambda = 24.5 \text{ \AA}/\text{pixel}$ ) and G141 ( $1.07 - 1.7 \mu\text{m}$ ,  $R \sim 130$ ,  $\Delta\lambda = 46.5 \text{ \AA}/\text{pixel}$ ). To aid in extracting the spectra from the slitless grism images and to mark the zero point for wavelength calibration, the WISP fields were also observed in direct imaging mode with filters chosen to match the grism spectral coverage: F110W for G102 and either F140W or F160W for G141. The WISP observing strategy depends on the length of each parallel opportunity and can therefore vary somewhat field-to-field. In general, grism integration times are  $\sim 6\times$  those for the direct images reflecting the sensitivities in both instrument modes. Of the 483 WISP fields, 155 are also observed with the WFC3 UVIS camera and a subset of the filters F475X, F600LP, F606W, and F814W. The transmission curves of the filters and grisms used in WISP observations are shown in Figure 2.1.

---

<sup>1</sup> <http://www.stsci.edu/hst/wfc3/>

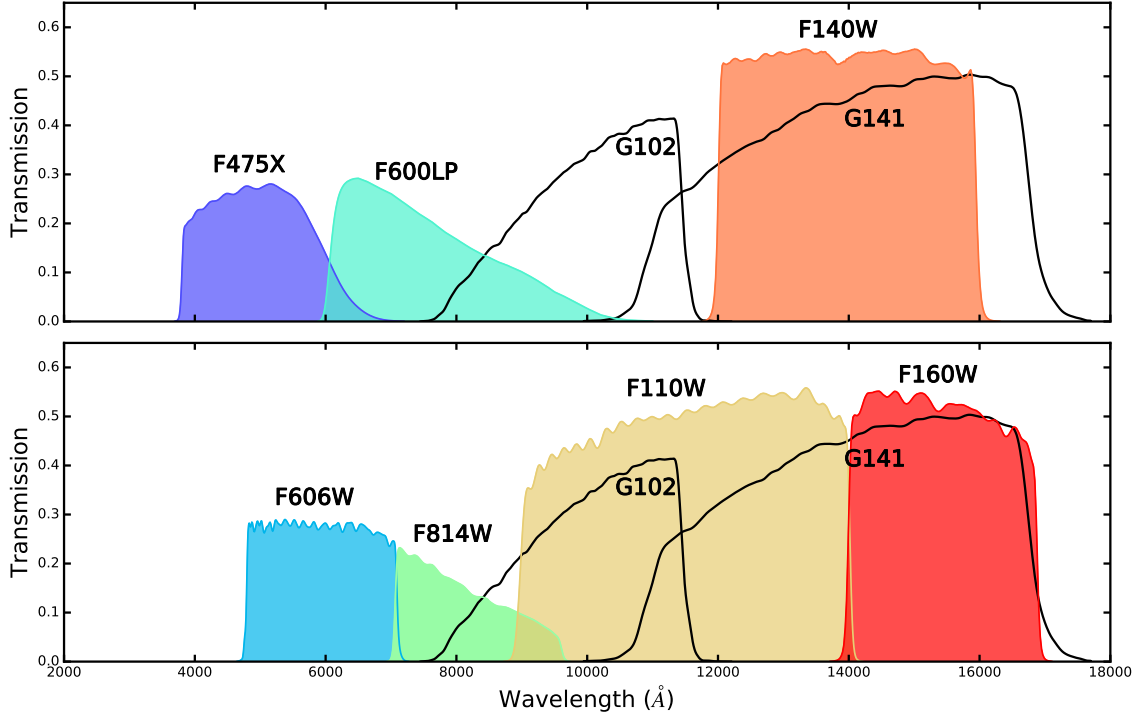


**Figure 2.1** The transmission curves of the WFC3 filters and grisms used in WISP observations. The filters are split between the top and bottom panels for clarity

The WISP Survey includes shallow fields observed for one to three continuous orbits and deeper fields observed for four or more continuous orbits. Typically, the G141 grism and one imaging filter are used to observe fields during the shorter opportunities. Both grisms, two near-infrared imaging filters, and one or more UVIS filters are usually used for the deeper fields observed during longer opportunities. For these deep fields, the integration times in the two grisms are  $\sim 5:2$  (G102:G141) in order to achieve approximately uniform sensitivity for an emission line of a given flux across the full wavelength range. The positions of the WISP fields that are included in the emission line catalog (see Section 2.4) are shown in Figure 2.2.

A total of 434 fields have been reduced with version 6.2 of the WISP reduction pipeline, which is briefly described in Section 2.2.

### 2.1.1 Slitless Grism Data

Spectroscopic observations measure the intensity of a source as a function of wavelength by dispersing the light from the source into its wavelength components. Spectroscopy is an

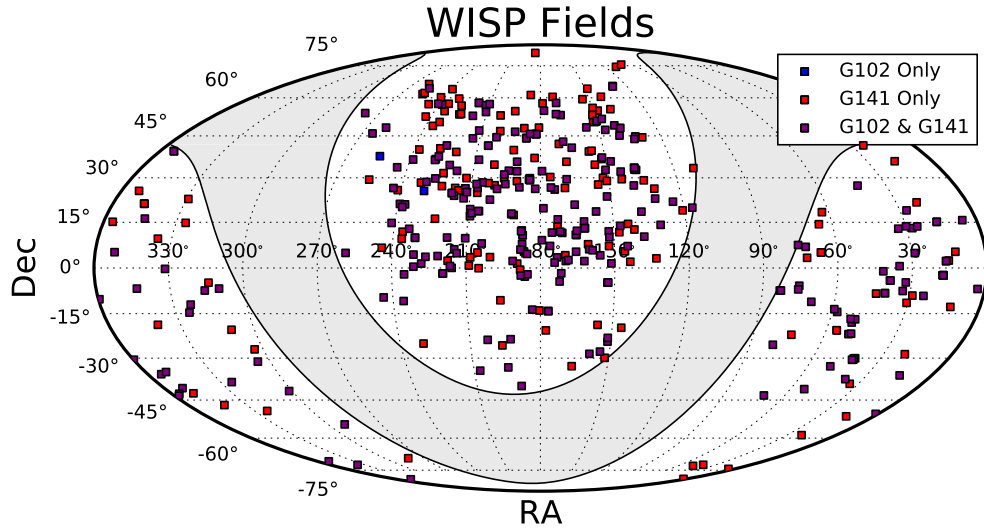


**Figure 2.2** The locations of the WISP fields included in the emission catalog that collectively cover  $\sim 1520$  arcmin<sup>2</sup>. The parallel nature of WISP observations results in hundreds of independent pointings, far less susceptible to the effects of cosmic variance than surveys covering larger areas in only a handful of pointings. In scheduling observations, we reject parallel opportunities that are within 20 degrees of the galactic plane (grey region) to avoid contamination and crowding from galactic sources.

incredibly valuable tool. With it, astronomers can study the composition of stars and galaxies in the universe, determine the distances to sources far outside our own galaxy, measure their motion towards or away from us, and much more. However, spectroscopy can be very expensive. Typically, spectroscopic techniques involve observing a source through a thin slit or fiber, blocking out all other light from the sky and nearby sources. Many multi-object spectrographs are limited in the number of objects that can be observed simultaneously, either due to constraints on the position of slits to avoid overlapping spectra or due to how close together fibers can be placed. Slit and fiber spectroscopy also require a knowledge of source positions and therefore preliminary imaging observations for target selection.

Slitless spectroscopy offers a solution. Rather than dispersing only the light from a source in a slit or small aperture, the entire field-of-view is dispersed. A spectrum is obtained simultaneously for every source in the field. There is no pre-selection required, and so there is even the possibility to detect high equivalent width emission lines from sources that are too faint in the continuum image to be detected. Unfortunately, this efficient spectroscopy comes with its own cost. The dispersed emission of nearby sources can overlap, contaminating their spectra. This spectral confusion is especially problematic

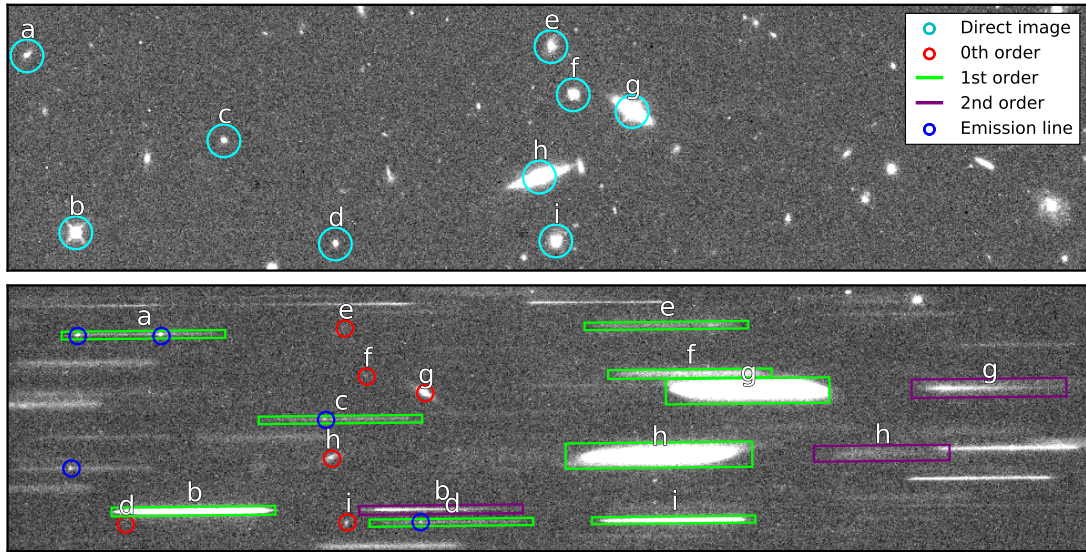


**Figure 2.3** An example of a direct image (top panel) and the corresponding slitless grism image for the same field (bottom panel). Sources are identified in the direct images (light blue circles), and the positions of the zeroth (red circles), first (green rectangles), and second orders (purple rectangles) are marked for each source. The size and shape of the spectral features in the grism image match those of the sources in the direct image (see sources *g* and *h*, for example). A few bright emission lines are also visible in the dispersed spectra and are identified by blue circles.

in crowded fields or in fields with bright sources. An example of slitless data from WISP is shown in Figure 2.3, where the spectra of several bright sources are identified.

Finally, the specifics of dispersive elements used in WFC3 spectroscopy have consequences for the contamination and completeness of the WISP emission line measurements. Incident light is dispersed by a grism, which is essentially a right triangular prism with a diffraction grating etched on the hypotenuse as a series of small steps. A small portion of the light that enters the grism passes right through and forms an image of the source on the detector. This image is called the zeroth order of the spectrum and can be confused with an emission line if it lines up with the spectrum of another source. Some of the zeroth orders are identified by red circles in Figure 2.3. The remaining light is dispersed as it passes through the grism, where the wavelength of the light determines the angle by which it is bent. Additionally, diffraction gratings produce multiple copies of the light, analogous to the multiple peaks created by constructive interference as light is diffracted through a double slit. Most of the energy is focused into the first order, identified in green in Figure 2.3. Second and higher orders for the brightest sources (usually stars) are also detected in WISP images and add to the possible spectral contamination.

## 2.2 WISP Data Reduction

All WISP data are reduced with the WFC3 pipeline CALWF3 in combination with custom scripts that account for the specific challenges of un-dithered, pure-parallel observations. The foundation of the WISP reduction pipeline (versions 4 and 5) is described in (Atek et al., 2010), and the crucial updates implemented for version 6.2 will be presented in Baronchelli et al. (in preparation).

One of the major additions included in version 6.2 is the implementation of a multiple component fit to the sky background in the grism images. Each pixel on the detector of a slitless grism observation records emission from the sky at all wavelengths, where each wavelength is coming from a slightly different position. While the “input” spectrum of the sky can be considered uniform across the field-of-view, the sky emission is not uniform on the detector. Along the left edge of the detector, the second and higher orders of the sky emission do not contribute to the background. This is also the case along the right edge where the sky’s zeroth order emission drops out. The position of the spectral orders therefore results in vertical bands in the background of the grism images, brighter where the spectral orders of the sky emission overlap and darker where fewer spectral orders are contributing emission (see the right panel for Figure 2.4). Typically a single “master sky” image is scaled and fit to remove the background in each grism image, under the assumption that the relative strength of the background components remain the same exposure to exposure. In the previous versions of the WISP pipeline, we used the master sky created for the WFC3 grisms by Kümmel et al. (2011).

However, as noted by Brammer et al. (2012), the structure in the sky of WFC3 grism images is highly variable. There are two main components of the variable emission: the zodiacal light and a helium emission line at  $1.083 \mu\text{m}$ . The zodiacal light is a diffuse glow in the solar system caused by sunlight reflecting off of dust grains. The strength of the zodiacal light decreases with distance from the Sun, and the component in the grism background should stay relatively constant throughout a full set of exposures taken on the same date. The helium emission comes from Earth’s upper atmosphere and can vary on timescales shorter than the length of an exposure as *HST* moves closer or farther from Earth and the telescope pointing changes. Brammer et al. (2015) isolate these components in WFC3 grism exposures and create separate master skies for each, which are displayed in the two images on the top right of Figure 2.4. See Brammer et al. (2015) for a full explanation of the need for and the creation of these images.

Implementing this multi-component background fit involves the following steps. We

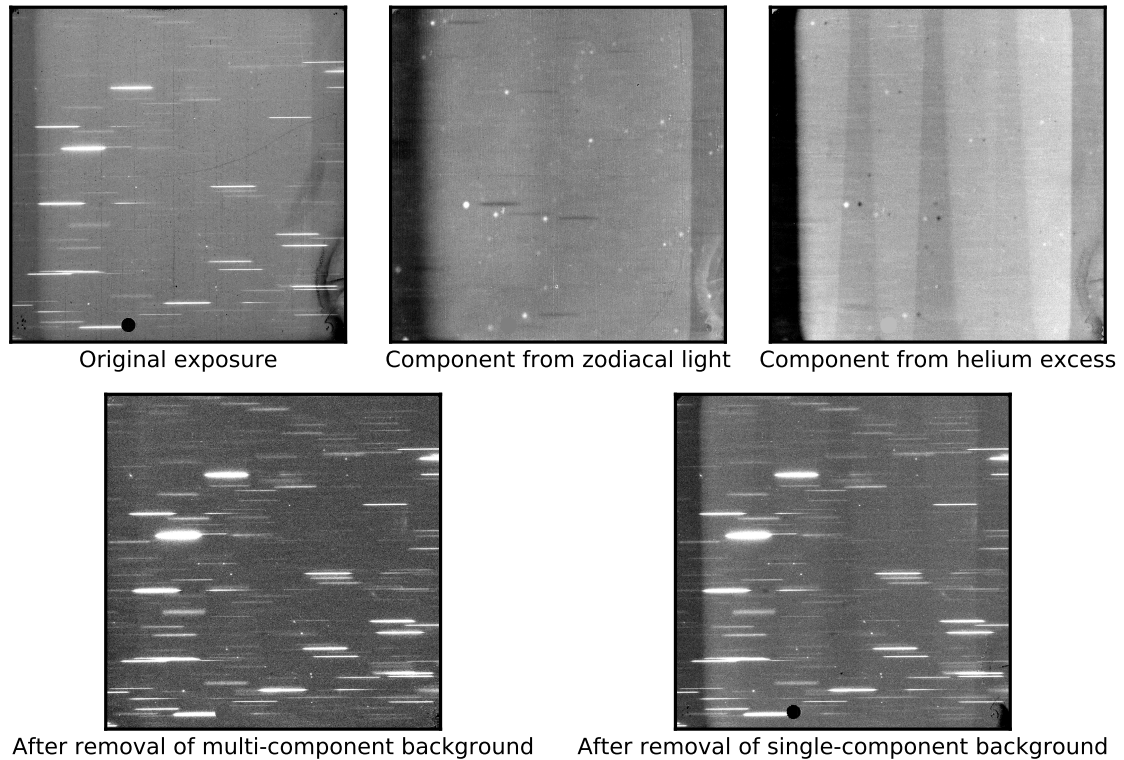


**Figure 2.4** An example of the fitting and removal of multiple components of the sky background. *Top row:* The original exposure (left), the contribution from the zodiacal light (middle), and the contribution from the helium 1.08s  $\mu\text{m}$  emission from Earth’s atmosphere (right). *Bottom row:* The background-subtracted image resulting from fitting the multiple components (left) compared with the same image when only the single “master sky” from Kümmel et al. (2011) is fit. Note that the white point sources visible in the zodiacal light image (middle top) are IR “Blobs,” locations where the sensitivity decreases by  $\sim 15\%$ . These blobs are caused by the mirror that diverts light into the WFC3 IR channel. The grism effectively disperses the blobs, creating the darker streaks to their right (Pirzkal et al., 2010).

first carefully mask out all pixels in each grism exposure that contain source flux. Next, we remove the flat-field correction (Brammer et al., 2015) from the master sky images. This step ensures that the multiplicative features, such as the wagon wheel structure in the lower right corner, are not fit as part of the additive sky background. We model the background with a linear combination of the zodiacal light and helium images. We calculate the amplitudes of each sky component with two iterations of a least squares fit, including the pixel weights of the input image in the second iteration. Although the zodiacal light component should be constant between exposures from the same observing sequence, we

fit it separately to each exposure but note that the amplitudes vary by at most 2%. The individually-calculated background models are subtracted off of each exposure. Finally, bad pixels are identified and replaced with noise generated from a Gaussian distribution fit to the full background.

We use the `AstroDrizzle` software Gonzaga (2012) to combine the individual exposures, correcting for astrometric distortions and any potential alignment issues. The IR direct and grism images are drizzled onto a  $0''.08$  per pixel scale. Object detection in the IR direct images (F110W, F140W, and F160W) is performed with *Source Extractor* (version 2.5, Bertin & Arnouts, 1996). For fields with imaging in two filters, we create a combined detection image and supplement the catalog with sources detected individually in only one of the filters. We use the `aXe` software package (Kümmel et al., 2009) to extract and calibrate the spectra.

In addition to the processes of the CALWF3 pipeline, the UVIS images are also corrected for the charge transfer efficiency degradation of the WFC3/UVIS detector and processed with customized darks based on the methodology of Rafelski et al. (2015). We do not use the UVIS images for source detection, but plan to do so in a future version of the WISP pipeline. Specifically, the footprint of WFC3/UVIS images covers  $\sim 2.7$  arcmin<sup>2</sup> more than WFC3/IR images. The extra area coverage will be particularly useful along the right edge of the grism images because source positions in the UVIS images can be used to determine the locations of the missing zeroth orders of bright sources.

Finally, while our main work uses the  $0''.08$  pixel scale of the IR data, we also drizzle all direct images (IR and UVIS) onto both the UVIS scale ( $0''.04$ ) and the original IR scale ( $0''.13$ ). Each scale is appropriate for different science goals. For example, we use the higher-resolution UVIS scale for the photometric catalog (see Section 2.3) and the Ly $\alpha$ -emitter candidate selection (see Chapter 4) because drizzling all images onto the lower-resolution IR pixel scale reduces the depth in the UVIS images, especially for small compact objects. These new pixel scales only affect the final drizzled images used for photometry. All other data reduction, cosmic ray rejection, and spectral calibration are done on the original pixel scales.

In total, 434 WISP fields have been successfully reduced. Of the remaining fields, 22 require specialized attention and 27 are unusable either because of field crowding, persistence, or corrupted data. Subsets of these 434 fields are used throughout this thesis depending on the specific project goal and the data quality and depth required. We present the creation of the photometric and emission line catalogs in Sections 2.3 and Section 2.4, respectively, and use them for analysis in the following chapters.

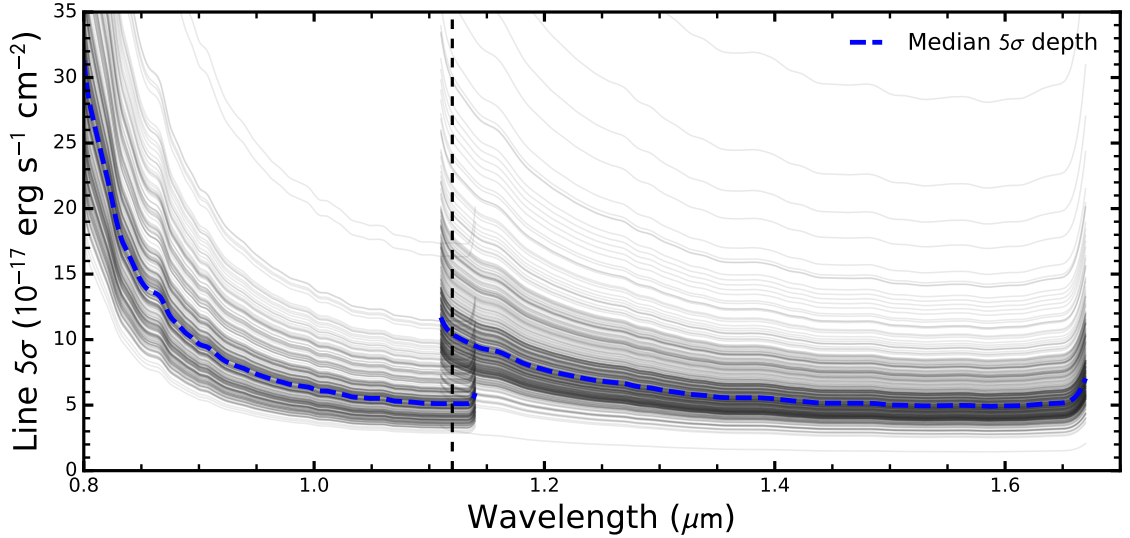


**Figure 2.5** The  $5\sigma$  emission line sensitivities in the individual WISP fields (light grey curves). The blue dashed line indicates the median  $5\sigma$  field depth. The depth varies significantly field-to-field due to variations in the background levels in each field.

### 2.2.1 Grism Depths

Since the visit lengths depend on the specifics of the primary observations, we do not reach a uniform depth in all WISP fields. Additionally, the sky background in each field is affected to varying degrees by zodiacal light, Earth limb brightening, and telescope thermal emission. While sky subtraction removes these effects from the grism images, their contributions to the noise in each field remain and affect the sensitivity limits achieved for the detection of emission lines. (See Section 2.2 for information on the grism sky subtraction.) The median  $5\sigma$  detection limit for emission lines in both grisms is  $\sim 5 \times 10^{-17}$  erg s $^{-1}$  cm $^{-2}$ , yet the detection limit in a given field can differ from this median by more than a factor of 2. In what follows, we describe how we calculate the depth reached in each WISP field.

In slitless spectroscopy, each sky pixel receives flux from all dispersed wavelengths, and so the sky (in units of counts/s) is constant with wavelength. We can therefore measure the sky anywhere across the full image, provided we have removed the flux contributed by sources. We begin by masking out the footprints of all identified spectra in the dispersed images. We also mask all pixels in the left-most 100 columns with fluxes greater than  $1.5\sigma$  above the median background. This extra masking helps remove source flux from off-image sources for which we do not have positional information and therefore cannot identify their first and second orders. We compute and bin the fluxes measured in  $\sim 5000$  rectangular

**Table 2.1** WISP Fields

Field	RA	Dec	$1\sigma$ Depth G102 <sup>a</sup> (erg s <sup>-1</sup> cm <sup>-2</sup> )	$1\sigma$ Depth G141 <sup>a</sup> (erg s <sup>-1</sup> cm <sup>-2</sup> )
1	01:06:35.29	+15:08:53.8	$9.67 \times 10^{-18}$	$9.57 \times 10^{-18}$
2	01:25:10.02	+21:39:13.7	...	$1.17 \times 10^{-17}$
5	14:27:06.64	+57:51:36.2	$7.72 \times 10^{-18}$	$5.30 \times 10^{-18}$
6	01:50:17.18	+13:04:12.8	$1.15 \times 10^{-17}$	$8.76 \times 10^{-18}$
7	14:27:05.90	+57:53:33.7	$1.54 \times 10^{-17}$	$8.56 \times 10^{-18}$
8	11:51:51.62	+54:40:41.2	$6.89 \times 10^{-18}$	$7.75 \times 10^{-18}$
9	12:29:44.31	+07:48:23.5	$2.30 \times 10^{-17}$	$2.86 \times 10^{-17}$
10	09:25:07.84	+48:57:03.0	$8.74 \times 10^{-18}$	$9.54 \times 10^{-18}$

Note — This table is available in its entirety in an upcoming paper describing the WISP catalog (Bagley et al. *in prep*).

apertures placed randomly across the unmasked portions of the image. The apertures are 5 and 3 pixels wide in the spatial and dispersion axes, respectively. The width of the apertures along the spatial axis is  $\sim 0''.65$ . The width along the dispersion axis is chosen to match one of the requirements for emission line identification by our automatic line-detection software — three contiguous pixels above a signal-to-noise (S/N) threshold. See Section 2.4 for a description of the emission line identification process.

We fit a Gaussian to the distribution of fluxes and use the standard deviation to measure the dispersion in the sky background. The measured dispersion depends slightly on the locations of the randomly-placed apertures across the image, and subsequent calculations can yield slightly different  $\sigma$ 's. To help mitigate this problem, we repeat the process described above five times and take the median of the resulting  $\sigma$ 's to be the true dispersion for the field. Dividing the  $\sigma$ 's calculated above by the sensitivity curve for the grism provides the  $1\sigma$  line sensitivity for the field as a function of wavelength. This sensitivity, in units of erg s<sup>-1</sup> cm<sup>-2</sup>, is that of an integrated line flux. The sensitivity in the continuum (erg s<sup>-1</sup> cm<sup>-2</sup> Å<sup>-1</sup>) is obtained by dividing by the aperture size used in calculating  $\sigma$  and the dispersion of the grisms:  $3\Delta\lambda$ . The detection limits of the WISP fields are presented in Figure 2.5 and Table 2.1.

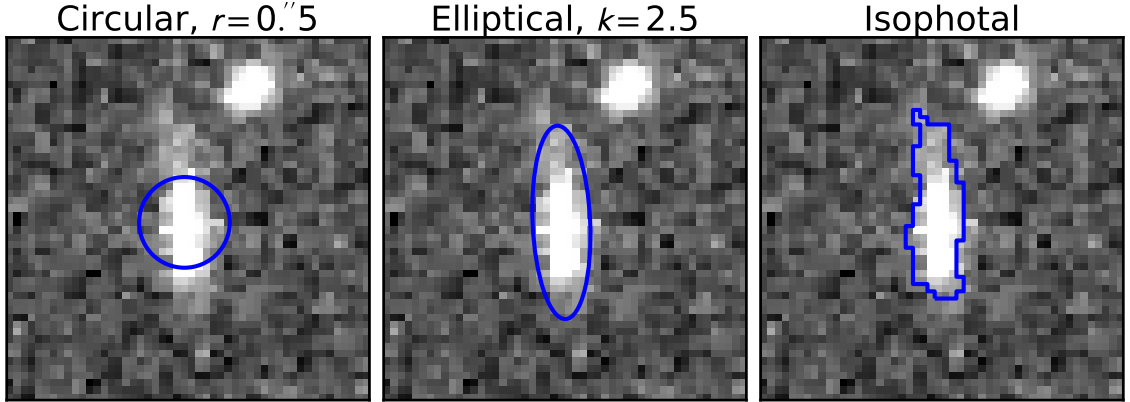


**Figure 2.6** An illustration of the three types of apertures used in the photometric catalog.

## 2.3 Photometric catalog

Photometry is the measurement of how bright a source is, performed by calculating the flux or intensity of the source in an image. There are several sets of photometric measurements we have performed on WISP imaging data, each optimized for specific purposes. We describe in this section the photometry that is used throughout the rest of this thesis.

A photometric measurement consists of summing the flux of all pixels inside of a specified aperture after subtracting the contribution that comes from the background or sky pixels. The choice of aperture shape and size can strongly affect the results. The ideal aperture will contain all of the light from the source but no flux from the sky background outside of the source or contamination from nearby sources. This optimization is a challenge, and so photometry is calculated for each source in a variety of aperture types. These types are illustrated in Figure 2.6 and described below.

**Circular aperture** — We calculate photometry in circular apertures with radii ranging from  $0''.2$ , appropriate for the most compact sources, up to  $1''.5$ . For elongated sources, circular apertures can often miss source flux while including too much non-source background. However, they are useful for comparing the fluxes of sources in multiple filters, where the circular aperture probes the same region regardless of how the source size or shape varies with wavelength. We use circular apertures to measure the colors of sources in Section 4.3, where a color is defined as the difference in magnitudes measured in two filters, and magnitudes are expressed in the AB system:  $m_{\text{AB}} = -2.5 \log_{10} f_{\nu} - 48.6$  for a flux  $f_{\nu}$  in units of  $\text{erg s}^{-1} \text{Hz}^{-1}$  (Oke & Gunn, 1983).

**Elliptical aperture** — As can be seen in Figure 2.6, elliptical apertures can be a better

choice than circular apertures for elongated sources. *Source Extractor* uses a flexible elliptical aperture based on a method presented by Kron (1980), which computes a characteristic radius based on the first moment or weighted average of the intensity  $I$  within a radius  $r$  (Bertin & Arnouts, 1996):

$$r_1 = \frac{\sum rI(r)}{\sum I(r)}. \quad (2.1)$$

*Source Extractor* then creates elliptical apertures with axes  $\epsilon kr_1$  and  $kr_1/\epsilon$ , where  $\epsilon$  is the ellipticity and  $k$  is a factor that scales the ellipse up to include almost all ( $\sim 90\%$ ) of the light from the source. We therefore use elliptical apertures when a measurement of the total source flux is required.

**Isophotal aperture** — *Source Extractor* identifies sources in images as groups of contiguous pixels above a set threshold. The outline of the source detected in this way consists of lines connecting pixels of equal intensity and defines an isophotal area. The isophotal flux or magnitude is calculated within this isophotal aperture. Like circular apertures, isophotal apertures are often used in calculating galaxy colors, provided that the same isophotes are used in both filters.

A proper color measurement, however, must take into account the shape and width of each filter’s point spread function (PSF), or the wavelength-dependent response of the telescope and instrument to a point source. If the PSFs of the two filters are not matched, the apertures in each filter will not be truly consistent. We therefore create a catalog of PSF-matched photometry in the UVIS and IR images. As discussed in Section 2.2, we use UVIS and IR images that are drizzled onto the UVIS pixel scale ( $0''.04$ ). We choose  $0''.04$  to preserve the depth reached in the UVIS images, which is crucial for detecting true high-redshift dropout candidates (see Section 4.3 for more information). The higher-resolution UVIS images are then degraded to match the lowest-resolution filter, F160W. This degradation is achieved by convolving all images with Gaussian kernels that match their PSF with that of the F160W image.

### 2.3.1 PSF-Matched Photometry

The first version of the UVIS/IR photometric catalog is created using *Source Extractor* to both detect sources and calculate the photometry in each filter. Source detection and photometry are performed in dual image mode using a combined detection image made from all *HST* images of the field. We construct the detection image as the weighted average of the images in all four PSF-matched filters:

$$\frac{1}{n} \sum_i \frac{I_i}{\sqrt{w_i}}. \quad (2.2)$$

Combining the F110W and F160W images produces a deeper image than either individual filter and enables the detection of additional objects that would be missed by using a single filter for detection. The UVIS images are included in our detection image to ensure that there is adequate coverage of all pixels. As we cannot dither the telescope, we do not have sufficient exposures to cover all IR pixels at the  $0''.04$  pixel scale. As a result, the IR images drizzled to the UVIS pixel scale contain “bad” pixels that lack the information to have a reliable flux. These pixels have weights of zero, and we have confirmed that they do not affect the photometry. This version of the UVIS/IR catalog is used in the search for high-redshift Lyman- $\alpha$  emitters presented in Chapter 4.

We calculate two sets of photometry in each UVIS filter: once on the original, unconvolved image, and once on the image convolved to match the resolution of the F160W filter. The unconvolved UVIS images (at the original resolution) are deeper than those that have been convolved. The photometry calculated on the unconvolved images is therefore used in Section 4.3 to determine which sources are undetected in the UVIS filters.

Running *Source Extractor* on the images with the new pixel scale unfortunately results in a catalog of sources that do not perfectly match those identified by the WISP pipeline using the original IR images. The source sizes and shapes are not identical, and some faint sources are missed entirely. Since the spectral extraction regions in the grism images are defined by the source sizes and shapes on the original IR images, it is crucial to have photometry that matches these source definitions. We therefore create a new version of the UVIS/IR photometric catalog using the *Source Extractor* segmentation maps created on the original IR images. We use the Astropy affiliated package `reproject` to project the original segmentation maps onto the  $0''.04$  pixel scale, and perform photometry in manually-defined apertures that match those used by *Source Extractor*. In Figure 2.7, we compare for a test field the isophotal photometry calculated on the  $0''.04$ /pixel F110W image with that from the original F110W image. The left panel shows the results from the first version of the UVIS/IR catalog with incorrect source footprints on the  $0''.04$  images. The first version can underestimate the photometry of faint sources by more than a magnitude, while the improved version results in a much better agreement.

## 2.4 Emission line catalog

There are two versions of the WISP emission line catalog referenced in this thesis. Both versions are created via the same general steps: an automatic detection algorithm that identifies emission line candidates followed by a visual inspection performed by two reviewers

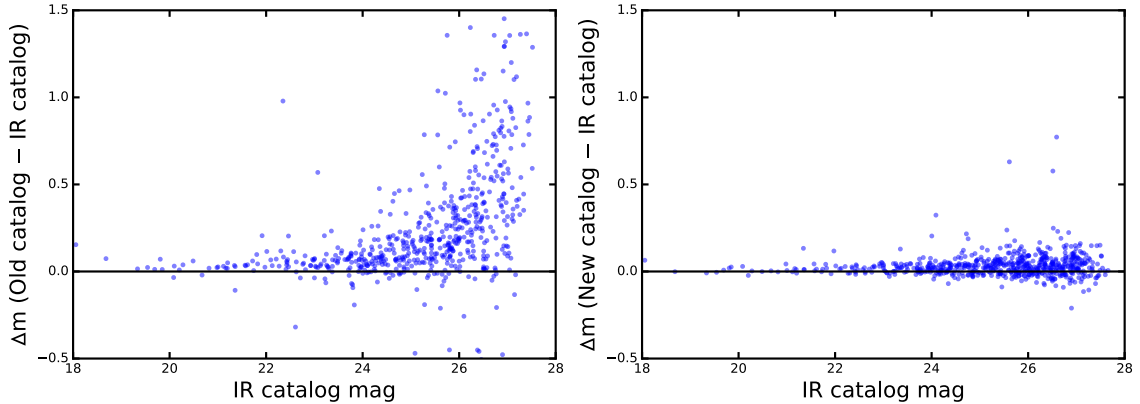


**Figure 2.7** A comparison between the isophotal photometry from the old and new versions of the WISP photometric catalog. In each panel, the F110W photometry on the new pixel scale is compared with that on the original pixel scale. There is much better agreement in the new catalog, which uses source definitions — size and shape — that more closely match those of the original catalog. This discrepancy only occurs for isophotal apertures, and so the circular apertures used to calculate the colors of Ly $\alpha$ -emitter candidates in Chapter 4 produce reliable photometry.

on each candidate. The first version of the detection algorithm identified emission lines as groups of contiguous pixels above the continuum. The resulting lists of line candidates were dominated by spurious sources and fake emission lines, and the inspection and cleaning of these lists required a prohibitive amount of time from reviewers. This version of the catalog was generated from only 139 WISP fields and included  $\sim 5800$  emission line objects, approximately 15-20% of which are marginal detections and/or likely contaminants from 0th orders or overlapping spectra. Subsets of this catalog are used in the work presented in Chapter 4 and in WISP publications such as Atek et al. (2010); Colbert et al. (2013); Henry et al. (2013); Mehta et al. (2015); Bagley et al. (2017).

The second version of the detection algorithm, described in detail in this section, improves on this method by including a continuous wavelet transform and additional quality checks aiming to remove most spurious sources before the inspection stage. This new catalog was constructed after processing and inspecting the spectra from 419 WISP fields and includes  $\sim 8000$  emission line objects. This version is used in Chapter 6 and in WISP publications currently in preparation. In the remainder of this section, references to the WISP emission line catalog refer to this updated version.

Of the 419 WISP fields included in the catalog, 162 are from short opportunities during which G141 was the only grism used, 254 were observed with both grisms, and 3 with only G102. The positions of the WISP fields included in the catalog are shown in Figure 2.2. In

total, these fields cover  $\sim 862$  arcmin<sup>2</sup> and  $\sim 1518$  arcmin<sup>2</sup> in G102 and G141, respectively. We note that the effective grism area of the WISP survey is  $\sim 3.55$  arcmin<sup>2</sup> in G102 and  $\sim 3.8$  arcmin<sup>2</sup> in G141, less than the nominal 4.3 arcmin<sup>2</sup> of the WFC3 IR channel. We remove area on the right side of each pointing because contaminating zero order images cannot be identified for the spectra. This lost strip amounts to  $\sim 32''$  along the dispersion axis in G102 and  $\sim 25''$  in G141, where the difference is due to the dispersion solution in the two grisms.

The WISP emission line catalog is created in three steps. First, an automatic detection algorithm examines every extracted spectrum to identify emission line candidates. Next, each candidate is independently inspected by two reviewers both for confirmation of the lines and to measure the source redshift and emission line properties. These first two steps are performed by the `wisp_analysis`<sup>2</sup> software package. Finally, the output from the two reviewers is combined following a type of decision tree. We describe each step in this process in the following sections.

### 2.4.1 Emission Line Candidate Identification

We identify emission line candidates with a peak detection algorithm that uses a continuous wavelet transform (CWT) to select appropriately-shaped peaks in one-dimensional spectra. A wavelet transform breaks a signal into its base components, each of which is a modified version of the same “mother” wavelet function. This process is similar to Fourier analysis, but rather than sinusoidal components of varying frequencies, the base components identified by a wavelet analysis are scaled or shifted versions of the mother wavelet. The CWT is an improvement over the previous WISP line detection method, which identified emission lines as contiguous pixels above a signal-to-noise (S/N) threshold (Colbert et al., 2013). This amplitude-based peak finding process is strongly dependent on the fit to the continuum and the amount of smoothing applied to the spectrum. It also resulted in many spurious detections as noise spikes can be mis-identified as faint emission lines. The benefit of the CWT is in fitting not only the amplitude, but also the shape, of emission line features in the spectrum. In what follows, we describe the steps of applying a CWT and using the results to identify emission line candidates.

Emission line identification is performed on the one-dimensional spectra extracted and calibrated by `aXe`. We first remove from each spectrum flux introduced by the overlapping continua from nearby objects. For this purpose we use the contamination model created by `aXe` during spectral extraction, where all objects detected in the direct images

<sup>2</sup> [https://github.com/HSTWISP/wisp\\_analysis](https://github.com/HSTWISP/wisp_analysis)

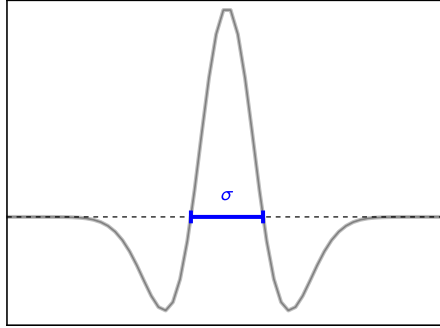


**Figure 2.8** The Ricker wavelet used for emission line detection in the continuous wavelet transform. It is proportional to the second derivative of a Gaussian function and is defined by a width parameter,  $\sigma$ .

are approximated as two-dimensional Gaussians defined by the size and shape measured by *Source Extractor*. A contamination-corrected spectrum is shown in black in the top panel of Figure 2.9 and is used throughout this discussion as an illustration of the emission line identification process.

Next, we perform a continuous wavelet transform on the spectrum using a Ricker wavelet, which is proportional to the second derivative of a Gaussian function. The Ricker wavelet models the function

$$f = \frac{2}{\sqrt{3}\sigma\pi^{\frac{1}{4}}}\left(1 - \frac{x^2}{\sigma^2}\right)e^{-\frac{x^2}{2\sigma^2}} \quad (2.3)$$

and is illustrated in Figure 2.8. The transform is performed using  $N_\sigma = 10$  kernels or wavelets of varying widths, with the minimum width set to 1.5 pixels, corresponding to  $\sim 36\text{\AA}$  ( $\sim 70\text{\AA}$ ) in G102 (G141), and the maximum width equal to twice the full width at half maximum (FWHM) estimate for the object. Spectra obtained in slitless mode are essentially images of the source at each wavelength, and so the width of emission lines will be correlated with the source size. We approximate the FWHM as twice the dispersion measured along the semi-major axis (`A_IMAGE` reported by *Source Extractor*), and use this  $\text{FWHM}_{\text{est}}$  to define upper bounds for both the wavelet widths and the FWHM of the emission line profile fits described in Section 2.4.3.

The CWT transform compares the wavelet with the 1D spectrum, shifting the wavelet to cover all wavelengths and scaling or stretching to cover all input widths. The resulting array of CWT coefficients is a matrix of dimension  $N_\sigma \times N_\lambda$  representing the correlation of the spectrum and wavelet at each scale and wavelength. Large CWT coefficients indicate regions of the spectrum with a strong correlation with the wavelet, and so the largest coefficients will occur where both the position and width of the wavelet best match a spectral feature.

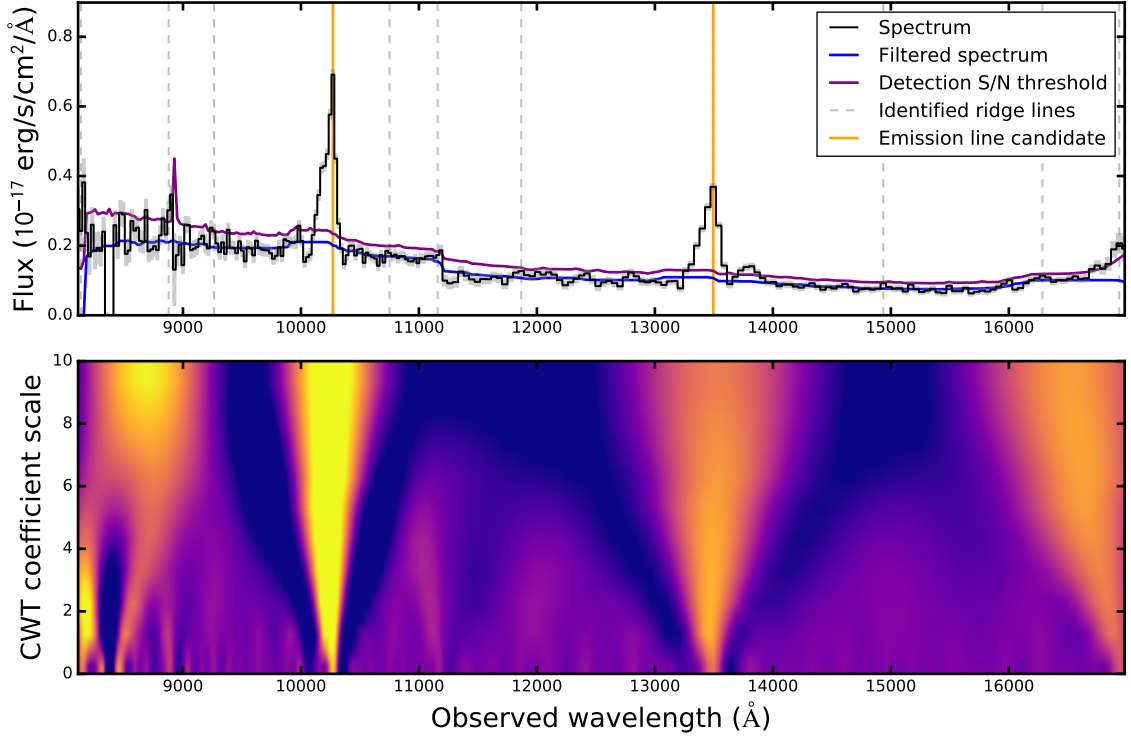


**Figure 2.9** An example of the emission line detection algorithm. *Top panel:* The input spectrum is plotted in black. The filtered spectrum (blue curve) is used as an estimate of the continuum. The purple curve is the detection threshold, defined as a minimum  $S/N \geq 2.31$  above the continuum. *Bottom panel:* The two-dimensional CWT coefficient matrix represents the correlation of the spectrum and wavelet at each scale and wavelength. Larger coefficients (yellow colors) identify regions of higher correlation. Emission lines are correlated with the wavelet at many scales, creating connected ridge lines in the CWT matrix. The dashed grey lines in the top panel show the positions of detected ridge lines. The yellow solid lines show the ridges that passed our additional selection criteria to be identified as true emission line candidates.

An example coefficient matrix is displayed in the bottom panel of Figure 2.9.

As can be seen in the bottom panel of Figure 2.9, strong emission peaks in the spectrum are strongly correlated with the Ricker wavelet at many scales. The resulting peaks in the two-dimensional CWT coefficient matrix extend to multiple scales and can be visualized as mountain ridges. Emission line features in the spectrum can now be identified using the ridges in the CWT coefficient matrix. For this step, we use the `scipy` program `find_peaks_cwt`, which is an implementation of the procedure presented in Du et al. (2006). We briefly summarize the process here and refer the reader to Du et al. (2006) for a full description of the algorithm.

**Table 2.2** Emission Line Detection Parameters

Parameter	Value	Description
<b><u>Continuous Wavelet Transform</u></b>		
$N_\sigma$	10	number of CWT kernels (widths) used in transform
$\sigma_{\min}$	1.5 [pixels]	minimum CWT kernel width
$\sigma_{\max}$	2.0	maximum CWT kernel width fraction of $\text{FWHM}_{\text{est}}$
<b><u>Ridge and peak definitions</u></b>		
$d_{\max}$	$\sigma + 1$ [pixels]	maximum acceptable separation distance between local maxima at each scale on the same ridge line
$g_{\max}$	1 [kernels]	maximum acceptable gap between connected ridges
$l_{\min}$	3 [kernels]	minimum acceptable # of kernels in which peak is significant
$S/R_{\min, \text{CWT}}$	1	minimum acceptable ridge S/N at each scale
<b><u>Requirements for real lines</u></b>		
$C_{\min}$	0.15	minimum acceptable contrast between peak and continuum fluxes
$d_{\text{edge}}$	5 [pixels]	minimum acceptable distance to edge of spectrum
$n_{\min}$	3 [pixels]	minimum number of pixels above the noise threshold
$S/N_{\min, \text{pix}}$	2.31	minimum S/N per pixel

The first step in the peak identification process involves identifying ridge lines in the coefficient matrix. At each scale, a local maximum is matched with the nearest maximum calculated for the adjacent scale. The two local maxima constitute a ridge provided they are within a set distance,  $d_{\max}$ , which we define as one pixel larger than the width of the wavelet at the given scale. A ridge line continues through the matrix as long as the local maximum at each scale is within  $d_{\max}$  of the previously identified maximum. The ridge line is terminated if a local maximum is not matched at more than  $g_{\max}$  consecutive scales. We conservatively use  $g_{\max} = 1$ .

The second step is to identify peaks from the detected ridge lines. We only consider ridge lines that cover at least  $l_{\min} = 3$  scales and have a ridge signal-to-noise of  $S/N_{\min, \text{CWT}} \geq 1$ . The ridge S/N is estimated at each scale, and is taken to be the maximum CWT coefficient value on the ridge divided by the overall noise floor. The noise floor is calculated as the 10th percentile of the coefficients around the ridge line at the smallest scale ( $\sigma_{\min}$ ). These identified peaks are represented as dashed grey lines in the top panel of Figure 2.9.

Following the peak finder, we additionally screen the selected peaks to remove sources that are likely to be spurious. The spectrum is filtered to remove noise using a median

filter with a window size of 31 pixels, corresponding to  $\sim 760\text{\AA}$  in G102 and  $\sim 1440\text{\AA}$  in G141. The purpose of this filtering is to obtain a crude measure of the continuum, which will be used in evaluating the strength of any identified peaks. The large window is chosen so that emission lines will not significantly affect the continuum measurement. From this continuum estimate, the contrast between the peak and the continuum is calculated  $C = (f_{\lambda,\text{peak}} - f_{\lambda,\text{continuum}})/f_{\lambda,\text{continuum}}$ , and any peak with  $C < C_{\text{min}} = 0.15$  is rejected. This criterion is approximately equivalent to a cut on very low equivalent width (EW) emission lines and is implemented in order to remove noise spikes. Next, all peaks that overlap with zeroth orders of nearby bright ( $m < 23$ ) sources are rejected. Recall that we also do not consider any spectra on the right edge of the detector where we cannot determine the position of zeroth orders. We additionally remove peaks that are within  $d_{\text{edge}} = 5$  pixels of the edge of the spectrum to avoid convolution edge effects. Finally, we require that emission line candidates have at least three contiguous pixels each with a signal-to-noise of  $S/N_{\text{min,pix}} \geq 2.31$ , where here  $S/N$  is defined traditionally as the flux in the continuum divided by the error. This noise threshold results in an overall  $S/N$  of the emission line of  $S/N_{\text{line}} \geq 4$  and is displayed as the purple curve in Figure 2.9.

This process is performed on the one-dimensional spectra of each grism individually, allowing for  $500\text{\AA}$  of overlap between the two grisms. We next require that at least two reviewers inspect each emission line candidate, both to confirm the candidates and to measure the line properties.

#### 2.4.2 Emission Line Candidate Inspection

The original, amplitude-based WISP line detection software resulted in a false detection rate of  $\gtrsim 70\%$ , depending on the depth of the fields. Although the improvements presented here — identifying emission lines using both amplitude and shape combined with the EW criterion — reduce this rate significantly to approximately  $55\%$ , the visual inspection remains necessary for constructing a clean catalog.

For each emission line candidate, reviewers simultaneously inspect the direct images of the source, the two-dimensional spectral stamps, the one-dimensional extracted spectrum in units of  $f_{\lambda}$ , and a spectrum in units of  $S/N$ . An example of the full display from the interactive portion of the process is shown in Figure 2.10. We now briefly describe the inspection process and the series of checks reviewers perform for each candidate. The source displayed in Figure 2.10, object 93 from WISP field Par94 (hereafter 94-93), will be used as an example to illustrate the process. The two main questions reviewers must answer are whether the emission line candidate identified by the detection algorithm is real,

and whether it belongs to the object to which it is associated. In the first case, reviewers are validating the results of the detection software. In the second, they are considering and ruling out possible sources of contamination.

Candidate confirmation is required because spurious or false emission lines are occasionally identified by the detection program. False emission lines typically arise in two cases, when detector artifacts are identified as lines and when the continuum is improperly fit. The first case is a particular problem for a pure parallel survey such as WISP, since the telescope is not dithered between exposures. Combining multiple exposures therefore does not remove all cosmic rays, hot pixels, and other artifacts. Those that remain are sometimes selected as emission line candidates. Reviewers can often reject these by comparing the shape of the emission line candidate in the two-dimensional spectral stamp (top row of Figure 2.10) with the source shape in the direct image (middle row). Recall that an emission line in the spectral stamp is an image of the source at the given wavelength. The size, ellipticity, and position angle of the source are expected to be reflected to some degree in the emission line. This comparison is approximate, however, since the emission regions in a galaxy need not directly correlate with the broadband continuum emission detected in the imaging filters.

In the second case, false emission line candidates are identified in objects with continua that are poorly fit by the automatic software, which uses a cubic spline to fit the spectrum at eight wavelengths nodes. A steep rise in the continuum of an object, often caused by contamination from the spectrum of a nearby object, that is not reflected in the model fit can be incorrectly selected as a spectral peak. Given the large range of object sizes, fluxes, and levels of spectral confusion, one set of parameters will not work perfectly for all objects. The software's continuum fit is therefore treated as a first pass. The dashed blue line in Figure 2.10 is the continuum model for object 94-93, which in this case represents a good fit to the observed continuum. For objects with improperly fit continua, reviewers can tweak the model by adding, removing, or changing the wavelengths of the nodes used in the spline fit (black circles).

The reviewers must next determine whether the identified emission feature belongs to the source in question. With only a single role angle, WISP spectra are often contaminated by overlapping spectra from other sources along the dispersion direction. This check generally involves four parts. First, the comparison between source and emission line shape described above can help identify emission lines coming from another object. We do not expect a galaxy to be much larger or much brighter in an emission line than it is in imaging. Second, the emission should be vertically centered in the trace of the spectral stamps, indicated by

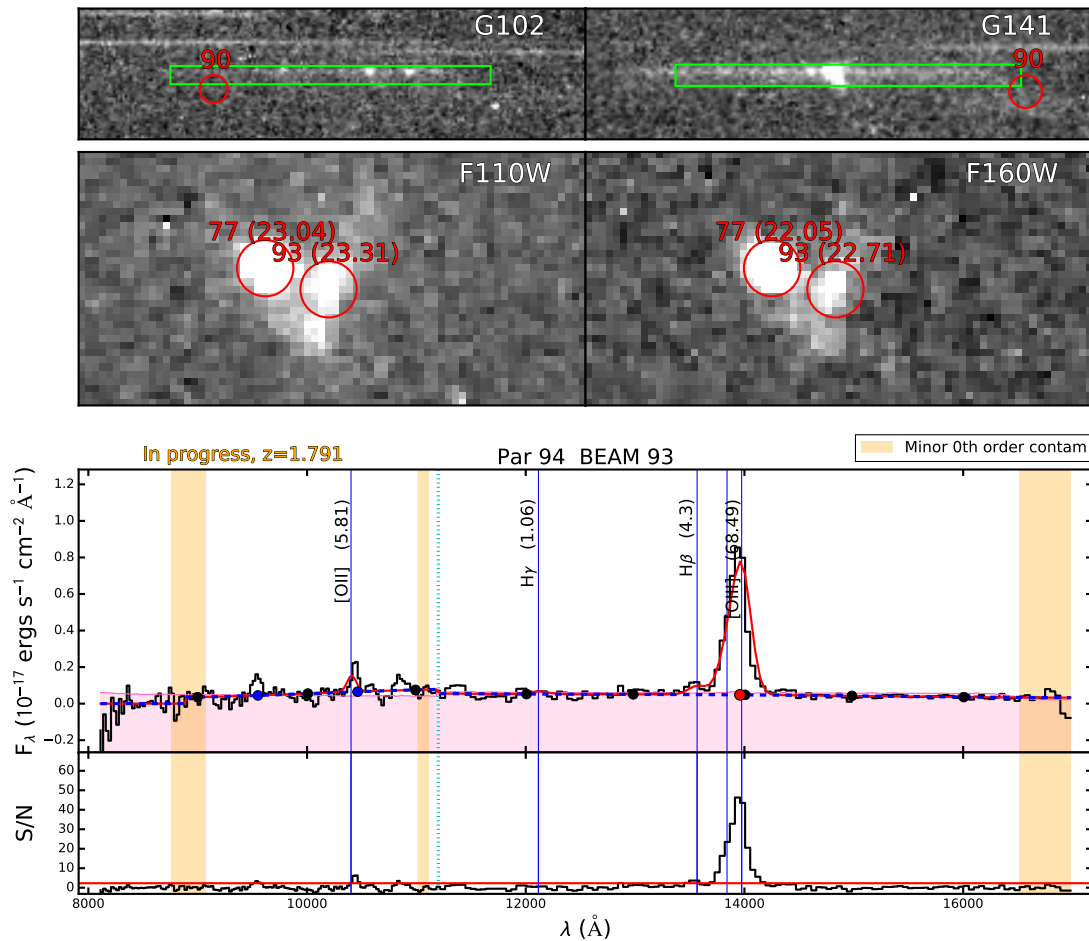


**Figure 2.10** The display from the interactive portion of the emission line finding process. Reviewers inspect all available information for a given object. *Top row:* The two-dimensional spectral stamps for G102 (left) and G141 (right) are displayed with a green box indicating the trace of the spectra. Red circles identify the positions of zeroth orders of bright ( $m < 23$ ) objects that may contaminate the spectra. *Middle row:* The direct images in all available filters, F110W (left) and F160W (right), with the positions of all objects and their corresponding magnitudes marked. The source of interest, here object 93, is centered in the direct images. *Bottom row:* The one-dimensional spectrum is displayed in both flux units ( $f_\lambda$ , top) and signal-to-noise (bottom). In the example shown here, the emission features identified in the spectrum of object 93 are not centered in the green box because they are coming from object 77. The emission line offset is clearest in the G102 spectrum. Object 93 was rejected as an emission line candidate and these emission features were instead measured for object 77.

the green box in the top panels of Figure 2.10. We can see that the line candidates in the spectrum of 94-93 are not centered, evidence that they likely belong to the nearby, brighter object 77. We note that it is of course possible that the emitting region of a source may not be centered on the continuum emission, and by rejecting emission lines that are off the center of the trace we may also be rejecting real emission line galaxies. Third, if there are multiple emission lines visible in the spectrum, their relative wavelengths should match. The wavelength solution of the grism is determined by the source position in the direct image, and will therefore only be correct for the spectrum of that source. For example, in Figure 2.10, given the assumed redshift for this object, the spectral peak around  $\lambda \sim 10500\text{\AA}$  should be [O II] $\lambda 3727$ . However, it does not line up exactly with the expected wavelength for [O II] at this redshift (indicated by the blue vertical line), further indication that these emission lines are contaminants from object 77.

Finally, the reviewers must consider the position of zeroth orders. We consider a portion of a spectrum to suffer from “major” zeroth order contamination if it directly overlaps with a zeroth order from a bright source ( $m < 23$  magnitude). The position of these bright zeroth orders are indicated by red circles in the grism stamps in Figure 2.10. The chance alignment of a bright zeroth order, especially from a compact source, can appear as a very convincing emission line. Spectral peaks that suffer from this major contamination are automatically rejected by the automatic software. Meanwhile, “minor” zeroth order contamination could be caused by (1) bright zeroth orders that are close to but not directly overlapping the spectral trace or (2) from direct overlap with zeroth orders of fainter sources ( $m > 23$ ). In some cases, again especially for the most compact objects, these fainter zeroth orders can be bright enough to masquerade as emission lines, and so the reviewers must remain vigilant for this possibility. The minor zeroth order contamination regions for object 94-93 are shown as orange bands in the spectrum of Figure 2.10.

### 2.4.3 Emission Line Measurements

Once an emission line candidate has been confirmed, the reviewers fit a model to the spectrum. The fitting is performed via Levenberg-Marquardt least-squares minimization. It is implemented with the software `mpfit`, based on the MINPACK-1 FORTRAN package (Moré, 1978) and translated to Python by Mark Rivers<sup>3</sup>. With `mpfit`, each parameter can be held fixed or can be constrained with upper and lower bounds. The full model includes over 20 parameters, which are described below and listed in Table 2.3.

The model spectrum fit to the data consists of a continuum with the following emission

---

<sup>3</sup> University of Chicago, <http://cars9.uchicago.edu/software/python/mpfit.html>

**Table 2.3** Model Spectrum Parameters

Parameter	Description	Initial Value	Limits
$n_{\text{nodes}}$	Number of spline nodes used in continuum fit	8	Fixed
$\Delta\lambda_{\text{fitting}}$	Size of region used for line fitting	1500 Å	Fixed
$z_{\text{init}}$	Input redshift	$\left(\frac{\lambda_{\text{obs}}}{\lambda_{\text{H}\alpha}} - 1\right)^{\text{a}}$	$\pm 0.02$
$\Delta z_{[\text{O III}]}$	Shift in redshift allowed for [O III] profile fit	0	$\pm 0.02$
$\Delta z_{[\text{O II}]}$	Shift in redshift allowed for [O II] profile fit	0	$\pm 0.02$
$\Delta z_{[\text{S III, He I}]}$	Shift in redshift allowed for [S III] and He I fits	0	$\pm 0.02$
$r_{\text{FWHM}}$	Ratio of FWHM in the blue and red grisms	0.5	Fixed
$\text{FWHM}_{\text{init}}$	Input FWHM	$2a \Delta\lambda_{\text{G141}}$ Å <sup>b</sup>	$^{-0.3\text{FWHM}_{\text{init}}}$ $^{+2.0\text{FWHM}_{\text{init}}}$
$A_{\text{line}}$	Input amplitude for each emission line	$\dots^{\text{c}}$	$0, 1^{\text{c}}$
$r_{[\text{S III}]\lambda 9532/\lambda 9069}$	Ratio of [S III]λ9532 to [S III]λ9069 fluxes	2.48	Fixed
$\lambda_{\text{T}}$	Grism transition wavelength	11200 Å	Fixed
$\lambda_{\text{blue}}$	Blue wavelength cutoff for the G102 grism	8100 Å	Fixed
$\lambda_{\text{red}}$	Red wavelength cutoff for the G141 grism	17000 Å	Fixed

<sup>a</sup>The input redshift is that which will give H $\alpha$  for the current line, or is a redshift guess provided by the user.

<sup>b</sup> $\text{FWHM}_{\text{init}}$  is taken as twice the source semi-major axis (`A_IMAGE`) multiplied by the dispersion in the red grism.

<sup>c</sup>Emission line amplitudes are estimated as the flux value at line center and are constrained to be positive.

lines added: [O II] $\lambda\lambda$ 3727 + 3729, H $\gamma$ , H $\beta$ , [O III] $\lambda\lambda$ 4959 + 5007, H $\alpha$ , [S II] $\lambda\lambda$ 6716 + 6730, [S III] $\lambda$ 9069, [S III] $\lambda$ 9531, and He I $\lambda$ 10830. The continuum is modeled using a cubic spline fit to a series of spectral nodes, and emission lines are modeled as Gaussians:

$$f(\lambda) = Ae^{-\frac{(\lambda-\lambda_{\text{line}})^2}{2\sigma^2}}, \quad (2.4)$$

where the input amplitude  $A$  is estimated for each line, the line center  $\lambda_{\text{line}}$  is determined by the redshift guess for the source, and the standard deviation  $\sigma$  depends on the source size and the dispersion of the grism in which the line appears. Emission lines are not fit individually. The entire spectrum — continuum plus all lines — is fit simultaneously, and all line profiles are constrained to have the same FWHM, reflecting the fact that all emission lines are images of the same host source.

As a consequence of the use of a full spectral model, all emission lines listed above will be fit provided they fall within the grism wavelength coverage at the assigned redshift. Emission lines that were not identified by the detection algorithm will therefore be measured along with the identified lines. We refer to the lines strong enough to have been identified by the detection algorithm as “primary lines”, while the remaining lines are called “secondary lines”. This distinction is an important one for the emission line catalog completeness, which is discussed in the next section (Section 2.4.4). The S/N and EW of all emission lines in the catalog are shown in Figure 2.11. The vast majority of the H $\alpha$  emission lines (blue circles) have a S/N greater than 4 (vertical dashed line), indicating that H $\alpha$  is most often the primary line in a spectrum. Emission line fluxes to the left of the dashed line were likely fit as secondary lines and are therefore at a lower S/N. Lines with a flux S/N < 1 are set at  $1\sigma$  and reported as upper limits in flux and therefore EW. These limits are calculated by summing in quadrature the error array within  $2\times$ FWHM of line center. We find, however, that the error arrays calculated by `axE` are underestimates of the spectral noise properties. The  $1\sigma$  limits are all systematically lower than the sensitivity limits measured for the fields. We therefore apply a correction factor to the flux limits, correcting the magnitude of the limits while preserving the scatter in the measurements.

We now discuss the parameters specific to the spectral fitting. A preliminary fit to the spectrum is performed to obtain an initial guess for the continuum. The spectrum is masked in regions  $\pm\Delta\lambda_{\text{fitting}}$  around the expected emission line wavelengths given the redshift guess for the source, and all emission line amplitudes,  $A_{\text{line}}$ , are set to zero. The continuum is fit with  $n_{\text{nodes}}$  spline nodes, the number and wavelengths of which can be changed by the reviewer. In the second round of fitting, the initial guesses for line amplitudes are approximated by the peak flux (minus the continuum model) again within  $\pm\Delta\lambda_{\text{fitting}}$  of

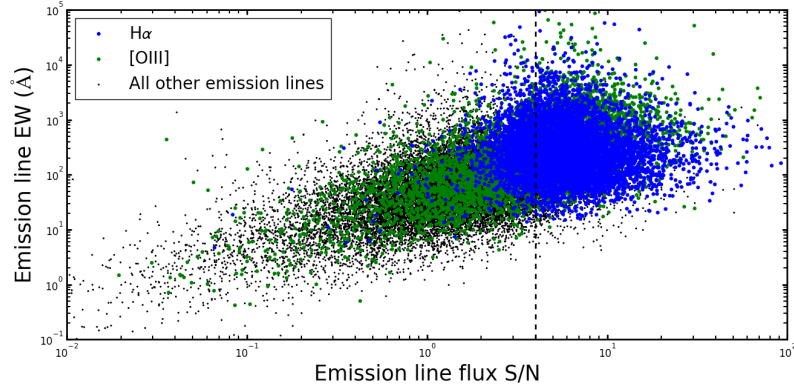


**Figure 2.11** The emission line S/N and EW of all emission lines in the catalog.  $H\alpha$  is the two most commonly identified “primary line” and therefore the majority of  $H\alpha$  in the catalog has a  $S/N > 4$ . The majority of the lower-S/N lines were fit as a consequence of the redshift assigned by identification of a primary line.

line center. The initial guess for the FWHM used for all lines is approximated as twice the semi-major axis of the source multiplied by the dispersion in the G141 grism:

$$\text{FWHM}_{\text{init}} = 2 (\text{A\_IMAGE} [\text{pixels}]) (\Delta\lambda_{\text{G141}} [\text{\AA}/\text{pixel}]), \quad (2.5)$$

where the relationship between the FWHM and standard deviation for a Gaussian is  $\text{FWHM} = 2\sqrt{2\ln(2)}\sigma$ . The FWHM for the lines that fall in G102 are corrected by a factor of  $r_{\text{FWHM}} = 0.5$  to account for the smaller dispersion of the blue grism. The source redshift is determined mainly by the center of the profile fit to the  $H\alpha$  line if it is in the grism. At  $z \gtrsim 1.6$ , when  $H\alpha$  has redshifted out of the G141 grism, the  $[\text{O III}]\lambda 5007$  line is the dominant feature in the redshift determination. The redshifts fit to each additional line are allowed to vary up to a maximum of  $\Delta z_{\text{line}} = 0.02$ . Emission line fluxes are calculated as the integrated area of a Gaussian:

$$\sqrt{2\pi} A_{\text{line}} \sigma, \quad (2.6)$$

where the amplitude  $A_{\text{line}}$  is fit for each line,  $\sigma = \text{FWHM}_{\text{fit}}/2.35$ , and  $\text{FWHM}_{\text{fit}}$  is again corrected by  $r_{\text{FWHM}}$  for lines in the blue grism. Finally, we note several emission lines —  $H\alpha$  and  $[\text{N II}]$ , the  $[\text{S II}]\lambda\lambda 6716 + 6731$  doublet, the  $[\text{O II}]\lambda\lambda 3727 + 3730$  doublet, and the  $[\text{O III}]\lambda 4959 + 5007$  doublet — are blended at the resolution of the WFC3 grisms. The fluxes measured for  $H\alpha$  therefore include the contribution from  $[\text{N II}]\lambda 6583$  and  $[\text{N II}]\lambda 6550$ , and those for  $[\text{O II}]$ ,  $[\text{S II}]$ , and  $[\text{O III}]$  each include both doublet lines. The flux of the  $[\text{S III}]\lambda 9532$  line is held to be  $r_{[\text{SIII}]\lambda 9532/\lambda 9069} = 2.48$  times that of the  $[\text{S III}]\lambda 9069$  line.

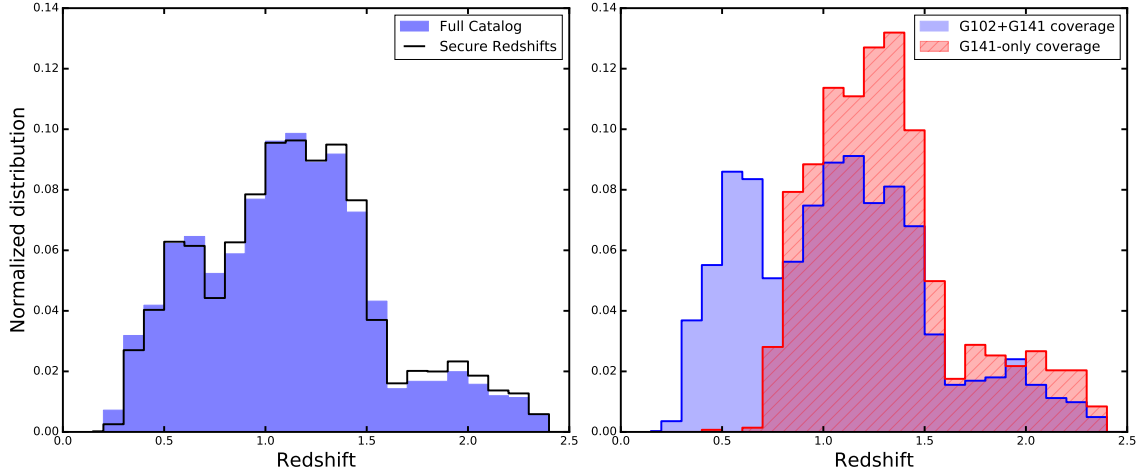


**Figure 2.12** Redshift distribution of sources in the catalog. *Left:* The distribution of all sources in catalog (blue shaded region) and of the sources with secure redshifts as detailed in Section 2.4.3 (black). *Right:* The distribution of sources with secure redshifts is divided into those in fields covered by both grisms (blue histogram) and those in fields covered by only G141 (red histogram).

While inspecting each spectrum, reviewers can change multiple parameters in order to improve the automatic fit to the spectrum. In addition to changing, adding, or subtracting nodes for the continuum fit, reviewers can provide a new redshift guess for the source or, equivalently, a new wavelength guess for the center of a specific line. In the absence of multiple emission lines, single lines are assumed to be  $H\alpha$  unless the clear asymmetry of the  $[O\ III]+H\beta$  line profile is visible. Reviewers can also modify the wavelength where the transition between grisms occurs,  $\lambda_T$ , a change that is most useful when fitting lines in the grism overlap region. Similarly, they can increase or decrease the wavelength cutoff at either end of the spectrum,  $\lambda_{\text{blue}}$  and  $\lambda_{\text{red}}$ , either to fit lines at the grism edges or to remove especially noisy regions of the spectrum at the edges where the sensitivity drops rapidly. Reviewers sometimes provide a new guess for the  $\text{FWHM}_{\text{init}}$ , usually decreasing the default guess for sources where the dispersion axis is along the minor-axis. Finally, reviewers can mask regions of the spectrum that suffer from severe contamination from either zeroth orders or nearby continua, thereby making sure they do not affect the full spectral model.

There are 8025 unique objects in the emission line catalog. Of these, 4963 have secure redshifts, meaning either both reviewers agreed on the redshift or one reviewer found three or more emission lines in the spectrum each with a  $S/N > 3$ . The redshift distribution of sources in the catalog is shown in Figure 2.12. Sources at  $0.23 \lesssim z \lesssim 1.6$  are primarily identified via  $H\alpha$ , while at  $z > 1.6$ , the primary emission line is  $[O\ III]$ . At lower redshifts,

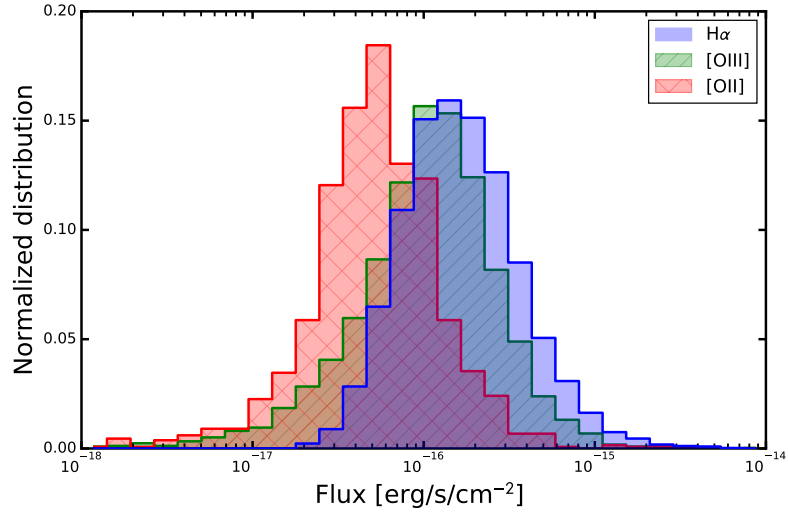


**Figure 2.13** Emission line flux distributions for H $\alpha$  (blue), [O III] (green), and [O II] (red) in the catalog.

there are a small number of objects for which the [S III] $\lambda$ 9606, [S III] $\lambda$ 9532, and He I lines are detected. The dip in the redshift distribution at  $z \sim 0.7$  corresponds to where the H $\alpha$  emission line lies in the transition region between the two grisms, where the sensitivity drops significantly. There is also the possibility, addressed in Chapter 4, that a small subset of objects with a single detected emission line are in fact Ly $\alpha$ -emitting galaxies at much higher redshift ( $z \gtrsim 6$ ).

The distributions of emission line fluxes for the main lines in the catalog are displayed in Figure 2.13. Emission line galaxies are almost always selected for their H $\alpha$  or [O III] emission lines, making these two emission lines the two most common “primary lines” in the catalog. For this reason, the median H $\alpha$  and [O III] fluxes are similar,  $\sim 1 \times 10^{-16}$  erg s $^{-1}$  cm $^{-2}$ . The tail to fainter fluxes in the [O III] distribution comes from sources where H $\alpha$  is the primary line and [O III] is the secondary. Similarly, as [O II] is almost always detected as a secondary line, both the median [O II] flux ( $\sim 5 \times 10^{-17}$  erg s $^{-1}$  cm $^{-2}$ ) and the full distribution of [O II] fluxes are fainter.

#### 2.4.4 Catalog Completeness

The completeness of a survey or catalog is a description of how accurately the detected sample represents the true population in the universe. Understanding a survey’s completeness is necessary before the results can be used to conclude anything about the true underlying

distribution of sources and source properties, such as in the case of the galaxy number densities presented in Chapter 6. A survey such as WISP can suffer from incompleteness for a variety of reasons. Sources may be lost amidst the noise in images if their fluxes are close to the detection limit. Some sources may not be detected, or their emission lines missed in their spectra, because they overlap or are blended with nearby bright objects. The completeness of a survey depends on the specific selection function used to detect sources. In the case of the WISP emission line catalog, the selection function includes the detection of sources in the direct images, the identification of emission line candidates via the detection algorithm, and the acceptance during the visual inspection. We must understand the fraction of sources and emission lines that are not detected through this full process as a function of their properties such as size, shape, and the strength of their emission.

In quantifying the completeness corrections that must be applied to a catalog, we are determining the types and numbers of sources that are missed. We must therefore know the true distribution that we are sampling. We create a simulated catalog of 10000 sources and their spectra, 5000 each for the shallow and deep portions of the WISP Survey. We insert these simulated sources into real WISP images, 25 sources at a time, and run them through the full WISP pipeline and emission line detection software. The creation of the simulated data is described in Chapter 3. In order to save time and the effort required during the visual inspection stage, the reviewers only inspect the spectra of simulated sources that were identified by the line finding algorithm. Yet not all of the emission line candidates were real. Some were noise spikes, contamination, or the result of poorly fit continua. We note, however, that because of this choice we cannot use the simulations to measure the rates of contamination or redshift mis-identification in the catalog.

Of the 10000 input sources, 7721 were recovered by the WISP reduction pipeline, with an equal number recovered in the shallow and deep fields. The majority of the sources that are not recovered in the imaging catalog, and which therefore have no extracted spectra, are faint and/or extended. In Figure 2.14 the semi-major axis sizes are shown as a function of magnitude for the simulated sources that were input and recovered. The distributions of real sources are shown for reference. The sources that are not recovered in imaging mainly have a semi-major axis of  $a \geq 0''.7$  and are fainter than 24.5 magnitudes in the  $H$  band.

For the simulated sources recovered in imaging, we calculate the fraction of these that are recovered by the full line finding process. We find that the completeness depends on source size and shape and emission line EW and S/N. The S/N dependence is essentially a dependence on line flux, but includes the effects of the variable depths of the WISP fields (see Figure 2.5). While we can measure the S/N of observed emission lines, there is no

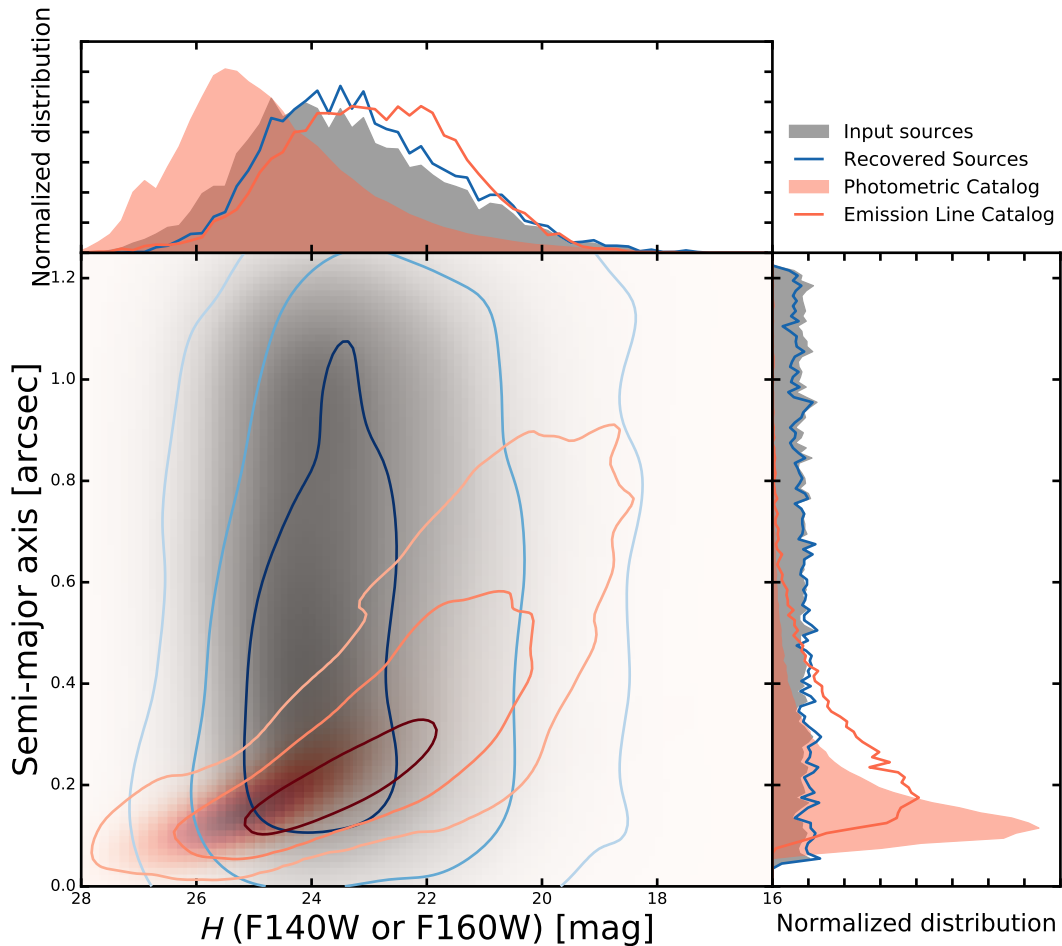


**Figure 2.14** The semi-major axis as a function of the  $H$  band magnitude for all input sources (grey) and those recovered in imaging (blue contours). The real sources from the photometric and emission line catalogs are shown in red. The imaging completeness is a function of the magnitude and size of the sources. The recovery fraction drops for large ( $a \geq 0''.7$ ) and faint ( $H > 24.5$ ) sources.

analogous definition of the input S/N for the simulated lines. The input template spectra do not include noise, and while we have added shot noise to the simulated grism data based on the integration times of the exposures into which they are added, this is not the only source of noise that will affect the flux measurements. The depths reached in each field depend also on the level of the zodiacal background for each pointing. We therefore instead characterize the completeness as a function of emission line “scaled flux”, or the emission line flux (input or recovered) divided by the sensitivity limit of the field at the wavelength

of the line.

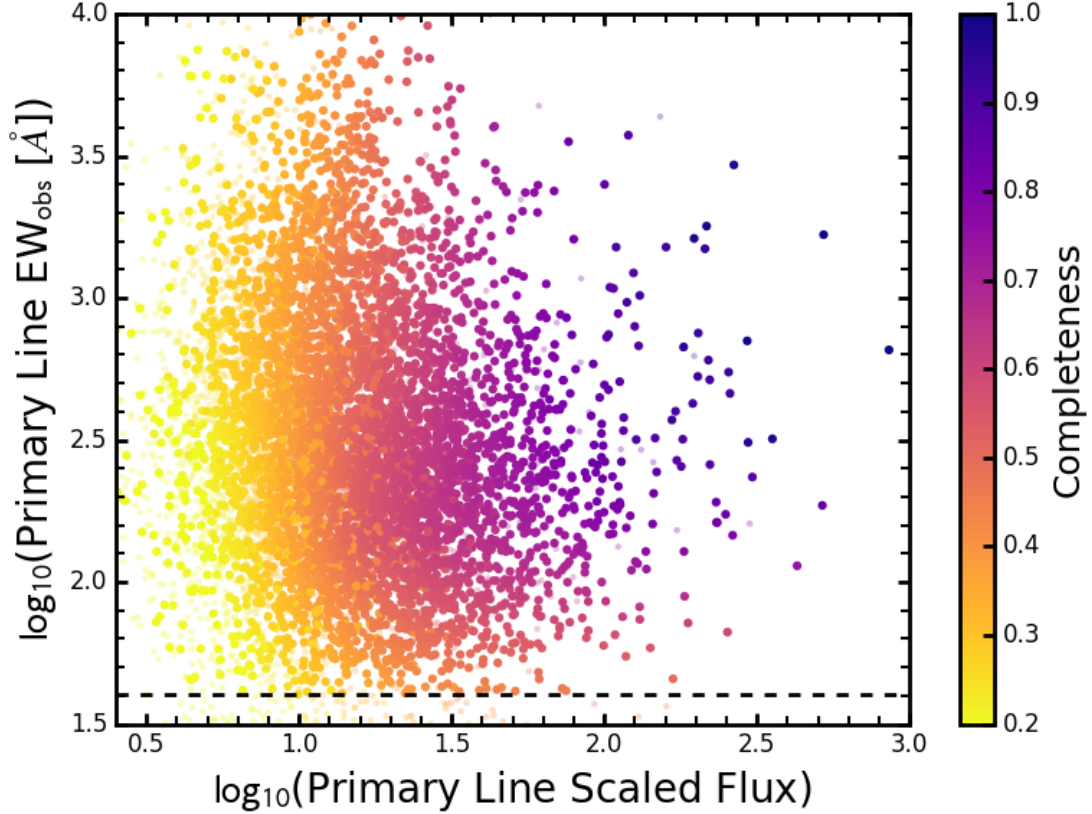


**Figure 2.15** The completeness of the emission line catalog as a function of the scaled flux and observed EW of the strongest line for each source. The dashed horizontal line indicates the EW completeness limit 40 Å. The small, transparent points indicate that lines with  $\text{EW} < 40 \text{ \AA}$  and/or  $S/N < 5$ .

As discussed in Section 2.4.3, a source will enter the catalog because of the detection of the primary lines. We consider only one line per spectrum — both for the input simulated and the output measured spectra — taking the line with the brightest scaled flux as the source’s primary line. As we are not attempting to quantify the rates of redshift mis-identification, we consider a detected emission line recovered regardless of whether the reviewers have properly identified it, i.e., regardless of what redshift is assigned to the object. We recover 868 of the 5000 simulated sources added to deep WISP fields covered by both grisms and 1541 of the 5000 added to shallow, G141-only fields.

The object size and shape will strongly affect the completeness, as large, low surface brightness emission lines may be missed by the peak finder. However, the large sources that suffer from the highest levels of incompleteness, those with  $a \geq 0''.7$ , constitute less than

1% of the total catalog. We simulate sources with a uniform distribution of sizes, but then weight the input sources by the distribution of observed sizes in the emission line catalog. This step both reflects the observed distribution and allows us to consider a two-parameter completeness correction, maintaining sufficient number counts for the completeness analysis without requiring reviewers to visually inspect tens of thousands of sources.

The completeness is calculated in four bins of scaled flux and five bins of EW. The bin edges are determined by the distribution of sources in the real WISP emission line catalog such that there are an approximately equal number of real sources in each bin. The one exception is the bin of lowest EW, which we add in order to probe an area of the parameter space with low completeness ( $EW_{\text{obs}} < 40\text{\AA}$ , see Colbert et al., 2013). We use a radial basis function to approximate the three-dimensional surface formed by the bin centers and recovery fractions calculated in each bin. The resulting completeness corrections calculated for each source in the WISP emission line catalog are shown in Figure 2.15. They are applied according to the scaled flux and observed EW of the strongest line in the spectrum, which is most often  $H\alpha$  or [O III] but is occasionally [O II] when  $H\alpha$  or [O III] are masked out due to overlap with a bright zeroth order or other major contaminant. These completeness corrections are applicable at the source level or for the primary lines for each source. They are not appropriate for secondary lines. As expected, very few low-EW emission lines were recovered in the simulations, making the completeness corrections calculated in bins with  $EW_{\text{obs}} < 40\text{\AA}$  very uncertain. We therefore find that the EW criterion presented in Colbert et al. (2013) applies to the new version of the line finding process as well. We also recommend applying an emission line flux S/N cut at  $S/N > 5$  when using this catalog.

## Chapter 3

# Simulated Data

Simulations are often required in astronomy to determine the effect a set of selection criteria will have on the results. We must understand both how the criteria will sample the true population of sources in the universe and how to optimize the selection of the desired type of source. In this chapter, we create simulated data for two purposes: to characterize the completeness of the WISP Survey presented in Chapter 2, and to optimize the color selection of high-redshift galaxies in Chapter 4. Section 3.1 describes the grism and image simulations used to determine the number and type of sources that are recovered in WISP data. In Section 3.2, we build a catalog of synthetic photometry for galaxies at redshifts  $0.1 \leq z \leq 8.5$  to develop a Lyman break color selection and quantify the expected fraction of lower-redshift contaminants.

### 3.1 Completeness of the WISP Survey

The selection function in slitless spectroscopic data is complex, depending on line signal-to-noise (S/N), equivalent width (EW), galaxy size and concentration, and observed wavelength. Extensive simulations exploring the full parameter space are required. Moreover, the completeness strongly depends on the observing strategy and depth of the datasets. We therefore perform two sets of simulations, one each for the shallow and deeper WISP fields. We add synthetic sources to a selection of real WISP fields and reprocess the fields through the WISP pipeline and line finding procedures presented in the previous chapter. We describe the full process below.

We create 10000 simulated galaxies and divide them equally between the shallow and deep fields. All sources are assigned a spectral template from the models of Bruzual &

**Table 3.1** Input parameters for simulated sources

Parameter	Deep Fields	Shallow Fields
Redshift	$0.3 \leq z \leq 2.3$	$0.7 \leq z \leq 2.3$
Semi-major axis <sup>a</sup>	$0''.05 \leq a \leq 1''.2$	$0''.05 \leq a \leq 1''.2$
Observed H $\alpha$ flux ( $\text{erg s}^{-1} \text{cm}^{-2}$ )	$1 \times 10^{-17} \leq f \leq 1 \times 10^{-16}$	$5 \times 10^{-17} \leq f \leq 1 \times 10^{-15}$
Observed H $\alpha$ EW ( $\text{\AA}$ )	$20 \leq EW_{\text{obs}} \leq 700$	$20 \leq EW_{\text{obs}} \leq 700$
H $\alpha$ /[O III] $\lambda$ 5007 ratio	Gaussian : $\mu = 0, \sigma = 0.2$	Gaussian : $\mu = 0, \sigma = 0.2$

<sup>a</sup>The semi-major axis  $a$  is treated as the profile RMS along the major axis

Charlot (2003) created with a Chabrier (2003) initial mass function, a constant star formation history observed 100 Myr after the beginning of star formation, and one of three metallicities:  $Z/Z_{\odot} = 0.02, 0.2, \text{ or } 1$ . The template spectra are redshifted to the observed frame such that all emission line and continuum fluxes are normalized to the desired observed values. We add the following emission lines to the spectra: [O II] $\lambda$ 3727, [O III] $\lambda$ 4363, H $\beta$ , [O III] $\lambda$ 4959, [O III] $\lambda$ 5007, H $\alpha$ , [S II] $\lambda$ 6716, [S II] $\lambda$ 6730, [S III] $\lambda$ 9069, and [S III] $\lambda$ 9531. Each emission line is modeled as a Gaussian with  $\sigma = 3 \text{ \AA}$ .

The basic question addressed by completeness corrections is whether an input source or emission line is recovered by the reduction and processing performed on real data. As it is not a measure of the rates of source misclassification or redshift misidentification, the inputs need not represent the physical distributions observed in the universe. Unless otherwise noted, we therefore uniformly populate the input parameter space so we can determine the ranges most affected by incompleteness.

For each parameter, we choose input ranges that bracket the observed values. Source redshifts are pulled from a uniform distribution ranging from the redshift at which H $\alpha$  enters the wavelength coverage to that at which [O III] $\lambda$ 5007 leaves.<sup>1</sup> We adopt conservative wavelength cutoffs for each grism to avoid the wavelengths where the sensitivity drops rapidly:  $8500 \leq \lambda_{\text{G102}} \leq 11200 \text{ \AA}$  and  $11200 \leq \lambda_{\text{G141}} \leq 16500 \text{ \AA}$  for the G102 and G141 grisms, respectively. Real emission lines that lie outside of these wavelength ranges are

<sup>1</sup> We do not add any emission lines to the spectrum in the two narrow wavelength ranges that **axSIM** uses for spectral normalization: 10400–10600 (G102) and 15400–15600  $\text{\AA}$  (G141). Emission lines in these ranges would artificially boost the normalization factor thereby significantly reducing the simulated continuum of the spectrum. For more information, see the **axSIM** manual available at [axe.stsci.edu/axesim/](http://axe.stsci.edu/axesim/). There are therefore several narrow redshift ranges that we do not populate with synthetic sources.

flagged in the catalog. These cutoffs correspond to redshift ranges of  $0.3 \leq z \leq 2.3$  for the deep fields with coverage in both grisms and  $0.7 \leq z \leq 2.3$  for the shallow fields. Input  $H\alpha$  fluxes for sources in shallow fields are pulled uniformly from  $5 \times 10^{-17} \leq f_{H\alpha} \leq 1 \times 10^{-15}$   $\text{erg s}^{-1} \text{cm}^{-2}$ , with a lower limit of  $1 \times 10^{-17} \text{ erg s}^{-1} \text{cm}^{-2}$  in the deep fields. We increase the number of faint line fluxes in the deep fields by separating the synthetic sources into two groups: half with fluxes pulled from a uniform distribution with a maximum at  $1 \times 10^{-16} \text{ erg s}^{-1} \text{cm}^{-2}$  and half with fluxes extending up to  $1 \times 10^{-15}$ . Using two upper flux limits allows us to populate the bright end where sources should be easily detected in the deep fields, while ensuring we have an adequate number of faint objects even if the recovered fraction is small. The input observed EW distribution is uniform across the range  $20 \leq \text{EW}_{H\alpha, \text{obs}} \leq 700 \text{ \AA}$ . The flux density in the continuum at the observed wavelength of  $H\alpha$  — i.e., the ratio of input  $H\alpha$  flux and EW — is used to normalize the spectral template to the desired observed units and brightness.

There is a range of observed emission line ratios in the WISP catalog, which we account for in the simulations by varying the input  $H\alpha/[\text{O III}]\lambda 5007$  ratios in the synthetic spectra. Although we are not attempting to quantify the redshift misidentification in the catalog, simulating emission lines with a variety of flux ratios is necessary to include any biases related to single versus multi-line emitters. For example, reviewers are more likely to identify low S/N lines if there are additional emission lines visible in the spectrum to confirm the source’s redshift. Input  $\log_{10}(H\alpha/[\text{O III}]\lambda 5007)$  ratios are drawn from a Gaussian distribution centered at  $\mu = 0$  with  $\sigma = 0.2$ , matching the observed distribution in the catalog but with a slightly larger full width at half maximum. The intrinsic  $H\alpha/H\beta$  ratio for case B recombination is adopted for all sources, 2.86 (Osterbrock, 1989). For the remaining emission lines, we adopt the ratios from Anders & Fritze-v. Alvensleben (2003) with respect to  $[\text{O III}]\lambda 5007$  for each metallicity assuming an electron density of  $n_e = 100 \text{ cm}^{-3}$  and electron temperature of  $T_e = 10000 \text{ K}$ . We do not add the effects of dust to the spectra, but instead rely on the range of line ratios to cover observed values. We note that the adopted case B Balmer decrement,  $H\alpha/H\beta$ , is the only line ratio that remains unchanged and therefore always exhibits the value expected for dust-free galaxies. However, we remind the reader that as we are not trying to replicate reality, this choice will not affect the resulting completeness calculations.

The completeness of sources in the WISP catalog depends strongly on object size and shape. Object size first affects the completeness in imaging, where the low surface brightness of faint, extended objects may fall below the adopted *Source Extractor* detection thresholds while the higher surface brightnesses of more compact sources are detected. In addition,

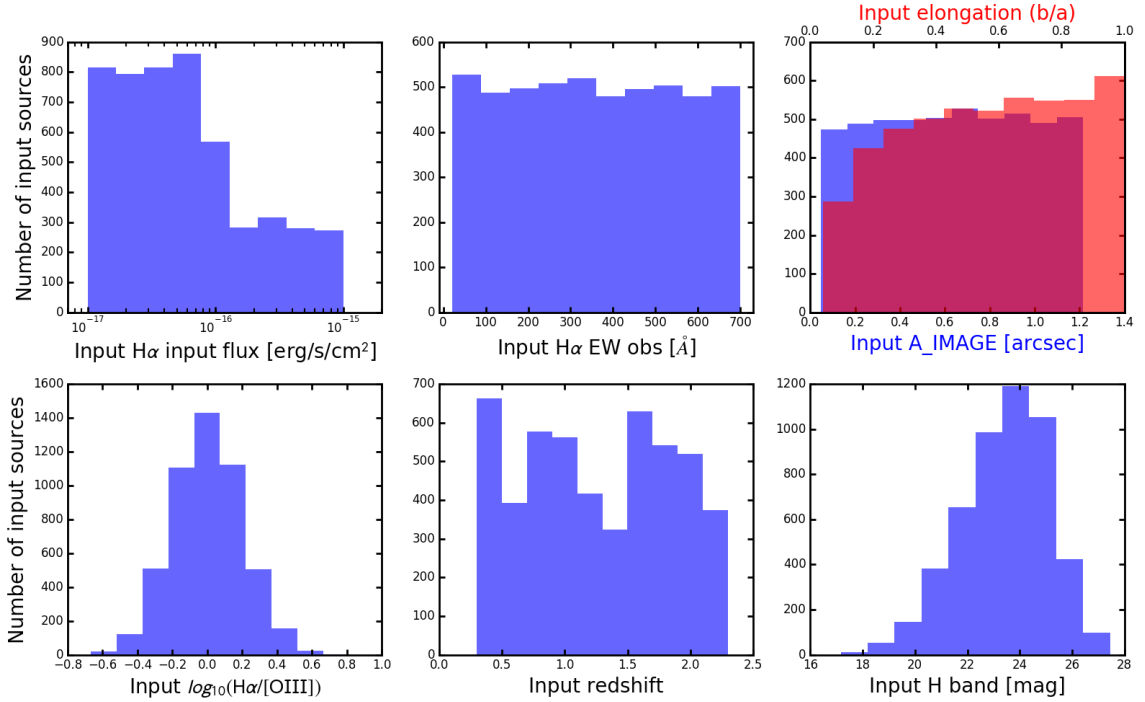


**Figure 3.1** Input parameter distributions for deep fields, all of which are pulled from uniform distributions except the H $\alpha$ /[O III] $\lambda$ 5007 ratios. Half of the H $\alpha$  fluxes are concentrated below  $1 \times 10^{-16}$  erg s $^{-1}$  cm $^{-2}$ , to ensure we recover enough faint emission lines for a reliable completeness calculation. The apparent dips in the redshift distribution are from narrow gaps related to the spectral normalization. See the text for details. The input  $H$  band magnitudes are not assigned to the sources, but instead are the result of the flux normalization of the template spectral continua and depend on the H $\alpha$  fluxes and EWs of each source.

the pipeline removes the most extremely elongated detected sources from the catalog in an attempt to remove artifacts such as diffraction spikes and persistence from bright first orders. Since emission lines observed via slitless spectroscopy are essentially images of the sources at the given wavelengths, the source shape and size will also affect the completeness of the line finding procedure. Extended sources with a low EW will be missed by the peak finder, and reviewers are more consistent with their treatment of compact, high-S/N emission lines. We therefore assign each object a profile RMS along the major (minor) axis pulled from a uniform distribution in the range  $0''.05 \leq a \leq 1''.2$  ( $0''.05 \leq b \leq a$ ), again matching the range but not the shape of the observed distribution in the catalog. The input parameter distributions are shown in Figure 3.1 and summarized in Table 3.1.

We add 25 simulated sources at random locations to the raw images for a set of WISP fields, using the aXeSIM (Kümmel et al., 2007) software package to create the synthetic direct and grism images of each source. These fields are then fully processed as real data,

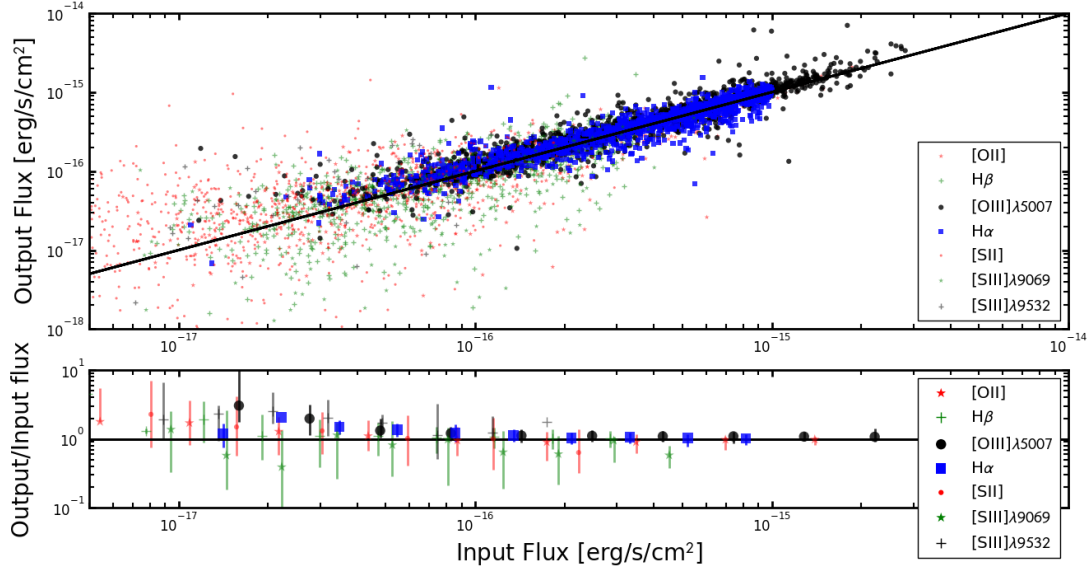


**Figure 3.2** A comparison between the input and measured (or “output”) emission line fluxes for the simulated sources described in Section 3.1. In the top panel, the output flux of all recovered emission lines is plotted as a function of input flux, where  $H\alpha$  and [O III] $\lambda$ 5007 are emphasized because they are the most common primary lines. In the bottom panel, we show the median flux ratio for each line in bins of input flux with  $1\sigma$  error bars. There is good flux agreement for  $H\alpha$  and [O III] $\lambda$ 5007. Almost all of the other lines are fit as secondary lines, and their fainter fluxes and lower S/N lead to the increased scatter.

including the visual inspection by two reviewers. As mentioned in Chapter 2, in order to save on the time and effort required for this step, the reviewers only inspect the spectra of simulated sources that were identified by the line finding algorithm. This is not to say that all emission line candidates were real. Some were noise spikes, contamination, or the result of poorly fit continua. However, it does mean we cannot use the simulations to measure the rates of contamination or redshift mis-identification in the catalog.

The WISP completeness calculations, described in Section 2.4.4, involve determining the fraction of sources that have been recovered in bins of source size and emission line flux and EW. After the simulated sources are fully processed through the WISP software, we compare all properties of the recovered sources with their input values. This step is necessary to confirm that the recovered sources are counted in the proper bins, i.e., that the parameter values are not systematically different due to the simulation and reduction processes. In Figure 3.2, we compare the input emission line fluxes with their output values measured during the line finding process. The input and output fluxes for  $H\alpha$  and [O III] $\lambda$ 5007 are clearly correlated down to  $f \sim 7 \times 10^{-17}$   $\text{erg s}^{-1} \text{cm}^{-2}$ . At fainter fluxes, there is a

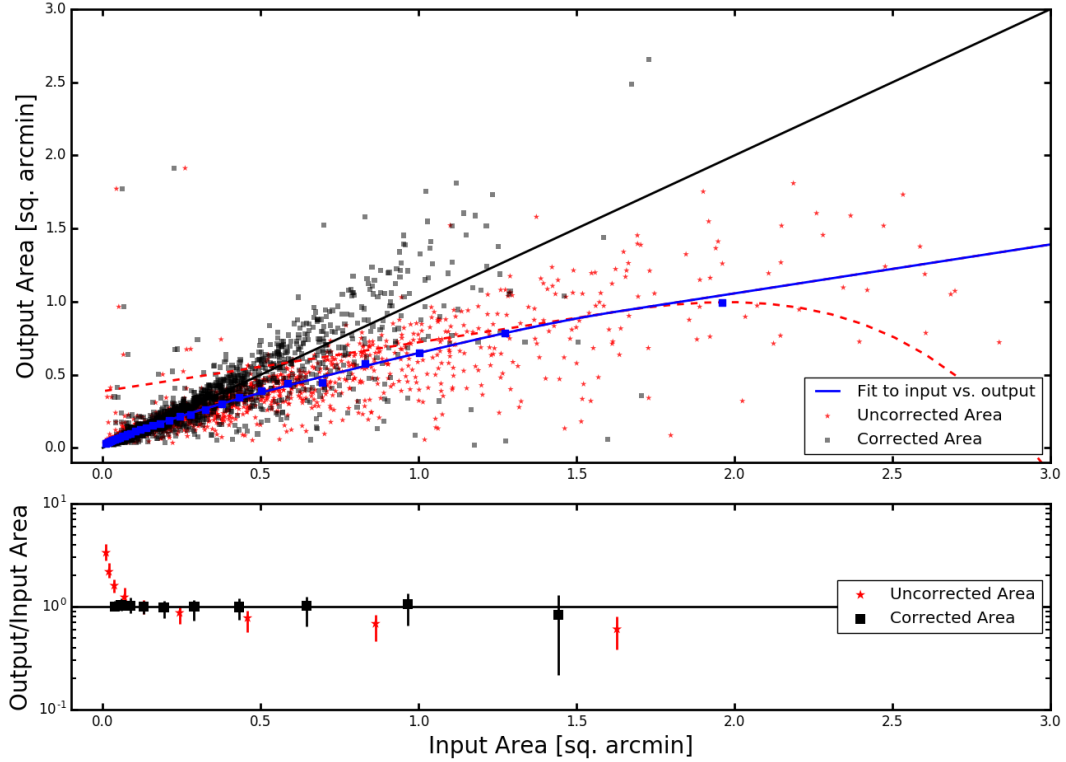


**Figure 3.3** A comparison between the input and output source areas (red stars) and the scaled or “corrected” sizes (black squares). The dependence between input and output sizes is fit with a fourth order polynomial that switches to a line at an area  $\gtrsim 1.6 \text{ arcsec}^2$ . The model (blue curve) is fit to the median values in the bins identified by blue squares. The dashed red curve shows the extensions of the linear fit (polynomial fit) below (above)  $1.6 \text{ arcsec}^2$ . As in Figure 3.2, the median size ratio is shown in bins of input area in the bottom panel, where the dependence has been successfully removed in the corrected points. The correction is performed individually on the semi-major and minor axes sizes, rather than on the source area as is shown here.

slight trend toward brighter output fluxes, which may be caused by spectral contamination. Overlapping spectra can boost a source’s measured emission line flux, and we expect the severity of this contamination to increase with decreasing line flux. Yet there are far too few recovered  $\text{H}\alpha$  or  $[\text{O III}]$  lines with fluxes  $< 7 \times 10^{-17} \text{ erg s}^{-1} \text{ cm}^{-2}$  to properly evaluate the trend. The other emission lines are almost always fit as secondary lines and will therefore be fainter and at a lower S/N than the primary lines, explaining the significant increase in scatter in Figure 3.2. There is a similarly good agreement between input and output  $\text{H}\alpha$  and  $[\text{O III}]\lambda 5007$  EWs.

A comparison of the source sizes, however, shows that the inputs are systematically

larger than the outputs. This effect is not surprising, since the flux in the wings of the simulated Gaussian sources can fall below the *Source Extractor* detection limit. The extracted ‘footprints’ of the sources will then be smaller than what was simulated. We must understand the relationship between the input and output sizes in order to properly determine the number of sources that are recovered as a function of size. We model this relationship with a combination of a fourth order polynomial for semi-major and minor axes  $\lesssim 0''.6$  and a linear fit for larger sizes. An example model fit to the source area is displayed in Figure 3.3, though we actually perform the fit for  $a$  and  $b$  individually. The WISP survey completeness will be applied to sources according to their observed fluxes, EWs, and sizes, as their intrinsic values are unknown. The completeness must therefore be calculated as a function of the output values measured for the simulated sources rather than the input values. We use the models to scale the input  $a$  and  $b$  to their measured values. This step is necessary to ensure that input sources that are not recovered are counted in the correct bins. See Section 6.3.2 for a discussion of the effect the object size has on the measured line fluxes.

## 3.2 Simulated template library

For the purposes of deriving the optimal color selection for  $z \geq 6$  galaxies that will be used in Chapter 4, we generate a catalog of 20000 synthetic sources based on the models of Bruzual & Charlot (2003). Our goal is twofold: to derive criteria that will select real high-redshift galaxies, and to properly quantify the contamination we can expect from lower-redshift galaxies. The synthetic sources described in this section therefore cover a much larger redshift range than those in Section 3.1, and their luminosities are chosen to replicate reality as closely as possible. The catalog will be used to determine the broadband colors of galaxies with a variety of properties, and so we will be calculating the mean flux density of each template spectrum in the four WFC3 filters used in Chapter 4. Strong emission lines that fall within a filter passband can contribute significantly to the photometry, as much as 0.75 magnitudes or more, and can therefore have a large impact on broadband colors (e.g., Atek et al., 2011). In order to account for this effect in our synthetic catalog, we add emission lines to exactly half of the 20000 templates. In what follows, we describe the templates and their properties in more detail. Unless otherwise noted, all properties — redshift, metallicity, star formation history, dust content, etc. — are drawn randomly from uniform distributions.

The simulated galaxies’ redshifts range from  $0.1 \leq z \leq 8.5$ . The luminosities of the

**Table 3.2** Luminosity Functions used in synthetic catalog

Redshift	$M_{UV}^*$ <sup>a</sup>	$\phi^*(10^{-3} \text{ Mpc}^{-3})$	$\alpha$	Reference
$0.1 \leq z < 0.6$	$-21.03 \pm 0.25$	$5.0 \pm 0.6$	$-1.26 \pm 0.15$	Scarlata et al. (2007)
$0.6 \leq z < 1.5$	$-21.24 \pm 0.12$	$4.9 \pm 0.3$	$-1.22 \pm 0.10$	Scarlata et al. (2007) <sup>b</sup>
$1.5 \leq z < 2.7$	$-20.01 \pm 0.24$	$2.54 \pm 0.15$	$-1.74 \pm 0.08$	Alavi et al. (2014)
$2.7 \leq z < 3.4$	$-20.97 \pm 0.14$	$1.71 \pm 0.53$	$-1.73 \pm 0.13$	Reddy & Steidel (2009)
$3.4 \leq z < 4.5$	$-20.88 \pm 0.08$	$1.97^{+0.34}_{-0.29}$	$-1.64 \pm 0.04$	Bouwens et al. (2015)
$4.5 \leq z < 5.5$	$-21.17 \pm 0.12$	$0.74^{+0.18}_{-0.14}$	$-1.76 \pm 0.05$	Bouwens et al. (2015)
$5.5 \leq z < 6.5$	$-20.94 \pm 0.20$	$0.5^{+0.22}_{-0.16}$	$-1.87 \pm 0.10$	Bouwens et al. (2015)
$6.5 \leq z < 7.5$	$-20.77 \pm 0.28$	$0.34^{+0.24}_{-0.14}$	$-2.03 \pm 0.13$	Bouwens et al. (2015)
$7.5 \leq z \leq 8.5$	$-20.21 \pm 0.33$	$0.45^{+0.42}_{-0.21}$	$-1.83 \pm 0.25$	Bouwens et al. (2015)

<sup>a</sup>Values of  $M_{UV}^*$  are derived at the rest frame wavelengths of the  $B$ -band 4420Å for  $0.1 \leq z < 1.5$ , 1500Å for  $1.5 \leq z < 2.7$ , 1700Å for  $2.7 \leq z < 3.4$ , and 1600Å for  $3.4 \leq z \leq 8.5$ .

<sup>b</sup>LF is calculated for  $0.6 \leq z \leq 0.8$  but here has been extended down to  $z = 0.1$  and up to  $z = 1.5$ .

synthetic sources in each redshift bin are distributed according to the luminosity function (LF) at that redshift. To achieve this, in each of eight redshift bins, we integrate the appropriate LF down to a luminosity that corresponds to the  $1\sigma$  magnitude limit of our survey and assign each source a luminosity extracted from this cumulative LF. Table 3.2 lists the LFs used in each redshift bin.

Each source is then assigned a spectral template extracted from a library of Bruzual & Charlot (2003) templates. We allow for either Chabrier (2003) or Salpeter (1955) initial mass functions, composite stellar populations of constant metallicity ( $Z/Z_\odot = 0.005, 0.02, 0.2, 0.4, \text{ or } 1$ ), and exponentially-declining star formation histories with characteristic timescales of  $\tau = 0.01, 0.5, \text{ and } 5.0$  Gyr. The timescales considered here approach those of models with, at either extreme, a constant star formation history (large  $\tau = 5$ ) and a single burst of star formation (small  $\tau$ ). We restrict the template metallicity with redshift such that the maximum possible metallicity (in units of  $Z_\odot$ ) is  $Z \leq 0.4$  at  $1 < z \leq 2$ ,  $Z \leq 0.2$  at  $2 < z \leq 3$ , and  $Z \leq 0.02$  for  $z > 3$ . The full metallicity range is available for synthetic galaxies at  $z \leq 1$ . The spectra are extracted from these templates in logarithmic time steps such that the spectral evolution is better sampled for younger ages. Sources are then randomly assigned an age ranging from 10 Myr to the age of the universe at the given redshift.

When adding emission lines to the templates, the line luminosity for  $H\beta$  is determined from the flux of hydrogen-ionizing photons output by the Bruzual & Charlot (2003) models.

Emission line coefficients for  $H\alpha$  and  $Ly\alpha$  are from Table 1 of Schaerer (2003). We assume a  $Ly\alpha$  escape fraction of  $f_{\text{esc}}^{Ly\alpha} = 1$ . The ratios of other rest-frame optical emission lines, relative to  $H\beta$ , depend on each template’s metallicity, the electron temperature and density. We assume  $n_e = 100 \text{ cm}^{-3}$  and  $T_e = 10000 \text{ K}$  and take the resulting ratios from Anders & Fritze-v. Alvensleben (2003).

These templates of stellar and nebular emission are next reddened using two distinct dust geometries (see Scarlata et al., 2009): (1) a uniform slab of dust in front of the source, and (2) a clumpy slab in front of an extended source. In the first case, extinction follows the classical  $I_o/I_i = e^{-\tau_\lambda}$ , where  $I_o$  and  $I_i$  are the observed and intrinsic intensities, respectively, and  $\tau_\lambda = \kappa_\lambda E(B-V)/1.086$ . We use the Calzetti et al. (2000) reddening curve for  $\kappa_\lambda$ , with color excess values in the stellar continuum drawn randomly from a uniform distribution between  $0 < E_s(B-V) < 1$ . For the second model, we assume all clumps have the same optical depths,  $\tau_{c,\lambda}$ , and they are distributed according to a Poisson distribution with mean equal to the average number of clumps along the line of sight,  $N$ . The number of clumps is randomly drawn from a uniform distribution between  $1 \leq N \leq 10$ . We assign each clump an optical depth in the  $V$  band such that  $0.1 \leq \tau_{c,V} \leq 10$ . Each clump acts as a uniform dust screen and follows the Cardelli et al. (1989) extinction law. The extinction from the interstellar medium (ISM) extinction then goes as  $I_o/I_i = \exp[-N(1 - e^{-\tau_{c,\lambda}})]$  (Natta & Panagia, 1984). We randomly assign one of the two dust geometries to each template. Assuming the dust content of the universe decreases exponentially with increasing redshift, we restrict the maximum available extinction  $E_{B-V}$  (either in the uniform ISM or in the clumps) following Hayes et al. (2011), where  $E_{B-V}(z) = C_{EBV} \exp(z/z_{EBV})$ ,  $C_{EBV} = 0.386$  and  $z_{EBV} = 3.42$ .

The reddened spectra are then attenuated by the neutral hydrogen in the intergalactic medium (IGM) using the recipe from Inoue et al. (2014), which is an updated version of the Madau (1995) attenuation model. Inoue et al. (2014) include absorption from the full Lyman series, Lyman limit systems and damped  $Ly\alpha$  systems, as well as a more accurate representation of absorption in the Lyman continuum. In Figure 3.4, we show the result of each step on an example template spectrum, including both extinction models for comparison.

For each simulated galaxy, we compute the  $V_{606}$ ,  $I_{814}$ ,  $J_{110}$ , and  $H_{160}$  magnitudes. Finally, we add errors to the synthetic magnitudes to account for the photometric uncertainties in our observed catalog. Photometric scatter is one of the dominant causes of contamination in Lyman break samples (e.g., Stanway et al., 2008). It operates in both directions, scattering galaxies both into and out of the selection window, thus affecting both the contamination

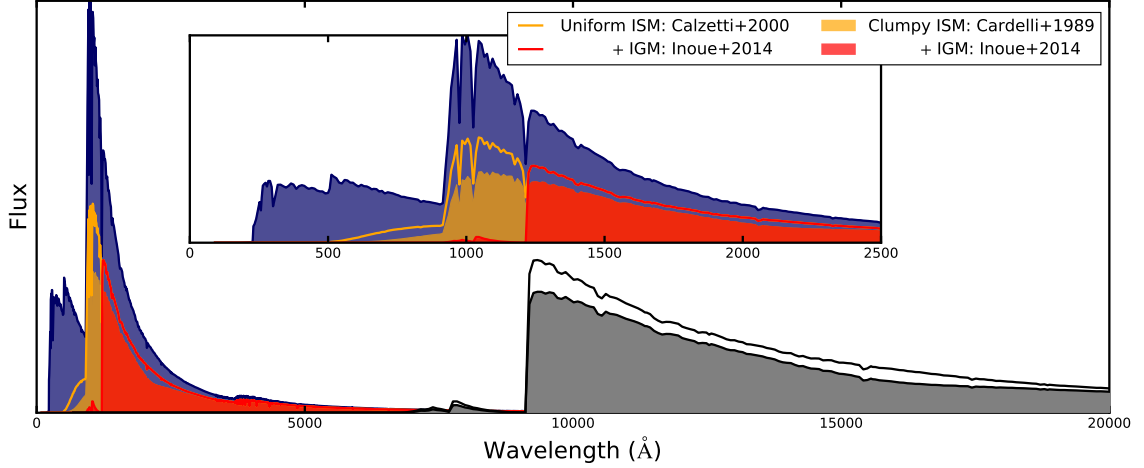


**Figure 3.4** An example of a Bruzual & Charlot (2003) template spectrum (blue) after applying ISM reddening (orange) and IGM attenuation (red), and redshifting to  $z = 6.5$  (black). The template uses a Chabrier (2003) IMF, a metallicity of  $Z = 0.005Z_{\odot}$ , and an exponentially declining star formation history. The spectrum represented by the orange curve has been extinguished using the Calzetti et al. (2000) reddening curve with  $E(B-V) = 0.05$ . The extinction applied to the filled orange spectrum is that of a clumpy medium (Natta & Panagia, 1984) with an average of 5 clumps along the line of sight, each of which has  $\tau_{c,V} = 0.05$  with Cardelli et al. (1989) reddening. The IGM attenuation follows the prescription in Inoue et al. (2014) for a source at  $z = 6.5$ .

and recovery fractions.

We add photometric scatter to our synthetic catalog in the following way. From the WISP photometric catalog, we determine the average uncertainty as a function of magnitude for each filter. The magnitudes of the synthetic sources are then allowed to vary according to Gaussian distributions with standard deviations set by the median uncertainty in the corresponding magnitude bins. We create 10 such realizations of the synthetic photometry resulting in a final catalog of  $2 \times 10^5$  sources. This catalog is used in Section 4.3.1 to choose the selection criteria for  $z > 6$  Ly $\alpha$ -emitting galaxies, and also to characterize possible sources of contamination in the sample in Section 4.4.

## Chapter 4

# A High Space Density of Luminous Ly $\alpha$ Emitters at $z \sim 6.5$

*This chapter is largely taken from a paper by the same title published in the Astrophysical Journal with the following bibliographic reference: Bagley et al. (2017) — Bagley, M. B., Scarlata, C., Henry, A., et al., 2017, ApJ, 837, 11.*

### 4.1 Introduction

The dark ages that followed recombination ended with the appearance of metal-free stars and the subsequent formation of numerous low-mass, metal-poor galaxies. The collective ionizing background from these newly-forming galaxies is thought to be responsible for the reionization of the diffuse hydrogen in the intergalactic medium (IGM) between  $6.5 \lesssim z \lesssim 10$  (e.g., Fan et al., 2006; Robertson & Ellis, 2012; Madau & Haardt, 2015; Planck Collaboration et al., 2016b). The progression of the reionization history depends on the nature of these first sources – their number densities, luminosities, clustering, and production rates of ionizing photons – which is currently the subject of considerable observational and theoretical efforts.

The evolving neutral hydrogen fraction in the IGM can be constrained using observations of the Ly $\alpha$  output from galaxies around the end of reionization. Ly $\alpha$  photons are produced by a resonant transition and so are sensitive to the presence of even a small fraction of neutral hydrogen. In a partially neutral IGM, the Ly $\alpha$  photons are resonantly scattered out of the line of an Earth observer. Therefore, a drop in both the observed number density of Ly $\alpha$  emitters and in the observed fraction of Ly $\alpha$  emitters among star-forming galaxies is expected at  $z \gtrsim 6$  due to the increase in neutral hydrogen in the IGM.

Observational studies comparing the  $z \simeq 5.7$ ,  $z \simeq 6.5$ , and  $z \geq 7$  Ly $\alpha$  luminosity functions (LFs) have so far reached inconsistent conclusions. Some find a deficit with increasing redshift in the number density of Ly $\alpha$  emitters (LAEs) either at the bright end of the LF (e.g., Kashikawa et al., 2011), the faint end of the LF (e.g., Matthee et al., 2014, 2015), or at all luminosities (Konno et al., 2014). The differences in completeness associated with each survey could contribute to this disagreement. For example, the large discrepancy between the faint ends of the Ly $\alpha$  LFs of Kashikawa et al. (2011) and Hu et al. (2010) is likely due to the former’s deeper spectroscopic observations. Cosmic variance may also contribute to the discrepancies at the bright end. Recent and ongoing narrowband surveys are covering much larger areas than previous surveys. For example, Matthee et al. (2015) and Santos et al. (2016) present the results of their 7 sq. degree survey while Hu et al. (2016) report on findings in 3 sq. degrees of their 24 sq. degree survey. On the other hand, Hu et al. (2010) covered just 1.16 sq. degrees, and Kashikawa et al. (2011) went very deep in a single pointing of  $\sim 0.25$  sq. degrees. It is possible that the older surveys, more susceptible to cosmic variance due to their narrow redshift windows, did not cover volumes large enough to probe the true variation in the number densities of these rare, brightest objects.

While observational issues do exist, the observed disagreement could also be caused by real astrophysical phenomena. Reionization is not expected to proceed at the same rate on all scales (e.g., Mesinger & Furlanetto, 2008; Zheng et al., 2011; Treu et al., 2012), but rather to be a patchy and inhomogeneous process depending on the luminosity of ionizing sources and the galaxy clustering properties. The effect of both luminosity and clustering is to produce large ionized bubbles (on scales of a few megaparsecs, depending on the exact luminosity) that allow Ly $\alpha$  photons to redshift out of resonance before encountering the IGM. Therefore, we may expect the most luminous LAEs to be visible out to earlier times. Conversely, it will take the fainter galaxies longer to ionize bubbles large enough to allow Ly $\alpha$  photons to escape (e.g., Matthee et al., 2015; Ono et al., 2012; Stark et al., 2016). Additionally, around luminous sources and/or highly clustered regions, we may expect an enhancement in the number density of galaxies showing Ly $\alpha$  in emission (Castellano et al., 2016).

Small sample sizes and contamination by lower-redshift interlopers are both major concerns in high-redshift LAE searches. Tilvi et al. (2010) and Krug et al. (2012) claim to find evidence that the number density of LAEs either does not evolve or slightly increases from  $z = 5.7 - 7.7$ . These results were likely due to contamination. Indeed, the follow-up observations of Faisst et al. (2014) find no Ly $\alpha$  emission in the spectrum of either LAE candidate

from Krug et al. (2012). Due to the challenges of performing ground-based narrowband searches at  $z > 7$ , the majority of candidates targeted for spectroscopic confirmation are identified from broadband colors indicative of a Lyman break (e.g., Vanzella et al., 2011; Pentericci et al., 2011, 2014; Ono et al., 2012; Schenker et al., 2012). Such “dropout” samples, however, can suffer from large contamination fractions, especially for fainter galaxies (e.g., Dickinson et al., 2004; Stanway et al., 2008). Moreover, as surveys for ultra-faint Ly $\alpha$  emitters have shown (Dressler et al., 2011, 2015; Henry et al., 2012), continuum-based searches may miss significant fractions of faint galaxies that are important for reionizing the IGM.

Spectroscopic surveys with *HST*’s WFC3/IR grism are well suited to address the still-uncertain evolution of the bright end of the Ly $\alpha$  LF at  $z \sim 6 - 7$ . The WFC3 Infrared Spectroscopic Parallel (WISP, PI: M. Malkam, Atek et al. 2010) Survey covers more than 1700 sq. arcmin in 386 uncorrelated fields. Here we present the results of a search for  $z \sim 6 - 7$  galaxies in the 48 deepest WISP fields available, covering  $\sim 160$  sq. arcmin. We compensate for the small area by covering a broad redshift range ( $6 \lesssim z \lesssim 7.6$ ) enabling us to probe a volume of  $8 \times 10^5$  Mpc<sup>3</sup> at  $z > 6$ . We are also able to rule out almost all lower-redshift contaminants thanks to the broad spectral coverage of the WISP survey.

This chapter is organized as follows: in Section 4.2 we describe our WISP observations and data reduction. We present the selection of  $z > 6$  LAEs in Section 4.3 and the expected contamination fraction in Section 4.4. We present our results in Section 4.5 and discuss the implications in Section 4.6.

## 4.2 Observations - The WISP Survey

The WISP Survey (PI: M. Malkam, Atek et al., 2010) is described in detail in Chapter 2. While the full survey includes 483 fields covering more than 2000 arcmin<sup>2</sup>, in this chapter we consider a subset of the deep survey consisting of the first 48 deep fields that were fully reduced at the time of writing. They comprise about one third of the full set of deep WISP fields with UVIS coverage. All these fields were observed with F110W and F160W, hereafter  $J_{110}$  and  $H_{160}$ , respectively. Of these 48 fields, 21 were observed with both F606W and F814W ( $V_{606}$  and  $I_{814}$ ), and the remaining 27 have only  $I_{814}$  imaging. The images reach  $5\sigma$  depths in the IR of  $m_{AB} \sim 26 - 26.8$  and UVIS  $1\sigma$  depths of  $m_{AB} \geq 27$ . The exposure times and flux limits for the 48 fields are listed in Table 4.1.

**Table 4.1** WISP Fields used in this work, exposure times and depths

Field	$t_{G102}$ (sec)	G102 <sup>a</sup> ( $\text{erg s}^{-1} \text{cm}^{-2}$ )	$t_{V606}$ (sec)	$V_{606}$ <sup>b</sup> (mag)	$t_{I814}$ (sec)	$I_{814}$ (mag)	$t_{J110}$ (sec)	$J_{110}$ (mag)	$t_{H160}$ (sec)	$H_{160}$ (mag)
96	28079	$5.69 \times 10^{-18}$	1500	28.40	1500	27.65	4294	27.39	1765	26.49
256	4218	$6.08 \times 10^{-17}$	...	...	1500	27.14	1015	26.20	406	25.34
257	8229	$3.30 \times 10^{-17}$	900	28.11	1500	27.67	1818	26.86	759	25.84
258	6021	$1.45 \times 10^{-17}$	...	...	1500	27.73	1215	26.08	609	25.09
260	7526	$8.82 \times 10^{-18}$	...	...	1500	27.70	1365	26.66	609	25.65
261	6021	$1.16 \times 10^{-17}$	...	...	1500	27.55	1215	26.28	609	25.57
271	4015	$1.92 \times 10^{-17}$	...	...	1500	27.36	809	26.31	406	25.31
288	4218	$1.44 \times 10^{-17}$	...	...	1500	27.62	1015	26.48	406	25.43
294	4218	$1.36 \times 10^{-17}$	...	...	1500	27.62	1015	26.52	406	25.44
295	4318	$1.29 \times 10^{-17}$	...	...	1500	27.57	1015	26.45	406	25.41
295	4318	$1.29 \times 10^{-17}$	...	...	1500	27.57	1015	26.45	406	25.41
296	13544	$8.82 \times 10^{-18}$	1500	27.85	2500	27.52	2376	26.60	1015	25.90
297	4518	$1.20 \times 10^{-17}$	...	...	1500	27.53	1015	26.24	406	25.31
298	11835	$1.00 \times 10^{-17}$	1200	28.06	2000	27.55	2407	26.16	1015	25.60
300	6921	$1.16 \times 10^{-17}$	...	...	1500	27.54	1262	26.11	609	25.61
302	7023	$1.40 \times 10^{-17}$	900	27.86	1500	27.49	1412	26.69	812	25.73
303	7623	$8.09 \times 10^{-18}$	900	28.16	1500	27.35	1315	26.28	609	25.62
304	13038	$4.22 \times 10^{-17}$	1500	28.32	2500	27.94	2960	26.95	1015	25.95
307	7323	$1.08 \times 10^{-17}$	900	27.81	1500	27.52	1215	26.61	812	25.72
308	4518	$1.85 \times 10^{-17}$	...	...	1500	27.67	1015	26.53	406	25.48
309	5315	$1.29 \times 10^{-17}$	...	...	1500	27.53	1015	26.52	456	25.60
311	7821	$8.82 \times 10^{-18}$	...	...	1500	27.74	1468	26.42	609	25.46
312	5818	$1.10 \times 10^{-17}$	...	...	1500	27.56	1165	26.81	609	25.76
313	7226	$1.49 \times 10^{-17}$	...	...	1500	27.55	1315	26.82	609	25.68
314	16147	$2.84 \times 10^{-17}$	1500	28.28	2500	27.81	2901	26.40	1543	26.07
315	6318	$1.35 \times 10^{-17}$	...	...	1500	27.60	1218	26.78	609	25.76
317	4518	$2.34 \times 10^{-17}$	...	...	1500	27.48	1015	26.40	406	25.45
319	8326	$1.40 \times 10^{-17}$	2200	28.31	2200	27.76	1621	26.61	609	25.69
320	12732	$1.24 \times 10^{-17}$	2400	28.23	2400	27.62	2782	26.73	1065	25.88
321	12035	$9.65 \times 10^{-18}$	2200	28.46	2200	27.80	2154	26.85	887	25.94
324	12135	$9.78 \times 10^{-18}$	2200	28.14	2200	27.54	2204	26.41	912	25.69
325	9223	$3.03 \times 10^{-17}$	2400	28.21	2400	27.51	2023	26.78	762	25.78
326	11535	$1.27 \times 10^{-17}$	1500	28.09	1800	27.55	2126	26.65	859	25.94
333	15941	$9.26 \times 10^{-18}$	2200	27.24	2200	27.64	2866	26.79	1193	26.05
340	7421	$8.30 \times 10^{-18}$	2400	28.49	2400	27.81	1721	26.55	709	25.88

Table 4.1

Field	$t_{G102}$ (sec)	G102 <sup>a</sup> (erg s <sup>-1</sup> cm <sup>-2</sup> )	$t_{V606}$ (sec)	$V_{606}$ <sup>b</sup> (mag)	$t_{I814}$ (sec)	$I_{814}$ (mag)	$t_{J110}$ (sec)	$J_{110}$ (mag)	$t_{H160}$ (sec)	$H_{160}$ (mag)
341	5921	$1.17 \times 10^{-17}$	...	...	1500	27.63	1215	26.01	609	25.55
345	8021	$9.03 \times 10^{-18}$	2400	28.66	2400	27.78	1421	26.65	609	25.72
347	6015	$1.51 \times 10^{-17}$	2400	27.99	2400	27.67	1771	26.39	1012	25.83
348	6615	$1.13 \times 10^{-17}$	...	...	2000	27.74	1165	26.55	609	25.63
349	5412	$9.56 \times 10^{-18}$	...	...	2400	27.76	962	26.33	609	25.68
352	6721	$1.19 \times 10^{-17}$	...	...	2000	27.49	1671	26.64	684	25.74
357	9223	$1.11 \times 10^{-17}$	2400	28.44	2400	27.80	2023	26.48	812	25.75
360	7721	$1.08 \times 10^{-17}$	...	...	2400	27.76	1721	26.40	759	25.79
364	6921	$1.05 \times 10^{-17}$	...	...	2200	27.85	1318	26.77	609	25.68
368	6518	$1.38 \times 10^{-17}$	...	...	2400	27.78	1696	26.80	734	25.92
369	9629	$1.10 \times 10^{-17}$	2200	28.51	2200	27.77	2276	26.73	759	25.86
371	6618	$1.18 \times 10^{-17}$	...	...	2600	27.82	1218	26.61	534	25.47
379	2809	$1.13 \times 10^{-17}$	...	...	2400	27.97	1721	26.69	759	25.94
385	2406	$1.22 \times 10^{-17}$	...	...	1996	27.55	1165	26.57	609	25.68

<sup>a</sup>The  $G_{102}$  flux limits depend on wavelength with the sensitivity of the grism. Values presented here are the  $1\sigma$  limits at  $\lambda = 1\mu\text{m}$ .

<sup>b</sup>Limits are  $1\sigma$  in the UVIS filters  $V_{606}$  and  $I_{814}$  and  $5\sigma$  in the IR filters  $J_{110}$  and  $H_{160}$ , matching the selection criteria described in Section 4.3.

For this analysis, we use the earlier versions of the photometric and emission catalogs described in Sections 2.3.1 and 2.4, respectively. In the case of the photometry, the measurements are performed with *Source Extractor* on images drizzled to the  $0''.04$  pixel scale and using a combined image for detection. We run *Source Extractor* twice for each UVIS filter: once on the original image, and once on the image convolved to match the resolution of the F160W filter. Convolution decreases the depth in the images, and so we use the photometry calculated on the unconvolved images at the original resolution to determine which sources are undetected in the UVIS filters. We use magnitudes calculated in circular apertures with  $r = 0''.3 = 7.5$  pixels on the convolve images to measure galaxy colors. All other analysis is done with *Source Extractor*'s AUTO elliptical apertures.

The emission line catalog is created by the process described in Colbert et al. (2013), the earlier version of the updated line finding algorithm and fitting procedures that are described in Chapter 2. As a brief summary, emission line candidates are identified using an automatic algorithm that selects groups of contiguous pixels above the continuum. Every candidate is then carefully inspected by two reviewers. This visual inspection is necessary to reject cosmic rays, hot pixels, and other artifacts and sources of contamination that could not be removed during image reduction due to the lack of dithering. We adopt the completeness corrections from Colbert et al. (2013), which were derived using the same

line-finding procedure. In total, 2180 emission-line galaxies have been identified in these 48 WISP fields.

While the WISP Survey is optimized to detect  $H\alpha$  and [O III]-emitters at  $0.3 < z < 2.4$ , it is also well-suited for the search for LAEs at  $z > 6$ . In the WISP emission line catalog, all single emission lines with no visible asymmetry are assumed to be  $H\alpha$ . However, there is the possibility that some of the faintest single-line emitters are actually LAEs at  $z \geq 6$ . Most of the exposure time in the longer WISP parallel opportunities is devoted to  $G_{102}$  observations, enabling the grism images to reach the sensitivities necessary for detecting  $z > 6$  emission lines. The observed EW limit of the WISP Survey ( $40\text{\AA}$  Colbert et al., 2013) corresponds to a low limit of  $EW_0 = 5.3\text{\AA}$  in the rest frame of a galaxy at  $z = 6.5$ . In Section 4.3, we describe how we select LAE candidates from the single-line emitters in the WISP emission line catalog.

## 4.3 Sample Selection

### 4.3.1 Choosing the selection criteria

The selection criteria, which we present in Section 4.3.2, aim to select single-line emitters with colors indicative of a Lyman break. We choose the criteria after minimizing the number of lower- $z$  contaminants that enter the LAE sample. To do so, we create a large library of simulated spectral templates based on the models of Bruzual & Charlot (2003). From this library we generate a catalog of colors in the WISP bands for galaxies over  $0.1 \leq z \leq 8.5$ . The synthetic catalog is described in Section 3.2. We then use the synthetic catalog to determine the effect of varying three parameters: (1) the range of observed emission line wavelengths we consider, (2) the level of flux allowed in  $I_{814}$ , and (3) the location of the selection window in color space. In the following sections, we discuss each of these three parameters and their effect on the sample contamination. We define  $f_{\text{low-}z}$  as the number of lower- $z$  galaxies selected by our criteria divided by the total number of selected galaxies:  $f_{\text{low-}z} = N_{\text{low-}z} / (N_{\text{high-}z} + N_{\text{low-}z})$ , where  $N_{\text{high-}z}$  is the number of galaxies at  $6.00 \leq z \leq 7.63$ . Only lower- $z$  galaxies in very specific redshift ranges can enter the sample and contribute to  $N_{\text{low-}z}$  (see Section 4.4 for details). The contamination fraction we expect for the WISP sample, denoted  $f_{\text{contam}}$ , is much lower than  $f_{\text{low-}z}$  because we can use the broad wavelength coverage and typical emission line ratios from the WISP catalog to exclude lower-redshift interlopers. We discuss  $f_{\text{contam}}$  in Section 4.4. Likewise, the recovery fraction,  $f_{\text{recover}}$ , is defined as the number of high- $z$  galaxies selected by our criteria divided by the total number of high- $z$  galaxies in the full synthetic catalog. The

maximum  $f_{\text{recover}}$  achieved over the full parameter space is 0.9. We choose values for the three parameters that minimize  $f_{\text{low-}z}$  while keeping  $f_{\text{recover}}$  within 10% of this maximum.

### Wavelength of emission

The range of observed wavelengths we consider in selecting single-line emitters determines the range of redshifts we probe for both high- $z$  LAEs and lower- $z$  contaminants. The  $G_{102}$  grism covers  $0.85 \lesssim \lambda_{\text{obs}} \lesssim 1.13 \mu\text{m}$ , corresponding to  $6.0 \leq z_{\text{Ly}\alpha} \leq 8.3$ . However, including sources with emission lines across this full wavelength range results in an unacceptable number of contaminants. Additionally, we do not have the grism depth to detect galaxies at  $z \gtrsim 8$  (a Ly $\alpha$  luminosity of  $\log_{10}(L_{\text{Ly}\alpha}) = 10^{43}$  erg s $^{-1}$  at  $z = 8$  has a flux of  $\sim 1.3 \times 10^{-17}$  erg s $^{-1}$  cm $^{-2}$ , below the  $3\sigma$  sensitivities we reach in  $G_{102}$ ). We therefore apply a wavelength cut in our selection of single-line emitters. We vary this maximum wavelength from 1.0–1.13  $\mu\text{m}$ , and find that  $\lambda_{\text{obs,max}} = 1.05 \mu\text{m}$  results in  $f_{\text{recover}} = 0.84$  while  $f_{\text{low-}z}$  is just below 0.3.

### Flux in $I_{814}$

A  $z > 6$  galaxy may emit enough flux in  $I_{814}$  to register a signal at greater than  $1\sigma$ . For example, the Lyman break in the spectrum of a  $z \sim 6.6$  galaxy occurs at  $\lambda_{\text{obs}} \sim 9000 \text{\AA}$ ,  $\sim 1000 \text{\AA}$  blueward of the edge of the  $I_{814}$  filter. With imaging in at most one additional filter blueward of  $I_{814}$ , we cannot confirm that a  $z \geq 6$  galaxy with some flux in  $I_{814}$  has truly dropped out of the optical. The level of  $I_{814}$  source flux above the background we allow in selecting candidates will therefore strongly affect the expected contamination fraction. We consider  $I_{814}$  detection thresholds from  $1\sigma - 3\sigma$ , and find that  $1\sigma$  is the best option in terms of recovery and contamination fractions ( $f_{\text{recover}} = 0.83$ , and  $f_{\text{low-}z} = 0.29$ ). Including galaxies that are nondetections at the  $1.5\sigma$  level increases the contamination to  $f_{\text{low-}z} \sim 0.4$ . There are two single-line emitters in the WISP catalog that are nondetections in  $I_{814}$  at  $1.5\sigma$ . We conservatively reject these to avoid contamination from faint, lower-redshift interlopers. We include their spectra and direct image stamps in Appendix B of Bagley et al. (2017).

### Selection window

Figure 4.1 shows the color-color plot used to identify  $z > 6$  dropout galaxies. In choosing the selection criteria, we vary the shape and size of the color selection window, covering the range indicated by the dashed lines in Figure 4.1. The red limit in  $(J_{110} - H_{160})$  has the largest effect on both  $f_{\text{recover}}$  and  $f_{\text{low-}z}$ . We consider windows as red as  $(J_{110} - H_{160}) = 1.3$

and choose 0.5 with  $f_{\text{recover}} = 0.8$  and  $f_{\text{low-}z} = 0.22$ . Only 1% of the  $z < 6$ , UVIS-undetected galaxies in the selection window come from the lower-right corner of our selection region. For simplicity, we therefore use a rectangular selection region rather than the more complicated windows used by, e.g. Oesch et al. (2010) and Bouwens et al. (2015). The requirement for emission line detection in our sample removes any concern over contamination from this region.

### 4.3.2 Selection criteria

A WISP single-line emitter is identified as a  $z > 6$  LAE candidate if and only if it:

1. has a single emission line at  $\lambda_{\text{obs}} \leq 1.05\mu\text{m}$ ;
2. is detected with a signal-to-noise (S/N) ratio in  $J_{110}$  of  $(S/N)_{J_{110}} \geq 5$ ;
3. has colors consistent with those of a  $z \geq 6$  galaxy:

$$\begin{aligned} (I_{814} - J_{110}) &\geq 0.5 \\ (J_{110} - H_{160}) &\leq 0.5; \end{aligned} \tag{4.1}$$

4. is undetected at the  $1\sigma$  level in all available UVIS filters (“UVIS dropouts”).

We derive the color selection criteria in Section 4.3.1 and identify it by the shaded region in Figure 4.1. These color criteria are comparable to those used in similar searches for  $z \sim 6-7$  galaxies, e.g. Oesch et al. (2010), Schenker et al. (2013) and Bouwens et al. (2015) who employ color cuts of  $(I - J) > 0.7 - 1$  and  $(J - H) < 0.4 - 1$  in the same or similar filters as those used here.

We adopt the  $1\sigma$  limiting magnitudes for all galaxies that are  $1\sigma$  nondetections<sup>1</sup> and plot them in Figure 4.1 as limits. Each LAE candidate is then inspected by eye to confirm the emission lines are real and the galaxy is truly undetected in the UVIS filters.

## 4.4 Contamination

High-redshift samples selected via the Lyman break technique can be highly contaminated by lower-redshift interlopers. If, for example, there is any overlap between the red and blue

<sup>1</sup> In order to confirm the detection or non-detection of each source, we measure the residual flux of the surrounding sky. We place the same size circular apertures ( $r = 0''.3 = 7.5$  pix) randomly on the sky around each source out to a radius of  $5''$ . A source that is fainter than  $\geq 84\%$  of these sky apertures is considered a  $1\sigma$  nondetection in that filter.

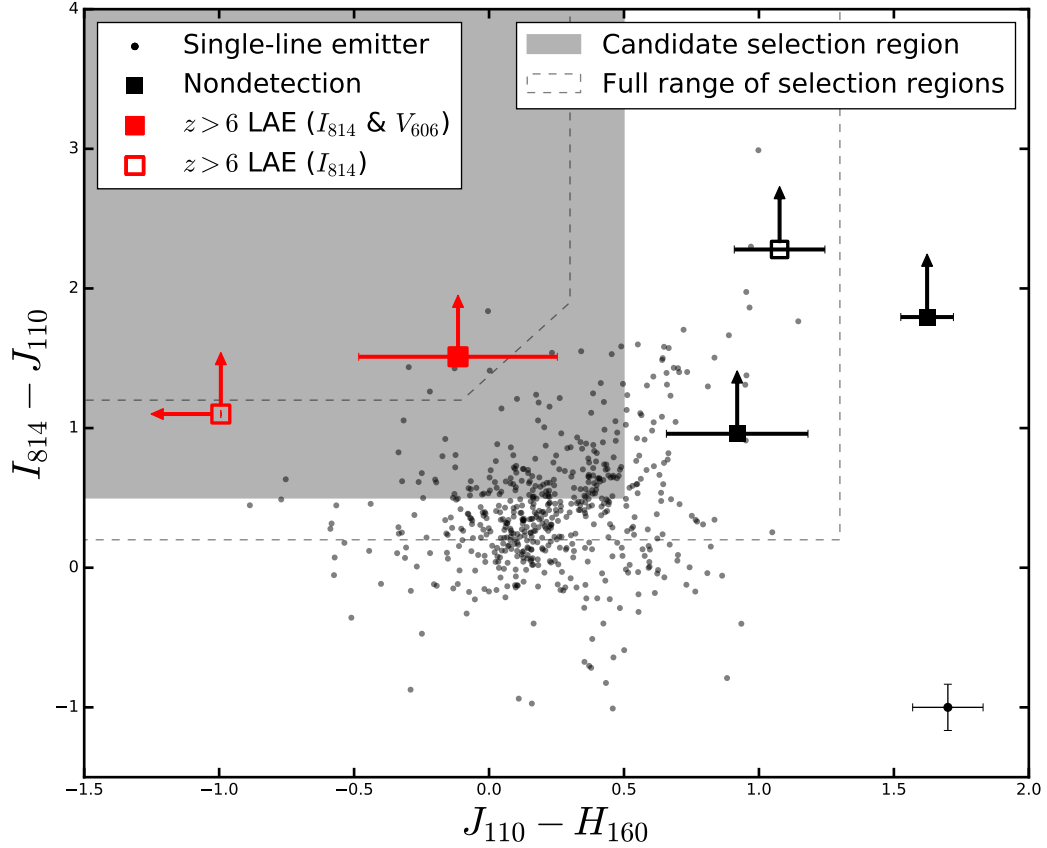


**Figure 4.1**  $I_{814} - J_{110}$  vs.  $J_{110} - H_{160}$  color-color plot used to identify  $z > 6$  dropout galaxies. The grey region shows the candidate selection region. The dashed lines indicate the range of selection regions we consider in order to minimize  $f_{\text{low-}z}$ . All galaxies plotted here are single-line emitters with  $\lambda_{\text{obs}} \leq 1.05 \mu\text{m}$ . Galaxies that are undetected in the UVIS filter(s) are plotted as squares: either solid if both  $V_{606}$  and  $I_{814}$  imaging are available or open if we have only  $I_{814}$ . The selected LAE candidates are indicated by red squares.  $1\sigma$  error bars are shown, and nondetections are plotted at the  $1\sigma$  magnitude limits calculated for their fields. Typical error bars for the UVIS-detected galaxies are plotted in the lower right corner. There are three additional UVIS nondetections (black squares) that lie outside of the selection region. We discuss these sources in Appendix B of Bagley et al. (2017) but do not consider them  $z > 6$  LAE candidates due to their red IR colors.

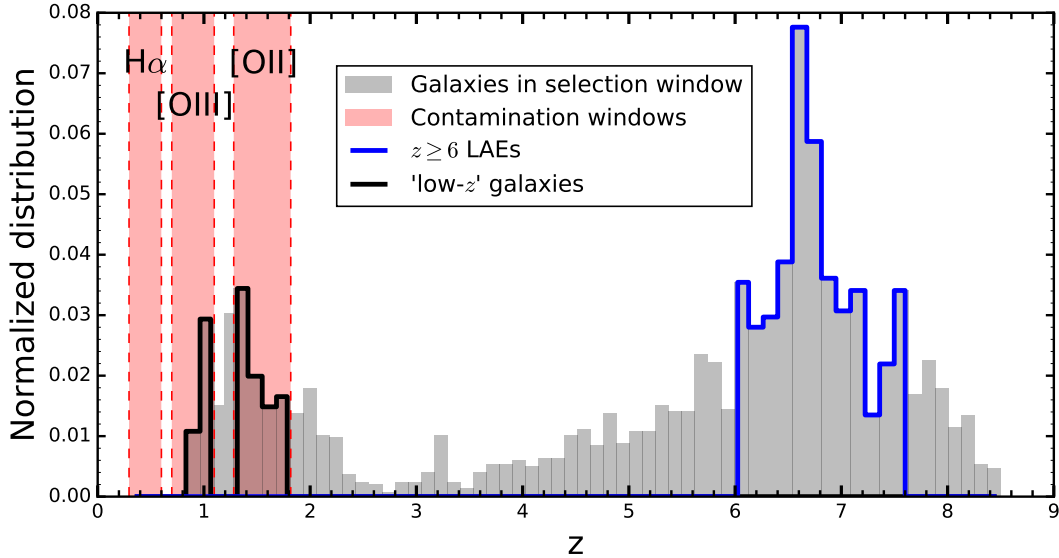


**Figure 4.2** Characterization of the expected contamination in the LAE sample from the synthetic catalog derived in Section 3.2. The redshift distribution of UVIS nondetections in the color selection window is shown in grey. The distribution of the high- $z$  population we are targeting ( $6.0 \lesssim z \lesssim 7.6$ ) is outlined in blue. The shaded red bands indicate redshift windows capable of contributing contaminants to the high- $z$  sample, and the distributions of galaxies within these bands are outlined in black. These galaxies account for 29% ( $f_{\text{low-}z}$ ) of the total selected sample (*blue + black*). WISP has the spectral coverage to detect multiple emission lines in the spectra of these “low- $z$ ” galaxies. As a result, only those with additional emission lines fainter than the WISP sensitivity would contaminate the LAE sample ( $\sim 2\%$ , see Section 4.4).

filters, as between  $I_{814}$  and  $J_{110}$ , the dropout color as a function of redshift can flatten into a ‘color plateau’ (Stanway et al., 2008). Photometric uncertainty can scatter lower-redshift galaxies into the selection window while simultaneously scattering real high-redshift sources out. Additionally, Balmer break galaxies at  $1.3 \lesssim z \lesssim 2.5$  can mimic the colors of  $z \geq 6$  galaxies in filters chosen to bracket the Lyman break (e.g., Mobasher et al., 2005; Henry et al., 2009; Pirzkal et al., 2013).

We characterize the expected contaminants to the LAE sample in Figure 4.2. The grey histogram shows the redshift distribution of sources from our synthetic catalog that lie in the selection window and are nondetections in both  $V_{606}$  and  $I_{814}$ . These sources range from  $0.7 \lesssim z \lesssim 8.5$  and include a large number of  $z < 6$  galaxies.

However, as described in Section 4.3.1, we consider single-line emitters with lines in the range  $0.85 \lesssim \lambda_{\text{obs}} \leq 1.05 \mu\text{m}$ . We remind the reader that the red wavelength limit is chosen to minimize contamination and the blue limit is determined by the rapid drop in the grism

sensitivity. Given these wavelengths, we are probing Ly $\alpha$  at

$$6.00 \lesssim z_{\text{Ly}\alpha} \lesssim 7.63. \quad (4.2)$$

Galaxies in this redshift range are identified by the blue histograms in Figure 4.2. The wavelength selection also restricts contaminants to very narrow redshift ranges (identified as shaded red regions in Figure 4.2):

- H $\alpha$  between  $0.3 \lesssim z_{\text{H}\alpha} \lesssim 0.6$ ,
- [O III] between  $0.7 \lesssim z_{[\text{O III}]} \lesssim 1.1$ , and
- [O II] between  $1.3 \lesssim z_{[\text{O II}]} \lesssim 1.8$ .

The galaxies from these redshift regions are outlined in black, and the resulting fraction of lower- $z$  sources that are selected alongside the  $z > 6$  galaxies is  $f_{\text{low-}z} = 0.29$ . This fraction, however, is much higher than the contamination fraction we expect for the LAE sample,  $f_{\text{contam}}$ , which is limited to lower-redshift galaxies with very specific emission line ratios (see Section 4.4.1). In what follows, we show that very few galaxies ( $\lesssim 2\%$ ) in these redshift ranges could contaminate our results.

If the LAE candidates are lower- $z$  contaminants, we would expect to detect additional emission lines in the  $G_{141}$  grism. For the purposes of illustration, we plot a simplified emission-line spectrum in Figure 4.3 at four redshifts:  $z = 6.5$  (black), 1.4 (red), 0.8 (orange), and 0.4 (blue). Because we select the LAE candidates from the sample of single-line emitters in the WISP catalog, no additional emission lines are detected in the spectra of these galaxies over the full wavelength coverage of the WISP survey. Therefore, if they are lower-redshift galaxies, the additional emission lines must fall below the sensitivity of the WISP spectra<sup>2</sup>. We discuss this possibility in the following section.

#### 4.4.1 Emission line misidentification

In the case that the Ly $\alpha$  emission line has been misidentified, it would likely be either H $\alpha$ , [O III], or [O II] from lower- $z$  galaxies. It is difficult to rule out H $\alpha$ -emitters based on the candidates' spectra because there are few emission lines detected redward of H $\alpha$  in WISP spectra. From our synthetic catalog, however, we find that all galaxies in the redshift

<sup>2</sup> It is also possible that a second emission line could fall on the overlapping edge of the two grisms and be lost due to the drop in sensitivities. Such galaxies would be mistakenly identified as single-line emitters. This would only occur, however, for a small subset of emission lines in the range  $1.13 \lesssim \lambda_{\text{obs}} \lesssim 1.15 \mu\text{m}$ , and does not affect the LAE candidates. If the candidates are lower- $z$  galaxies, the additional emission lines such as [O III] and H $\alpha$  would not fall in the affected wavelength range.

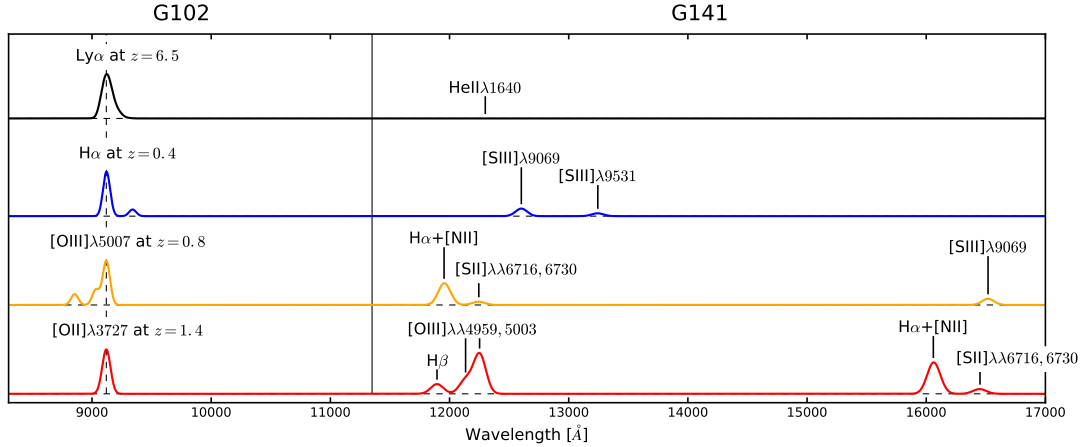


**Figure 4.3** An illustrative example of how the full wavelength coverage of WISP can be used to rule out lower- $z$  interlopers. We show here three possible misidentifications, where  $H\alpha$  at  $z = 0.4$  (blue),  $[O\ III]$  at  $z = 0.8$  (orange) and  $[O\ II]$  at  $z = 1.4$  (red) are mistaken for  $Ly\alpha$  at  $z = 6.5$  (black). In each case, we expect to detect additional emission at longer wavelengths. We can therefore rule out all lower- $z$  contaminants but those where the redder emission lines fall below the WISP sensitivity. The spectra plotted here have been convolved to match the resolutions of the  $G_{102}$  and  $G_{141}$  grisms.

range in which  $H\alpha$  can enter our sample are detected in the UVIS images (see Figure 4.2). Therefore, we conclude that contamination from  $H\alpha$  is negligible.

For the remaining likely contaminants,  $[O\ III]$ - and  $[O\ II]$ -emitters, we look to the full WISP emission line catalog for information on the expected line ratios of galaxies at  $z \lesssim 2$ . The  $[O\ III]$  doublet is blended at the resolution of the WFC3 grisms, and so we use  $[O\ III]$  to refer to  $[O\ III]\lambda\lambda 4959, 5007$  in what follows. Similarly,  $H\alpha$  fluxes are not corrected for  $[N\ II]$ . Figure 4.4 shows the  $H\alpha/[O\ III]$  (left panel) and  $[O\ III]/[O\ II]$  (right) line ratios for sources in the WISP catalog. Here we consider all sources for which the bluer of the two emission lines lies in our wavelength selection range ( $0.85 \lesssim \lambda_{obs} \leq 1.05\mu m$ ). For example, if an emission line at  $\lambda_{obs} = 0.9\mu m$  is  $[O\ III]$  instead of  $Ly\alpha$ , then we would expect to detect  $H\alpha$  at  $\lambda_{obs} = 1.18\mu m$ . The shaded areas in Figure 4.4 show the approximate regions of lower limits in the case where  $H\alpha$  (left) or  $[O\ III]$  (right) are undetected in the WISP spectra. For both cases we adopt  $2 \times 10^{-17} \text{ erg s}^{-1} \text{ cm}^{-2}$  as the limiting line flux, which is the average line flux limit in the deep WISP fields<sup>3</sup>. The line ratios for the  $z = 0.8$  and  $z = 1.4$  spectra plotted in Figure 4.3 are indicated in Figure 4.4 by orange and red squares, respectively,

<sup>3</sup> Emission lines with fluxes below this value are either in the deepest fields or are detected at lower significance than the rest of the catalog. If there are multiple emission lines in the spectra, the secondary lines are measured even if they are at lower S/N.

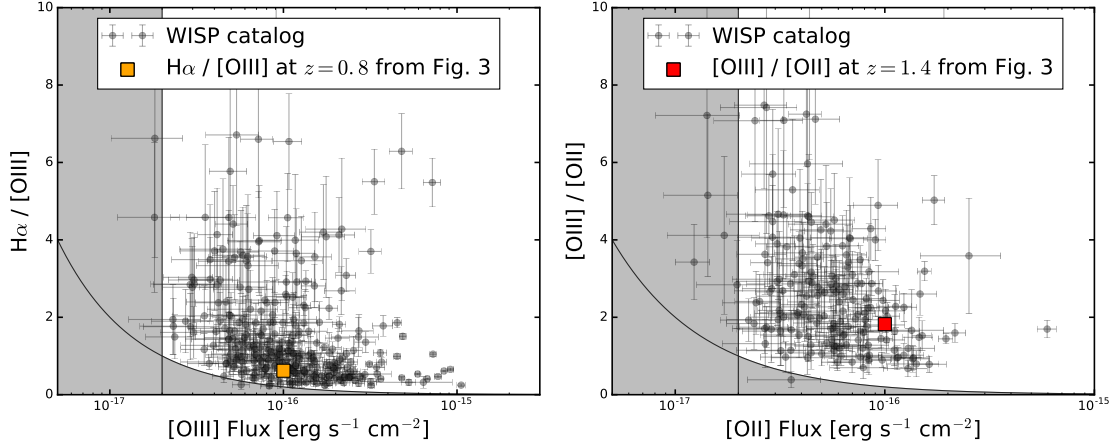


**Figure 4.4** The line ratios for all sources in the WISP catalog for which the bluer of the two emission lines lies in our wavelength selection range ( $0.85 \lesssim \lambda_{obs} \leq 1.05 \mu\text{m}$ ). *Left:*  $\text{H}\alpha/[\text{O III}]$  as a function of  $[\text{O III}]$  flux. *Right:*  $[\text{O III}]/[\text{O II}]$  as a function of  $[\text{O II}]$  flux. The shaded areas show the regions where one of the emission lines is below the detection limit of the WISP spectra, assuming  $2 \times 10^{-17} \text{ erg s}^{-1} \text{ cm}^{-2}$  as the limiting line flux. For reference, the orange and red squares show the line ratios for the  $z = 0.8$  (orange) and  $z = 1.4$  (red) spectra in Figure 4.3.

and are meant as illustrative examples for reference only.

The median line flux ratios in the WISP catalog are  $\text{H}\alpha/[\text{O III}] \sim 1$  and  $[\text{O III}]/[\text{O II}] \sim 2.5$ , consistent with previous results from both individual galaxies (Mehta et al., 2015) and stacked WISP spectra (Domínguez et al., 2013; Henry et al., 2013). If the LAE candidates are lower- $z$  contaminants, their line ratios would have to be extreme:  $\text{H}\alpha/[\text{O III}]$  or  $[\text{O III}]/[\text{O II}] \lesssim 0.2$  for fluxes of  $\sim 1 \times 10^{-16} \text{ erg s}^{-1} \text{ cm}^{-2}$ . In other words, if the single detected emission line is actually  $[\text{O III}]$  ( $[\text{O II}]$ ), then  $\text{H}\alpha$  ( $[\text{O III}]$ ) must be a factor of  $\gtrsim 5$  fainter to fall below our sensitivity.

As can be seen from the right panel of Figure 4.4,  $[\text{O II}]$ -emitters will not contaminate the LAE sample. At line fluxes of  $f = 1 \times 10^{-16} \text{ erg s}^{-1} \text{ cm}^{-2}$ , virtually no galaxies have  $[\text{O III}]/[\text{O II}] < 0.2$ . Because  $[\text{O III}]$  is so much stronger than  $[\text{O II}]$ , we are guaranteed not to mistake  $[\text{O II}]$  for  $\text{Ly}\alpha$ . On the other hand, 2% of galaxies with  $7 \times 10^{-17} \leq f_{[\text{O III}]} \leq 2 \times 10^{-16} \text{ erg s}^{-1} \text{ cm}^{-2}$  have  $\text{H}\alpha/[\text{O III}] < 0.25$ . Hence, contamination from  $[\text{O III}]$ -emitters is very rare but still a possibility.

There is always the possibility that hot pixels, cosmic rays, and other artifacts are masquerading as emission lines, although we expect only an  $\sim 8.5\%$  contamination rate due to false emission lines (Colbert et al., 2013). Due to the different dispersion solutions,

the spectra do not fall on exactly the same pixels in  $G_{102}$  and  $G_{141}$ . By comparing the full dispersed images in each grism, we performed a check for hot pixels, detector artifacts, and persistence that could have been incorrectly identified as emission lines. We also inspected each individual grism exposure to ensure that we are not detecting cosmic rays. Finally, we have checked that the emission lines in our sample are not zeroth orders from nearby objects. All galaxies in our sample lie sufficiently far from the right edge of the detector, and so zeroth order images are easily identified for their spectra.

Considering contamination from both lower- $z$  and false emission lines, we expect the contamination fraction in the LAE sample to be no higher than  $f_{\text{contam}} \sim 2 - 8\%$ .

## 4.5 Results

### 4.5.1 $z > 6$ LAEs

We find two robust candidates according to the selection criteria described in Section 4.3, *WISP368* at  $z = 6.38$  and *WISP302* at  $z = 6.44$ . Table 4.2 summarizes the spectroscopic and photometric properties. For both sources, a large fraction of the flux density in  $J_{110}$  is due to the emission line, and we include this fraction,  $f_{J_{110}}^{\text{neb}}/f_{J_{110}}^{\text{total}}$  in Table 4.2. We calculate the rest frame EW of Ly $\alpha$  using the  $H_{160}$  magnitudes for the continuum measurement, as the  $H_{160}$  magnitudes are not contaminated by Ly $\alpha$  emission. In the case of *WISP368*, we adopt the  $3\sigma$   $H_{160}$  magnitude limit. We also present the UV absolute magnitudes calculated at rest frame wavelengths of 1500Å and 2000Å, corresponding to  $J_{110}$  and  $H_{160}$ , respectively.  $M_{1500}$  is calculated using the  $J_{110}$  magnitude corrected for the emission line flux. Still,  $M_{1500}$  is uncertain and so we do not calculate the UV slope  $\beta$ . Finally, we measure  $3\sigma$  upper limits for HeII $\lambda$ 1640 and CIII] $\lambda$ 1909 fluxes.

We present images of each candidate in Figure 4.5. The stamps are 3" on a side and are each smoothed with a Gaussian kernel with  $\sigma = 1$  pixel. The candidates have dropped out of the UVIS filters:  $V_{606}$  and  $I_{814}$  for *WISP302* and  $I_{814}$  for *WISP368*.

Figure 4.6 shows the one- and two-dimensional  $G_{102}$  and  $G_{141}$  spectra for each candidate. The Ly $\alpha$  emission lines are circled in white. Additional "emission features", identified in black in Figure 4.6, are present in the dispersed images of both objects. After careful examination of the images, we conclude that these features belong to nearby sources. The wavelengths of HeII $\lambda$ 1640 and CIII] $\lambda$ 1909 are also labeled.

We use a Monte Carlo process to measure the line fluxes: we fit the line with a Gaussian, allow the flux at each wavelength step to vary within the uncertainties, and refit. The flux uncertainties in Table 4.2 are the  $1\sigma$  dispersion in the distribution of measured fluxes.

**Table 4.2** WISP LAEs

	<b>WISP302</b>	<b>WISP368</b>
RA (J2000)	02:44:54.72	23:22:32.26
Dec (J2000)	-30:02:23.3	-34:51:03.7
$z_{\text{Ly}\alpha}$	6.44	6.38
$f_{\text{Ly}\alpha}$ (erg s <sup>-1</sup> cm <sup>-2</sup> )	$9.9 \pm 5.8 \times 10^{-17}$	$10.2 \pm 3.9 \times 10^{-17}$
$EW_0$ (Å)	$798 \pm 531$	< 1172
$L_{\text{Ly}\alpha}$ (erg s <sup>-1</sup> )	$4.67 \times 10^{43}$	$4.71 \times 10^{43}$
$f_{\text{HeII}}^{\text{a}}$ (erg s <sup>-1</sup> cm <sup>-2</sup> )	< $6.0 \times 10^{-17}$	< $3.9 \times 10^{-17}$
$f_{\text{CIII}}^{\text{a}}$ (erg s <sup>-1</sup> cm <sup>-2</sup> )	< $4.3 \times 10^{-17}$	< $2.8 \times 10^{-17}$
$V_{606}^{\text{b}}$ (mag)	> 27.86	...
$I_{814}^{\text{b}}$ (mag)	> 27.49	> 27.78
$J_{110}^{\text{b}}$ (mag)	$26.0 \pm 0.11$	$26.3 \pm 0.20$
$f_{J110}^{\text{neb}}/f_{J110}^{\text{total}}$	0.67	0.96
$H_{160}^{\text{b}}$ (mag)	$26.1 \pm 0.35$	> 27.67
$M_{1500}^{\text{c}}$ (mag)	-19.6	-17.0
$M_{2000}$ (mag)	-20.7	> -19.1

<sup>a</sup>Flux limits are  $3\sigma$ .

<sup>b</sup>Total magnitudes as measured by *Source Extractor*'s AUTO elliptical apertures.

<sup>c</sup> $M_{1500}$  is calculated using the  $J_{110}$  magnitude corrected for the emission line flux.

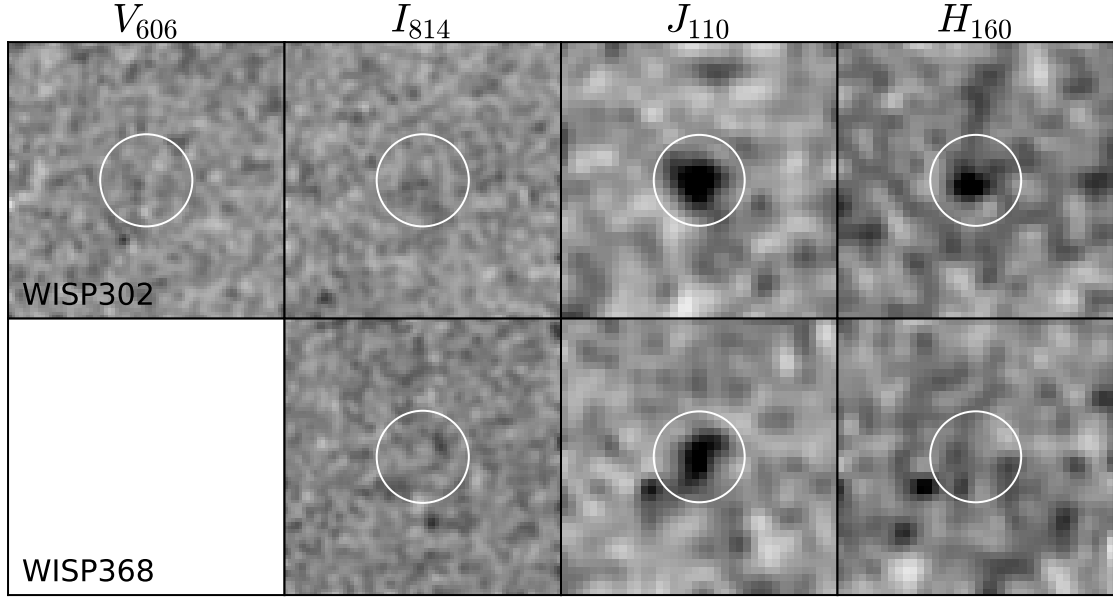


**Figure 4.5** Direct image postage stamps of the LAEs. Columns show, from left to right,  $V_{606}$ ,  $I_{814}$ ,  $J_{110}$ , and  $H_{160}$ . All stamps are  $3''$  on a side. The UVIS stamps have a pixel scale of  $0''.04/\text{pix}$  and the IR stamps have been re-drizzled here onto a pixel scale of  $0''.08/\text{pix}$ . All stamps are smoothed with a Gaussian kernel with  $\sigma = 1$  pixel ( $\sigma = 0''.04$  and  $0''.08$  in the UVIS and IR, respectively). The white circles are  $0''.5$  in radius.

#### 4.5.2 What are the redder UVIS dropouts?

There are three additional sources (black squares in Figure 4.1) that are too red to fall in our selection window yet meet all other criteria. As single-line emitters that drop out of the UVIS filters, these sources are worth further consideration. These three galaxies are small and compact and lie in the region of color space that contains a higher fraction of the dusty, red, lower- $z$  galaxies in our synthetic library. Such galaxies may belong to a population of galaxies at  $z \sim 1.5 - 1.8$  that are either very dusty or have strong  $4000\text{-\AA}$  breaks, causing them to mimic the broadband colors of the Lyman break. The emission line is most likely [O II]. According to Maiolino et al. (2008), the observed limit of  $[\text{O III}]/[\text{O II}]$  ( $[\text{O III}]/[\text{O II}] \lesssim 0.2 - 0.25$ ) would imply high metallicities at these redshifts. Understanding the nature of these sources is very important, but beyond the scope of this chapter. We do not consider these three sources in our analysis and instead present their spectra and direct image stamps in Appendix B of Bagley et al. (2017).

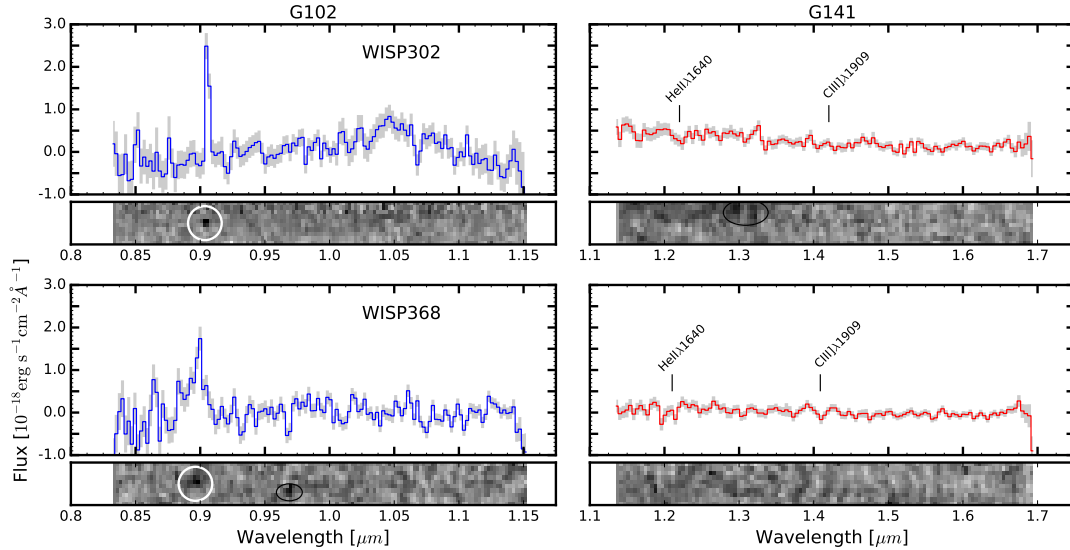


**Figure 4.6** The one- and two-dimensional spectra of the LAE candidates in  $G_{102}$  (left column) and  $G_{141}$  (right). In the one-dimensional spectra, the  $1\sigma$  errors are plotted in grey. The grism spectral stamps have been smoothed by 0.5 pixels. The Ly $\alpha$  emission lines are circled in white, and nearby “emission features” are identified in black.

### 4.5.3 Calculation of the number density

Given the two LAEs presented above, we calculate the number density as:

$$n_{\text{LAE}} = \sum_i C_i \frac{1}{V_i}, \quad (4.3)$$

where  $C_i$  is an emission line dependent completeness correction and  $V_i$  is the volume within which the emission line could be detected. The dominant sources of incompleteness in the WISP survey are (1) confusion from nearby objects and partially- or fully-overlapping spectra, and (2) the failure of the line-finding process to identify emission lines. Colbert et al. (2013) simulate the full emission line identification process and derive completeness corrections that depend on emission line equivalent width (EW) and line flux S/N. We do not detect continua in the LAE spectra, and so use the completeness corrections appropriate for the highest-EW lines in the WISP catalog.

The WISP fields reach a range of depths. In determining  $V_i$  we use a modified version of the  $V_{\text{MAX}}$  method (Felten, 1977) that depends on the  $G_{102}$  sensitivity limit reached in each WISP field. The maximum volume within which a galaxy with the given absolute Ly $\alpha$

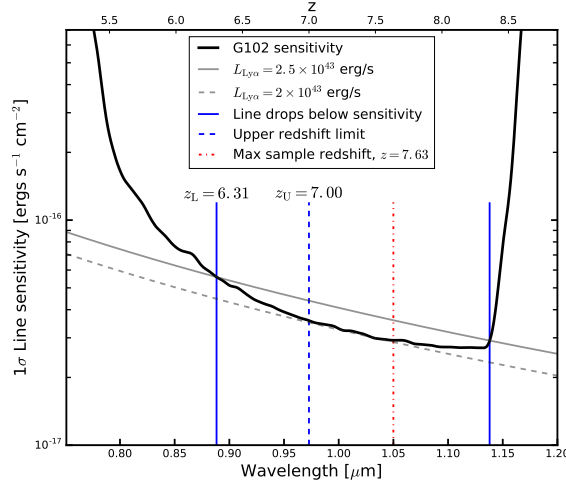


**Figure 4.7** Schematic representation of the modified  $V_{\text{MAX}}$  method used to calculate the volume within which an emission line of a given luminosity is detectable by the WISP survey. The black curve is the G102 sensitivity limit calculated for one of the fields. The solid grey curve shows the observed flux of a Ly $\alpha$  emission line with  $L_{\text{Ly}\alpha} = 2.5 \times 10^{43}$  erg/s at a range of redshifts. The redshifts at which the emission line drops below the sensitivity curve are indicated by blue solid lines. In calculating the volume at  $z \sim 6.5$ , we set  $z_U = 7$  (blue dashed line), while the maximum redshift limit of our sample ( $z = 7.63$ ) is indicated by a red dashed-dotted line. The dashed grey curve shows the observed Ly $\alpha$  flux for  $L_{\text{Ly}\alpha} = 2 \times 10^{43}$ , which would not be detected in this field.

luminosity could be detected is:

$$V_{\text{MAX}}(\text{LAE}) = \sum_{i=1}^{N_{\text{fields}}=48} \Omega_i \int_{z_{L,i}}^{z_{U,i}} \frac{dV}{dz} dz. \quad (4.4)$$

Here,  $\Omega_i$  is the effective area of one WISP field (3.3 sq. arcmin),  $z_L$  is the lower redshift at which the galaxy's Ly $\alpha$  luminosity would fall below the G102 grism sensitivity, which cuts off steeply at the blue end.  $z_U$  is the minimum of (1) the redshift at which the galaxy's line flux would fall below the sensitivity on the red side, and (2) the upper redshift limit set by our selection criteria,  $z = 7.63$ . The Ly $\alpha$  LF, however, is expected to evolve rapidly above  $z = 7$ . For the purposes of comparing our number counts with those of other studies at  $z \sim 6.5$ , we limit this maximum redshift to  $z = 7$ . We present an upper limit for the volume at  $7.0 \leq z \leq 7.63$  in Section 4.6.2.

The integration limits in Equation (4.4) are calculated for each of the 48 fields because the depth is not uniform across all fields. This corresponds to different redshift limits,  $z_U$  and  $z_L$ , and therefore different volumes probed in each field. Smaller effective volumes are

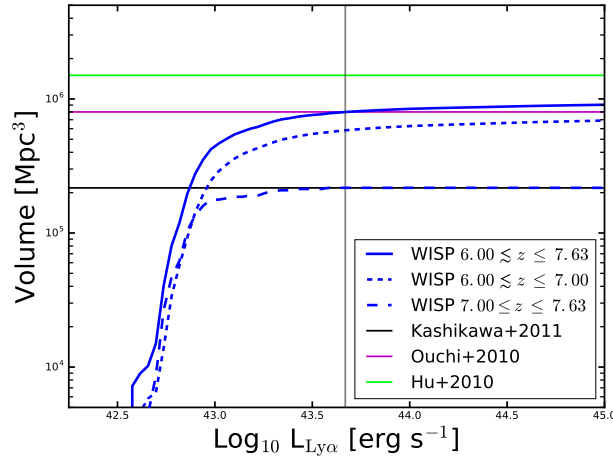


**Figure 4.8** The total effective volume reached in all 48 WISP fields as a function of luminosity. The solid curve shows the volume probed over the full redshift range,  $6.00 \lesssim z \leq 7.63$ . The lower redshift limit comes from the drop in sensitivity of the  $G_{102}$  grism at the blue end, while the upper redshift limit corresponds to our wavelength criterion  $\lambda_{\text{obs,max}} = 1.05 \mu\text{m}$ . The dashed curve shows the volume probed from  $6 \lesssim z \leq 7$ , which is used to calculate the number density of WISP LAEs in Figure 4.9. The dotted curve shows that from  $7.00 \leq z \leq 7.63$ , which is used to place a limit on the number of WISP LAEs at  $z > 7$  (see Figure 4.12).

probed in the shallower fields. In some cases, the emission line may not be detectable in a shallow field at any of the relevant redshifts.

Figure 4.7 shows a schematic representation of this process. As an example, two curves are plotted in grey showing the flux of a Ly $\alpha$  emission line as it would be observed if the galaxy were placed at a range of redshifts. The curves show the fluxes corresponding to  $L_{\text{Ly}\alpha} = 2 \times 10^{43} \text{ erg s}^{-1}$  (dashed) and  $L_{\text{Ly}\alpha} = 2.5 \times 10^{43} \text{ erg s}^{-1}$  (solid). In the first case, the emission line is too faint to be detected in this field at any redshift. In the second case, the redshifts at which the flux would drop below the grism sensitivity are marked by solid blue lines. The redshift limits in this field would be  $z_L = 6.31$  and  $z_U = 7.00$ , where we fix  $z_U$  to calculate the effective volume at  $z \sim 6.5$ . For the volume calculation at  $z \geq 7$ ,  $z_L = 7$  and  $z_U = 7.63$ . Figure 4.8 shows the total effective volume calculated in all 48 WISP fields as a function of line luminosity. The total volume probed in WISP fields at the luminosity of the LAEs is  $5.8 \times 10^5 \text{ Mpc}^3$  between  $6 \lesssim z \leq 7$ . For comparison, the volumes covered by the  $z \simeq 6.5$  ground-based narrowband surveys we consider in this chapter are  $1.5 \times 10^6 \text{ Mpc}^3$  (Hu et al., 2010),  $8 \times 10^5 \text{ Mpc}^3$  (Ouchi et al., 2010),  $2.17 \times 10^5 \text{ Mpc}^3$  (Kashikawa et al., 2011), and  $42.6 \times 10^5 \text{ Mpc}^3$  (Matthee et al., 2015). Extending the redshift range out

to  $z = 7.63$  would add another  $\sim 2.2 \times 10^5 \text{ Mpc}^3$  to the WISP volume.

We compare the number density of  $z \sim 6.5$  LAEs in the WISP survey to measurements of the Ly $\alpha$  cumulative LF in Figure 4.9. The completeness-corrected number density calculated according to Equation (4.4) is plotted as the solid red circle. The observed number density – calculated without the completeness correction – is plotted as the smaller, open red circle. The uncertainty on  $n$  is plotted as the Poissonian error for small number statistics, and is taken from Gehrels (1986). The uncertainty on  $\log(L_{\text{Ly}\alpha})$  is dominated by the large flux uncertainty of *WISP302*.

The WISP LAEs are among the brightest discovered at these redshifts. Recently a handful of comparably bright LAEs have been detected and spectroscopically confirmed in the COSMOS field. The two brightest, CR7 (Sobral et al., 2015; Matthee et al., 2015) and COLA1 (Hu et al., 2016) are plotted here in blue. The number density for CR7 is calculated using the full volume that Matthee et al. (2015) probe in the UDS, COSMOS and SA22 fields,  $42.6 \times 10^5 \text{ Mpc}^3$ . Hu et al. (2016) cover an additional  $\sim 2 \text{ deg}^2$  in COSMOS, which we roughly convert to a volume using the width of the narrowband filter *NB921* the authors used to discover the bright LAEs. COLA1 was discovered in this additional area, which probed a combined volume of  $\sim 58.6 \times 10^5 \text{ Mpc}^3$ . In each luminosity bin, the open blue circles show the observed number densities. The closed blue circles are the number densities corrected for the shape of the *NB921* filter profile using the luminosity-dependent correction factors presented in Matthee et al. (2015).

We plot the  $z \sim 6.5$  cumulative LFs of Hu et al. (2010), Ouchi et al. (2010), Kashikawa et al. (2011), Matthee et al. (2015), and Konno et al. (2018) in Figure 4.9 and discuss this comparison in Section 4.6.1.

#### 4.5.4 Extended Ly $\alpha$ emission

LAEs are expected to have extended Ly $\alpha$  emission. Ly $\alpha$  photons created in star-forming regions are resonantly scattered outwards, creating large diffuse halos of extended Ly $\alpha$  emission (Zheng et al., 2010). At  $z \geq 6$ , where the surrounding IGM is partially neutral, the Ly $\alpha$  halo could extend as far as 1 Mpc from the galaxy (Zheng et al., 2011). Evidence for extended Ly $\alpha$  halos has been detected around galaxies at  $z \sim 0$  (Hayes et al., 2014),  $z \sim 2 - 3$  (e.g., Steidel et al., 2011; Matsuda et al., 2012), and  $z = 3 - 6$  (Wisotzki et al., 2016). At  $z \geq 6$ , these analyses are incredibly difficult to perform on individual galaxies and narrowband images are almost always stacked (Momose et al., 2014).

In the two-dimensional WISP spectra extracted from the full grism images, spatial information is preserved along the cross-dispersion axis. We can therefore measure the

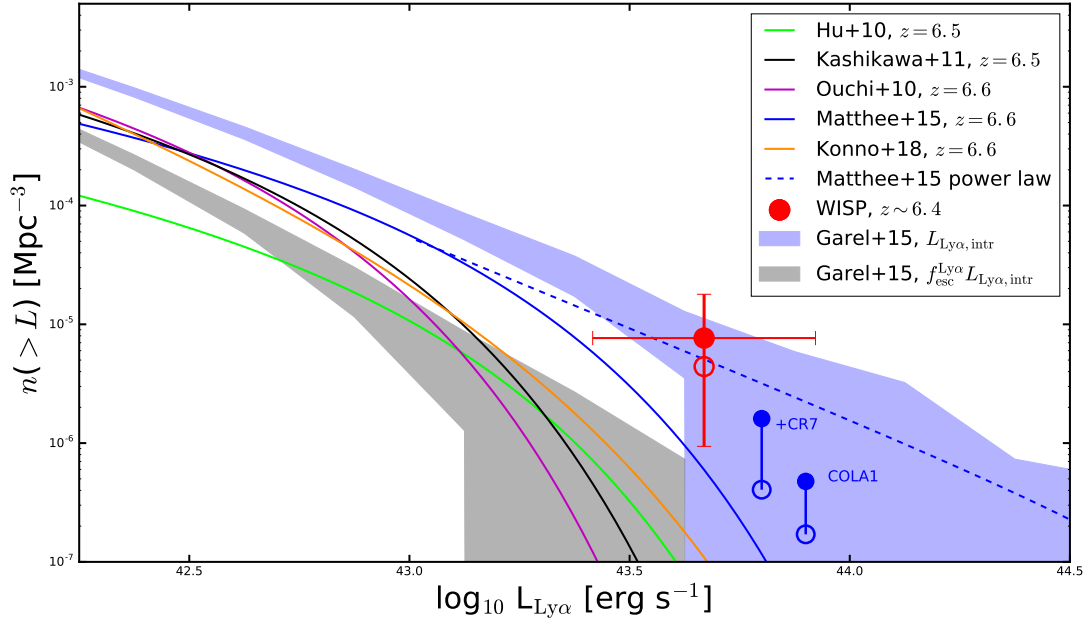


**Figure 4.9** The number density of WISP LAEs at  $z \sim 6.5$ . The WISP number densities are plotted in red, both with (solid circle) and without (open circle) completeness corrections. The observed (open blue circles) and corrected (solid blue circles) number densities calculated using the brightest LAEs discovered in COSMOS, CR7 and COLA1, are shown for comparison. The cumulative LFs of Hu et al. (2010), Kashikawa et al. (2011), Ouchi et al. (2010), Matthee et al. (2015), and Konno et al. (2018) are plotted as solid lines. The dashed blue line shows the integration of the power law fit to the bright end of the LF from Matthee et al. (2015). The shaded regions show the  $1\sigma$  dispersions of the cumulative LF calculated from 100 realizations of the mock light cones from Garel et al. (2015). The light blue and grey regions show, respectively, the results using the intrinsic Ly $\alpha$  emission and that which is able to escape.

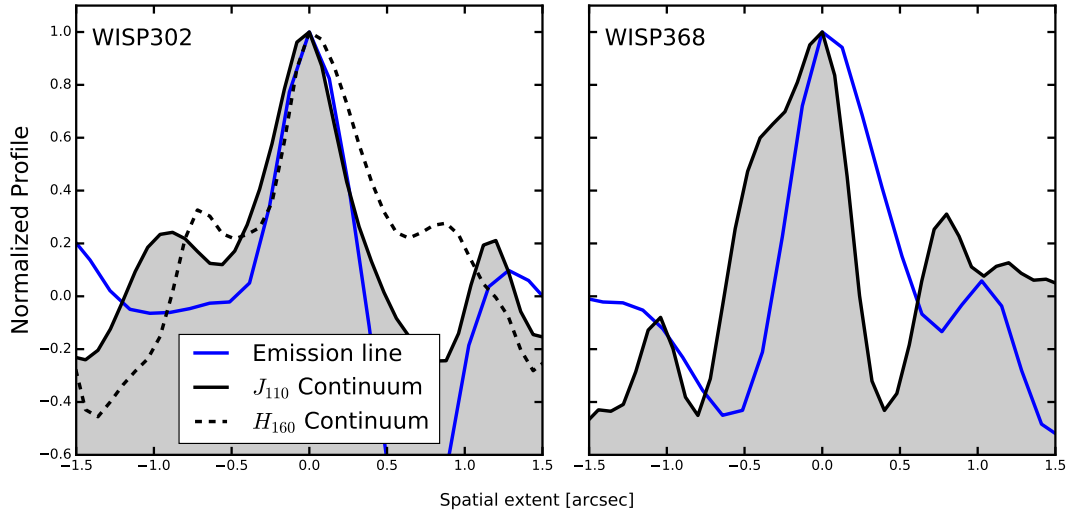


**Figure 4.10** The spatial profile of emission from the LAEs. The  $\text{Ly}\alpha$  profile is measured in the two-dimensional spectral stamps and is plotted in blue. The solid and dashed black curves show the extent of the continuum emission measured in the  $J_{110}$  and  $H_{160}$  image stamps, respectively. Both the  $\text{Ly}\alpha$  and continuum emission are compact. The  $\text{Ly}\alpha$  spatial profiles have  $\text{FWHM} = 0''.38$  (left, *WISP302*) and  $0''.46$  (right, *WISP368*). There is a slight offset ( $\sim 0''.3$  measured at half-maximum) between the  $\text{Ly}\alpha$  and continuum profiles of *WISP368*.

spatial extent of  $\text{Ly}\alpha$  emission around the LAEs in our sample. We create stamps of the 2-D spectra around the emission line of each LAE. There is no continua detected in the spectra, but to be sure we fit the background row by row on either side of the emission line and subtract it out of the spectral stamp.

In each stamp, four columns of pixels ( $\sim 100\text{\AA}$ ) centered on the emission line are collapsed along the wavelength direction. This results in a one-dimensional profile of the  $\text{Ly}\alpha$  emission along the spatial axis as shown in blue in Figure 4.10. In the same way we collapse the continuum image of the galaxy in  $J_{110}$  and  $H_{160}$  along the same axis and plot these profiles in solid and dashed lines, respectively. As *WISP368* is not detected in  $H_{160}$ , we plot only the  $J_{110}$  profile for this LAE. All profiles are normalized to the peak values for easy comparison of the profile shapes.

We measure  $\text{Ly}\alpha$  and continuum emission that are both equally compact, with full widths at half maximum (FWHM) of  $\sim 0''.4$ . This corresponds to  $\sim 2.2$  kpc at these redshifts. Unfortunately, our measurements are limited by the depth of the WISP spectra. Extended  $\text{Ly}\alpha$  emission may be present below our surface brightness limit. We discuss this

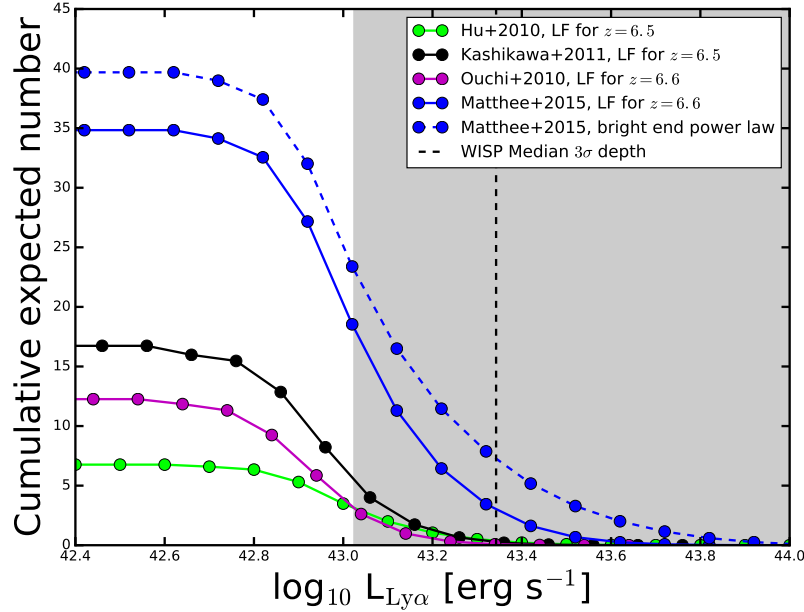


**Figure 4.11** Expected number counts of LAEs at  $z > 7$  assuming no evolution in the Ly $\alpha$  LF from  $z \sim 6.5$ . The shaded region indicates the range of  $3\sigma$  depths in the WISP fields. The median  $3\sigma$  depth is indicated by the vertical dashed line. Based on the four LFs from Figure 4.9, we would expect to detect between  $\sim 0 - 3$  LAEs in the volume probed by the WISP survey at  $7 \leq z \leq 7.63$ . We can rule out evolution in the Ly $\alpha$  LF of Matthee et al. (2015), but are unable to make a similar conclusion about the other three LFs.

possibility in Section 4.6.3.

## 4.6 Discussion

### 4.6.1 The number density of $z \sim 6.5$ LAEs

The WISP survey is probing the most luminous LAEs at  $z \geq 6$ , a population that can provide important information about the state of the IGM at these redshifts. It is expected that the observed number density of LAEs decreases as the volume-averaged neutral hydrogen fraction of the IGM,  $x_{\text{HI}}$ , increases. Upon encountering neutral hydrogen, photons at the Ly $\alpha$  resonance are scattered out of the line of sight. Drops in the observed number densities of LAEs from  $z \sim 5.5 - 7$  (e.g., Hu et al., 2010; Ouchi et al., 2010; Kashikawa et al., 2011) are often interpreted as evidence of an increasingly neutral IGM and indirect measurements of the end of reionization.

$\text{Ly}\alpha$  photons can escape from the surroundings of a galaxy during the epoch of reionization if the galaxy lies in an ionized bubble large enough to allow the photons to redshift out of resonance before encountering the neutral IGM at the edge of the H II region. We can expect, then, to preferentially observe the most luminous LAEs – those capable of ionizing the largest bubbles – at earlier times during reionization (e.g., Matthee et al., 2015; Hu et al., 2016). As  $x_{\text{HI}}$  increases with redshift,  $\text{Ly}\alpha$  emission from fainter galaxies – those that cannot create bubbles out to sufficiently large radii – will be increasingly suppressed. The more luminous galaxies are already surrounded by ionized media and so are less affected.

Recent studies have indicated that the observed number density of bright LAEs is relatively unchanged from  $z \sim 6.5$  to  $z = 5.7$  compared with that of the fainter LAEs (Matthee et al., 2015; Santos et al., 2016). This effect can be seen as a flattening of the  $\text{Ly}\alpha$  LF at the bright end. Matthee et al. (2015) find that the bright end of the  $z = 6.6$   $\text{Ly}\alpha$  LF is best fit by a power law, indicating that there are more bright LAEs than expected for a Schechter-like LF. In a continuation of the same survey, Santos et al. (2016) find that while there is a drop in the number densities of faint LAEs from  $z = 5.7$  to  $z = 6.6$ , there is almost no evolution at the bright end. This result could indicate that the brightest galaxies already reside in ionized bubbles by  $z \sim 6.5$ . Remarkably, our results are consistent with the measurements of Matthee et al. (2015) and Santos et al. (2016).

Other studies show the opposite effect. Kashikawa et al. (2011) find a deficit of bright LAEs at  $z = 6.5$  as compared with  $z = 5.7$ . Additionally, at  $z = 6.5$ , the number densities of bright LAEs measured by Hu et al. (2010), Ouchi et al. (2010) and Kashikawa et al. (2011) are all far below those of the WISP fields (see Figure 4.9). For example, Kashikawa et al. (2011) find only one LAE with  $L_{\text{Ly}\alpha} > 10^{43}$  erg s $^{-1}$ . This result, however, may be heavily influenced by cosmic variance. While Kashikawa et al. (2011) survey a much larger area ( $\sim 900$  sq. arcmin) than that presented here ( $\sim 160$  sq. arcmin), they cover only a single pointing in a narrow redshift range. Meanwhile, the 48 pure parallel WISP fields presented in this chapter are completely uncorrelated. We estimate that the cosmic variance in the WISP sample is  $< 1\%$  (Trenti & Stiavelli, 2008), compared with the  $\sim 30\%$  of Kashikawa et al. (2011). The 24 – 34% decrease Kashikawa et al. (2011) find in the number density of LAEs from  $z = 5.7$  to  $z = 6.5$  may be due in part to cosmic variance. However, at  $\log(L_{\text{Ly}\alpha}) \sim 43.5$ , Matthee et al. (2015) observe a number density that is  $\sim 100$  times higher than that of Kashikawa et al. (2011), a difference that cannot be explained by cosmic variance alone. Enhanced clustering of LAEs introduced by reionization (e.g., McQuinn et al., 2007) could explain some of this observed difference.

We note that the surveys presented in Figure 4.9 have different EW limits, a situation

that can affect the measured LFs (see, for example, the SED models presented by Konno et al., 2016). However, Ouchi et al. (2008) show through Monte Carlo simulations that when they consider all LAEs down to a rest frame EW of  $EW_0 = 0\text{\AA}$ , the normalization of the Schechter LF,  $\phi^*$ , increases by  $\lesssim 10\%$  compared with that for EW limits of  $EW_0 \sim 30 - 60\text{\AA}$ . This exercise indicates that the  $\sim 5 - 10\text{\AA}$  difference between the EW limits of the WISP Survey and those of, e.g., Ouchi et al. (2010) and Kashikawa et al. (2011) will have at most a minor effect on the number density of LAEs we observe. Additionally, given their fluxes and EWs, the WISP LAEs and those discovered by Matthee et al. (2015) at the bright end would have been easily detected in the narrowband surveys of Ouchi et al. (2010) and Kashikawa et al. (2011).

In Figures 4.9 and 4.12, we also compare our results to predictions from mock light cones based on the model of Garel et al. (2015) and adapted for the area and redshift range covered by the WISP fields. Garel et al. (2015) combine the GALICS semi-analytic model with numerical simulations of Ly $\alpha$  radiation transfer through spherical, expanding shells of neutral gas and dust (Verhamme et al., 2006) to predict the emission of Ly $\alpha$  photons in high-redshift galaxies and their transfer in galactic outflows, ignoring the effect of IGM attenuation. GALICS describes the formation and the evolution of galaxies within dark matter halos extracted from a large cosmological simulation box ( $L_{\text{box}} = 100h^{-1}$  comoving Mpc). For each model galaxy, Garel et al. (2015) use scaling relations to connect the expansion velocity, column density and dust opacity of the shell to the galaxy properties output by GALICS (see Garel et al., 2012, for more details). The Ly $\alpha$  line profiles and escape fractions are then estimated using the library of Ly $\alpha$  transfer models in shells presented in Schaerer et al. (2011).

The shaded regions in Figure 4.9 are the  $1\sigma$  dispersion of the LF measured over 100 realizations of the mock light cones. The grey region, labeled  $f_{\text{esc}}^{\text{Ly}\alpha} L_{\text{Ly}\alpha, \text{intr}}$ , shows the LF dispersion for mock light cones in which  $f_{\text{esc}}^{\text{Ly}\alpha}$  is calculated as described above. We see that this model is in better agreement with the data of Hu et al. (2010), Ouchi et al. (2010) and Kashikawa et al. (2011), but it cannot reproduce the high number density of bright LAEs ( $\log(L_{\text{Ly}\alpha}) \gtrsim 43.5$ ) found in the WISP survey or by Matthee et al. (2015).

We see from Figure 4.9 that the dispersion of the LFs estimated from the mock light cones is significant at the bright end, which provides hints to the cosmic variance expected in our survey. However, the  $1\sigma$  dispersion from the mock light cones cannot be reconciled with our data point even within the error bars, so it seems unlikely that field-to-field variation is responsible for the difference between our LF measurement and the LF estimated from the mock light cones or from the other surveys. Nevertheless, we note that cosmic variance is

underestimated in the mock light cones of Garel et al. (2015) because of the finite volume of the simulation box they use, which misses the fluctuations on the very large scales.

Another interpretation of the difference between our measurements and the predictions from Garel et al. (2015) could arise from the fact that they do not account for the growth of the H II bubbles during the epoch of reionization when dealing with the Ly $\alpha$  transfer. Instead, for all model galaxies, Ly $\alpha$  photons need to travel through outflows of neutral gas and dust (as described above) which unavoidably reduce their observed luminosities. Interestingly, we find that our observed number density lies close to the mean LF of the Garel et al. (2015) models in which  $f_{\text{esc,Ly}\alpha} = 1$  (the blue region, labeled  $L_{\text{Ly}\alpha,\text{intr}}$ , in Figure 4.9). This might suggest that most Ly $\alpha$  photons can easily escape the bright WISP LAEs, and that there is very little neutral hydrogen in their surrounding medium (see also Section 4.6.4).

The observed number density of the WISP LAEs is consistent with the density of the brightest LAEs detected to date at similar redshifts, CR7 and COLA1. The WISP number density is also consistent with that of model galaxies in a completely ionized IGM with  $f_{\text{esc}}^{\text{Ly}\alpha} = 1$ . We expect the WISP LAEs, like CR7 and COLA1, to reside in highly ionized bubbles. Such bubbles would enhance the field-to-field variations in the observed number counts of LAEs and may also partially explain the differences at the bright end between the LFs in Figure 4.9. We discuss these bubbles in Section 4.6.4.

If the ionized bubbles are large enough that emission blueward of the Ly $\alpha$  line center is not suppressed by the damping wings of the neutral IGM, we may expect the WISP LAE Ly $\alpha$  line profiles to have blue wings. Line profiles with both blue and red emission peaks are predicted for galaxies with low neutral hydrogen column densities (e.g., Verhamme et al., 2015). Double-peaked emission is common among Green Pea galaxies (Henry et al., 2015), and has been detected in the spectra of COLA1 (Hu et al., 2016; Matthee et al., 2018). The detection of blue wings is beyond the resolution of WISP spectra and is one goal of planned follow-up observations.

As Konno et al. (2016) point out, at  $z=2.2$  all LAEs with  $\log(L_{\text{Ly}\alpha}) \gtrsim 43.4$  may be AGNs. High-ionization emission lines such as CIV $\lambda$ 1549, HeII $\lambda$ 1640 and CIII $\lambda$ 1909 can be useful in identifying AGNs. However, these strong UV nebular emission lines may also indicate galaxies with young, metal-poor stellar populations and large ionization parameters (Panagia, 2005; Stark et al., 2014, 2015, 2016). At the redshifts of the WISP LAEs, CIV $\lambda$ 1549 falls on the overlap region between  $G_{102}$  and  $G_{141}$ , where the sensitivity in the WISP spectra decreases significantly. We instead measure upper limits for HeII $\lambda$ 1640 and

CIII] $\lambda$ 1909 fluxes (see Table 4.2). The limits on the line ratios with respect to Ly $\alpha$  we measure are too uncertain to allow us to determine the dominant source of photoionization, and we cannot distinguish between AGN, metal-poor galaxies and normal star-forming galaxies (Stark et al., 2014; Schaerer, 2003). The emission lines we detect are unresolved and therefore the FWHM is less than  $\sim 1500$  km/s. Although we can rule out broad-line AGN, this limit does not allow us to distinguish between narrow-line AGN and star-forming galaxies. We also notice that the Ly $\alpha$  rest frame EW for the WISP LAEs is many times larger than what Konno et al. (2016) observe for AGN of similar UV magnitudes. Finally, neither Sobral et al. (2015) nor Hu et al. (2016) find strong evidence of AGN emission in CR7 and COLA1 spectra, although the possibility of AGN contribution remains. We cannot draw specific conclusions about the physical characteristics of the LAEs from the present WISP data.

#### 4.6.2 Evolution to $z \gtrsim 7$

Moving to higher redshifts, Konno et al. (2014) find a deficit at all luminosities at  $z = 7.3$  compared to that at  $z = 6.6$ . This evolution of the Ly $\alpha$  LF may be the result of an increasing fraction of neutral hydrogen in the IGM during reionization. The authors also suggest that it could be due to the selective absorption of Ly $\alpha$  photons by neutral clumps in otherwise ionized bubbles. On the other hand, there have been several bright LAEs spectroscopically confirmed at  $z \geq 7$  (e.g., Iye et al., 2006; Vanzella et al., 2011; Shibuya et al., 2012). Roberts-Borsani et al. (2016) recently discovered four galaxies at  $z \sim 7 - 9$ , all of which are emitting Ly $\alpha$  (Stark et al., 2016). With fluxes  $f_{\text{Ly}\alpha} \sim 0.7 - 2.5 \times 10^{-17}$  erg  $\text{s}^{-1} \text{cm}^{-2}$ , these  $z > 7$  galaxies are all fainter than or on par with our detection limits.

We find no LAEs in the redshift range  $7.0 < z < 7.63$  in the volume covered by the WISP fields,  $2.17 \times 10^5 \text{ Mpc}^3$ . Assuming the Ly $\alpha$  LF does not evolve from  $z = 6.5$  to  $z = 7$ , how many would we expect to observe? We calculate the expected number of LAEs at  $7.00 \leq z \leq 7.63$  given the four  $z \sim 6.5$  LFs in Figure 4.9 and the volumes probed by the 48 WISP fields in this redshift range. In Equation (4.4), we limit the redshift range so that  $z_{L,i} \geq 7$  and  $z_{U,i} \leq 7.63$ , covering a volume of  $2.17 \times 10^5 \text{ Mpc}^3$ . The results are plotted in Figure 4.11. The shaded region shows the luminosity range to which the WISP fields are sensitive. The edge of the region is plotted at the  $3\sigma$  flux limit of the deepest field.

At the median  $3\sigma$  depth of the WISP fields (dashed black line), we would expect to detect 3.4 LAEs at  $7 \leq z \leq 7.63$  based on the Matthee et al. (2015) Schechter function LF (blue solid line). Given our non-detection at  $z \geq 7$ , we find that the probability that this  $z = 6.6$  LF also applies at  $z \geq 7$  is 3.3%. If we consider the authors' power-law fit to the

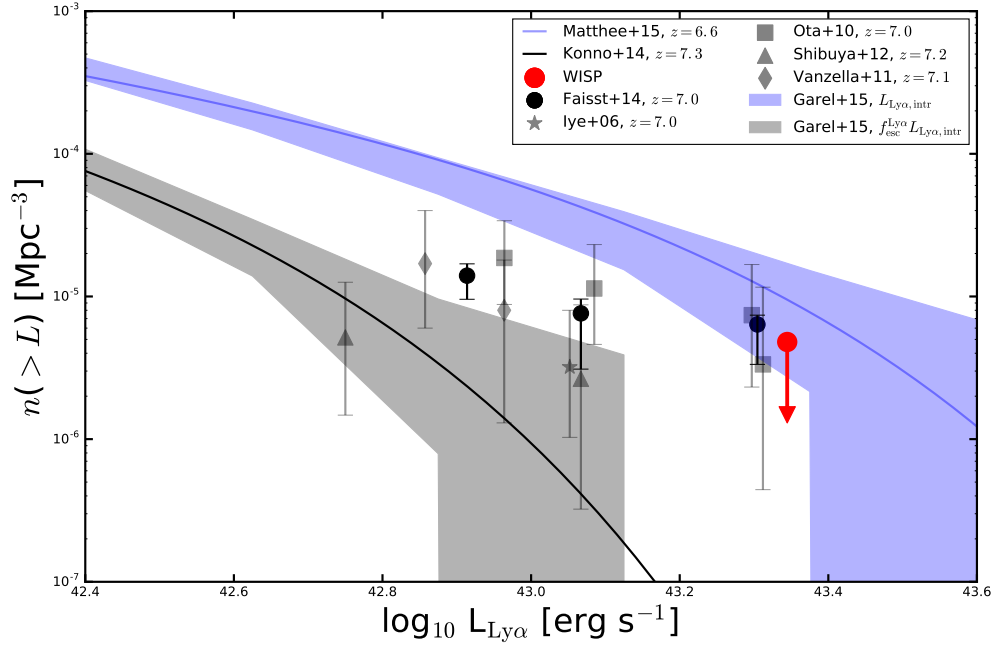


**Figure 4.12** Cumulative number densities of LAEs at  $z \sim 7$ . The red arrow shows the WISP upper limit calculated from the volume probed over the redshift range  $7 \leq z \leq 7.63$ . The grey symbols show the number densities of LAEs from other surveys at  $z \gtrsim 7$ . The cumulative LFs of (Konno et al., 2014,  $z = 7.3$ ) and (Matthee et al., 2015,  $z = 6.6$  for reference) are plotted in black and light blue, respectively. The shaded regions are the same as those plotted in Figure 4.9, but are calculated at these higher redshifts.

bright end (dashed blue line), the expected number of  $z \geq 7$  LAEs increases to 7.9, and the probability decreases to 0.037%. If either LF from Matthee et al. (2015) is representative at  $z \sim 6.5$ , we detect evolution in the Ly $\alpha$  LF from  $z \sim 6.5$  to  $z > 7$ . However, given the LFs of Ouchi et al. (2010), Hu et al. (2010), and Kashikawa et al. (2011), we would expect to detect only 0.1 – 0.5  $z \geq 7$  LAEs. Our observations are inconclusive if these three LFs are more indicative of galaxy number densities at  $z \sim 6.5$ .

We next use the volume probed at  $7 \leq z \leq 7.63$  to place a limit on the observable, yet undetected number density of LAEs over this redshift range. This limit is shown as a red arrow in Figure 4.12 and is calculated at the median  $3\sigma$  depth of the WISP fields presented in this chapter,  $f = 3.6 \times 10^{-17} \text{ erg s}^{-1} \text{ cm}^{-2}$ . At  $z = 7.25$ , this corresponds to  $L_{\text{Ly}\alpha} = 2.2 \times 10^{43}$ .

The highly uncertain cumulative LF at  $z = 7.3$  from Konno et al. (2014) is plotted in

black. The grey symbols show the number densities of LAEs at  $z \gtrsim 7$ , including Iye et al. (2006) at  $z = 6.96$ ; Ota et al. (2010) at  $z = 7$ ; Vanzella et al. (2011) at  $z = 7.008$  and  $7.109$ ; and Shibuya et al. (2012) at  $z = 7.215$ . These number densities are as presented by Faisst et al. (2014), where the authors have accounted for the different cosmologies and corrections used in the individual surveys. The black circles show the weighted median that Faisst et al. (2014) calculate for these  $z \geq 7$  surveys.

The WISP limit is consistent with the other  $z \sim 7$  measurements. Comparing this upper limit with the number density of the WISP  $z \sim 6.4$  LAEs and the  $z = 6.6$  Matthee et al. (2015) LF, we again find evidence for a decrease in the number density of LAEs from  $z \sim 6.5$  to  $z \gtrsim 7$ . This drop could be due to a higher neutral hydrogen fraction in the IGM. However, it could also at least in part be due to an evolution in the intrinsic properties of galaxies at these redshifts, such as in the escape fraction of Ly $\alpha$  photons (e.g., Dijkstra et al., 2014).

As in Figure 4.9, the shaded regions in Figure 4.12 show the  $1\sigma$  dispersions of the Ly $\alpha$  LFs measured from 100 realizations of mock light cones. While still within the region corresponding to galaxies with  $f_{\text{esc}}^{\text{Ly}\alpha} = 1$ , the WISP point is of course an upper limit.

### 4.6.3 Extent of Ly $\alpha$ halos

The detection, or lack thereof, of extended Ly $\alpha$  emission around a galaxy can provide important information about the presence and properties of its surrounding neutral hydrogen. Ly $\alpha$  photons may escape from a galaxy if they have been redshifted out of resonance by scattering through a shell of expanding material (e.g., Verhamme et al., 2006). The scattering process acts to diffuse the Ly $\alpha$  photons outwards from their point of origin. The extent of the resulting Ly $\alpha$  halo is an indirect probe of the fraction of neutral hydrogen present around the galaxy. Extended emission is expected to be common around galaxies surrounded by partially or mostly neutral hydrogen, while more compact emission is expected when the surrounding hydrogen is ionized (and therefore scattering is minimized). Extended Ly $\alpha$  emission has been detected at redshifts ranging from  $z \sim 0.03 - 6$ . The 14 well-studied galaxies in the Ly $\alpha$  Reference Sample (LARS, Hayes et al., 2013, 2014; Östlin et al., 2014) have Ly $\alpha$  emission that is  $\sim 3$  times more extended than either their H $\alpha$  or FUV emission. At  $z = 2.2$ , Momose et al. (2016) find scale lengths of Ly $\alpha$  halos ranging from 7 – 16 kpc, while Steidel et al. (2011) find evidence for Ly $\alpha$  halos extending out as far as 80 kpc at  $z = 2.6$ . At  $z \sim 3.1$ , Matsuda et al. (2012) detect Ly $\alpha$  halos out to  $\geq 60$  kpc. Wisotzki et al. (2016) study a sample of galaxies at  $3 \leq z \leq 6$  and find the Ly $\alpha$  emission is more extended than the UV by a factor of 5 – 10. On the other hand, compact Ly $\alpha$  emission

has been observed at both intermediate and high redshifts:  $z \simeq 2.1, 3.1$  (Feldmeier et al., 2013);  $z \simeq 5.7$  and  $6.5$  (Jiang et al., 2013). The observed compact emission could indicate that the galaxies at these redshifts are surrounded by highly ionized hydrogen, even at the end of reionization at  $z \sim 6.5$ .

It is likely, however, that measurements of compact Ly $\alpha$  emission such as those of Feldmeier et al. (2013) and Jiang et al. (2013) reflect the surface brightness limits of the observations (e.g., Steidel et al., 2011; Schmidt et al., 2016; Wisotzki et al., 2016) rather than the physical environments surrounding the galaxies. Guaita et al. (2015) redshift LARS galaxies to simulate observations of these galaxies at  $z \sim 2$  and  $z \sim 5.7$ . By  $z = 5.7$ , the extended Ly $\alpha$  emission is only detected in stacked narrowband images, and the stacked Ly $\alpha$  profile drops below the surface brightness limit at  $\sim 5$  kpc. Repeating this process for galaxies at  $z = 7.2$  for the Grism Lens-Amplified Survey from Space (GLASS), Schmidt et al. (2016) find that the surface brightness of the extended Ly $\alpha$  emission in LARS galaxies is too faint to be detected in their stacked spectra.

Both LARS and GLASS reach depths comparable to or slightly deeper than WISP:  $3 \times 10^{-18}$  erg s $^{-1}$  cm $^{-2}$  in the  $z = 5.7$  simulated LARS spectra and  $3.5 - 5 \times 10^{-18}$  erg s $^{-1}$  cm $^{-2}$  (observed, uncorrected for magnification) in the GLASS spectra. The WISP spectra are therefore only sensitive to the central, high surface brightness core of the Ly $\alpha$  emission. Indeed, the  $1\sigma$   $G_{102}$  depths reached in the two WISP fields are  $5.5 \times 10^{-17}$  erg s $^{-1}$  cm $^{-2}$  arcsec $^{-2}$ , a factor of 550 times brighter than that reached by Wisotzki et al. (2016). We therefore do not draw conclusions from the compact Ly $\alpha$  profiles we measure, but instead suggest the LAEs presented here are good candidates for targeted, deep follow-up observations aimed at exploring the extent of the Ly $\alpha$  halo at  $z \sim 6.5$ .

#### 4.6.4 Ionized bubbles

It is instructive to compare the observed Ly $\alpha$  luminosities with the intrinsic one, computed with basic assumptions on the stellar population of the WISP LAEs. We consider a range of parameters including both Chabrier (2003) and Salpeter (1955) IMFs, metallicities of  $Z/Z_{\odot} = 0.005, 0.02$  and  $0.2$ , and ages from 10 Myr to 1 Gyr. Assuming Case B recombination,  $n_e = 100$  cm $^{-3}$  and  $T_e = 10^4$  K, the intrinsic Ly $\alpha$  luminosity of a galaxy can be estimated from the production rate of ionizing photons as (e.g., Schaerer, 2003):

$$L_{\text{Ly}\alpha, \text{intr}} = C (1 - f_{\text{esc}}) N\gamma, \quad (4.5)$$

where  $C = 1.04 \times 10^{-11}$  erg and  $f_{\text{esc}}$  is the escape fraction of ionizing photons.  $N\gamma$  can be computed by scaling the stellar population model to the observed  $H_{160}$  magnitude (rest-frame  $2000\text{\AA}$ , not contaminated by the  $\text{Ly}\alpha$  emission). For reference, we adopt  $f_{\text{esc}} = 0$  and perform this calculation for *WISP302* only, since *WISP368* is undetected in the  $H_{160}$  continuum.

According to this model, and assuming the lowest metallicity covered by the BC03 models ( $Z = 0.0005Z_{\odot}$ ) and an age of 10 Myr, *WISP302* can produce  $5.1 \times 10^{54}$  ionizing photons per second. The ratio of observed to intrinsic  $\text{Ly}\alpha$  emission is therefore  $\sim 0.9$ , implying that we are detecting almost all of the  $\text{Ly}\alpha$  photons produced by this galaxy. More moderate parameter values result in an observed  $L_{\text{Ly}\alpha,\text{obs}}$  that is greater than the intrinsic  $L_{\text{Ly}\alpha,\text{intr}}$ . Only models with a very young age and low metallicity produce a ratio  $L_{\text{Ly}\alpha,\text{obs}}/L_{\text{Ly}\alpha,\text{intr}} < 1$ .

This exercise suggests that these photons are not only able to escape from the galaxy's ISM, but they are also not substantially attenuated by the surrounding IGM. In fact, local (i.e., where the IGM is not affecting the  $\text{Ly}\alpha$  profile) analogs to high- $z$  galaxies with large escape fractions of  $\text{Ly}\alpha$  radiation are characterized by an emission line profile showing substantial flux blueward and close to the systemic velocity (Henry et al., 2015; Verhamme et al., 2015). The neutral IGM at  $z \sim 6.5$  would attenuate this blue emission considerably, causing  $L_{\text{Ly}\alpha,\text{obs}}/L_{\text{Ly}\alpha,\text{intr}} \lesssim 0.5$ . Hence, we conclude that a sizable neutral fraction in the presence of this galaxy is unlikely. This conclusion is also supported by the agreement between the LF calculated from the intrinsic  $\text{Ly}\alpha$  emission (Garel et al., 2015) and the high number density of WISP LAEs (see Figure 4.9).

It is possible that the stellar population of *WISP302* is more extreme than our simple assumption. Both Pop III stars and models that include binaries have effectively harder spectra than typical Pop II stars, and can produce a factor of up to  $\sim 3$  more ionizing photons than the spectral template discussed above (Schaerer, 2002; Eldridge et al., 2008). A larger  $L_{\text{Ly}\alpha,\text{intr}}$  would imply a much lower  $L_{\text{Ly}\alpha,\text{obs}}/L_{\text{Ly}\alpha,\text{intr}}$  ratio removing the need for a fully ionized IGM around this object. We can search for evidence of extreme stellar populations in *WISP302* looking for the  $\text{He II}\lambda 1640\text{\AA}$  emission line (Panagia, 2005; Stanway et al., 2016) as well as other UV nebular emission lines (e.g., Stark et al., 2014).

The presence of dust could also reduce the  $L_{\text{Ly}\alpha,\text{obs}}/L_{\text{Ly}\alpha,\text{intr}}$  ratio. If dust were present,  $L_{\text{Ly}\alpha,\text{intr}}$  would be higher than what we estimate from our simple dust-free model. At the absolute magnitude of *WISP302*, however, Bouwens et al. (2016) show that the correction for dust extinction is negligible ( $< 0.2$  magnitudes). As we cannot reliably measure the UV slope  $\beta$ , we rely on this estimate of dust extinction.

If extreme stars are not important, then the high  $L_{\text{Ly}\alpha, \text{obs}}/L_{\text{Ly}\alpha, \text{intr}}$  ratio indicates that the IGM is mostly ionized around this galaxy. The current measurement of the Thomson optical depth from the cosmic microwave background radiation would allow for an end of the reionization process by as early as  $z \sim 6.5$  (Robertson et al., 2015; Planck Collaboration et al., 2016b). However, if this were the case, we would expect bright galaxies such as the WISP LAEs to be more common. Therefore, it is more likely that objects like *WISP302* reside in rare, localized bubbles of ionized gas.

We now investigate the sources that are needed to create a sufficiently large ionized bubble for the Ly $\alpha$  emission to escape the effects of the IGM damping wing. Ly $\alpha$  photons will be transmitted through the IGM if the optical depth they experience is  $\tau_{\text{IGM}} < 1$ . Miralda-Escudé (1998) shows that the minimum radius required is  $R_{\text{min}} \sim 1.216$  proper Mpc. Following Cen & Haiman (2000), we can define  $R_{\text{max}}$ , the maximum radius ionized over the course of *WISP302*'s lifetime as:

$$R_{\text{max}} = \left( \frac{3 N_{\text{ion}}}{4 \pi \langle n_{\text{H}} \rangle} \right)^{1/3}. \quad (4.6)$$

Here,  $\langle n_{\text{H}} \rangle$  is the mean hydrogen density within  $R_{\text{max}}$  and  $N_{\text{ion}}$  is the total number of ionizing photons emitted.  $N_{\text{ion}}$  can be expressed as the product of the rate of ionizing photons produced by the galaxy, the fraction of these that escape, and the galaxy's lifetime:  $N_{\text{ion}} = N_{\gamma} f_{\text{esc}} t$ . We assume the same stellar population as above, but we consider a longer star-formation episode (i.e.,  $t = 100$  Myr). This age will provide us with a conservative upper limit on the radius of the ionized region.

Following Stiavelli (2009), we calculate the hydrogen number density from the mean density of a virialized halo,  $\rho_{\text{vir}}$ :

$$\rho_{\text{vir}} = \xi \Omega_M \rho_0 (1+z)^3 \quad (4.7)$$

$$n_{\text{H}} = \frac{\rho_{\text{vir}} \Omega_b}{\mu m_{\text{p}} \Omega_M}. \quad (4.8)$$

$$(4.9)$$

where  $\xi \simeq 178$  is the ratio between the density of a virialized system and the matter density of the universe;  $\mu \simeq 1.35$  is the mean gas mass per hydrogen atom and accounts for the contribution of helium;  $m_{\text{p}}$  is the mass of a proton; and we adopt  $\Omega_b h^2 = 0.0223$  (Planck Collaboration et al., 2016a). We find  $R_{\text{max}} \simeq 0.45(f_{\text{esc}})^{1/3}$  Mpc. Even if all the ionizing photons escaped the galaxy's ISM ( $f_{\text{esc}} = 1$ ), the size would still be less than half of the minimum required radius,  $R_{\text{min}}$ .

Clearly, *WISP302* is not capable of ionizing a large enough bubble on its own. We consider two alternative sources for the needed ionizing photons: a population of faint

galaxies, as in, e.g., Vanzella et al. (2011) and Castellano et al. (2016), or a bright quasar close to the studied LAE but outside the WISP field of view.

We begin with the first possibility. From Equation (4.6) we find that at least  $1.45 \times 10^{57}$  photons/s are required to create a sufficiently large ionized bubble, where we have assumed an escape fraction of  $f_{\text{esc}} = 0.1$ . We next determine how many galaxies are needed to produce the required number of photons. To do so, we find the Ly $\alpha$  luminosity density by integrating

$$\int L \phi(L) dL, \quad (4.10)$$

where  $\phi(L)dL$  is the LF, and normalize by the observed number density of WISP LAEs. We then convert the Ly $\alpha$  luminosity density to a density of ionizing photons using Equation (4.5). Faint galaxies are the dominant source of ionizing photons, and so we assume a simple power law LF and begin by considering a slope of  $\alpha = -1.5$ , matching the slopes plotted in Figure 4.9. In order to reach the requisite  $10^{57}$  photons/s, we must integrate Equation (4.10) down to  $L_{\text{Ly}\alpha} \sim 0.001L_{\text{Ly}\alpha}^*$ . This luminosity limit is on par with the minimum UV luminosities adopted by, e.g., Robertson et al. (2015) and Rutkowski et al. (2016), in evaluating the contribution of star-forming galaxies to reionization. If we allow for a steeper faint-end slope such as  $-2.3 < \alpha < -2.0$  (e.g., Dressler et al., 2015), we need only integrate down to  $L_{\text{Ly}\alpha} \sim 0.04 - 0.1L_{\text{Ly}\alpha}^*$ . A substantial, but not unreasonable, number of faint galaxies is required to produce  $10^{57}$  ionizing photons in the volume. Alternatively, in the presence of an overdensity, an increase in the luminosity function normalization could further relax the need for faint galaxies. These calculations strongly depend on the escape fraction of Lyman continuum photons in these high- $z$  galaxies (e.g., Rutkowski et al., 2016; Vanzella et al., 2016; Smith et al., 2016).

We now consider the second possibility that *WISP302* resides in a bubble ionized by a nearby quasar. For the same UV luminosity, quasars produce approximately an order of magnitude more ionizing photons than star-forming galaxies. Moreover, the escape fraction of ionizing radiation is likely close to 100% (e.g., Loeb & Barkana, 2001; Cristiani et al., 2016). For a single QSO to produce the required number of ionizing photons, it would need to be as bright as  $H_{160} \sim 22$ , not unreasonable given the luminosities of  $z > 6$  QSOs observed by Fan et al. (2006). This object would be easily identified in the WISP survey, although none is detected in the region observed around *WISP302*. At  $z = 6.4$ , however, one Mpc corresponds to  $\sim 3'$ . Thus, it is possible that the quasar falls outside of the WFC3 field. At this redshift, the average baryonic density of the universe is such that the recombination time is of the order of the age of the universe, and shorter than typical QSO lifetimes (Trainor & Steidel, 2013). Once ionized, the bubble could then remain ionized after

the QSO has turned off. Imaging and spectroscopy over a wider area around *WISP302* are needed to investigate these possibilities.

## 4.7 Summary

In this chapter we present the results of a search for  $z > 6$  LAEs in the WISP survey. We find two  $z \sim 6.5$  LAEs in  $\sim 160$  sq. arcmin, probing a volume of  $5.8 \times 10^5$  Mpc<sup>3</sup>. We estimate the contamination fraction in our sample selection to be  $\lesssim 2\%$ , owing mainly to rare [O III]-emitters at  $z \sim 0.8$  with  $H\alpha/[O III] < 0.25$ .

Our number density of bright WISP LAEs at  $z \sim 6.5$  is higher than the previously reported measurements by Hu et al. (2010), Ouchi et al. (2010), and Kashikawa et al. (2011), and is consistent with the findings of Matthee et al. (2015). The discrepancy between the WISP measurement and these studies is likely due to a combination of our larger redshift coverage (and therefore comparable or even larger volume) and the almost negligible effect of cosmic variance in our sample.

We do not detect any  $z > 7$  LAEs, and determine that the  $z = 6.6$  Ly $\alpha$  LF as measured by Matthee et al. (2015) must evolve from  $z = 6.6$  to  $z > 7$ . Based on the expected number counts at the median depth of our fields, we cannot make a similar claim for the other  $z \sim 6.5$  LFs. Our upper limit on the observed number density of LAEs in the WISP volume from  $7 \leq z \leq 7.63$  is consistent with other  $z \sim 7$  measurements.

We argue that the WISP LAEs reside in large ionized bubbles in the IGM. Using simple assumptions on their stellar populations, we conclude that they are not capable of ionizing their surroundings. We suggest that either a nearby bright quasar or a substantial population of fainter galaxies is required.

The WISP LAEs are excellent targets for studies of the IGM towards the end of reionization as well as the sources contributing to the ionizing photon budget. Follow-up observations can explore whether there is evidence for extreme stellar populations in these galaxies by targeting the He II emission line as well as other UV nebular emission lines (e.g., Stark et al., 2014). We can look for the presence of a blue wing in the Ly $\alpha$  line profile, and obtain deep spectroscopic observations to investigate the absence (presence) of low surface brightness components around our LAEs to support (refute) the idea that these sources are located in ionized bubbles. Measurements of the LAEs' systemic velocities are also needed to determine whether the Ly $\alpha$  emission is close to the systemic velocity, as observed in some local galaxies with large Ly $\alpha$  escape fractions, or substantially redshifted. We note, however, that both the ISM and IGM can contribute to the redshifting of the line,

and these contributions cannot be separated at these high redshifts.

We can observe a wider field-of-view to search the surrounding volume for bright quasars, or probe down to fainter Ly $\alpha$  luminosities to study the population of fainter galaxies around the bright LAEs. These observations can provide information on the sources mainly responsible for ionizing the regions around the LAEs. Follow-up observations can confirm whether there really are sufficient galaxies to create the bubbles, or whether a more powerful source of ionizing photons is required.

Finally, upcoming space-based dark energy missions have the potential to discover thousands of these bright LAEs. For example, covering 40 sq. degrees at a  $3.5\sigma$  sensitivity of  $6 \times 10^{-17}$  erg s $^{-1}$  cm $^{-2}$ , the Euclid Deep Survey (Laureijs et al., 2012) has the potential to identify  $\sim 70$  LAEs per sq. degree at  $6.5 \lesssim z \lesssim 7.0$ . These targets would be ideal for ground-based and JWST follow-up.

# Chapter 5

## Local Analogs

### 5.1 Introduction

Observational studies at  $z > 7$  are limited to the brightest sources, and the more common, fainter, lower-mass galaxies that are expected to be responsible for reionization (e.g. Bouwens et al., 2015) remain largely inaccessible. Emission at  $\lambda < 1216\text{\AA}$  from galaxies at these redshifts is absorbed by the neutral hydrogen in the intergalactic medium (IGM), making it impossible to determine how much Lyman continuum (LyC;  $\lambda < 912\text{\AA}$ ), or hydrogen-ionizing, radiation is able to escape these galaxies. The James Webb Space Telescope will make it possible to study bright galaxies during reionization in unprecedented detail. For the faint, low mass sources, however, observations will generally be limited to medium and broadband imaging. Detailed studies of local galaxies with properties analogous to those of galaxies at high redshift are therefore necessary to calibrate and contextualize the results from bright sources during reionization.

While there are a handful of well-studied samples of local galaxies identified as analogs to those at high redshift — the Lyman Alpha Reference Sample (LARS; Östlin et al., 2014; Hayes et al., 2014), the Green Peas (Cardamone et al., 2009), and the Lyman Break Analog sample (Heckman et al., 2005; Hoopes et al., 2007), for example — they are at least an order of magnitude more massive than the  $10^{6-8} M_{\odot}$  galaxies required to maintain reionization (e.g. Boylan-Kolchin et al., 2014, 2015; Bouwens et al., 2015; Rutkowski et al., 2016; Stanway et al., 2016). The results are also limited by small sample sizes. The stellar masses and gas properties of local blue compact dwarf galaxies (BCDs; see review by Kunth & Östlin, 2000) match those expected of galaxies during reionization. In this chapter, we begin by motivating the selection of a sample of BCDs as local analogs of dwarf galaxies during reionization. We have identified a sample of 50 BCDs at  $0.03 \lesssim z \lesssim 0.06$  based on

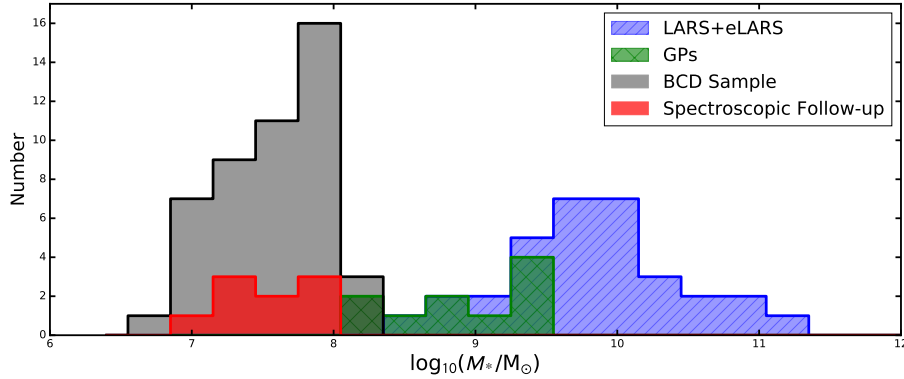


**Figure 5.1** The mass distribution of the sample of 50 BCDs selected from the SDSS catalog (grey). The mass distribution of the 9 galaxies targeted for spectroscopic follow-up is shown in red. The BCD sample galaxies are less massive than the compact star-forming Green Peas (green) and the LARS galaxies (blue). The masses of the BCD and eLARS samples (“extended LARS”, PI: G. Oestlin GO-13483), are taken from the MPA-JHU value-added catalog. Green Pea masses are from taken from Henry et al. (2015), and the LARS masses are from (Hayes et al., 2014).

their extreme emission line ratios. We then present high signal-to-noise (S/N) spectra we have obtained of 9 targets in the sample along with some preliminary results. This project is in progress, and so we conclude this chapter with a discussion of the next steps and future work.

### 5.1.1 Sample Selection

Turning to the local universe for insight of the processes during reionization, we must first determine the properties that make galaxies true analogs of those at high redshift. Studies of the UV luminosity function during the epoch of reionization (e.g. Finkelstein et al., 2015; Livermore et al., 2017) are demonstrating the important contribution of faint, star-forming galaxies to the ionizing photon budget at high redshift. In fact even galaxies with masses in the range  $M \gtrsim 10^{8-9} M_\odot$  are unable to sustain reionization (Bouwens et al., 2015; Rutkowski et al., 2016). We therefore require detailed studies of galaxies with masses in the range  $10^{6-8} M_\odot$ . Next, given the composition of the early universe in which they formed, galaxies during the epoch of reionization are expected to have a low metal content. Local analogs should similarly have low-metallicity stellar populations and therefore stars with high surface temperatures and hard UV spectra (Schaerer, 2003; Panagia, 2005). Accordingly, analog galaxies may be expected to have extreme line ratios that probe the ionization parameter (such as [O III]/[O II]; Nakajima et al., 2013) and

high-ionization lines present in their spectra (e.g. Erb et al., 2010; Stark et al., 2014, 2015). Additionally, these analog galaxies should be actively forming stars, and due to their low masses, should therefore have high specific star formation rates (sSFR), or the star formation rate normalized by the stellar mass. The equivalent width (EW) of the Balmer lines provides a proxy for the sSFR, since it measures the emission created from on-going or recent star formation (e.g., H $\alpha$  flux) divided by the strength of the continuum. The EW is therefore proportional to the age of the starburst. Even the more massive galaxies ( $10^9\text{--}10^7 M_\odot$ ) at  $z \sim 6$  are expected to have H $\alpha$  EWs of  $\sim 300 - 600 \text{ \AA}$  (Faisst et al., 2016), and the high-EW Green Pea galaxies are also found to have escape fractions of ionizing radiation of  $f_{\text{esc}} \sim 6 - 13\%$  (Izotov et al., 2016a,b).

We select galaxies from the SDSS-DR8 spectroscopic catalog and use the emission line and stellar mass measurements available in the MPA-JHU value-added catalog (Kauffmann et al., 2003; Brinchmann et al., 2004; Tremonti et al., 2004). This sample was originally created as part of a proposal to obtain comprehensive observations of local analogs covering multiple wavelengths and emission lines. Specifically, the targets were limited to the redshift range  $0.028 \lesssim z \lesssim 0.06$  to allow for Ly $\alpha$  imaging in the synthetic narrowband filter created with the *HST*'s Advanced Camera for Surveys (ACS) Solar Blind Channel (SBC) filters F125LP and F140LP (Hayes et al., 2009). We only consider galaxies with a high signal-to-noise detection of H $\alpha$  (S/N>20) and additionally require a S/N $\geq 3$  in [O II] $\lambda 3727$ , [O III] $\lambda 5007$ , and H $\beta$ . We then select sources based on their oxygen ratios and H $\beta$  equivalent width (EW):

- $\log_{10}([\text{O III}]/[\text{O II}]) \geq 0.51$ ,
- $\log_{10}(\text{EW}_{\text{H}\beta}) \geq 1.7 \text{ \AA}$ .

The resulting sample contains 50 galaxies, almost all of which have stellar masses  $< 10^8 M_\odot$ . The mass distribution of the 50 galaxies is shown in Figure 5.1, with that of LARS galaxies and the Green Peas for comparison. The median stellar mass of the sample is  $\sim 3.8 \times 10^7 M_\odot$ . The sample galaxies all appear blue in the SDSS imaging filters. They contain dense knots of emission, and many also have extended morphologies possibly indicating the presence of extended star formation or outflowing gas. The most extreme emitter has [O III] $\lambda 5007$ /[O II]  $> 40$ , and high-ionization lines such as He II and [Ar IV] are present in many of the galaxy spectra.

The [N II] $\lambda 6584$ /H $\alpha$  and [O III] $\lambda 5007$ /H $\beta$  line ratios of the sample are shown in the BPT diagnostic diagram (Baldwin et al., 1981) in Figure 5.2. A BPT diagram uses pairs of line ratios to separate galaxies based on whether their ionizing radiation is dominated

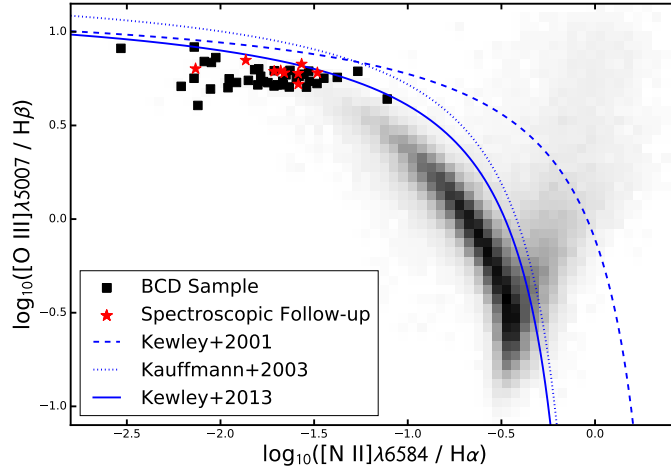


**Figure 5.2** The location of the BCD sample on the BPT diagnostic diagram, with emission line measurements from the MPH-JHU catalog. The density of SDSS sources in the MPH-JHU catalog is shown in grey, where we have selected galaxies in the same redshift range as the BCD sample,  $0.028 \gtrsim z \gtrsim 0.06$ , and consider only galaxies with a  $S/N \geq 3$  in all emission lines used for the diagram. The dotted line is the delineation between star-forming galaxies and AGN from Kauffmann et al. (2003), and the solid line is the updated, redshift-dependent classification curve from Kewley et al. (2013) plotted here for  $z = 0.04$ . The dashed line shows the maximum theoretical curve for starbursts from Kewley et al. (2001). Galaxies in between the solid and dashed lines are considered composite galaxies, with contributions from both starbursts and AGN. The BCD sample galaxies are all classified as star-forming or composite.

by star formation or by active galactic nuclei (AGN). The specific line ratios are chosen to be sensitive to the strength of ionizing radiation and to be close in wavelength so they are less susceptible to reddening from dust and uncertainties in the wavelength-dependent flux calibration. The ideal diagnostic emission lines should also be strong, unblended, optical lines for easy observation and to avoid the uncertainties associated with deblending. The aim of the BPT diagram is to separate galaxies based on the source of their ionizing emission. The emission lines in the spectra of star-forming galaxies are produced predominantly by gas ionized by O/B stars, while the more energetic ionizing radiation from AGN will enhance the strength of collisionally excited lines relative to the Balmer recombination lines. The line ratio diagnostics were developed through a combination of empirical relations and photoionization modeling (e.g. Baldwin et al., 1981; Veilleux & Osterbrock, 1987; Kewley et al., 2001; Kauffmann et al., 2003). For Figure 5.2, we choose the line ratios employed by Veilleux & Osterbrock (1987) and generally adopted in the literature. The dividing lines for separating the populations derived by Kewley et al. (2001), Kauffmann et al. (2003), and

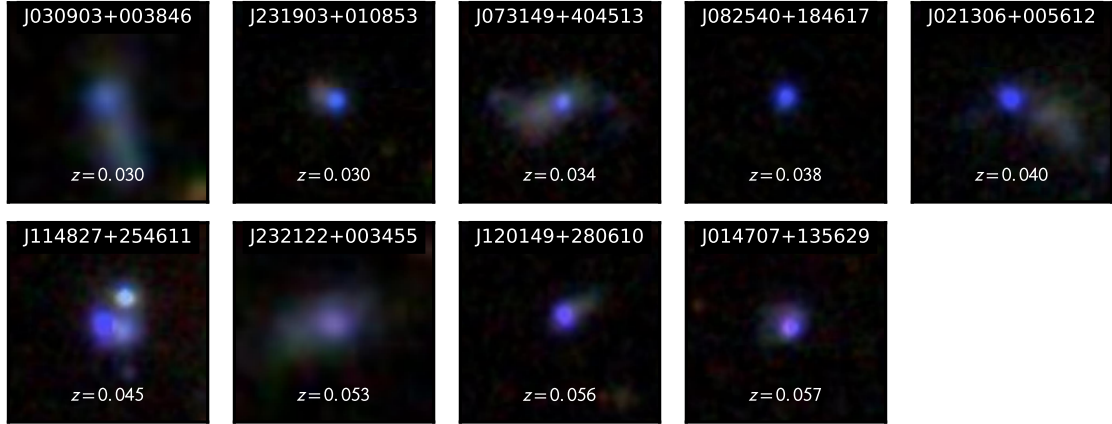


**Figure 5.3** SDSS postage stamps of the 9 BCDs targeted for high signal-to-noise spectroscopy. The BCDs all contain knots of emission that appear blue in the SDSS filters, and many also exhibit extended emission. The images are  $25''$  on a side.

Kewley et al. (2013) are shown in blue. The galaxies in the sample (black squares and red stars) all have a high  $[\text{O III}]\lambda 5007/\text{H}\beta > 0.5$ , but are almost entirely in the star-bursting section of the BPT. A few of the sources lie in or close to the region that typically identifies composite source with contributions from both star formation and AGN.

We observed 9 targets from this sample from 2016 to 2018. We describe the observations and data reduction in the following section. The SDSS postage stamps of these 9 BCDs are shown in Figure 5.3.

## 5.2 Observations

Five of the targets were observed with the Multi-Object Double Spectrographs<sup>1</sup> (MODS; Pogge et al., 2010) on the Large Binocular Telescope (LBT). There are two identical MODS spectrographs, each providing wavelength coverage from 3200 to 10000 Å through the use of a dichroic that transmits blue light ( $\lambda \lesssim 5700$  Å) and reflects red light ( $\lambda \gtrsim 5700$  Å) into a second spectrograph channel optimized for the longer wavelengths. We use the 400 line/mm G400L grating in the Blue channel with a dispersion of 0.5 Å/pixel and the 250 line/mm G670L grating in the Red channel (0.8 Å/pixel). The targets were observed with 60''-long slits with widths of 1'' and 1''.2, resulting in resolving power of  $R \sim 1000 - 1300$  at reference wavelengths for the two channels. All targets were observed for a total integration time of one hour. The atmospheric seeing during the majority of the observations was  $\lesssim 1''$ , but

<sup>1</sup> <http://abell.as.arizona.edu/~lbtsci/Instruments/MODS/mods.html>

**Table 5.1** Summary of Observations

Galaxy	$z$	Obs. Date	Instrument	Exptime	Seeing	$E(B - V)$
J030903.87+003846.9	0.030	2016 Oct 10,11	Magellan/LDSS3	$3 \times 1200, 3 \times 900$	$0''.55$	0.0897
J231903.23+010853.5	0.030	2016 Oct 10	Magellan/LDSS3	$5 \times 1200$	$0''.5$	0.0457
J073149.48+404513.2	0.034	2016 Nov 17	LBT/MODS	$3 \times 1200$	$1''.1$	0.0523
J082540.44+184617.2	0.038	2016 Nov 18	LBT/MODS	$3 \times 1200$	$0''.95$	0.0401
J021306.61+005612.4	0.040	2016 Nov 18	LBT/MODS	$3 \times 1200$	$1''.8$	0.0284
J114827.33+254611.7	0.045	2018 Feb 8	LBT/MODS	$3 \times 1200$	$0''.6 - 0''.7$	0.0169
J232122.50+003455.0	0.053	2016 Oct 11	Magellan/LDSS3	$8 \times 900$	$0''.6 - 0''.7$	0.0381
J120149.90+280610.6	0.056	2018 Feb 8	LBT/MODS	$3 \times 1200$	$0''.6 - 0''.7$	0.0161
J014707.04+135629.1	0.057	2016 Oct 11	Magellan/LDSS3	$7 \times 900$	$0''.6 - 0''.7$	0.0467

we note that the seeing increased to  $1''.8$  during the observation of J021306.61+005612.4. We perform the basic data reduction with the `modsCCDRed`<sup>2</sup> python package, which covers MODS-specific bias subtraction and flat field correction.

The remaining four targets were observed with the Low Dispersion Survey Spectrograph 3<sup>3</sup> (LDSS3) on the Magellan Clay telescope. We used the 1090 lines/mm volume phase holographic (VPH)-Blue grism, which provides wavelength coverage between  $\sim 3800$  and  $6200 \text{ \AA}$  with a spectral resolution of  $R \sim 1900$  and a dispersion of  $0.68 \text{ \AA/pixel}$ . The observations were obtained in long-slit mode with a  $4'.0 \times 0''.75$  slit. The pixel scale of LDSS3 is  $0''.188/\text{pixel}$ . The total exposure times ranged from 1.6 to 2 hours per target, with an average seeing of  $\sim 0''.6$  and airmasses of  $\sim 1.16-1.2$ . We increased the exposure time of the targets observed on October 11, 2016, to compensate for some light cirrus clouds in the second half of the night. The observations are summarized in Table 5.1. We used custom python scripts to perform basic data reduction including overscan correction and trimming, bias subtraction, and flat fielding. For consistency with the MODS spectra described above, we rotate the LDSS3 spectra by 90 degrees bringing the dispersion axis horizontal. The later steps of wavelength calibration, sky subtraction and flux calibration are applied in the same manner to both the LDSS3 and MODS observations and are described in Section 5.2.1.

### 5.2.1 Spectral Reduction and Calibration

We perform all calibration and processing with Python scripts developed specifically for this dataset. In this section we describe the following reduction steps: spectral derotation,

<sup>2</sup> <http://www.astronomy.ohio-state.edu/MODS/Software/modsCCDRed/>

<sup>3</sup> [www.lco.cl/Members/gblanc/ldss-3/ldss-3-user-manual-tmp](http://www.lco.cl/Members/gblanc/ldss-3/ldss-3-user-manual-tmp)

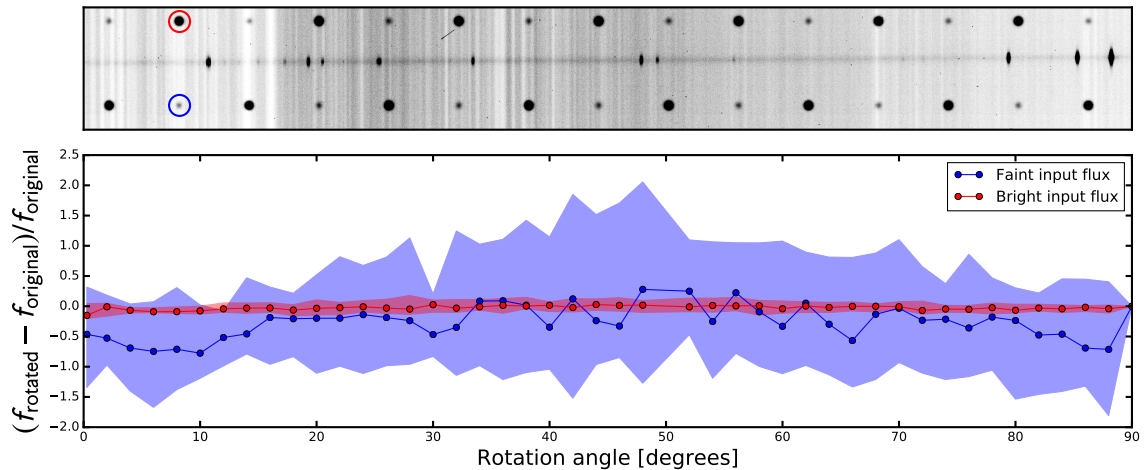


**Figure 5.4** A test for flux conservation under rotation. In the top panel, we show the point sources modeled as 2D Gaussians that were added above and below the trace of a spectrum. The image is then rotated through 90 degrees, and the difference in input and recovered flux is shown as a function of rotation angle in the bottom panel. Flux is conserved at the 0.5% level for the bright sources (red) and  $\sim 2\%$  for fainter sources (blue).

trace detection, wavelength calibration, sky subtraction, flux calibration, and the correction for Galactic extinction.

Both the MODS spectra and the LDSS3 spectra are slightly rotated with respect to the  $x$ -axis of the dispersed image. We wish to derotate the spectra in order to simplify calibration and extraction. However, we must first confirm that a rotation of the spectrum will conserve flux. We test for flux conservation by adding two-dimensional Gaussians to one of the Blue Channel flat-fielded MODS images, rotating the image through several angles, and measuring the flux of the extracted “point sources”. We add 30 Gaussians to the image, located above and below the trace of the target spectrum and covering the full wavelength range of interest. The Gaussians are normalized to have one of two input fluxes, one that is about half the integrated flux from the brightest emission line and one that is  $100\times$  fainter. The spectrum with the added Gaussians is shown in the top panel of Figure 5.4. The bottom panel shows the percent difference in fluxes measured for the original image and the rotated image as a function of the angle of rotation. We conclude that the flux is conserved at the 0.5% level for the brightest sources and  $\sim 2\%$  for fainter sources.

We next identify the trace of the spectrum in each exposure, which is a necessary step both for determining the angle by which to rotate the spectrum and for defining the extraction window. At each pixel along the dispersion direction, we fit the spectrum along

the cross-dispersion axis with a Gaussian. We use a central moving average with a window 5 pixels wide to smooth the spectrum before fitting. The trace is well-modeled by a line fit to the peaks of the Gaussian at each pixel step. With the trace defined, we calculate the rotation angles for the individual target exposures and derotate all target and associated arc lamp spectra used for calibration by the median angle. These median derotation angles range from  $\sim 0.3$  to 0.7 degrees.

Wavelength calibration<sup>4</sup> is performed across the full two-dimensional spectral image. Emission lines in the comparison lamp spectra are automatically detected in 20 separate apertures across the full spatial dimension of the image. The mapping of the pixel coordinates of each line to the proper wavelengths provides hundreds of sample points across the image. We then fit a fourth order two-dimensional polynomial function to these sample points using Levenberg-Marquardt least-squares minimization and apply it to all target spectra.

The sky is measured in two  $3''.75$  windows offset  $10''$  above and below the target trace. We take the median flux from all rows in the two sky windows to produce sky spectrum that is then subtracted from the entire image. We next remove cosmic rays from the individual exposures using a  $5\sigma$  outlier rejection for each pixel from the full stack of images, and finally median-combine all exposures. The MODS1 and MODS2 spectra are kept separate, and the one-dimensional spectra will be combined for increased signal-to-noise.

The SDSS spectrum for each target is used for flux calibration. We first extract the target spectrum from the two-dimensional median-combined image by summing the flux in each row in a window designed to match the SDSS fiber:  $3''$  window and centered on the SDSS `PLUG_RA` and `PLUG_DEC` coordinates. The goal is to compare the light from the exact portion of the galaxy that was covered by the SDSS fiber. After interpolating the SDSS spectrum onto the wavelength vector of the target spectrum, we mask out all emission lines and fit a continuum model to both spectra. The calibration function is approximated by the ratio of the SDSS and target continuum models normalized by the extraction width ( $3''$ ) to produce a per-pixel calibration. This wavelength-dependent function is then applied to the full dispersed image, so all future extractions will be flux-calibrated. We repeat this process, stepping the extraction windows both above and below the central position, to determine the uncertainty on the flux calibration. The uncertainty is then taken as the minimum and maximum difference between these windows and the original, central extraction.

We finally correct the spectra for the light absorbed through dust in the Milky Way. SDSS does not apply Milky Wave extinction corrections to the spectra in their data releases

---

<sup>4</sup> Custom Python scripts for wavelength calibration were developed in collaboration with M. S. Gordon.

because the survey includes a large number of Galactic stars. We obtain reddening estimates along the line of sight to each target from the NASA/IPAC Infrared Science Archive (IRSA) Galactic Reddening and Extinction Calculator.<sup>5</sup> We adopt the estimates Schlafly & Finkbeiner (2011), which is a recalibration of the reddening provided by Schlegel et al. (1998) based on SDSS spectra of stars in the Milky Way. Following Schlafly & Finkbeiner (2011), we assume a visual extinction to reddening ratio of  $A_V/E(B - V) = 3.1$ . Table 5.1 provides the reddening and  $A_V$  for each target. We use the extinction curve of Fitzpatrick (1999) and add the following correction to the observed fluxes  $f_{\text{obs}}$ :

$$f_{\text{corr}} = \frac{f_{\text{obs}}}{10^{-0.4 (k_\lambda E(B-V))}}. \quad (5.1)$$

This correction is applied to the full two-dimensional image so all extracted spectra will be corrected regardless of the extraction window used.

### 5.3 Early Results

So far we have completed the reduction and calibration for the 7 targets observed in 2016. In Figure 5.5, we show the spectrum of J021306.61+005612.4, observed with a seeing of almost  $2''$ , as an example of the quality of the spectra even under poor conditions. The strong [O III] emission can be seen relative to the strength of both the [O II] and  $H\alpha$  lines. High-ionization lines are also present in the spectrum, such as He II  $\lambda 4686$  and [Ar IV] (with ionization energies of 54.5 and 59.6 eV, respectively), indicating a hard ionizing spectrum. The He II and [Ar IV] lines are shown in the bottom panel of Figure 5.5.

In Figure 5.6, we show the [O III] $\lambda 5007$ /[O II] ratio of the observed sample as a function of their [O I]/[O III] $\lambda 5007$  ratio (left panel) and  $H\beta$  EWs (right). We also show all star-forming (bptclass = 1; Brinchmann et al., 2004) galaxies in the SDSS catalog in the redshift range  $0.01 \leq z \leq 0.3$  ans with  $S/N_{[\text{O I}]\lambda 6300} \geq 5$  in black. For this comparison, we have dereddened the SDSS emission line fluxes using the Balmer decrement,  $H\alpha/H\beta$ , to estimate the reddening (e.g. Momcheva et al., 2013):

$$E(B - V) = \frac{2.5}{\kappa_{\lambda H\beta} - \kappa_{\lambda H\alpha}} \log_{10} \left[ \frac{(f_{H\alpha}/f_{H\beta})_{\text{obs}}}{(f_{H\alpha}/f_{H\beta})_{\text{int}}} \right] \quad (5.2)$$

where  $(f_{H\alpha}/f_{H\beta})_{\text{int}} = 2.86$  is the intrinsic ratio for Case B recombination and for an electron density of  $10^2 \text{ cm}^{-2}$  and temperature of 10000 K (Osterbrock, 1989). We assume the Calzetti et al. (2000) extinction curve, and  $\kappa_{\lambda H\alpha}$  and  $\kappa_{\lambda H\beta}$  are the values of the extinction curve at 6563 and 4861 Å. All seven BCDs (red stars) lie at the extreme ends of the SDSS population.

<sup>5</sup> [irsa.ipac.caltech.edu/applications/DUST/](http://irsa.ipac.caltech.edu/applications/DUST/)

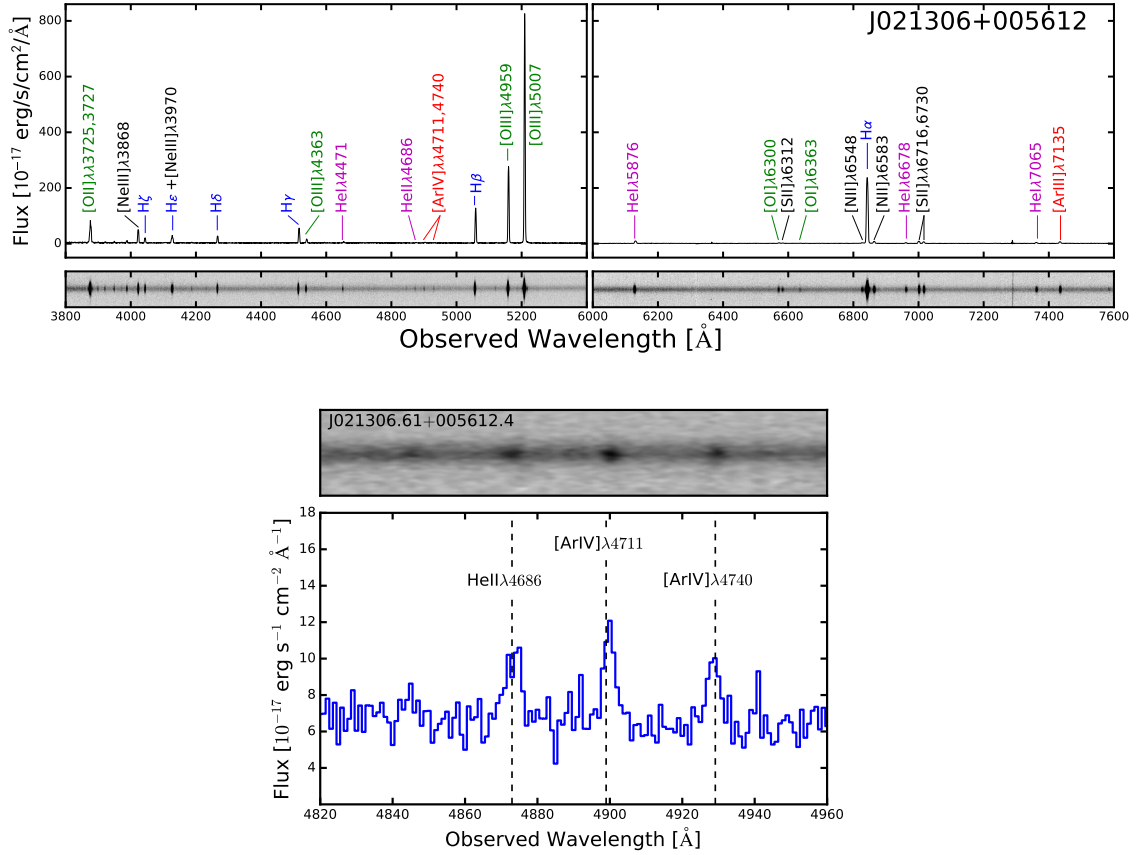


**Figure 5.5** The spectrum of J021306.61+005612.4 obtained with MODS on the LBT. *Top panel:* the full spectrum showing the coverage from the Blue Channel (left) and Red Channel (right). Many of the emission lines are labeled. *Bottom panel:* Zooming in on the wavelength range showing the high-ionization lines He II and [Ar IV].

They have very similar properties as the sample from Izotov et al. (2016b) (green squares), which have escape fractions of LyC radiation of  $\sim 6 - 13\%$ . The more extreme sample from Izotov et al. (2017) (blue diamonds) were selected as candidate LyC leakers based on their [O III]/[O II] ratios but have not yet been confirmed.

### 5.3.1 Spatial extent of emission lines

We also note that the emission lines in many of the spectra are extended, matching the morphologies visible in the SDSS postage stamps in the cases where the slit was aligned with the extended emission. An example of this extended emission is shown in the top panel of Figure 5.7. This spatially-resolved emission allows us to measure line fluxes and ratios at a range of positions, as shown in the bottom panel. Here we have extracted one-dimensional spectra in windows 4 pixels wide, stepping across the full extent of the

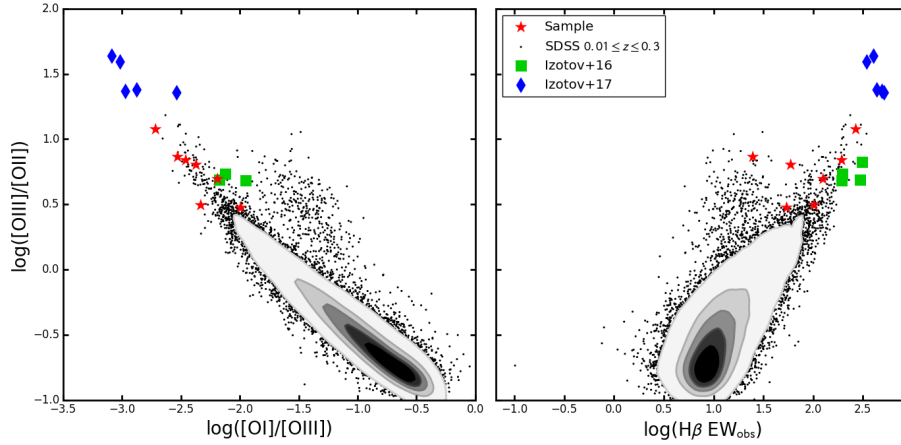


**Figure 5.6** *Left panel:* The  $[\text{O III}]\lambda 5007/[\text{O II}]$  and  $[\text{O I}]\lambda 5007/[\text{O III}]\lambda 5007$  ratios of the 7 BCDs we have analyzed so far. We compare the line ratios with those from the sample of Izotov et al. (2016b) (green squares), the sample of Izotov et al. (2017) (blue diamonds), and the SDSS galaxies in the redshift range  $0.01 \leq z \leq 0.3$ . The contours contain 20, 40, 60, 80, and 98% of the total SDSS galaxies. *Right panel:* The  $[\text{O III}]\lambda 5007/[\text{O II}]$  ratio as a function of the  $\text{H}\beta$  EW. The BCDs presented in this chapter have line ratios and  $\text{H}\beta$  EWs that are similar to those of known and expected LyC leakers.

emission. The  $[\text{O III}]/\text{H}\beta$  ratio changes by a factor of  $\sim 2$  depending on the distance from the continuum. A single measurement of the line ratio from the total emission of this source will wash out this structure.

## 5.4 Discussion and Future Work

The results presented in the previous section are preliminary. Once all 9 targets are completely reduced and calibrated, we will undertake a comprehensive study of galaxy properties that can be inferred from the spectra. We plan to investigate the star formation rates, stellar population ages, feedback mechanisms, gas metallicity, and gas velocities. In this section we briefly describe our plans for the future analysis of this BCD sample. This work will be essential to help understand the faint, low-mass galaxies that JWST will easily image during reionization.

We begin by discussing some emission line measurements accessible in our spectroscopic observations that can provide an estimate of important galaxy properties. For example, Chevallard et al. (2018) show a correlation between the production rate of LyC photons and the equivalent width of the  $[\text{O III}]\lambda\lambda 4959, 5007$  doublet. This correlation is expected because in lower-metallicity gas, there is less cooling from metals leading to a hotter electron

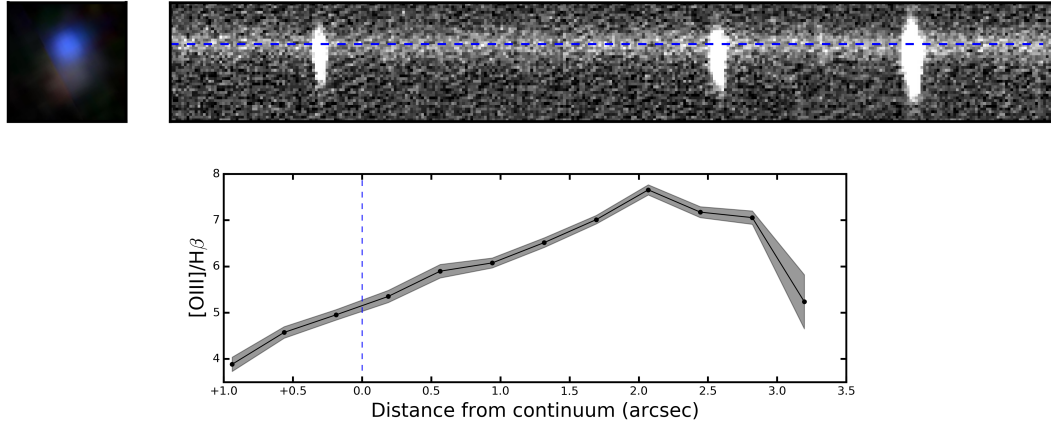


**Figure 5.7** We show the two-dimensional spectral image of  $H\beta$  and the  $[O\text{ III}]\lambda\lambda 4959, 5007$  doublet of J231903+010853 as an example of the spatially extended emission we measure for many BCDs in the sample. The SDSS postage stamp (left) and the MODS spectrum (right) are spatially aligned and each span  $8''$  in the  $y$  direction, or  $\sim 4.8$  kpc at the redshift of this galaxy. In the bottom panel, we show the  $[O\text{ III}]\lambda 5007/H\beta$  ratio measured as a function of the distance from the center of the continuum, which is identified by the dashed blue line.

temperature and therefore more collisionally excited atoms such as  $[O\text{ III}]$ . Larger  $[O\text{ III}]$  EWs will therefore be observed in low-metallicity systems with young stellar populations — the same properties that are expected to produce high fractions of ionizing radiation. As another example, Izotov et al. (2017) provide a method for estimating the electron density and optical depth in H II regions using the He I  $\lambda 3889$ ,  $\lambda 6678$ , and  $\lambda 7065$  lines. These recombination lines are also partially enhanced by collisional excitation making them sensitive to the electron density. It may therefore be possible to use the He I line ratios to determine whether the emission from these star-forming galaxies is coming from density-bounded regions, where the surrounding neutral hydrogen has been completely ionized allowing LyC radiation to escape.

For a more robust analysis, we will compare the spectra with ionization models computed with CLOUDY (Ferland et al., 2017) to determine galaxy properties such as gas temperature, metallicity, and ionizing photon production. CLOUDY<sup>6</sup> is a plasma simulation code that predicts the observed spectral features of a gas that is subject to a radiation field. Given an input ionizing source and geometry, the code models the resulting ionization state of the atomic and molecular gas as a function of density and temperature. The predicted emission line strengths and line ratios can then be compared with observations to derive a best-fit model of the observed source. This process generally involves fitting spectral templates

<sup>6</sup> [www.nublado.org](http://www.nublado.org)

from stellar population models such as those of STARBURST99 (Leitherer et al., 1999) or Bruzual & Charlot (2003) to a galaxy’s continuum emission. The best-fit template is then used as the input ionizing source for CLOUDY’s calculations. We aim to improve on the predictive power of this method by using CLOUDY models to simultaneously fit the continuum and emission line fluxes. Given the spatially-extended nature of the MODS and LDSS3 spectra, we can perform this analysis at a range of distances from the central, compact core of each galaxy. The variation in emission line ratios, composition, and inferred ionization states may provide insight into the properties of any extended star formation or outflowing gas. Such an analysis is especially useful given that supernovae-driven outflows and winds from Wolf-Rayet stars may facilitate the escape of ionizing radiation from star-forming regions by creating gaps in the neutral hydrogen of the interstellar medium (e.g. Heckman et al., 2011; Jaskot & Oey, 2013; Borthakur et al., 2014; Jaskot et al., 2017).

#### 5.4.1 High [O III]/[O II] and the Escape of Lyman Continuum Photons

In evaluating the contribution of low-mass, star-forming galaxies to reionization, it is crucial to understand both their total ionizing radiation output and how much of this ionizing radiation is capable of reaching the IGM. In order to maintain reionization, high-redshift star-forming galaxies need escape fractions of 15–20% (Ouchi et al., 2009; Finkelstein et al., 2015; Rutkowski et al., 2016). Yet despite significant effort to detect LyC radiation from galaxies (Siana et al., 2007, 2010; Cowie et al., 2009; Vanzella et al., 2010; Sandberg et al., 2015; Grazian et al., 2016; Guaita et al., 2016; Rutkowski et al., 2016; Vasei et al., 2016), very few with  $f_{\text{esc}} \gtrsim 20\%$  have been detected (e.g., de Barros et al., 2016; Vanzella et al., 2016; Bian et al., 2017; Izotov et al., 2018).

Galaxies with extreme [O III]/[O II] ratios may be good candidates for LyC leakage (Jaskot & Oey, 2013; Nakajima & Ouchi, 2014), making these BCDs important targets for additional analysis. Yet a strong [O III]/[O II] ratio may not be a reliable indication of escaping radiation, as it is sensitive to the ionization parameter,  $f_{\text{esc}}$ , and heating from radiative shocks among other effects (Giammanco et al., 2005; Jaskot & Oey, 2013; Izotov et al., 2017). More LyC observations of galaxies with extreme [O III]/[O II] are needed to quantify this correlation with  $f_{\text{esc}}$  and to test other proposed indicators such as the He I line ratio diagnostic proposed by (Izotov et al., 2017).

## Chapter 6

# Forecasts for ESA's Euclid Dark Energy Mission

### 6.1 Introduction

The nature of the dark energy, a possible explanation of the observed cosmic acceleration (Riess et al., 1998; Perlmutter et al., 1999), is one of the most important unsolved problems in cosmology today. A galaxy redshift survey enables us to measure the cosmic expansion history via the measurement of baryon acoustic oscillations, as well as the growth history of large scale structure via the measurement of large scale redshift-space distortions. The combination of these two measurements allows us to differentiate between an unknown energy component and the modification of general relativity as the cause of the observed cosmic acceleration (Guzzo et al., 2008; Wang, 2008).

Two future space missions, ESA's Euclid (Laureijs et al., 2011, 2012) and NASA's WFIRST-AFTA (Green et al., 2012; Spergel et al., 2015), will carry out mutually complementary galaxy redshift surveys to probe dark energy. Both Euclid and WFIRST will use  $H\alpha$  and [O III] selected emission line galaxies as tracers of the large scale structure at  $1 \lesssim z \lesssim 2$  ( $H\alpha$ ) and  $2 \lesssim z \lesssim 2.7$  ([O III]). The uncertainties in the cosmological parameters derived from a Baryonic Acoustic Oscillations survey are inversely proportional to the number of galaxies used in the survey. To optimize these redshift surveys for the study of dark energy, it is therefore critical to have a reliable and sufficiently precise knowledge of the expected numbers of  $H\alpha$  and [O III] galaxies in the survey volume.

In the redshift range of interest for the dark-energy surveys ( $0.7 < z < 2.2$ ), existing  $H\alpha$  and [O III] luminosity function (LF) measurements show large uncertainties and are often inconsistent with one another. In the relevant redshift range,  $H\alpha$  and [O III] LFs are

being estimated with two main techniques (Shim et al., 2009; Colbert et al., 2013; Sobral et al., 2013; Mehta et al., 2015). Ground-based narrowband surveys cover large areas, but are limited by very thin redshift slices ( $\Delta(z) \sim 0.03$ ). Space-based spectroscopic surveys, with NICMOS first and WFC3 more recently, simultaneously probe a large redshift range ( $\Delta(z) \sim 0.7$ ) over much smaller areas. Despite the enormous effort, the uncertainties on the LFs remain substantial. These uncertainties prevent accurate forecasts of dark energy constraints for *Euclid* and WFIRST.

In addition to accurate number counts, cosmological N-body simulations will be needed to generate realistic mock catalogs for forecast predictions for both surveys. The first version of the *Euclid* Flagship mock galaxy catalog was released in June, 2017, and contains more than  $2 \times 10^9$  galaxies distributed over *Euclid*'s cosmological survey volume. The mocks for the WFIRST galaxy redshift survey will be more challenging because of its greater depth and higher spectral resolution. It is crucial that these simulations correctly assign line fluxes to galaxies as a function of galaxy size, luminosity and mass. The proper assignment of galaxy properties is necessary to correctly account for observational selection effects, which depend on galaxy size as well as emission line signal-to-noise (S/N) and equivalent width (EW; see Chapter 3). Ultimately, suitable simulations should be able to reproduce the observed joint distribution of emission line fluxes and these galaxy properties.

While the details of the WFIRST-AFTA survey are still under development, the *Euclid* Consortium is in the process of finalizing the observing strategy for the *Euclid* mission. In this chapter, we therefore focus on the projected characteristics for *Euclid* and use available slitless spectroscopic data from *HST* grism surveys to make predictions for this survey. In what follows we calculate the number densities of  $H\alpha$  and [O III]-emitting galaxies, measure the size and equivalent width distributions for  $H\alpha$ -emitters, and quantify the expected number of contaminating redshifts from mis-identified single emission lines as a function of survey depth and redshift. We estimate the number density of  $H\alpha$ -emitters available to dark energy searches by applying selection criteria matching the *Euclid* Wide Survey. We note, however, that similar predictions can be tuned for WFIRST by adjusting the selection criteria appropriately.

## 6.2 *Euclid* Sample

For this work, we use existing spectroscopic data from two *HST* grism programs: the WISP and 3D-HST+AGHAST surveys (see Section 6.2.1 below). Both programs perform near-infrared slitless spectroscopic observations using one or both of the the WFC3 IR grisms:

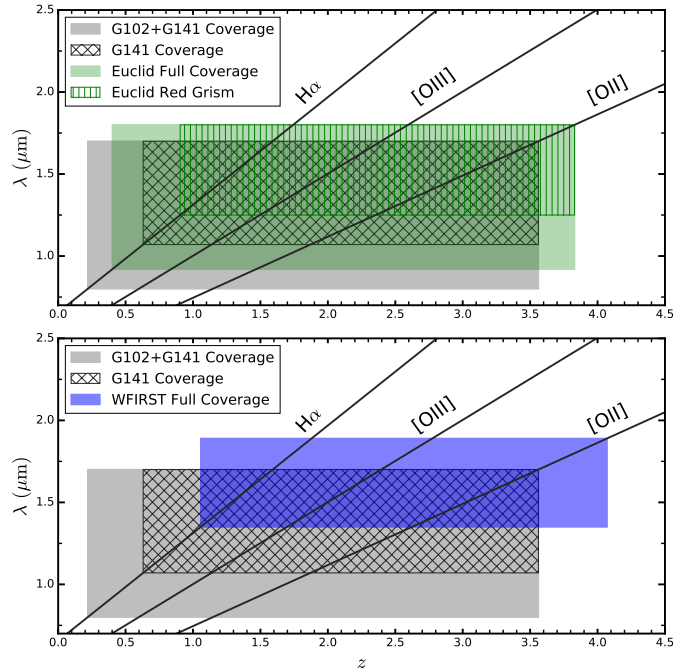


**Figure 6.1** The redshift and wavelength coverage for planned and existing slitless surveys. The coverage of the WFC3 grisms (gray) is compared with that of Euclid (green, top) and the current plan for WFIRST (bottom, blue). The wavelengths of  $H\alpha$ ,  $[O III]$ , and  $[O II]$  as a function of redshift are designated by black lines. The shaded and hatched regions indicate the redshift range in which at least one of these three emission lines is accessible to the given survey. The coverage of the WFC3 grisms is comparable to that planned for Euclid and WFIRST, making the HST grisms important tools for exploring the performance of the future surveys.

G102 ( $0.8 - 1.1 \mu\text{m}$ ,  $R \sim 210$ ) and G141 ( $1.07 - 1.7 \mu\text{m}$ ,  $R \sim 130$ ). The wavelength range of the G141 grism in particular covers a comparable redshift range as that planned by the Euclid and WFIRST dark energy surveys (see Figure 6.1). The WISP and 3D-HST observations together cover a total area of  $0.56 \text{ degree}^2$ , which is approximately equal to the field-of-view of the Euclid spectrograph (NISIP).

The survey characteristics of WISP and the creation of the emission line catalog are presented in Chapter 2. In the following section, we briefly describe the specifics of the 3D-HST+AGHAST survey and the emission line measurements we perform for these data. We discuss the creation of the sample that will be used in calculating predictions for the future Euclid observations in Section 6.2.2.

### 6.2.1 The 3D-HST+AGHAST Survey

The 3D-HST Survey (PI: P. van Dokkum; Brammer et al., 2012; Skelton et al., 2014; Momcheva et al., 2016) and the AGHAST Survey (PI: B. Weiner; Weiner, 2009) together obtained spectroscopic observations of the CANDELS (Grogin et al., 2011; Koekemoer et al., 2011) fields. In  $\sim 150$  pointings, the 3D-HST+AGHAST Survey covered each field to a uniform two-orbit depth, including G141 observations and direct imaging in the F140W filter. We add the 3D-HST+AGHAST pointings from the AEGIS, COSMOS, GOODS-North (GOODS-N) and GOODS-South (GOODS-S) fields,  $\sim 507$  arcmin<sup>2</sup> in total, to the WISP fields. Including these fields in our analysis has several benefits in addition to the increase in area coverage. With the extensive multi-wavelength catalogs available for the well-studied CANDELS fields, we can identify regions in color space indicative of mis-identified single emission lines (see Section 6.4.3).

The 3D-HST+AGHAST team has released a catalog with emission line measurements for all galaxies detected in imaging (Momcheva et al., 2016). Their method involves combining the CANDELS photometry with the grism spectroscopy to determine augmented photometric redshifts, which are then used as a prior for detecting and measuring emission lines in the grism data. The *Euclid* Wide survey observations will, at a minimum, include imaging in the *Y*, *J*, and *H* filters of the NISP instrument as well as the very broadband VIS filter covering  $\sim 5500 - 9000$  Å. While additional ground-based imaging in the *g*, *r*, *i*, and *z* bands will be obtained, the SEDs of sources will not be as fully sampled as in the CANDELS fields. The amount of information *Euclid* obtains for each source will be closer to the level obtained in WISP observations. We therefore reprocess all 3D-HST+AGHAST data in a consistent manner with the WISP fields. We note, however, that time scales and effort required to run even the improved WISP emission line procedure on all 15,000 degree<sup>2</sup> of the *Euclid* Wide survey will be impossibly unrealistic. Alternative emission line detection algorithms will be needed, such as the citizen science pilot program described in Dickinson et al. (2018) or the integration of machine learning and human classification such as that of Beck et al. (2018)

Rutkowski et al. (2016) describe the reduction of the 3D-HST data using the WISP pipeline with minor modifications to account for the dithered observations. Emission line detection and measurement are performed using the first version of the WISP line finding procedure, described in Section 2.4 and in Colbert et al. (2013). The completeness corrections from Colbert et al. (2013) are adopted for this 3D-HST+AGHAST catalog to match the line finding method.

## 6.2.2 Sample Selection

The *Euclid* Mission will be composed of two surveys. The Wide Survey aims to obtain redshift measurements for 1.5 billion galaxies in 15000 degrees<sup>2</sup>, using the *Euclid* Red grism (1.25 – 1.85 $\mu\text{m}$ ,  $R \sim 380$ ) and achieving a  $3.5\sigma$  line flux sensitivity of  $2 \times 10^{-16}$  erg s<sup>-1</sup> cm<sup>-2</sup> for a 0''.5 extended source. The Deep Survey will cover 40 degrees<sup>2</sup> in three separate pointings, reaching a depth of  $6 \times 10^{-17}$  erg s<sup>-1</sup> cm<sup>-2</sup>. In addition to the Red grism, the Deep Survey will make use of a Blue grism (0.9 – 1.3 $\mu\text{m}$ ,  $R \sim 250$ ). In this chapter, we focus on observational constraints relevant for the Wide Survey but note that *HST* grism observations are valuable for Deep Survey predictions as well.

From the full WISP+3D-HST catalog, we create a Wide Sample (WS) of emission line galaxies (ELGs) selected to match *Euclid*'s planned Wide Survey. We leave the construction of a Deep Sample (DS) for future work, but capitalize on the depth of the WISP+3D-HST catalog to discuss contamination and redshift mis-identification in Section 6.4.3. We begin by imposing a selection in emission line S/N and observed EW to match the completeness limits of the full WISP+3D-HST catalog:  $S/N > 5$  and  $EW_{\text{obs}} \geq 40\text{\AA}$  (see Section 2.4.4 as well as Colbert et al., 2013). The remaining selection criteria depend on emission line flux and observed wavelength. For the WS, we select sources with at least one emission line with flux  $f \geq 2 \times 10^{-16}$  erg s<sup>-1</sup> cm<sup>-2</sup> and  $\lambda_{\text{obs}} \geq 1.25\mu\text{m}$ . The DS will include additional sources down to  $f \geq 6 \times 10^{-17}$  erg s<sup>-1</sup> cm<sup>-2</sup> and  $\lambda_{\text{obs}} \geq 0.9\mu\text{m}$ . Given the drop in the sensitivity of the G141 grism at wavelengths longer than  $\sim 1.7\mu\text{m}$ , this wavelength selection results in H $\alpha$  ([O III]) coverage from  $0.9 \leq z \leq 1.6$  ( $1.5 \leq z \leq 2.4$ ) for the WS and  $0.4 \leq z \leq 1.6$  ( $0.8 \leq z \leq 2.4$ ) for the DS, respectively. See Table 6.1 for a summary of the selection criteria.

The WS consists of 1278 ELGs ( $\sim 2270$  degree<sup>-2</sup>), the majority of which are H $\alpha$ -emitters below redshift  $z \lesssim 1.6$  (85%, see Figure 6.2). There are 73 galaxies in the redshift range  $1.5 \lesssim z \lesssim 1.6$ , where both H $\alpha$  and [O III] are accessible to *Euclid*'s Red grism. Of these, only 8 ( $\sim 14$  degree<sup>-2</sup>) have both H $\alpha$  and [O III] bright enough for the *Euclid* WS selection. The median H $\alpha$ /[O III] of these 8 galaxies is  $\sim 1.4$ , though this ratio depends on line flux, as can be seen in Colbert et al. (2013) and Mehta et al. (2015). Additionally, there are 26 sources ( $\sim 46$  degree<sup>-2</sup>) with emission lines brighter than the flux limit yet fainter than  $H \geq 24$  magnitude, (the sources to the right of the dashed line in the bottom panel of Figure 6.2). The *Euclid* NISP instrument will reach a  $5\sigma$  sensitivity of 24 magnitude in all three of its imaging filters. Fainter sources will of course be in the photometric catalogs, but the current observing strategy calls for spectral extraction only for sources brighter than 24. This strategy will help minimize the contamination and spectral confusion from

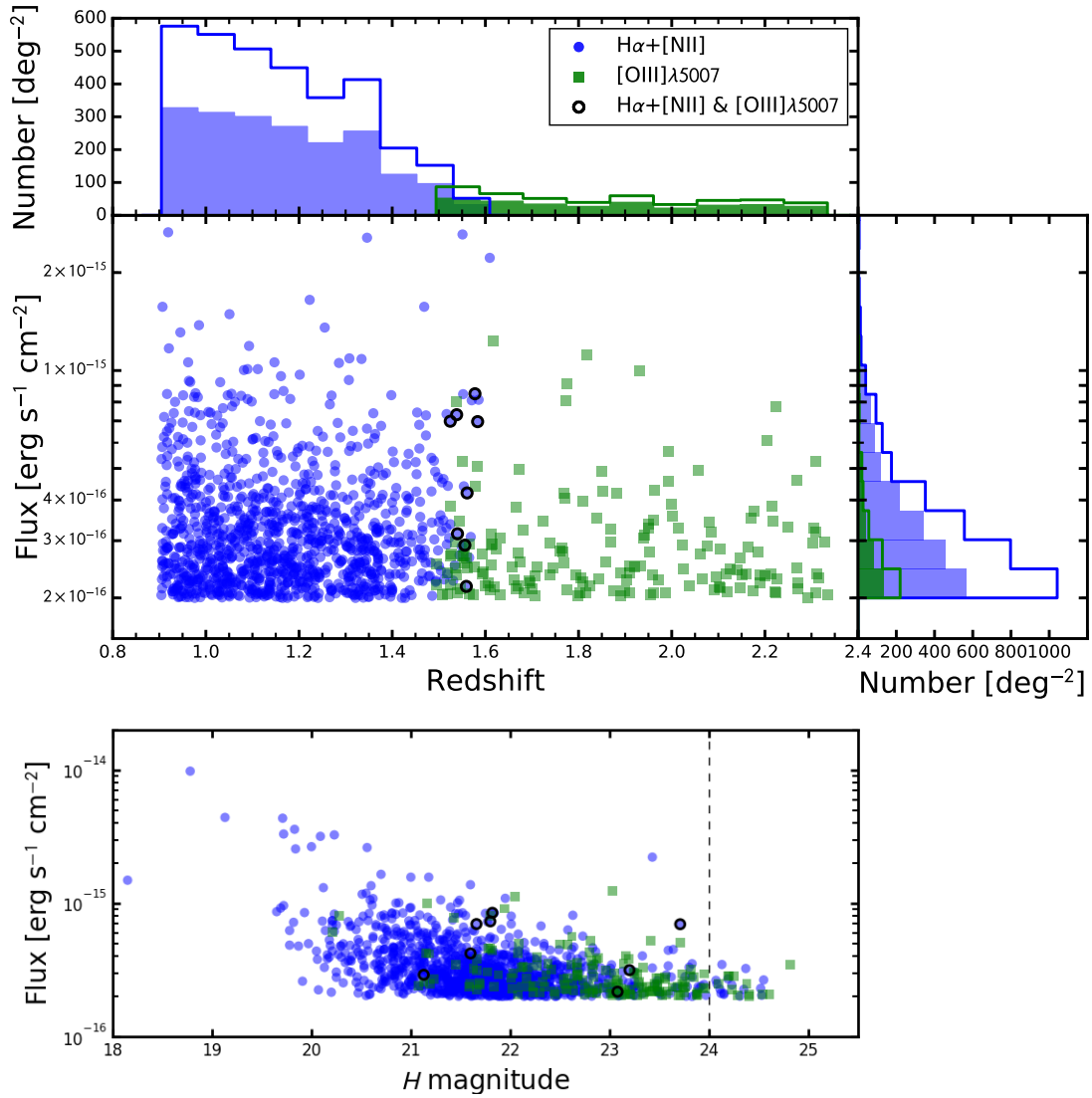


**Figure 6.2** The  $H\alpha+[N II]$  and  $[O III]\lambda 5007$  line fluxes of sources in the Wide Sample as a function of redshift (top panel) and  $H$  magnitude (bottom panel). The handful of sources with both lines detected at the redshift and depth of the Euclid Wide Survey are identified by black circles. The majority of sources in the WS are  $H\alpha+[N II]$ -emitters at  $z \lesssim 1.5$ . The sources to the right of the dashed line will be missed if Euclid spectral extraction is only performed for sources with  $H < 24$ .

**Table 6.1** Euclid Sample Selection Criteria

	<b>Euclid WS</b>	<b>Euclid DS</b>
S/N	$\geq 5$	$\geq 5$
$EW_{\text{obs}}$	$\geq 40 \text{ \AA}$	$\geq 40 \text{ \AA}$
Flux	$\geq 2 \times 10^{-16} \text{ erg s}^{-1} \text{ cm}^{-2}$	$\geq 6 \times 10^{-17} \text{ erg s}^{-1} \text{ cm}^{-2}$
$\lambda_{\text{obs}}$	$\geq 12500 \text{ \AA}$	$\geq 9200 \text{ \AA}$
$H\alpha$ Coverage	$0.9 \leq z \leq 1.6$	$0.4 \leq z \leq 1.6$
[O III] Coverage	$1.5 \leq z \leq 2.4$	$0.8 \leq z \leq 2.4$
[O II] Coverage	$2.5 \leq z \leq 3.5$	$1.5 \leq z \leq 3.5$

Note — The Euclid DS selection criteria are presented here for reference as we have not yet created an official DS. In Section 6.4.3, however, we extend our analysis of the WISP+3D-HST catalog down to the flux and wavelength limits of the Deep Survey in order to explore sample contamination from redshift misidentification.

overlapping spectra, but at the cost of  $\sim 50$  sources per degree<sup>2</sup> that are real ELGs. The decision to extract spectra for fainter sources will depend on the expected increase in the rates of contamination.

We note that given the spectral resolution of the planned missions,  $H\alpha$ + [N II] will be blended for many sources in Euclid (and likely WFIRST) spectra. This is also the case for the observations obtained with the WFC3 grisms. For the purpose of predicting the number, size and EW distributions of the  $H\alpha$ -emitters that will be detected by the dark energy surveys, we do not correct the observed  $H\alpha$  fluxes for the contribution by [N II]. Unless otherwise noted, all measurements presented here of  $H\alpha$  flux, EW, and size refer to  $H\alpha$ + [N II]. However, Euclid will resolve [N II] and  $H\alpha$  for small, compact objects, and so [N II]-corrected  $H\alpha$  number counts will also be necessary for accurate predictions. We will explore the [N II] correction which depends on galaxy stellar mass (e.g. Erb et al., 2006; Faisst et al., 2018), in future work. Similarly, the [O III] $\lambda\lambda 4959, 5007$  doublet is partially blended at the resolution of the WFC3 grisms. The [O III] fluxes are obtained by fitting two blended Gaussians to the doublet line profile using amplitudes fixed in a 1 : 3 ratio. Since the [O III] doublet will be resolved by Euclid and WFIRST, we correct the observed [O III] $\lambda 5007$  flux for the contribution from the 4959 $\text{\AA}$  line. All measurements presented here of [O III] flux therefore refer to [O III] $\lambda 5007$  only.

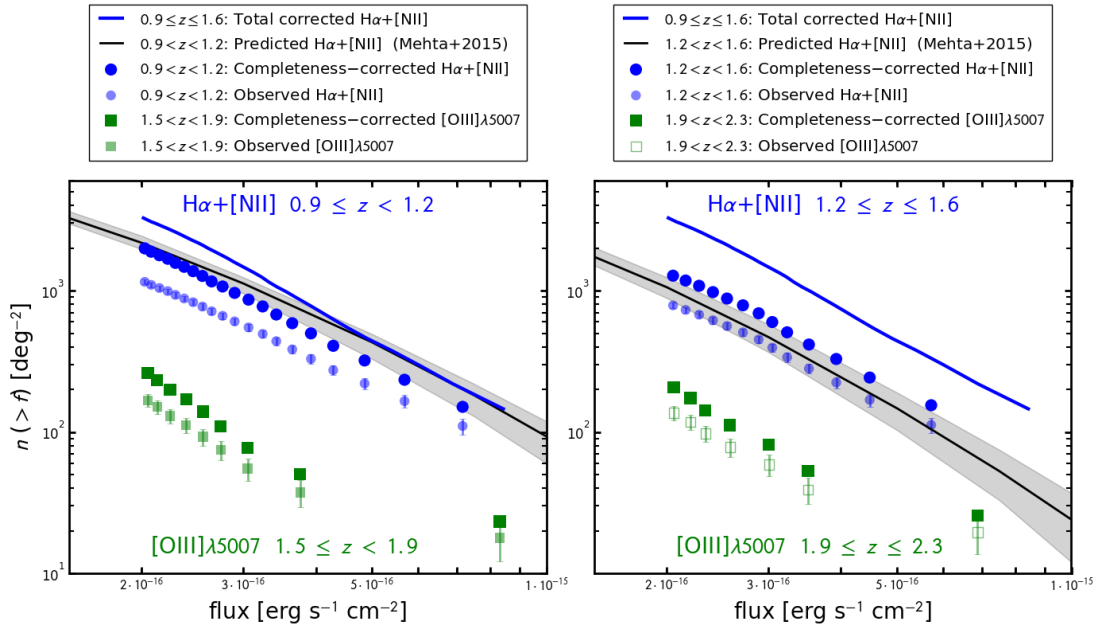


**Figure 6.3** The cumulative number density of  $\text{H}\alpha + [\text{N II}]$  and  $[\text{O III}]\lambda 5007$ -emitters in the WS, identified by blue circles and green squares, respectively. We have separated the number counts into two redshift bins to demonstrate the evolution in the number density of each line with redshift. The black curve shows the  $\text{H}\alpha + [\text{N II}]$  number counts predicted by Mehta et al. (2015), based on an earlier sample from the WISP emission line catalog. The fainter points show the observed number counts and the larger, solid symbols indicate those that have been corrected for survey incompleteness. The blue curve shows the total, completeness-corrected  $\text{H}\alpha + [\text{N II}]$  number density across the full redshift range.

## 6.3 Results

### 6.3.1 Emission Line Number Counts

We begin by considering the number of ELGs that meet the selection criteria for the Euclid WS. Galaxies emitting  $\text{H}\alpha + [\text{N II}]$  are the main target for the dark energy science, as they will be used to trace the large scale structure at  $z \sim 1 - 2$ . There are  $\sim 1940$   $\text{H}\alpha + [\text{N II}]$ -emitters per degree<sup>2</sup> in the WS from  $0.9 \leq z \leq 1.6$  and an additional  $\sim 290$   $[\text{O III}]\lambda 5007$ -emitters per degree<sup>2</sup> up to  $z = 2.3$ . Correcting these observed counts for the incompleteness of the WFC3 grism data, there are  $\sim 3270$  ( $\text{H}\alpha + [\text{N II}]$ ) and  $\sim 440$  ( $[\text{O III}]\lambda 5007$ ) per degree<sup>2</sup>, respectively.

The cumulative area number density of both  $\text{H}\alpha + [\text{N II}]$ -emitters and  $[\text{O III}]\lambda 5007$ -emitters is shown in Figure 6.3. The number counts are separated into two redshift bins to highlight the evolution in the number density with redshift. There is a factor of more than

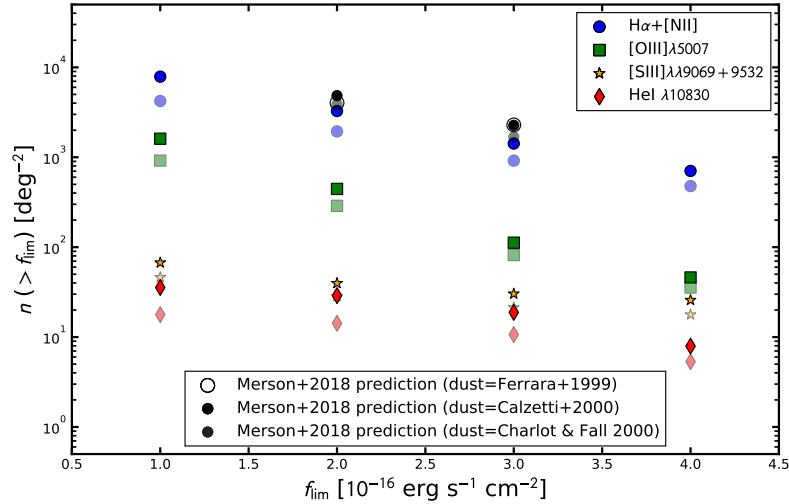


**Figure 6.4** The total number density of emission line sources brighter than a specified flux limit. The fainter symbols show the observed number densities and the brighter symbols show the completeness-corrected counts. We compare these number densities with the predictions from Merson et al. (2018). Though their predictions are larger than the WISP+3D-HST counts, Merson et al. (2018) use the entire redshift range (out to  $z \sim 1.8$ ) and the *HST* grism can only observe  $\text{H}\alpha + [\text{N II}]$  up to  $z \sim 1.6$ . We show here the number of emission line sources brighter than

1.5 times more  $\text{H}\alpha + [\text{N II}]$ -emitters at  $0.9 \leq z < 1.2$  than at  $1.2 \leq z \leq 1.6$ . The observed number counts are in good agreement with the predictions from Mehta et al. (2015), calculated using a subset of WISP fields from the earlier data reduction and original line finding procedure. In addition to the WS sources with  $\text{H}\alpha + [\text{N II}]$  and  $[\text{O III}]\lambda 5007$  emission, there are a handful of sources at lower redshift ( $z \sim 0.4$ ) that were selected due to the strength of the  $[\text{S III}]$  and He I emission. The number counts with and without completeness corrections of all selected emission lines are presented in Table 6.2. In Figure 6.4, we also compare the observed number counts with predictions from Merson et al. (2018), who use the GALACTICUS galaxy formation model and the dust attenuation methods from Ferrara et al. (1999), Calzetti et al. (2000), and Charlot & Fall (2000) to predict  $\text{H}\alpha + [\text{N II}]$  number counts in the full Euclid redshift range  $0.9 \leq z \leq 1.8$ . Merson et al. (2018) over-predict the  $\text{H}\alpha + [\text{N II}]$  counts compared to the WISP+3D-HST observations, finding  $\sim 600$ – $1500$  more galaxies per square degree depending on the dust model.

The predictions from WISP+3D-HST observations slightly underestimate the numbers of galaxies that Euclid will observe. We remind the reader that the upper wavelength of the Euclid Red grism is  $\sim 18500 \text{ \AA}$ ,  $1500 \text{ \AA}$  redder than the WFC3 G141 grism. The Euclid  $\text{H}\alpha + [\text{N II}]$  and  $[\text{O III}]\lambda 5007$  observations will therefore extend out to  $z \sim 1.8$  and  $z \sim 2.7$ ,

**Table 6.2** WS Number counts for lines with  $\lambda_{\text{obs}} \geq 12500 \text{ \AA}$ 

	Flux ( $\text{erg s}^{-1} \text{ cm}^{-2}$ )	$N_{\text{obs}}$	$N_{\text{obs}}/\text{deg}^2$ S/N $\geq 5$ (S/N $\geq 3.5$ )	$N_{\text{corr}}/\text{deg}^2$
H $\alpha$ + [N II]	$\geq 4 \times 10^{-16}$	269 (286)	478.1 (508.3)	704.5 (752.6)
	$\geq 3 \times 10^{-16}$	516 (561)	917.2 (997.1)	1421.0 (1553.9)
	$\geq 2 \times 10^{-16}$	1091 (1229)	1939.2 (2184.5)	3266.0 (3725.1)
	$\geq 1 \times 10^{-16}$	2378 (2984)	4226.7 (5303.8)	7887.3 (10364.2)
[O III] $\lambda$ 5007	$\geq 4 \times 10^{-16}$	20 (20)	35.5 (35.5)	46.0 (46.0)
	$\geq 3 \times 10^{-16}$	46 (46)	81.8 (81.8)	112.2 (112.2)
	$\geq 2 \times 10^{-16}$	162 (163)	287.9 (289.7)	444.6 (450.3)
	$\geq 1 \times 10^{-16}$	517 (578)	918.9 (1027.4)	1608.5 (1859.3)
[S III] $\lambda$ 9069	$\geq 4 \times 10^{-16}$	6 (7)	10.7 (12.4)	14.6 (16.7)
	$\geq 3 \times 10^{-16}$	6 (8)	10.7 (14.2)	14.6 (21.2)
	$\geq 2 \times 10^{-16}$	6 (11)	10.7 (19.6)	14.6 (34.3)
	$\geq 1 \times 10^{-16}$	6 (15)	10.7 (26.7)	14.6 (46.6)
[S III] $\lambda$ 9532	$\geq 4 \times 10^{-16}$	4 (4)	7.1 (7.1)	11.2 (11.2)
	$\geq 3 \times 10^{-16}$	6 (7)	10.7 (12.4)	15.7 (18.2)
	$\geq 2 \times 10^{-16}$	10 (14)	17.8 (24.9)	25.1 (36.4)
	$\geq 1 \times 10^{-16}$	20 (36)	35.5 (64.0)	52.6 (95.7)
He I $\lambda$ 10830	$\geq 4 \times 10^{-16}$	3 (5)	5.3 (8.9)	7.9 (15.1)
	$\geq 3 \times 10^{-16}$	6 (9)	10.7 (16.0)	18.8 (28.6)
	$\geq 2 \times 10^{-16}$	8 (12)	14.2 (21.3)	28.9 (42.9)
	$\geq 1 \times 10^{-16}$	10 (18)	17.8 (32.0)	35.6 (61.6)

Note — Numbers presented here are for unique sources, i.e., ELGs with both H $\alpha$ + [N II] and [O III] $\lambda$ 5007 are counted only for H $\alpha$ + [N II].

respectively. Euclid will detect more sources per square degree than those reported here, perhaps more in line with the number counts from Merson et al. (2018), who use Euclid’s full redshift range for their predictions. However, as can be seen in Figure 6.2, at the depth of the Euclid Wide Survey, the number of ELGs drops quickly with redshift. The majority of the ELGs that Euclid detects will be H $\alpha$ + [N II] at  $z \lesssim 1.5$ .

The minimum number of H $\alpha$ + [N II]-emitters required to detect a statistically significant BAO-induced signal on the clustering of galaxies is  $\sim 3000$  per degree<sup>2</sup> (Laureijs et al., 2011). With these observations, we show that Euclid will meet this goal. We also stress that a careful analysis of the contribution from [N II] is required, especially for compact galaxies

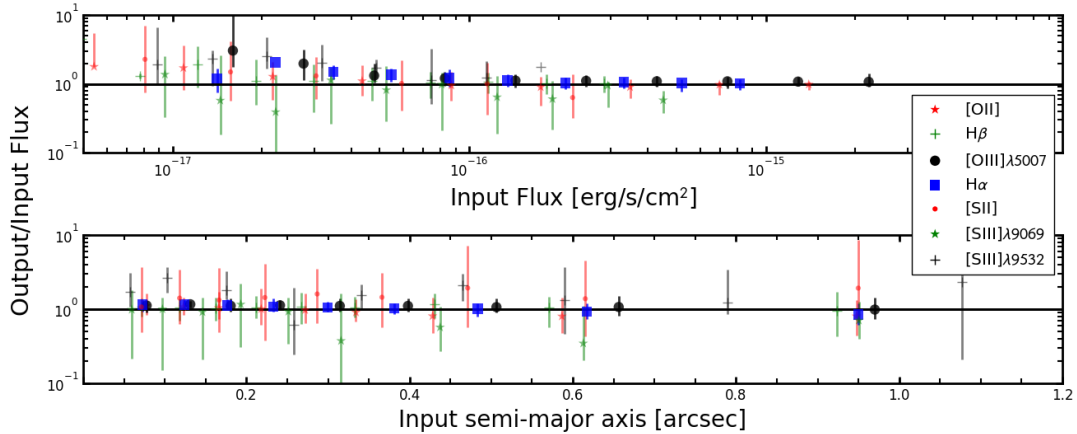


**Figure 6.5** A comparison between the input and measured (or “output”) emission line fluxes for the simulated sources described in Section 3.1. The median flux ratios for each line along with  $1\sigma$  error bars are shown in bins of input flux (top) and input source semi-major axis (bottom). The top panel is repeated here for reference from Figure 3.2, and we have added the comparison as a function of source semi-major axis (bottom panel) to show that there is no dependence on source size. The  $H\alpha$  and  $[O\text{ III}]\lambda 5007$  lines are emphasized because they are the most common primary lines. We conclude from the flux agreement for  $H\alpha$  and  $[O\text{ III}]\lambda 5007$  that we are not systematically missing flux in our measured spectra.

where the  $[N\text{ II}]$  and  $H\alpha$  lines will be resolved.

### 6.3.2 Emission and continuum sizes

The location and size of the window used for spectral extraction from grism images depend on the detection of the galaxy in a direct image. In the case of the WISP and 3D-HST+AGHAST spectra, the spectral extraction is performed using the `aXe` software (see Section 2.2). The spatial width of the extraction window is a factor of  $4\times$  the projected size of the source (either semi-major or semi-minor axis depending on the source orientation) onto the extraction direction<sup>1</sup>. This process relies on a few assumptions, including (1) that the full extent of the source has been detected in the direct image, and (2) that the emission line size is correlated with the source size in the direct image. We briefly explore both assumptions below.

The first case is analogous to slit or fiber losses in spectroscopic observations obtained with apertures smaller than the source. In this case, flux loss depends partially on the color and morphology of the galaxies (e.g., Brinchmann et al., 2004) and therefore is not a simple systematic flux offset. We can test the extent of the flux lost in WFC3 slitless

<sup>1</sup> See Figure 1.12 of the `aXe` User Manual (version 2.3), [www.stsci.edu/institute/software\\_hardware/stsdas/axe/extract\\_calibrate/axe\\_manual](http://www.stsci.edu/institute/software_hardware/stsdas/axe/extract_calibrate/axe_manual)

grism data with the simulations described in Section 3.1. The `axSIM` software generates the synthetic spectrum of a source by convolving an imaging template with a template spectrum. We use two-dimensional Gaussians to model the sources, but in principle any image of the source can be used. Regardless, the shape and size of the emission at each wavelength in the synthetic spectrum is assumed to be the same as in the direct image. The one-dimensional spectrum is then produced by collapsing the extracted spectral stamp along the spatial axis. If the extraction window is too small in the spatial direction, the flux in the one-dimensional spectrum will underestimate the total. We can therefore determine what fraction of flux is lost in the emission lines by comparing the input values with those recovered and measured by the full analysis process. The ratio of the measured to input flux is shown in Figure 6.5 as a function of input line flux and input semi-major axis, where we find that the fluxes are consistent for the primary lines  $H\alpha$  and  $[\text{O III}]\lambda 5007$ . Additionally, there is no clear dependence on source size (bottom panel), indicating that the extraction windows are adequate even for the largest sources, i.e., those most likely to have a surface brightness that drops below our detection threshold. However, we note that due to incompleteness, there are very few sources at  $a > 0''.7$  (see Section 2.4.4 for a discussion on the effects of source size on survey completeness). We also note that some real galaxies will be more centrally concentrated than simple, two-dimensional Gaussians. We therefore next discuss the sizes of real sources.

### Emission Size Measurements

We measure the sizes of each ELG in both the continuum and the  $H\alpha + [\text{N II}]$  emission. The continuum sizes are measured on  $9'' \times 9''$  stamps created from the  $H$  band direct images in either the F140W or F160W filters. The emission line sizes are measured on stamps created from the two-dimensional spectra extracted from the full grism images. We create stamps for each emission line from the 2D spectra. The stamps extend 35 pixels in the wavelength direction ( $\sim 850 \text{ \AA}$  in G102,  $\sim 1600 \text{ \AA}$  in G141) on either side of the center of the emission line. We fit the continuum row by row in the stamp excluding 8 pixels centered on the emission line and subtract it out of the spectral stamp. We are left with a map of each galaxy in the given emission line.

Observations of a source performed with WFC3, and therefore any resulting measurements of the source size and shape, are the result of the convolution of the real source and the point spread function (PSF) of the instrument. The PSF is a description of the instrument response to a point-like source such as a star and represents the minimum size

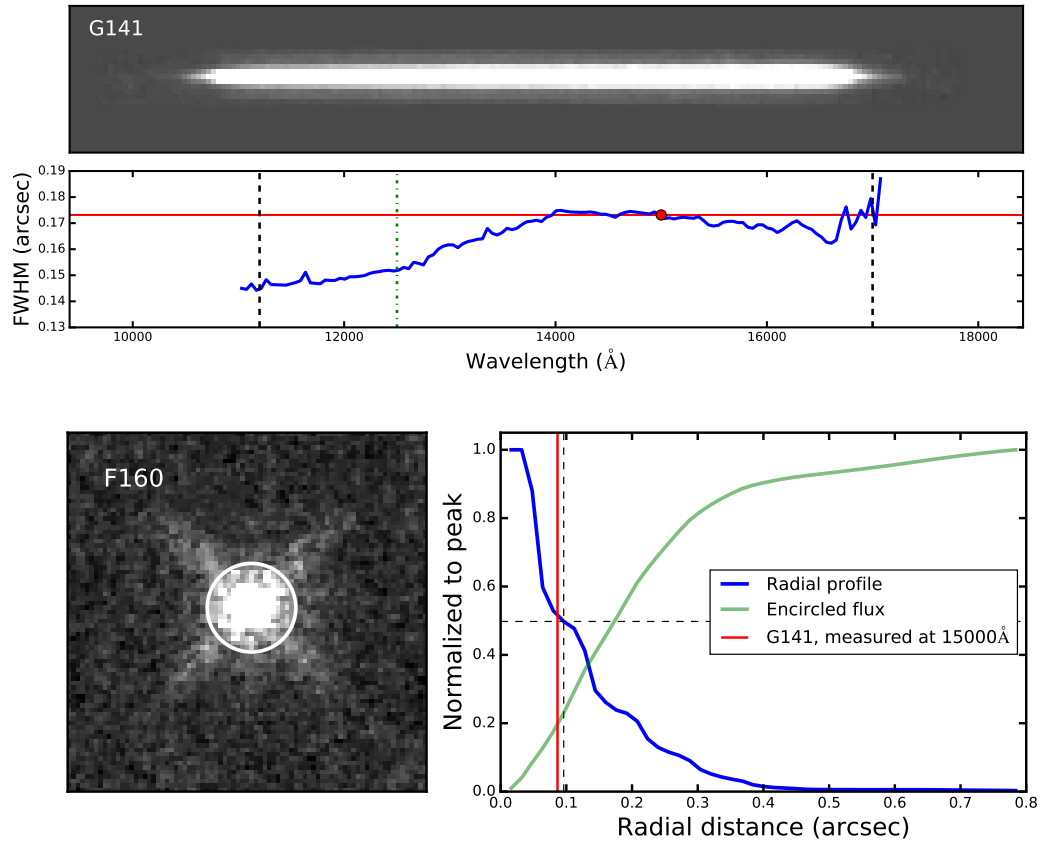


**Figure 6.6** The measurement of the empirical *HST* WFC3 PSF. We combine the G141 spectra and F160W image stamps of 20 isolated stars and measure the FWHM in both. The horizontal line in the second panel from the top identifies the FWHM of the G141 spectrum measured at the effective wavelength of the grism. The lower right panel shows the radial profile of the stacked F160W images (blue). Here the half width at half max is displayed for both the image profile (dashed line) and the grism measurement (red vertical line). We repeat this process with the G102 grism and F110W images and measure FWHMs of  $\sim 0''.15$  and  $\sim 0''.17$  at  $11000 \text{ \AA}$  (using F110W/G102) and  $15000 \text{ \AA}$  (F160W/G141), respectively. These empirically measured PSFs are larger than the reported values of  $0''.130$  and  $0''.145$ , probably because of centering and focus issues.

and the characteristic shape a point source will have in images. The PSF depends on wavelength, increasing in size with wavelength. In order to reconstruct the intrinsic sizes and shapes of the ELGs in the Euclid sample, we must therefore first determine the PSF at the wavelength of the emission.

We construct an empirical PSF by median-combining the spectral stamps extracted for 20 isolated stars in randomly-selected WISP fields. We require stars in isolation to minimize the amount of spectral overlap with nearby sources. The combined stellar spectra are displayed in the top panel of Figure 6.6. We measure the size of the spectrum along the spatial axis (vertically in Figure 6.6) by fitting a Gaussian to the flux profile at each wavelength. The full width at half maximum (FWHM) measured in this manner is plotted as a function of wavelength in the next panel. Similarly, we median-combine the imaging for the same stars in the available imaging filters, shown in the lower-left panel of Figure 6.6. We create a radial profile of this imaging PSF by calculating the azimuthally averaged flux in circular annuli of increasing radii. The FWHM of this radial profile is shown as dashed black lines in the lower right panel of Figure 6.6. The G141 FWHM at the pivot wavelength of the F160W filter, 15000 Å, is shown as the red vertical line. While the measured FWHMs match at this wavelength, we note that small centering differences for the stellar images and spectra will act to spread out the combined stamps. Even subpixel shifts can increase the FWHM of the PSF measured with this method. Additionally, if the WISP observations are not completely in focus, the measured FWHM will be larger than the nominal value. We therefore adopt the FWHM reported in the WFC3 Instrument Handbook<sup>2</sup> for Cycle 26, 0'145 for F160W for the continuum images. For the emission line sizes, we normalize the measured FWHM as a function of wavelength value at 15000 Å, preserving the measured wavelength-dependence of the PSF in the grism spectra.

Next, we consider two possible models for the shapes of the continuum and H $\alpha$  emission for the Euclid WS sources: a two-dimensional Gaussian and a Sérsic profile. A two-dimensional elliptical Gaussian is given by:

$$\begin{aligned} f(x, y) &= A \exp \left[ -a(x - x_0)^2 - b(x - x_0)(y - y_0) - c(y - y_0)^2 \right], \\ a &= \left( \frac{\cos^2(\theta)}{2\sigma_x^2} + \frac{\sin^2(\theta)}{2\sigma_y^2} \right), \\ b &= \left( \frac{\sin(2\theta)}{2\sigma_x^2} + \frac{\sin(2\theta)}{2\sigma_y^2} \right), \\ c &= \left( \frac{\sin^2(\theta)}{2\sigma_x^2} + \frac{\cos^2(\theta)}{2\sigma_y^2} \right). \end{aligned} \tag{6.1}$$

Here,  $A$  is the amplitude,  $x_0$  and  $y_0$  are the coordinates of the center, and  $\sigma_x$  and  $\sigma_y$  are the standard deviations along each axis. The Sérsic profile describes the intensity of the

<sup>2</sup> [urlhttp://www.stsci.edu/hst/wfc3/documents/handbooks/currentIHB](http://www.stsci.edu/hst/wfc3/documents/handbooks/currentIHB)

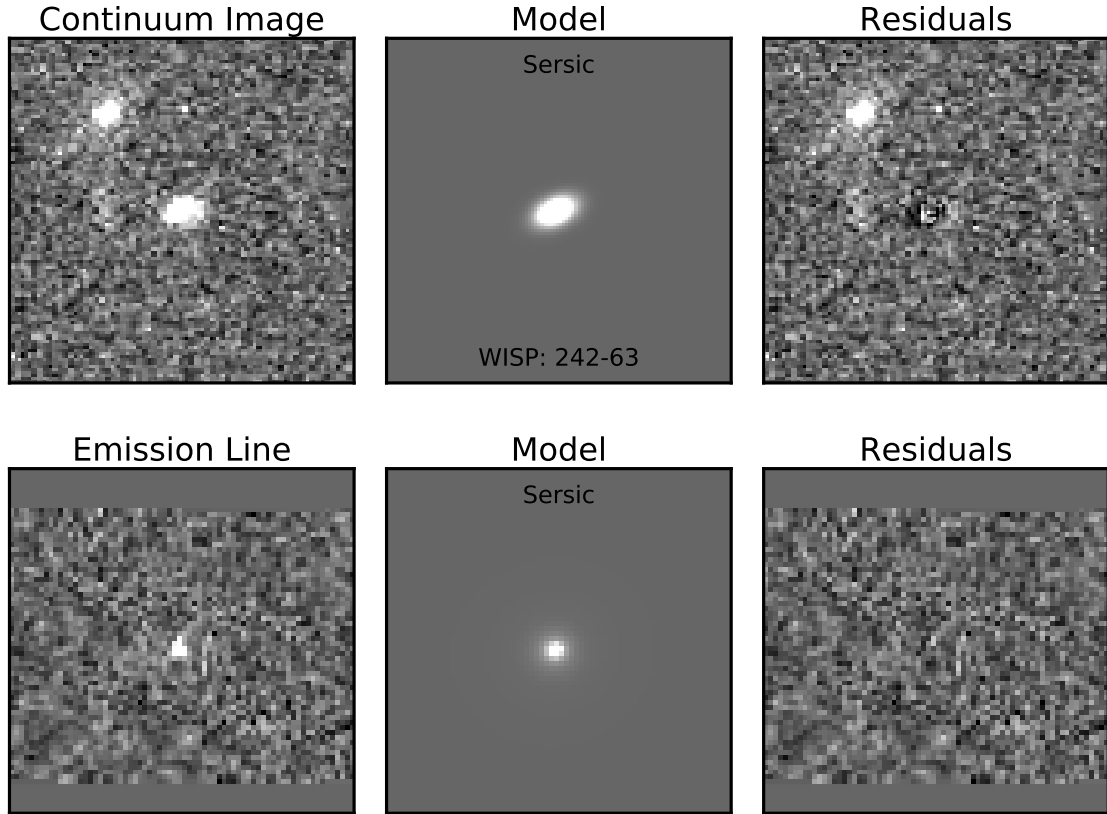


**Figure 6.7** The best-fit Sérsic models for the continuum image (top row) and H $\alpha$  emission line map (bottom row) for an example source. The columns from left to right show the input image stamps, the model, and the residuals.

source as a function of radius (Sérsic, 1963, 1968). The functional form is given by:

$$I(R) = I_{1/2} \exp \left\{ -b_n \left[ \left( \frac{r}{r_{1/2}} \right)^{1/n} - 1 \right] \right\}, \quad (6.2)$$

where  $r_{1/2}$  is the half-light radius, or the radius that encircles half the light emitted by the source, and  $I_{1/2}$  is the intensity at  $r_{1/2}$ . The parameter  $n$  is called the Sérsic index and determines the shape of the light profile, with larger values corresponding to more centrally concentrated sources. A value of  $n = 1$  results in an exponential profile that is a good approximation of disk galaxies, while  $n = 4$  gives the de Vaucouleurs (1948) profile approximating elliptical galaxies.

For each image stamp and emission line map, we determine the best-fit Gaussian and Sérsic models using Levenberg-Marquardt least-squares minimization. The stamps, Sérsic

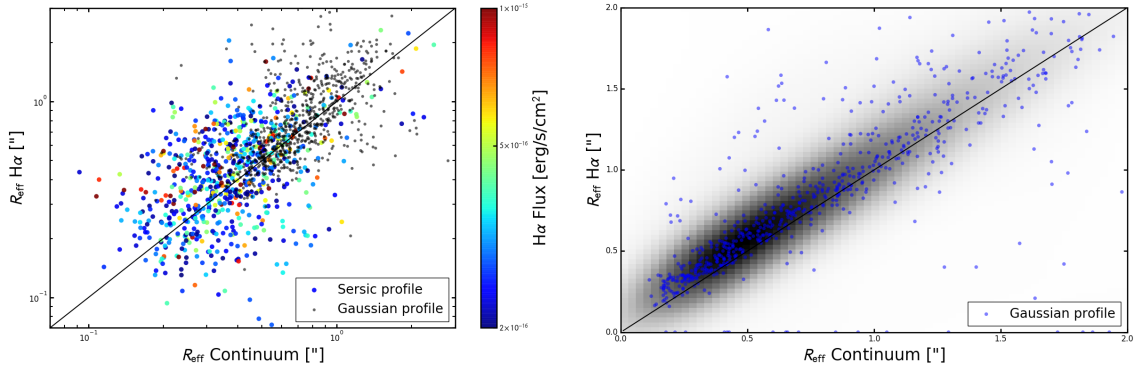


**Figure 6.8** The effective radius of sources measured in both the continuum images and the H $\alpha$  emission line map are compared in the left panel. Here we display the best-fit models for each source using a two-dimensional Gaussian (black points) and a Sérsic profile (color-coded by the source H $\alpha$  flux). In the right panel we show  $R_{\text{eff}}$  measured for the simulated sources presented in Section 3.1 using Gaussian models. Note that the simulated sources are generated with the same size in both the continuum and emission line. The black points in the left panel are reproduced here to show that the scatter in the observed relationship is on par with that measured on the simulated data.

models, and residuals for one of the WISP sources are shown in Figure 6.7 as an example of the model fitting. We compare the resulting effective radii,  $R_{\text{eff}}$ , in the continuum and the H $\alpha$ + [N II] emission in Figure 6.8, showing both the Gaussian and Sérsic measurements for each galaxy. For the Sérsic profiles,  $R_{\text{eff}} = r_{1/2}$ . For the Gaussian profiles, we define  $R_{\text{eff}} = \pi \sqrt{\sigma_x \sigma_y}$ . We have removed from this figure the handful of sources for which the models could not be successfully fit. The two sizes are correlated, but with significant scatter, though the relation is tighter for the Gaussian radii.

We perform the same size measurement on the simulated data discussed in Section 3.1. Recall that the simulated sources are the same size and shape in both the continuum and emission lines. The effective radii should therefore be tightly correlated, and we can use the scatter as an estimate of the error of our model fitting. The size measurements on the simulated data are represented as a two-dimensional density map in the right panel of Figure 6.8. The synthetic sources were simulated as two-dimensional Gaussians, and so we only show the comparison here for the Gaussian model fits. The Gaussian  $R_{\text{eff}}$  for the real sources (black points in the left panel of Figure 6.8), are shown here in blue. The majority of the continuum and emission line sizes for the real sources lie within the simulated distribution. The standard deviation of the relation between the continuum and emission line  $R_{\text{eff}}$  of the simulated sources is  $\sim 0''.2$  arcsec.

Many of the sources above the one-to-one correlation in the left panel of Figure 6.8, where

the measured  $H\alpha$   $R_{\text{eff}}$  is larger than that of the continuum, have broad  $H\alpha$  line profiles along the dispersion direction. The extent of this emission is not spatial, and these sources are erroneously fit with elongated profiles. For some of the sources with  $H\alpha$   $R_{\text{eff}}$  smaller than the continuum, we may be measuring small knots of emission concentrated within a smaller radius than the full galaxy. For others, we may be observing  $H\alpha$  emitted in the central core of the galaxy while the more extended line emission has a surface brightness below our detection sensitivity.

Part of the scatter may be due to the fact that both Gaussian and Sérsic models are simplified representations of galactic light profiles. For example, most disk galaxies, such as the Milky Way, have a bulge component that is best fit with larger  $n$ . More realistic models may be achieved by allowing for a two-component model fit consisting of both disk-like and bulge-like profiles. The resulting measurements could then be compared with the distributions of the lengths and axis ratios of bulges and disks in the Euclid Flagship mock catalog. However, it is equally important to compare the simulated and observed  $R_{\text{eff}}$  distributions for the purposes of evaluating the effects of the Euclid selection function. The extraction of galaxy spectra from Euclid grism observations will depend on the size and shape of the sources in the continuum imaging. It is therefore crucial that the distribution of continuum sizes in the mock catalog match the observations, that simulations reproduce the scatter observed here in order to produce a realistic realization of the universe, and that the relation between continuum and emission line size be fully understood.

### 6.3.3 Equivalent Width of $H\alpha+[N II]$

The emission line EW, a measure of the strength of the emission, is a very important property of ELGs that must be correctly included in forecasts for emission line studies. Hydrogen recombination lines such as  $H\alpha$  and  $H\beta$  are created by the ionizing radiation from young, massive stars while the strength of the stellar continuum reflects the buildup of emission from the older, less massive population. The EW of  $H\alpha$  is therefore an estimate of the ratio between the average star formation from current and past events. It is a measure of the specific star formation rate of a galaxy, or the star formation rate per unit stellar mass, which with the assumption of a star formation history can be converted to an age of the galaxy.

It is crucial that the simulations created to evaluate the survey design of missions such as Euclid reproduce the physical properties, and not just the number counts, of the selected population that will be observed. The emission line fluxes and physical properties of the simulated sources in the Euclid Flagship mock catalog are assigned through a combination

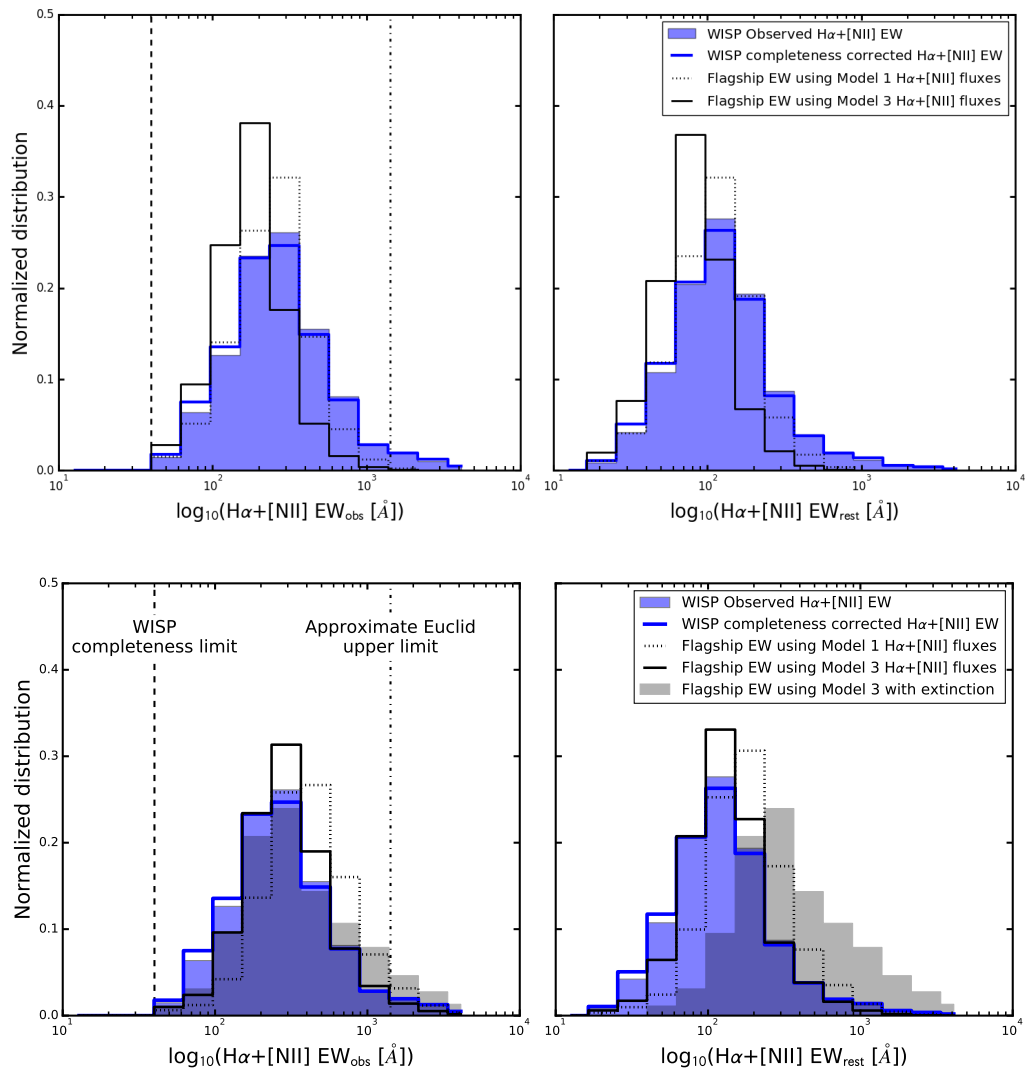


**Figure 6.9** The distribution of  $H\alpha+[N II]$  EW in the Euclid WS is compared with the Flagship mock galaxy catalog version 1.5.2 (top row) and version 1.6.11 (bottom row). It is crucial that the Flagship Mock catalog reproduce the observed EW distribution.

of prescriptive modeling and tweaking parameters to match observations. The stellar masses and star formation rates are derived from the colors and total luminosities of the galaxies, which are themselves tuned to match sources in the COSMOS catalog. The  $H\alpha$  luminosity is calculated from the star formation rate and then similarly calibrated against the empirical models of the  $H\alpha$  luminosity function and its redshift evolution presented in Pozzetti et al. (2016). The Flagship includes  $H\alpha$  flux measurements tuned to match Models 1 and 3 from Pozzetti et al. (2016). Model 3 most closely reproduces the number counts observed by WISP and 3D-HST, while Model 1 represents a slightly more optimistic  $H\alpha$  number density. However, the  $H\alpha$  EWs have not yet been validated for the Euclid Flagship catalog. While the catalog may reproduce observed number counts, it may be doing so in an unphysical way.

In Figure 6.9, we present the  $H\alpha$ + $[N\ II]$  EW distribution of the Euclid WS and compare it to that from version 1.6.11 of the Flagship mock catalog. We select sources from the mock catalog covering an area of 5 degree<sup>2</sup> and apply the same selection criteria as for the Euclid WS:  $\lambda_{\text{obs},H\alpha} \geq 12500\ \text{\AA}$ ,  $f_{H\alpha} \geq 2 \times 10^{-16}\ \text{erg s}^{-1}\ \text{cm}^{-2}$ , and  $\text{EW}_{\text{obs},H\alpha} \geq 40\ \text{\AA}$ . The EW of the simulated sources is approximated by dividing the  $H\alpha$ + $[N\ II]$  fluxes by the continuum fluxes in the broadband imaging filters closest to the wavelength of the  $H\alpha$  line. We use the reported filter fluxes that do not include the contribution from emission lines. We perform this calculation for both Model 1 and 3  $H\alpha$ + $[N\ II]$  fluxes. Additionally, since we have performed no corrections for extinction in the *HST* observations, we show the  $H\alpha$ + $[N\ II]$  EW calculated from Model 3 fluxes that include extinction from the Milky Way. As can be seen in Figure 6.9, the shapes of the simulated EW distributions generally match those of the observed WS. In the earlier version 1.5.2 (top row), the simulated distribution for Model 3 fluxes was offset to slightly smaller EWs. This may indicate that the stellar masses were overestimated in the mock catalog. Though the discrepancy appears to have been resolved in the newer version 1.6.11 (bottom row), we still recommend that the EW distributions of the emission lines be added as a required point of validation for the Flagship mock catalog.

## 6.4 Discussion

### 6.4.1 $[O\ III]$ Line Profile

As described in Section 2.4.3, we assume single emission lines in the grism spectra are  $H\alpha$  unless the line has noticeable asymmetry indicative of the  $[O\ III]$ + $H\beta$  line profile. We now briefly consider whether this assumption leads us to selectively identify  $[O\ III]$  lines with

asymmetric profiles.

We compare the [O III] line profiles of sources with multiple lines, and therefore secure redshifts, with the profiles of single line emitters that have been identified as [O III]. The question is whether a sample of sources with multiple lines have, on average, a more symmetric profile because the characteristic asymmetry is not needed for line identification. We create two subsets of [O III]-emitters randomly sampled from the WISP emission line catalog (described in Section 2.4). All sources have [O III] fluxes with  $S/N \geq 5$ . The  $H\alpha + [N II]$  fluxes in the first subset also have a  $S/N \geq 5$ , making this a sample of confirmed [O III]-emitters. The second subset is taken at  $z \geq 1.6$ , where  $H\alpha + [N II]$  has redshifted out of G141, and excludes any sources with an [O II]  $S/N \geq 2$ . We restrict both selections to  $z \geq 1.24$  so all emission lines are measured in G141 with the same resolution and dispersion. There are  $\sim 120$  sources in each sample. The individual one-dimensional spectra are represented by faint dots in Figure 6.10, and the median spectrum is shown as the black curve. We also median combine 20% of the two-dimensional spectra for each sample, displayed below the one-dimensional spectra. All spectra (one- and two-dimensional) are shifted to the restframe and normalized by the integrated [O III] line flux.

The [O III] line profiles for each sample are indicated in blue (confirmed) and red (unconfirmed). As can be seen in the inset in the bottom panel, the median profile of confirmed [O III]-emitters is indeed more symmetric than that of the unconfirmed. The median  $5\sigma$  depth in the WISP spectra at the wavelengths of the [O III] lines is  $6 \times 10^{-17} \text{ erg s}^{-1} \text{ cm}^{-2}$ . We expect this bias to be even more pronounced for shallower data such as that of the *Euclid* Wide survey, where the [O III] $\lambda 4959$  line will fall below the detection limit more often than in deeper spectra. The resulting [O III] $\lambda 5007$  line profiles may appear symmetric and be more likely to be identified as  $H\alpha$  under visual inspection. As discussed in Section 6.2.1, however, unaided human classification will not be a viable method for line identification in the *Euclid* data.

### 6.4.2 Redshift Accuracy

The measurement of the BAO signal in galaxy clustering requires accurate distance measurements to a large sample of galaxies. Specifically, it has been shown through simulations that the redshift accuracy for a survey such as *Euclid* must be  $\sigma_z/(1+z) \leq 0.1\%$  (Wang et al., 2010; Laureijs et al., 2011). Using the *HST* grism data, we perform two tests of the redshift accuracy that can be expected from slitless spectroscopy.

For the first measurement, we use the simulated data presented in Section 3.1 and compare the input redshifts of sources with the corresponding measured redshifts after the

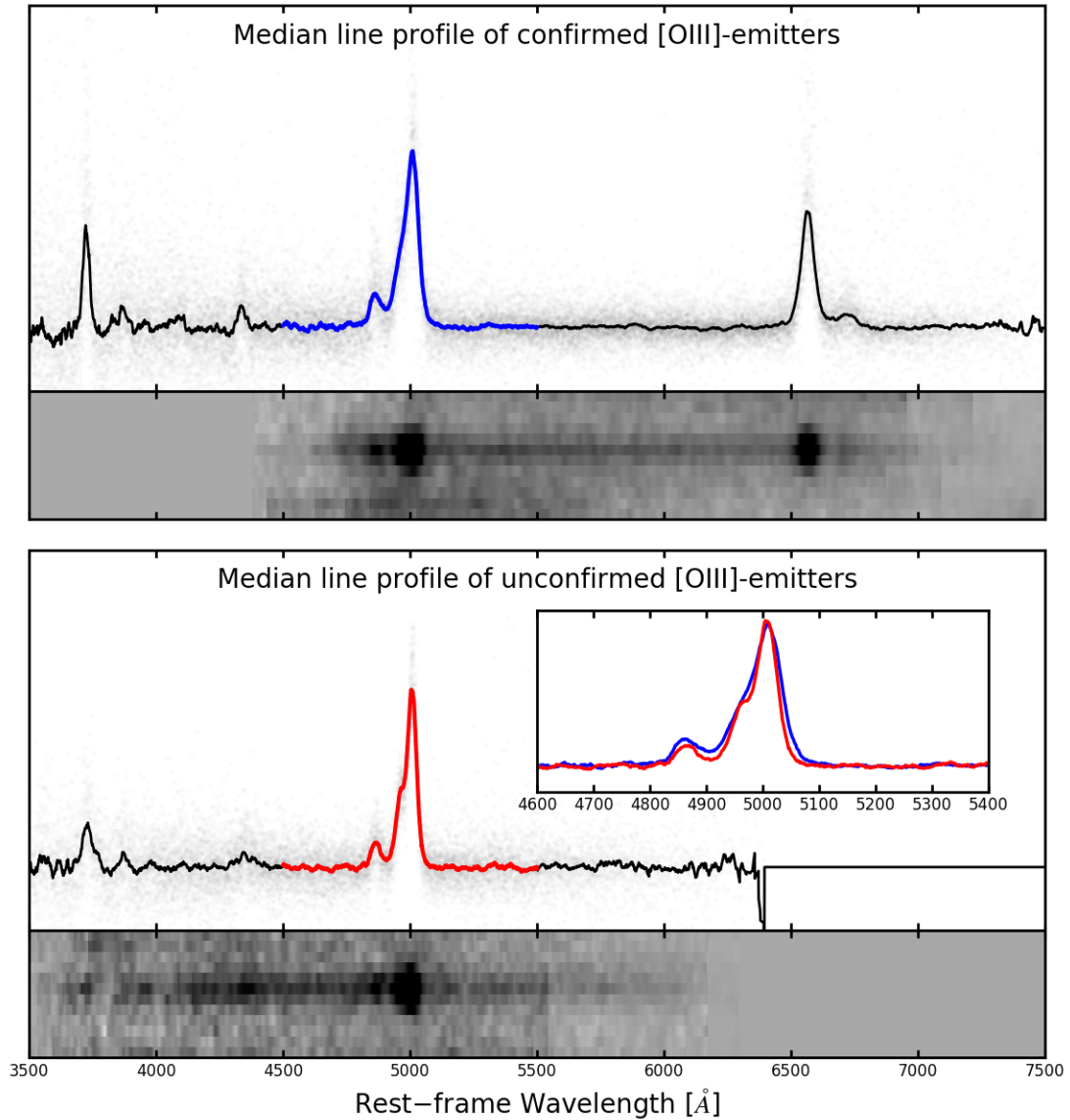


**Figure 6.10** The [O III] line profile of sources with secure redshifts (blue, top panel) is compared with that from sources with redshifts based on the detection of a single emission line (red, bottom panel). The line profile of the unconfirmed [O III]-emitters is more asymmetric than that of confirmed [O III]-emitters. The asymmetry is needed to make a reliable line identification in the absence of additional emission lines.

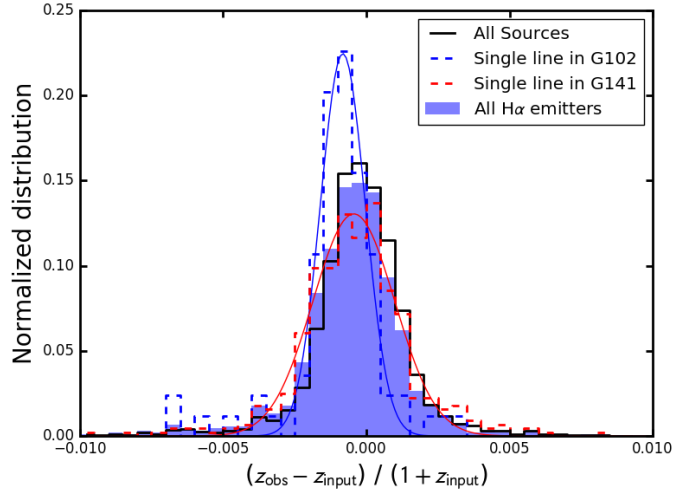


**Figure 6.11** The distribution of the redshift difference (output minus input) of simulated sources recovered in WISP spectra. The black histogram shows the distribution for all sources, and the blue shaded histogram is that for all H $\alpha$ -emitters. As most sources in the Euclid Wide Sample will be detected with only a single emission line, we also show the distributions for single line sources in both grisms. The redshift accuracy is on the order of  $\sigma_z/(1+z) \lesssim 0.1\%$  for all four sets of sources.

full line finding process. Recall that the redshifts are fit for the full spectrum simultaneously including all emission lines that are present (see Section 2.4.3 for details). The redshift accuracy for all recovered, simulated sources is shown in black in Figure 6.11 and is very similar to that for all H $\alpha$ -emitters (blue shaded histogram). However, the majority of sources detected in the Euclid Wide Survey will have only one emission line above the sensitivity limit. We therefore also check the redshift difference for all single-line emitters. We additionally separate this measurement by grism, since the higher resolution of the G102 grism should lead to a higher redshift accuracy. Indeed, we find that the delta redshift for single line emitters in G141 is similar to that of the full population, while that for sources in G102 is narrower. Fitting Gaussians to both distributions, we find that  $\sigma_z/(1+z) = 0.00078$  for single line emitters in G102 and 0.00143 for G141.

We also perform an empirical measurement of the redshift accuracy from fits to grism spectra. Thanks to six cycles of parallel observations, there are 36 WISP fields that overlap to some degree with another field. There are therefore  $\sim 140$  sources that have been observed multiple times, often with very different exposure times, field depths, and roll angles. In order to increase the sample size, we consider all possible permutations of pairs of observations of a given source. We randomize the order in which we calculate the delta redshift to avoid systematic shifts that may be introduced if a subset of these WISP fields have problems.

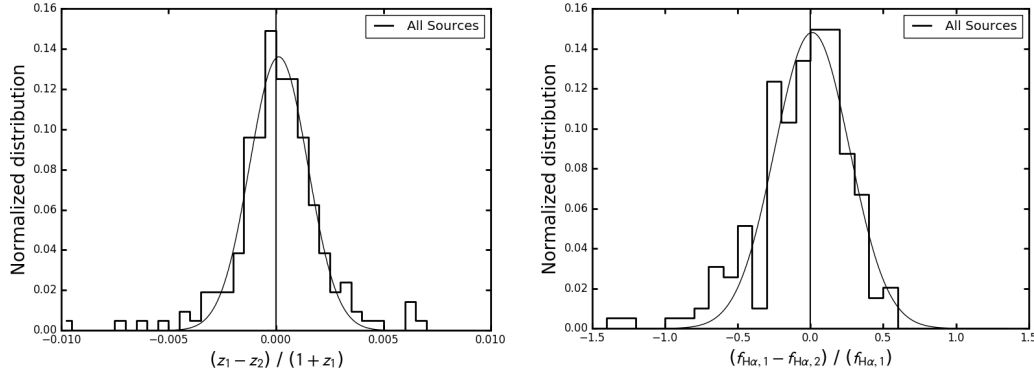


**Figure 6.12** The redshift and H $\alpha$  flux accuracies measured empirically from real WISP data are shown in the left and right panels, respectively. Here we are comparing the redshifts and H $\alpha$  fluxes from multiple measurements of the same set of sources observed in overlapping WISP fields.

Such problems could include issues with the wavelength calibration or noisy grism data, which would increase the uncertainty in the measured emission line centers. In Figure 6.12, we show this empirical measurement of the redshift accuracy ( $\sigma_z/(1+z) = 0.00136$ ) as well as a similar measurement of the accuracy of the H $\alpha$ + [N II] fluxes of these sources.

In both cases, the redshift accuracy measured from the WFC3 slitless grism data is on the order of 0.1%. We confirm that  $\sim 68\%$  (or  $\pm$  one standard deviation) of redshifts derived with the Euclid Red grism will be within this required limit. However, Euclid measurements will also have to contend with redshift contamination from mis-identified emission lines. We quantify the expected fraction of contamination as a function of survey flux limit in the following section.

### 6.4.3 Contaminating Redshifts

For proper forecasts of dark energy experiments, a critical parameter is the purity of the measured redshifts of galaxies, which can be quantified by the fraction  $f$  of targets with incorrectly identified emission-lines. There are two possible sources of contamination: spurious sources such as noise peaks incorrectly identified as emission features, and real lines that have been misidentified and are therefore assumed to be at the wrong redshift. The first case depends on the method used for line identification. For example, Colbert et al. (2013) find that  $\sim 8.5\%$  of emission lines in the first version of the WISP emission line catalog are in fact hot pixels, cosmic rays, or other artifacts. Though we have not quantified this fraction in the new catalog, the updated procedure using a continuous wavelet transform

should improve upon this false detection rate (see Section 2.4).

In the case of contamination from misidentified redshifts, we can use the CANDELS multi-wavelength observations available for the 3D-HST fields and the full wavelength coverage of the G102+G141 WISP observations to evaluate the purity of spectroscopic redshifts measured with grism data. The top panel of Figure 6.1 shows the redshift ranges for which multiple lines will be identified Euclid spectra. For many redshifts only one line will be available. In addition, depending on the intrinsic  $H\alpha + [N II] / [O III]\lambda 5007$  ratio and the amount of dust extinction, it is likely that  $H\alpha + [N II]$  will still be the only line detected, even in the redshift range where both  $[O III]\lambda 5007$  and  $H\alpha + [N II]$  are present. Indeed, only about 10% of the WS sources in the proper redshift range have both  $H\alpha + [N II]$  and  $[O III]\lambda 5007$ . When only individual lines are detected, these are operationally identified as  $H\alpha$  unless other information such as the emission line shape or galaxy color is available. However, it is possible that a substantial fraction of these single lines are in fact  $[O III]$  at  $z_{[OIII]} + 1 = (z_{H\alpha} + 1) \lambda_{H\alpha} / \lambda_{[OIII]}$ . We aim to constrain the purity of slitless-selected samples with two complementary approaches.

First, we use the photometric redshifts in the CANDELS catalog from SED fitting to determine which fraction of 3D-HST spectroscopic redshifts have been misidentified. Figure 6.13 shows this redshift misidentification as a function of the line flux. We consider all  $H\alpha$ -emitters in the 3D-HST catalog where the redshift is based on a single line. We select galaxies with a spectroscopic redshift of  $z \geq 0.9$  and a best-fit photometric redshift available from the CANDELS catalog. The prevalence of misidentified single emission lines depends on the survey depth. At the depth of the Euclid Wide Survey  $\sim 20\%$  of the single line emitters assumed to be  $H\alpha$  are in fact a different emission line. This percentage increases to  $\sim 60\%$  as the depth of the survey increases. Here we are only considering sources that have a single emission line down to a flux limit of  $\sim 7 \times 10^{-17}$  erg s $^{-1}$  cm $^{-2}$ . Next, we explore sources in the Euclid WS that have additional lines at fainter fluxes and how these are necessary for calibrating the Wide Survey.

The top level science requirements for Euclid necessitate a redshift sample purity of  $p > 99\%$ , where  $p = N_{\text{correct}} / N_{\text{measured}}$  the number of sources with correctly identified redshifts divided by the total number measured (Laureijs et al., 2011). We use the WISP data to estimate the purity of the emission line sample observed in the Euclid Deep Survey. From the full WISP emission line catalog (Section 2.4), we only consider fields with spectral coverage in both the G102 and the G141 grisms. Additionally, we include in the following analysis only emission line galaxies with secure redshifts (i.e., measured with at least two emission lines). Having observations in both grisms ensures a spectral coverage between

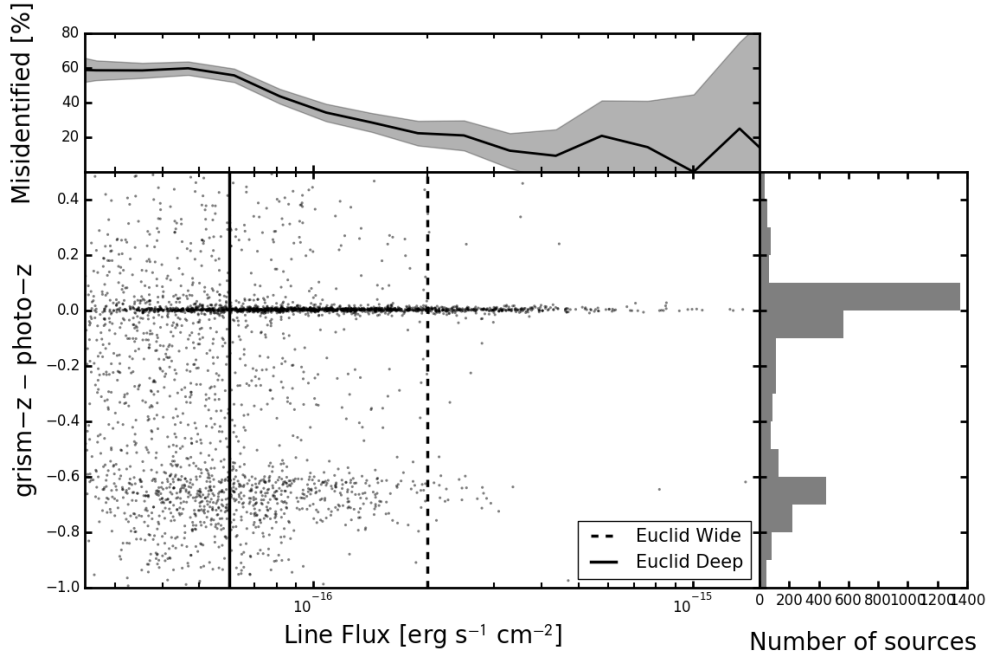


**Figure 6.13** The difference between the grism-identified spectroscopic redshifts and the photometric redshifts calculated in the CANDELS catalog is shown as a function of line flux. All sources were identified as  $H\alpha$ -emitters in the grism spectra, yet many appear to be lines at a different redshift (typically [O III]) based on their photo- $z$  measurements. This redshift misidentification rate depends on the survey flux limit and increases to  $\sim 60\%$  at the depth of the Euclid Deep Survey.

$0.85 \leq \lambda \leq 1.6 \mu\text{m}$ . Given the emission lines considered in the redshift determination ([O II],  $H\gamma$ ,  $H\beta$ , [O III],  $H\alpha$ + [N II], [S II], [S III] $\lambda$ 9069, [S III] $\lambda$ 9532, and He I $\lambda$ 10830) the catalog derived for the fields with both grisms spans the redshift range between 0.25 and 2.3. The approximate  $5\sigma$  depth of the selected WISP fields is  $5 \times 10^{-17} \text{ erg s}^{-1} \text{ cm}^{-2}$ , consistent with the line flux limit required in the Euclid Deep Survey observations with the Red grism.

From this 2-grism WISP catalog, we apply the same selection criteria described in Section 6.2 to create a sample analogous to that which will be selected using the NISP Red Euclid grism. We call this sample the Euclid Shallow (ES) sample, and it is the same as the WS of Section 6.2 but only includes WISP sources from fields observed with both grisms. The redshift distribution of the ES sample is shown in Figure 6.14 (blue histogram). In the WISP catalog, sources with redshift in the  $0.4 < z < 1.6$  are mostly selected via their  $H\alpha$  emission line. At redshifts  $z \gtrsim 1.6$ , galaxies are selected via the [O III] emission lines, while at redshifts  $z \lesssim 0.4$ , galaxies are identified because of the [S III] and He I lines. We stress that the WISP sample considered in this analysis only includes secure redshifts (measured

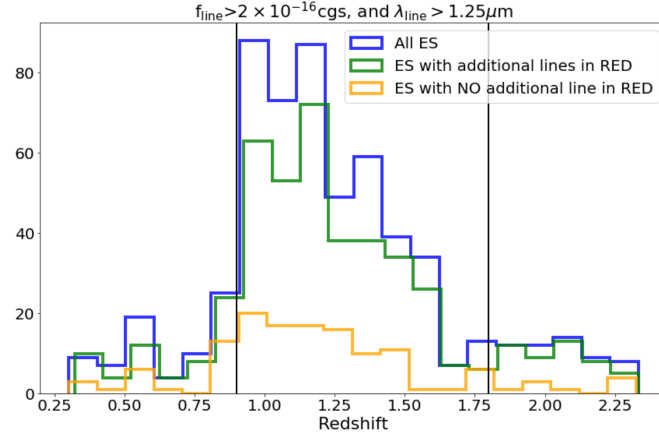


**Figure 6.14** Redshift distribution of galaxies in the Euclid Shallow sample, defined as all WISP sources with at least one emission line with  $\lambda_{\text{line}} > 1.25 \mu\text{m}$  and  $f_{\text{line}} > 2 \times 10^{-16} \text{ erg s}^{-1} \text{ cm}^{-2}$ , regardless of their redshifts (blue histogram). The green and orange histograms split the sample into objects with and without additional emission lines in the red grism at the depth of the deep survey. The objects in the orange histogram with  $z > 1.8$  and  $z < 0.9$  would result in catastrophic redshift determinations, and correspond to about 6% of the ES sample.

with two or more emission lines).

Multiple emission lines are required in order to be able to perform an unambiguous redshift identification. Thus, we look at the fraction of galaxies in the ES sample that would show additional lines in the wavelength range of the Euclid Red grism, with  $f_{\text{line}}^{\text{add}} > 2\sigma$  (where  $\sigma = 1.4 \times 10^{-17} \text{ erg s}^{-1} \text{ cm}^{-2}$  is the required spectroscopic depth of the Euclid deep survey). We find that 77% of the ES sample have multiple emission lines in the wavelength range of the Euclid Red grism and at the depth of the Deep Survey. The redshift distribution for this population is shown in Figure 6.14 (green histogram). The orange histogram in Figure 6.14 shows the redshift distribution of the remaining 23% of galaxies in the ES sample that would be single line emitters even in the Euclid Deep Survey.

For single line emitters the simplest assumption is that the line is  $\text{H}\alpha$ . The orange histogram, however, clearly shows that this assumption would get the redshift wrong for single-line emitters at  $z < 0.9$  and  $z > 1.8$ <sup>3</sup>. We find that the fraction of all ES galaxies with catastrophic redshift failure is 6%, corresponding to a purity of 94%. This fraction does not meet the Euclid top level science requirement (Laureijs et al., 2011). It is important to note that this analysis does not include catastrophic redshift failures due to noise spikes in the data. Their contribution to the purity of the sample needs to be quantified separately.

<sup>3</sup> We are assuming that Euclid will see  $\text{H}\alpha$  for the [O III]-selected WISP sources in the  $1.6 < z < 1.8$  redshift range.

Given the wavelength range of the G102 grism, we can quantify the extent to which the addition of the Euclid Blue grism will improve the sample purity. Almost all of the 6% of objects with misidentified redshifts have additional emission lines blueward of the Red Grism. The Euclid Blue grism reaches down to  $0.92 \mu\text{m}$ . If observations with the Blue grism are added to the Deep Survey, 85% of the catastrophic redshift failures would be removed, bringing the purity of the ES sample up to 99.1%.

# Chapter 7

## Summary

The epoch of reionization marks the last phase transition of the universe, when the cold, neutral hydrogen in the intergalactic medium (IGM) was heated and ionized. Despite significant observational efforts, the details of this transition are still largely unknown. In this thesis, as part of the attempt to understand the transition, we have presented observations of Lyman- $\alpha$  emitting galaxies (LAEs) at  $z > 6$  as well as spectroscopic follow-up of a sample of local galaxies expected to be analogs of those responsible for ionizing the IGM at high redshift.

With the discovery of two of the brightest known LAEs at  $z \sim 6.5$ , we found evidence for a “bright bump” in the Ly $\alpha$  luminosity function. This high space density of LAEs during reionization may indicate that bright LAEs are being detected from within ionized bubbles large enough to allow the Ly $\alpha$  photons to redshift out of resonance before encountering the neutral hydrogen in the IGM. This interpretation fits with the expectation that reionization proceeds through the expansion and coalescence of ionized bubbles. The distribution and size of these bubbles will then depend on the density of ionizing sources, their production rate of ionizing photons, and the amount of that ionizing radiation that can escape into the IGM. In Chapter 4, we showed that the WISP LAEs are not capable of ionizing their bubbles by themselves, even assuming all ionizing photons escape. A population of fainter galaxies is required. By  $z \sim 7$ , this bright bump disappears and the observed number density of LAEs decreases at all luminosities, indicating an increase in the global fraction of neutral hydrogen in the IGM.

Due to small sample sizes and current observational limitations, there remain significant unknowns in the observations and interpretations of bright LAEs during reionization. For example, the extent of the excess of bright LAEs detected at  $z \sim 6.5$  is still unconstrained. Bright LAEs such as those presented in Chapter 4 are ideal for follow-up with the James

Webb Space Telescope (JWST), both to spectroscopically constrain their physical properties and to directly image the fainter population of galaxies in the surrounding bubbles. Additionally, with the potential to detect hundreds more high-redshift bright LAEs, upcoming slitless cosmological surveys such as Euclid will shed more light on the bright end of the Ly $\alpha$  luminosity function. Covering 40 square degrees and a volume at  $z \geq 6.5$  that is 10 – 50 times larger than current LAE surveys, the Euclid Deep Survey will be much less susceptible to the effects of cosmic variance that may explain some of the discrepancy in current Ly $\alpha$  luminosity function measurements.

JWST will revolutionize our understanding of galaxies during the epoch of reionization, yet detailed studies will be limited to the brightest galaxies. In Chapter 5, we therefore presented a preliminary analysis of a sample of local blue compact dwarf galaxies identified as analogs of faint, low-mass galaxies at high redshift. We emphasized the potential of what we can learn from the high signal-to-noise spectra obtained with the LBT/MODS and Magellan/LDSS3 spectrographs, and discussed future plans to explore properties such as star formation rates, stellar ages, feedback mechanisms and metallicities. This work will be essential to help understand the faint, low-mass galaxies JWST will easily image during reionization, but for which spectroscopic measurements will be prohibitively difficult.

Since the Euclid telescope is still a few years from launch, we have also presented forecasting work we have done with *HST* grism surveys. In Chapter 6, we predicted the number densities of H $\alpha$ + [N II]-emitters and [O III] $\lambda$ 5007-emitters that will be detected in the Euclid Wide Survey volume. We also measured the sizes of the galaxies in both the continuum and H $\alpha$ + [N II] emission. We presented the equivalent width distribution of H $\alpha$ + [N II] and compared this with the Euclid Flagship Mock catalog. We measured the redshift accuracy that can be expected of low-resolution grism observations, both through recovered simulated data and real observations in overlapping WISP fields. Finally, we used the *HST* data to quantify the contamination fraction Euclid can expect and to motivate the inclusion of the Blue grism in the Deep Survey to help with redshift calibration and bring the catastrophic redshift failure rate within acceptable limits.

# References

- Alavi, A., Siana, B., Richard, J., et al. 2014, *ApJ*, 780, 143
- Anders, P., & Fritze-v. Alvensleben, U. 2003, *A&A*, 401, 1063
- Atek, H., Malkan, M., McCarthy, P., et al. 2010, *ApJ*, 723, 104
- Atek, H., Siana, B., Scarlata, C., et al. 2011, *ApJ*, 743, 121
- Atek, H., Richard, J., Kneib, J.-P., et al. 2014, *ApJ*, 786, 60
- . 2015, *ApJ*, 800, 18
- Bagley, M. B., Scarlata, C., Henry, A., et al. 2017, *ApJ*, 837, 11
- Baldwin, J. A., Phillips, M. M., & Terlevich, R. 1981, *PASP*, 93, 5
- Barone-Nugent, R. L., Trenti, M., Wyithe, J. S. B., et al. 2014, *ApJ*, 793, 17
- Beck, M. R., Scarlata, C., Fortson, L. F., et al. 2018, *MNRAS*, 476, 5516
- Becker, R. H., Fan, X., White, R. L., et al. 2001, *AJ*, 122, 2850
- Bertin, E., & Arnouts, S. 1996, *A&AS*, 117, 393
- Bian, F., Fan, X., McGreer, I., Cai, Z., & Jiang, L. 2017, *ApJ*, 837, L12
- Borthakur, S., Heckman, T. M., Leitherer, C., & Overzier, R. A. 2014, *Science*, 346, 216
- Bouwens, R., Aravena, M., Decarli, R., et al. 2016, *ArXiv e-prints*, arXiv:1606.05280
- Bouwens, R. J., Oesch, P. A., Illingworth, G. D., Ellis, R. S., & Stefanon, M. 2017, *ApJ*, 843, 129
- Bouwens, R. J., Illingworth, G. D., Oesch, P. A., et al. 2011, *ApJ*, 737, 90
- . 2015, *ApJ*, 803, 34

- Boylan-Kolchin, M., Bullock, J. S., & Garrison-Kimmel, S. 2014, *MNRAS*, 443, L44
- Boylan-Kolchin, M., Weisz, D. R., Johnson, B. D., et al. 2015, *MNRAS*, 453, 1503
- Brammer, G., Ryan, R., & Pirzkal, N. 2015, Source-dependent master sky images for the WFC3/IR grisms, Tech. rep.
- Brammer, G. B., van Dokkum, P. G., Franx, M., et al. 2012, *ApJS*, 200, 13
- Brinchmann, J., Charlot, S., White, S. D. M., et al. 2004, *MNRAS*, 351, 1151
- Bruzual, G., & Charlot, S. 2003, *MNRAS*, 344, 1000
- Calzetti, D., Armus, L., Bohlin, R. C., et al. 2000, *ApJ*, 533, 682
- Cardamone, C., Schawinski, K., Sarzi, M., et al. 2009, *MNRAS*, 399, 1191
- Cardelli, J. A., Clayton, G. C., & Mathis, J. S. 1989, *ApJ*, 345, 245
- Castellano, M., Dayal, P., Pentericci, L., et al. 2016, *ApJ*, 818, L3
- Cen, R., & Haiman, Z. 2000, *ApJ*, 542, L75
- Chabrier, G. 2003, *PASP*, 115, 763
- Chardin, J., Kulkarni, G., & Haehnelt, M. G. 2018, *MNRAS*, 478, 1065
- Charlot, S., & Fall, S. M. 2000, *ApJ*, 539, 718
- Chevallard, J., Charlot, S., Senchyna, P., et al. 2018, *MNRAS*, arXiv:1709.03503
- Colbert, J. W., Teplitz, H., Atek, H., et al. 2013, *ApJ*, 779, 34
- Cowie, L. L., Barger, A. J., & Trouille, L. 2009, *ApJ*, 692, 1476
- Cowie, L. L., & Hu, E. M. 1998, *AJ*, 115, 1319
- Cristiani, S., Serrano, L. M., Fontanot, F., Vanzella, E., & Monaco, P. 2016, *MNRAS*, 462, 2478
- de Barros, S., Vanzella, E., Amorín, R., et al. 2016, *A&A*, 585, A51
- de Vaucouleurs, G. 1948, *Annales d'Astrophysique*, 11, 247
- Dickinson, H., Scarlata, C., Fortson, L., et al. 2018, ArXiv e-prints, arXiv:1807.01687

- Dickinson, M., Stern, D., Giavalisco, M., et al. 2004, *ApJ*, 600, L99
- Dijkstra, M. 2014, *PASA*, 31, e040
- Dijkstra, M., Wyithe, S., Haiman, Z., Mesinger, A., & Pentericci, L. 2014, *MNRAS*, 440, 3309
- Domínguez, A., Siana, B., Henry, A. L., et al. 2013, *ApJ*, 763, 145
- Dressler, A., Henry, A., Martin, C. L., et al. 2015, *ApJ*, 806, 19
- Dressler, A., Martin, C. L., Henry, A., Sawicki, M., & McCarthy, P. 2011, *ApJ*, 740, 71
- Du, P., Kibbe, W. A., & Lin, S. M. 2006, *Bioinformatics*, 22, 2059. <http://dx.doi.org/10.1093/bioinformatics/btl355>
- Eldridge, J. J., Izzard, R. G., & Tout, C. A. 2008, *MNRAS*, 384, 1109
- Erb, D. K., Pettini, M., Shapley, A. E., et al. 2010, *ApJ*, 719, 1168
- Erb, D. K., Shapley, A. E., Pettini, M., et al. 2006, *ApJ*, 644, 813
- Faisst, A. L., Capak, P., Carollo, C. M., Scarlata, C., & Scoville, N. 2014, *ApJ*, 788, 87
- Faisst, A. L., Masters, D., Wang, Y., et al. 2018, *ApJ*, 855, 132
- Faisst, A. L., Capak, P., Hsieh, B. C., et al. 2016, *ApJ*, 821, 122
- Fan, X., Strauss, M. A., Becker, R. H., et al. 2006, *AJ*, 132, 117
- Feldmeier, J. J., Hagen, A., Ciardullo, R., et al. 2013, *ApJ*, 776, 75
- Felten, J. E. 1977, *AJ*, 82, 861
- Ferland, G. J., Chatzikos, M., Guzmán, F., et al. 2017, *RMXAA*, 53, 385
- Ferrara, A., Bianchi, S., Cimatti, A., & Giovanardi, C. 1999, *ApJS*, 123, 437
- Finkelstein, S. L., Ryan, Jr., R. E., Papovich, C., et al. 2015, *ApJ*, 810, 71
- Fitzpatrick, E. L. 1999, *PASP*, 111, 63
- Froning, C. S., & Green, J. C. 2009, *Ap&SS*, 320, 181
- Furlanetto, S. R., & Oh, S. P. 2005, *MNRAS*, 363, 1031

- Furlanetto, S. R., Zaldarriaga, M., & Hernquist, L. 2006, *MNRAS*, 365, 1012
- Garel, T., Blaizot, J., Guiderdoni, B., et al. 2015, *MNRAS*, 450, 1279
- . 2012, *MNRAS*, 422, 310
- Gehrels, N. 1986, *ApJ*, 303, 336
- Giammanco, C., Beckman, J. E., & Cedrés, B. 2005, *A&A*, 438, 599
- Gonzaga, S., e. 2012, *The DrizzlePac Handbook*
- Grazian, A., Giallongo, E., Gerbasi, R., et al. 2016, *A&A*, 585, A48
- Green, J., Schechter, P., Baltay, C., et al. 2012, *ArXiv e-prints*, arXiv:1208.4012
- Greig, B., & Mesinger, A. 2017, *MNRAS*, 465, 4838
- Grogin, N. A., Kocevski, D. D., Faber, S. M., et al. 2011, *ApJS*, 197, 35
- Guaita, L., Melinder, J., Hayes, M., et al. 2015, *A&A*, 576, A51
- Guaita, L., Pentericci, L., Grazian, A., et al. 2016, *A&A*, 587, A133
- Gunn, J. E., & Peterson, B. A. 1965, *ApJ*, 142, 1633
- Guzzo, L., Pierleoni, M., Meneux, B., et al. 2008, *Nature*, 451, 541
- Hayes, M., Östlin, G., Mas-Hesse, J. M., & Kunth, D. 2009, *AJ*, 138, 911
- Hayes, M., Schaerer, D., Östlin, G., et al. 2011, *ApJ*, 730, 8
- Hayes, M., Östlin, G., Schaerer, D., et al. 2013, *ApJ*, 765, L27
- Hayes, M., Östlin, G., Duval, F., et al. 2014, *ApJ*, 782, 6
- Heckman, T. M., Hoopes, C. G., Seibert, M., et al. 2005, *ApJ*, 619, L35
- Heckman, T. M., Borthakur, S., Overzier, R., et al. 2011, *ApJ*, 730, 5
- Henry, A., Scarlata, C., Martin, C. L., & Erb, D. 2015, *ApJ*, 809, 19
- Henry, A., Scarlata, C., Domínguez, A., et al. 2013, *ApJ*, 776, L27
- Henry, A. L., Martin, C. L., Dressler, A., Sawicki, M., & McCarthy, P. 2012, *ApJ*, 744, 149

- Henry, A. L., Siana, B., Malkan, M. A., et al. 2009, *ApJ*, 697, 1128
- Hibon, P., Kashikawa, N., Willott, C., Iye, M., & Shibuya, T. 2012, *ApJ*, 744, 89
- Hoopes, C. G., Heckman, T. M., Salim, S., et al. 2007, *ApJS*, 173, 441
- Hu, E. M., Cowie, L. L., Barger, A. J., et al. 2010, *ApJ*, 725, 394
- Hu, E. M., Cowie, L. L., Songaila, A., et al. 2016, *ApJ*, 825, L7
- Hu, W., et al. 2017, *ApJL*, 845, L16
- Inoue, A. K., Shimizu, I., Iwata, I., & Tanaka, M. 2014, *MNRAS*, 442, 1805
- Ishigaki, M., Kawamata, R., Ouchi, M., et al. 2015, *ApJ*, 799, 12
- . 2018, *ApJ*, 854, 73
- Iye, M., Ota, K., Kashikawa, N., et al. 2006, *Nature*, 443, 186
- Izotov, Y. I., Orlitová, I., Schaerer, D., et al. 2016a, *Nature*, 529, 178
- Izotov, Y. I., Schaerer, D., Thuan, T. X., et al. 2016b, *MNRAS*, 461, 3683
- Izotov, Y. I., Thuan, T. X., & Guseva, N. G. 2017, *MNRAS*, 471, 548
- Izotov, Y. I., Worseck, G., Schaerer, D., et al. 2018, *MNRAS*, 478, 4851
- Jaskot, A. E., & Oey, M. S. 2013, *ApJ*, 766, 91
- Jaskot, A. E., Oey, M. S., Scarlata, C., & Dowd, T. 2017, *ApJ*, 851, L9
- Jiang, L., Egami, E., Fan, X., et al. 2013, *ApJ*, 773, 153
- Kashikawa, N., Shimasaku, K., Matsuda, Y., et al. 2011, *ApJ*, 734, 119
- Kauffmann, G., Heckman, T. M., Tremonti, C., et al. 2003, *MNRAS*, 346, 1055
- Kewley, L. J., Dopita, M. A., Sutherland, R. S., Heisler, C. A., & Trevena, J. 2001, *ApJ*, 556, 121
- Kewley, L. J., Maier, C., Yabe, K., et al. 2013, *ApJ*, 774, L10
- Kimble, R. A., MacKenty, J. W., O'Connell, R. W., & Townsend, J. A. 2008, in *Society of Photo-Optical Instrumentation Engineers (SPIE) Conference Series*, Vol. 7010, Society of Photo-Optical Instrumentation Engineers (SPIE) Conference Series

- Kimble, R. A., Woodgate, B. E., Bowers, C. W., et al. 1998, *ApJ*, 492, L83
- Koekemoer, A. M., Faber, S. M., Ferguson, H. C., et al. 2011, *ApJS*, 197, 36
- Konno, A., Ouchi, M., Nakajima, K., et al. 2016, *ApJ*, 823, 20
- Konno, A., Ouchi, M., Ono, Y., et al. 2014, *ApJ*, 797, 16
- Konno, A., Ouchi, M., Shibuya, T., et al. 2018, *PASJ*, 70, S16
- Kron, R. G. 1980, *ApJS*, 43, 305
- Krug, H. B., Veilleux, S., Tilvi, V., et al. 2012, *ApJ*, 745, 122
- Kümmel, M., Kuntschner, H., & Walsh, J. 2007, *Space Telescope European Coordinating Facility Newsletter*, 43, 8
- Kümmel, M., Kuntschner, H., Walsh, J. R., & Bushouse, H. 2011, Master sky images for the WFC3 G102 and G141 grisms, Tech. rep.
- Kümmel, M., Walsh, J. R., Pirzkal, N., Kuntschner, H., & Pasquali, A. 2009, *PASP*, 121, 59
- Kunth, D., & Östlin, G. 2000, *A&A Rev.*, 10, 1
- Laporte, N., Nakajima, K., Ellis, R. S., et al. 2017, *ApJ*, 851, 40
- Larson, R. L., Finkelstein, S. L., Pirzkal, N., et al. 2018, *ApJ*, 858, 94
- Laureijs, R., Amiaux, J., Arduini, S., et al. 2011, *ArXiv e-prints*, arXiv:1110.3193
- Laureijs, R., Gondoin, P., Duvet, L., et al. 2012, in *Proc. SPIE*, Vol. 8442, *Space Telescopes and Instrumentation 2012: Optical, Infrared, and Millimeter Wave*, 84420T
- Leitherer, C., Schaerer, D., Goldader, J. D., et al. 1999, *ApJS*, 123, 3
- Livermore, R. C., Finkelstein, S. L., & Lotz, J. M. 2017, *ApJ*, 835, 113
- Livermore, R. C., Trenti, M., Bradley, L. D., et al. 2018, *ArXiv e-prints*, arXiv:1805.05038
- Loeb, A., & Barkana, R. 2001, *ARA&A*, 39, 19
- Madau, P. 1995, *ApJ*, 441, 18
- Madau, P., & Haardt, F. 2015, *ApJ*, 813, L8

- Mainali, R., Zitrin, A., Stark, D. P., et al. 2018, ArXiv e-prints, arXiv:1804.00041
- Maiolino, R., Nagao, T., Grazian, A., et al. 2008, *A&A*, 488, 463
- Malhotra, S., Rhoads, J. E., Pirzkal, N., et al. 2005, *ApJ*, 626, 666
- Mason, C. A., Treu, T., de Barros, S., et al. 2018, *ApJ*, 857, L11
- Matsuda, Y., Yamada, T., Hayashino, T., et al. 2012, *MNRAS*, 425, 878
- Matthee, J., Sobral, D., Gronke, M., et al. 2018, ArXiv e-prints, arXiv:1805.11621
- Matthee, J., Sobral, D., Santos, S., et al. 2015, *MNRAS*, 451, 400
- Matthee, J. J. A., Sobral, D., Swinbank, A. M., et al. 2014, *MNRAS*, 440, 2375
- McLure, R. J., Dunlop, J. S., Cirasuolo, M., et al. 2010, *MNRAS*, 403, 960
- McLure, R. J., Dunlop, J. S., Bowler, R. A. A., et al. 2013, *MNRAS*, 432, 2696
- McQuinn, M., Hernquist, L., Zaldarriaga, M., & Dutta, S. 2007, *MNRAS*, 381, 75
- Mehta, V., Scarlata, C., Colbert, J. W., et al. 2015, *ApJ*, 811, 141
- Merson, A., Wang, Y., Benson, A., et al. 2018, *MNRAS*, 474, 177
- Mesinger, A., & Furlanetto, S. R. 2008, *MNRAS*, 385, 1348
- Miralda-Escudé, J. 1998, *ApJ*, 501, 15
- Miralda-Escudé, J., Haehnelt, M., & Rees, M. J. 2000, *ApJ*, 530, 1
- Miyazaki, S., Komiyama, Y., Sekiguchi, M., et al. 2002, *PASJ*, 54, 833
- Mo, H., van den Bosch, F. C., & White, S. 2010, *Galaxy Formation and Evolution*
- Mobasher, B., Dickinson, M., Ferguson, H. C., et al. 2005, *ApJ*, 635, 832
- Momcheva, I. G., Lee, J. C., Ly, C., et al. 2013, *AJ*, 145, 47
- Momcheva, I. G., Brammer, G. B., van Dokkum, P. G., et al. 2016, *ApJS*, 225, 27
- Momose, R., Ouchi, M., Nakajima, K., et al. 2014, *MNRAS*, 442, 110
- . 2016, *MNRAS*, 457, 2318

- Moré, J. J. 1978, *The Levenberg-Merquardt Algorithm: Implementation and Theory*, ed. G. A. Watson (SpringerVerlag: Berlin), 105–116, doi:10.1007/BFb0067690
- Nakajima, K., & Ouchi, M. 2014, *MNRAS*, 442, 900
- Nakajima, K., Ouchi, M., Shimasaku, K., et al. 2013, *ApJ*, 769, 3
- Natta, A., & Panagia, N. 1984, *ApJ*, 287, 228
- Nussbaumer, H., & Schmutz, W. 1984, *A&A*, 138, 495
- Oesch, P. A., Bouwens, R. J., Illingworth, G. D., et al. 2010, *ApJ*, 709, L16
- . 2014, *ApJ*, 786, 108
- Oesch, P. A., van Dokkum, P. G., Illingworth, G. D., et al. 2015, *ApJ*, 804, L30
- Oke, J. B., & Gunn, J. E. 1983, *ApJ*, 266, 713
- Ono, Y., Ouchi, M., Mobasher, B., et al. 2012, *ApJ*, 744, 83
- Onoue, M., Kashikawa, N., Willott, C. J., et al. 2017, *ApJ*, 847, L15
- Osterbrock, D. E. 1989, *Astrophysics of gaseous nebulae and active galactic nuclei*
- Östlin, G., Hayes, M., Duval, F., et al. 2014, *ApJ*, 797, 11
- Ota, K., Iye, M., Kashikawa, N., et al. 2010, *ApJ*, 722, 803
- . 2017, *ApJ*, 844, 85
- Ouchi, M., Shimasaku, K., Akiyama, M., et al. 2008, *ApJS*, 176, 301
- Ouchi, M., Mobasher, B., Shimasaku, K., et al. 2009, *ApJ*, 706, 1136
- Ouchi, M., Shimasaku, K., Furusawa, H., et al. 2010, *ApJ*, 723, 869
- Panagia, N. 2005, in *Astrophysics and Space Science Library*, Vol. 327, *The Initial Mass Function 50 Years Later*, ed. E. Corbelli, F. Palla, & H. Zinnecker, 479
- Parsa, S., Dunlop, J. S., & McLure, R. J. 2018, *MNRAS*, 474, 2904
- Peebles, P. J. E. 1993, *Principles of Physical Cosmology*
- Pentericci, L., Fontana, A., Vanzella, E., et al. 2011, *ApJ*, 743, 132

- Pentericci, L., Vanzella, E., Fontana, A., et al. 2014, *ApJ*, 793, 113
- Perlmutter, S., Aldering, G., Goldhaber, G., et al. 1999, *ApJ*, 517, 565
- Pirzkal, N., Rothberg, B., Ryan, R., et al. 2013, *ApJ*, 775, 11
- Pirzkal, N., Viana, A., & Rajan, A. 2010, The WFC3 IR 'Blobs', Tech. rep.
- Planck Collaboration, Ade, P. A. R., Aghanim, N., et al. 2016a, *A&A*, 594, A13
- Planck Collaboration, Adam, R., Aghanim, N., et al. 2016b, *A&A*, 596, A108
- Pogge, R. W., Atwood, B., Brewer, D. F., et al. 2010, in *Proc. SPIE*, Vol. 7735, Ground-based and Airborne Instrumentation for Astronomy III, 77350A
- Pozzetti, L., Hirata, C. M., Geach, J. E., et al. 2016, *A&A*, 590, A3
- Rafelski, M., Teplitz, H. I., Gardner, J. P., et al. 2015, *AJ*, 150, 31
- Rahmati, A., Pawlik, A. H., Raičević, M., & Schaye, J. 2013, *MNRAS*, 430, 2427
- Reddy, N. A., & Steidel, C. C. 2009, *ApJ*, 692, 778
- Rhoads, J. E., Malhotra, S., Dey, A., et al. 2000, *ApJ*, 545, L85
- Rhoads, J. E., Dey, A., Malhotra, S., et al. 2003, *AJ*, 125, 1006
- Rhoads, J. E., Malhotra, S., Pirzkal, N., et al. 2009, *ApJ*, 697, 942
- Rhoads, J. E., Malhotra, S., Stern, D., et al. 2013, *ApJ*, 773, 32
- Riess, A. G., Filippenko, A. V., Challis, P., et al. 1998, *AJ*, 116, 1009
- Roberts-Borsani, G. W., Bouwens, R. J., Oesch, P. A., et al. 2016, *ApJ*, 823, 143
- Robertson, B. E. 2010, *ApJ*, 716, L229
- Robertson, B. E., & Ellis, R. S. 2012, *ApJ*, 744, 95
- Robertson, B. E., Ellis, R. S., Furlanetto, S. R., & Dunlop, J. S. 2015, *ApJ*, 802, L19
- Robertson, B. E., Furlanetto, S. R., Schneider, E., et al. 2013, *ApJ*, 768, 71
- Rutkowski, M. J., Scarlata, C., Haardt, F., et al. 2016, *ApJ*, 819, 81
- Rybicki, G. B., & Lightman, A. P. 1986, *Radiative Processes in Astrophysics*, 400

- Salpeter, E. E. 1955, *ApJ*, 121, 161
- Sandberg, A., Östlin, G., Melinder, J., Bik, A., & Guaita, L. 2015, *ApJ*, 814, L10
- Santos, S., Sobral, D., & Matthee, J. 2016, ArXiv e-prints, arXiv:1606.07435
- Scarlata, C., Carollo, C. M., Lilly, S., et al. 2007, *ApJS*, 172, 406
- Scarlata, C., Colbert, J., Teplitz, H. I., et al. 2009, *ApJ*, 704, L98
- Schaerer, D. 2002, *A&A*, 382, 28
- . 2003, *A&A*, 397, 527
- Schaerer, D., Hayes, M., Verhamme, A., & Teyssier, R. 2011, *A&A*, 531, A12
- Schechter, P. 1976, *ApJ*, 203, 297
- Schenker, M. A., Stark, D. P., Ellis, R. S., et al. 2012, *ApJ*, 744, 179
- Schenker, M. A., Robertson, B. E., Ellis, R. S., et al. 2013, *ApJ*, 768, 196
- Schlafly, E. F., & Finkbeiner, D. P. 2011, *ApJ*, 737, 103
- Schlegel, D. J., Finkbeiner, D. P., & Davis, M. 1998, *ApJ*, 500, 525
- Schmidt, K. B., Treu, T., Trenti, M., et al. 2014, *ApJ*, 786, 57
- Schmidt, K. B., Treu, T., Bradač, M., et al. 2016, *ApJ*, 818, 38
- Sérsic, J. L. 1963, *Boletín de la Asociación Argentina de Astronomía La Plata Argentina*, 6, 41
- . 1968, *Atlas de Galaxias Australes*
- Shibuya, T., Kashikawa, N., Ota, K., et al. 2012, *ApJ*, 752, 114
- Shim, H., Colbert, J., Teplitz, H., et al. 2009, *ApJ*, 696, 785
- Siana, B., Teplitz, H. I., Colbert, J., et al. 2007, *ApJ*, 668, 62
- Siana, B., Teplitz, H. I., Ferguson, H. C., et al. 2010, *ApJ*, 723, 241
- Skelton, R. E., Whitaker, K. E., Momcheva, I. G., et al. 2014, *ApJS*, 214, 24
- Smith, B. M., Windhorst, R. A., Jansen, R. A., et al. 2016, ArXiv e-prints, arXiv:1602.01555

- Sobral, D., Matthee, J., Darvish, B., et al. 2015, *ApJ*, 808, 139
- Sobral, D., Smail, I., Best, P. N., et al. 2013, *MNRAS*, 428, 1128
- Spergel, D., Gehrels, N., Baltay, C., et al. 2015, *ArXiv e-prints*, arXiv:1503.03757
- Spitzer, Jr., L., & Greenstein, J. L. 1951, *ApJ*, 114, 407
- Stanway, E. R., Bremer, M. N., & Lehnert, M. D. 2008, *MNRAS*, 385, 493
- Stanway, E. R., Eldridge, J. J., & Becker, G. D. 2016, *MNRAS*, 456, 485
- Stark, D. P., Ellis, R. S., Bunker, A., et al. 2009, *ApJ*, 697, 1493
- Stark, D. P., Ellis, R. S., Chiu, K., Ouchi, M., & Bunker, A. 2010, *MNRAS*, 408, 1628
- Stark, D. P., Richard, J., Siana, B., et al. 2014, *MNRAS*, 445, 3200
- Stark, D. P., Richard, J., Charlot, S., et al. 2015, *MNRAS*, 450, 1846
- Stark, D. P., Ellis, R. S., Charlot, S., et al. 2016, *ArXiv e-prints*, arXiv:1606.01304
- Steidel, C. C., Bogosavljević, M., Shapley, A. E., et al. 2011, *ApJ*, 736, 160
- Stiavelli, M. 2009, *From First Light to Reionization: The End of the Dark Ages*
- Strömgren, B. 1939, *ApJ*, 89, 526
- Tilvi, V., Rhoads, J. E., Hibon, P., et al. 2010, *ApJ*, 721, 1853
- Trainor, R., & Steidel, C. C. 2013, *ApJ*, 775, L3
- Tremonti, C. A., Heckman, T. M., Kauffmann, G., et al. 2004, *ApJ*, 613, 898
- Trenti, M., & Stiavelli, M. 2008, *ApJ*, 676, 767
- Treu, T., Trenti, M., Stiavelli, M., Auger, M. W., & Bradley, L. D. 2012, *ApJ*, 747, 27
- Vanzella, E., Giavalisco, M., Inoue, A. K., et al. 2010, *ApJ*, 725, 1011
- Vanzella, E., Pentericci, L., Fontana, A., et al. 2011, *ApJ*, 730, L35
- Vanzella, E., de Barros, S., Vasei, K., et al. 2016, *ApJ*, 825, 41
- Vasei, K., Siana, B., Shapley, A. E., et al. 2016, *ApJ*, 831, 38
- Veilleux, S., & Osterbrock, D. E. 1987, *ApJS*, 63, 295

- Verhamme, A., Orlitová, I., Schaerer, D., & Hayes, M. 2015, *A&A*, 578, A7
- Verhamme, A., Schaerer, D., & Maselli, A. 2006, *A&A*, 460, 397
- Wang, Y. 2008, *J. Cosmology Astropart. Phys.*, 5, 21
- Wang, Y., Percival, W., Cimatti, A., et al. 2010, *MNRAS*, 409, 737
- Weiner, B. 2009, Star formation, extinction and metallicity at  $0.7 < z < 1.5$ : H-alpha fluxes and sizes from a grism survey of GOODS-N, HST Proposal, ,
- Wisotzki, L., Bacon, R., Blaizot, J., et al. 2016, *A&A*, 587, A98
- Zheng, Z., Cen, R., Trac, H., & Miralda-Escudé, J. 2010, *ApJ*, 716, 574
- . 2011, *ApJ*, 726, 38
- Zheng, Z.-Y., Wang, J., Rhoads, J., et al. 2017, *ApJ*, 842, L22